POLITECNICO DI MILANO

Facoltá di Ingegneria Industriale

Corso di Laurea in Ingegneria Spaziale

Design and optimization of a low-weight baffle for the laser altimeter BELA on board the ESA BepiColombo mission

Relatore: Prof. Michéle LAVAGNA

Tesi di laurea di:
Simone DEL TOGNO
Matr. 675766

Anno Accademico 2009 - 2010

Index

List of figures

List of tables

Abstract

This dissertation concerns the design and the optimization, from a thermal point of view, of a protective baffle for the transmitter part of the BepiColombo Laser Altimeter (BELA), which will operate in the Mercury's orbit.
The peculiar characteristics of the environment, in particular the short distance from the Sun and the presence of harmful agents, such as charged particles and strong UV and V-UV radiation, lead to the necessity of protecting the instrument from the environment. An optical filter has been implemented to reject the planetary fluxes, whereas a protective baffle must be designed to reject the solar radiation. Two different designs were candidates for this task: a cylindrical tube and a complex Stavroudis shape, which makes use of ellipsoids and hyperboloids.
The properties of the environment have been analyzed, determining the maximal and minimal radiation for each position of Mercury in its orbit around the Sun and for each position of the satellite around the orbit. The peaks of radiation, and the maximal / minimal values averaged along one orbit, have been determined for the planetary IR radiation, for the albedo and for the direct solar fluxes, defining the thermal worst cases the s/c will experience.
The possible treatments and coatings that can be applied to the two designs of the baffle have been investigated, focusing on the thermo-optical properties and the effect of their degradation under the expected environmental conditions. A campaign of tests has been carried out in situ to determine the effects of some thermal and mechanical treatments on titanium samples, representative of the cylindrical baffle.
A brief introduction to the general thermal problem is then presented, describing the Lumped Parameter method and the software used for the radiative analysis and the solution of the thermal network: ESARAD and ESATAN. A method to implement wavelength-dependant thermo-optical properties has been introduced. Finally, the thermal models of the two versions of the baffle are illustrated, and the results from the thermal analyses presented. The two concepts have been analyzed comparing the thermal requirements of the unit and the indexes of performance. These indexes include the rejection efficiency, the heat fluxes dumped to the s/c and inside the instrument, the maximal temperatures of baffle and filter.

Keywords: Mercury, BepiColombo, BELA, baffle, Stavroudis, thermo-optical properties, coatings and finishing

1 Introduction

1.1 The BepiColombo mission

BepiColombo is the European cornerstone mission to the innermost planet of the solar system: Mercury. Until now, only two spacecrafts approached Mercury: the American Mariner 10 in the '70s and MESSENGER, another American mission launched in 2004[1]. Despite the relatively short distance of Mercury, the flying path to reach the planet is high propellant and time consuming; further, the proximity of the Sun, with all the subsequent problems, arises many technological problems, especially from a thermal point of view. These are the main reasons why only two missions have ever been launched towards the first planet of our solar system.

Consequently, Mercury is still a widely unexplored and a mysterious planet, since all the data known about it derive from long range observations and from the few fly-bys of the above mentioned missions: no spacecrafts ever inserted into Mercury orbit. The MESSENGER spacecraft is expected to insert into Mercury orbit in March 2011 [1].

The scientific purposes of the BepiColombo mission are to study Mercury's internal and external structures, geology, topography and composition, the planet's magnetic field and the dynamics of its vestigial atmosphere. Further, the mission is expected to test Einstein's theory of general relativity, to search for asteroids sunwards of Earth and to perform a number of minor scientific experiments.

BepiColombo is named in honor of the scientist, mathematician and engineer Giuseppe Colombo (Padua, 1920 – Padua, 1984), for his contributions to the study of Mercury, the discovery of its orbital resonance and the development of the gravity assist technique, which made possible the Mariner 10 mission, the first human attempt to have a close look at Mercury.

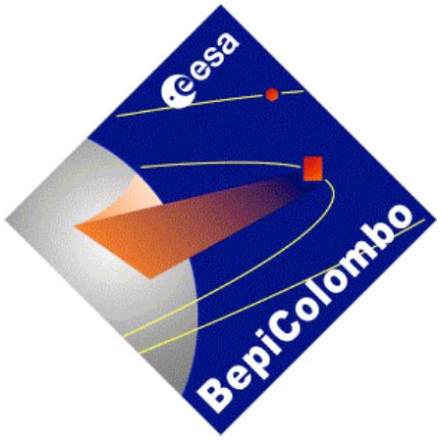

Figure 1-1: BepiColombo logo

The mission is carried out by the European Space Agency (ESA), with the support of the Japan Aerospace Exploration Agency (JAXA), and it involves two spacecrafts: the Mercury Planetary Orbiter (MPO) and the Mercury Magnetospheric Orbiter (MMO). The two satellites shall be launched together using an Ariane 5 carrier rocket from the Guiana Space Centre, located near Korou in French Guiana [2]. The launch is foreseen for July-August 2014: the two spacecrafts will fly together in a 6 year interplanetary course towards Mercury, with an expected arrival date of May 2020 [2]. During the cruise phase, the spacecrafts will be propelled by solar-electrical propulsion system, and they will perform Moon, Venus and Mercury gravity assists [3].

After few month of commissioning, the spacecrafts will start their one year long mission, with the possibility to extend their lifetime for another year.

The total estimated cost of the BepiColombo mission is 650 million Euros [4].

1.1.1 Comparison with other missions

A short description of Mercury-10 and MESSENGER will now be presented, in order to highlight the differences and the brand new characteristics of the BepiColombo mission.

1.1.1.1 Mariner 10

Mariner 10 was the first spacecraft ever to visit the planet Mercury. Launched in November 1973, it used the gravity assist of Venus to reach Mercury, performing only three fly-bys in a retrograde heliocentric orbit [5].
The scientific objective of Mariner 10 were to collect data and pictures about the planet, to study Mercury's environment, surface and atmosphere (if any); other important goals were to test the gravity assist maneuver and the capability of the technology of the time to withstand the harsh Mercury environment.
The s/c was a eight sides framework made of magnesium, approximately 1.39 m in diagonal and 0.46 m in depth, with a total mass of 502.9 kg [5].

Figure 1-2: Mariner 10 [6]

The scientific instruments included an optical imaging system, an IR radiometer, a UV airglow spectrometer and a UV occultation spectrometer, two magnetometers, a charged particles telescope and a plasma analyzer [7]. During the three fly-bys, the Mercury always presented the same side facing the Sun: therefore, the s/c was able to take photographs only of the 45% of the planet surface [1].

1.1.1.2 MESSENGER

The MEercury Surface, Space ENvironment, GEochemistry and Ranging (MESSENGER) is a NASA spacecraft launched in August 2004 [1] to study the planet Mercury. It will be the second human probe to visit the innermost planet and the first ever to insert into Mercury orbit. Orbital insertion is foreseen for March 2011 [1].
MESSENGER objectives are to characterize the chemical composition of the surface, to study the geological history of Mercury, the nature of its magnetic field, the size and the state of its core, the volatile inventory at the poles and its exosphere and magnetosphere. Another interesting goal would be to test the theory that Mercury is shrinking, contracting on itself as its core slowly freezes [1].
The MESSENGER probe is a squat box measuring 1.27 m x 1.42 m x 1.85 m [8], the total mass of the spacecraft is 1093 kg [1].

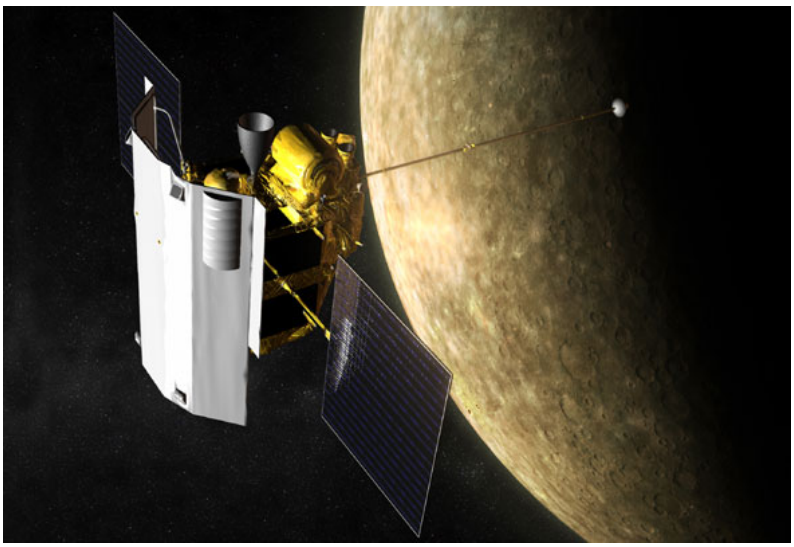

Figure 1-3: MESSENGER [9]

The s/c will be inserted in a strongly elliptical orbit, with the 200 km high periapsis at 60° north latitude, and an apoapsis of 15193 km; the orbital inclination will be 80° and the orbital period of 12 h [1]. Due to the orbit characteristics, MESSENGER will be able to have a close look only at the northern hemisphere, for which a topographical profile survey will be performed. The Mercury Laser Altimeter (MLA) is the main instrument which will be used to measure the surface relief and to provide for information about the s/c altitude.
MESSENGER has already successfully performed all the three expected fly-bys of the planet, providing for information and images of Mercury, including the previously unseen side of the planet.

1.2 The MPO and the MMO s/c

The MPO will have the shape of a flat prism and a mass of approximately 1075 kg [2]. The s/c is dedicated to the study of the planet's body and will carry a wide range of scientific instruments: spectrometers in the IR, UV, gamma and x-rays wavebands, a neutron spectrometer, wide-angle and narrow-angle cameras, a laser altimeter, a Near Earth Object telescope and detection system, and radio science experiments [3].

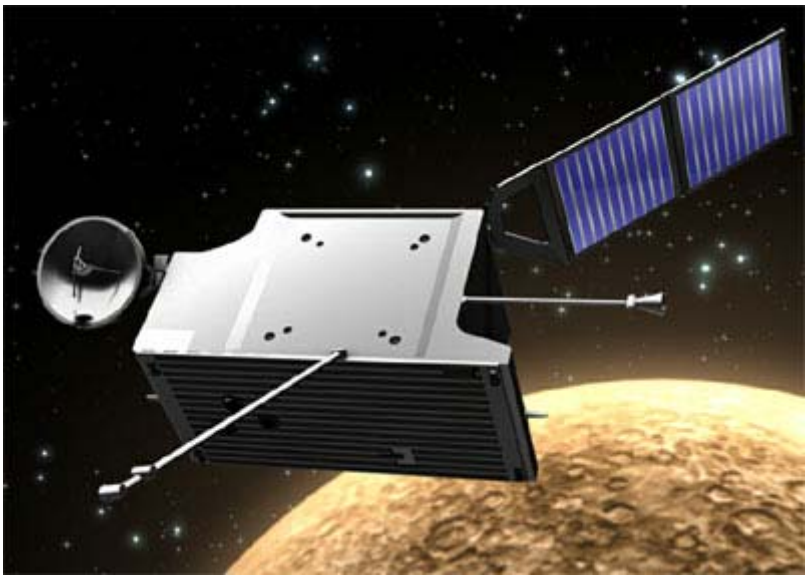

Figure 1-4: BepiColombo MPO [10]

The MMO s/c is developed with the contribution of the JAXA: it is a smaller satellite dedicated mainly to the study of the planet magnetosphere. The shape is a flat cylinder, for a total mass of about 250 kg [2]. The

MMO is planned to carry charged particles detectors, a wave receiver, a set of fluxgate magnetometers, a positive ion emitter and an imaging system [2],[11].

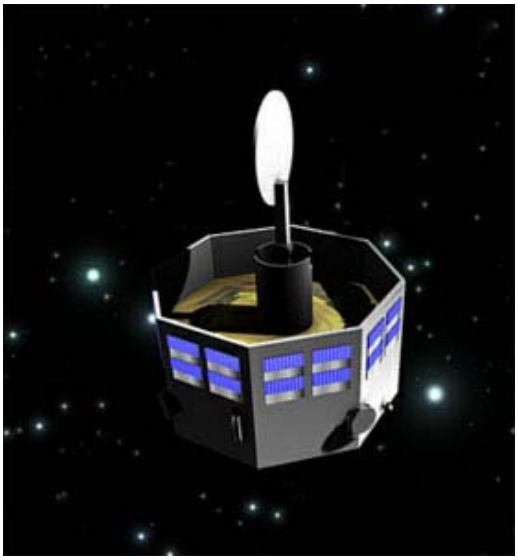

Figure 1-5: BepiColombo MMO [12]

1.3 The laser altimeter

The BepiColombo Laser Altimeter (BELA) is one of the instruments selected to fly on board the MPO.
While laser altimetry is a standard technique among airborne systems and for terrestrial satellites [13], its application for remote sensing on space systems outside Earth orbit is a very recent development. Up to now, only a few deep space missions involved laser altimeters: the Clementine probe to the Moon [14], the Mars Global Surveyor (MGS) to Mars [15], the NEAR Shoemaker probe to the asteroid Eros [16],[17] and the MESSENGER s/c towards Mercury [1],
The experiment will be the Europe's first planetary laser altimeter system: although the BELA has some similarities with the MLA, the s/c specific orbit and construction, together with a different approach to the base-lined range-finding, led to the research for and the development of novel concepts.
The BepiColombo Laser Altimeter is a joint Swiss-German project, developed by the Physikalisches Institut (Universität Bern, Switzerland) and the Institut für Planetenforschung (DLR, Berlin, Germany). The scientific tasks of the instruments are [17]:

- to measure the figure parameters of Mercury to establish accurate reference surfaces
- to determine the topographic variations relative to the reference figures and a geodetic network based on accurately measured positions of prominent topographic features
- to gauge the tidal deformation of the surface
- to measure the surface roughness, local slopes and albedo variations, also in permanently shaded craters near the poles

The selected orbit for the MPO represents a trade-off between accuracy requirements, which lead to low altitude orbits, and thermal requirements, which lead to high altitude orbits (in order to avoid high IR radiation from the planet). The resulting orbital period (2.32 h) is short, and comparable with the time constant for thermal equilibration of internal hardware [17]. The s/c is permanently nadir pointed: this entails that the Sun illuminates any instrument aperture up to an angle of 38° from the nadir direction immediately before and after the eclipse [17]. Further, the MPO spends a significant amount of time in the dayside hemisphere at low altitudes, receiving then simultaneously planetary radiation and sun light. These factors make the thermal design of the BELA, and of any instrument with clear aperture, considerably more challenging than any other system flown on space mission so far [17], MESSENGER included.

The peculiar characteristics of the orbit and of the environment led to the development of a high efficient insulator system, and underlined the necessity to protect the instruments from both direct sun light and planetary radiation: for these reason, it has been decided to implement baffles for both the transmitter and the receiver units.
A schematic of the BELA can be seen in Figure 1-6:

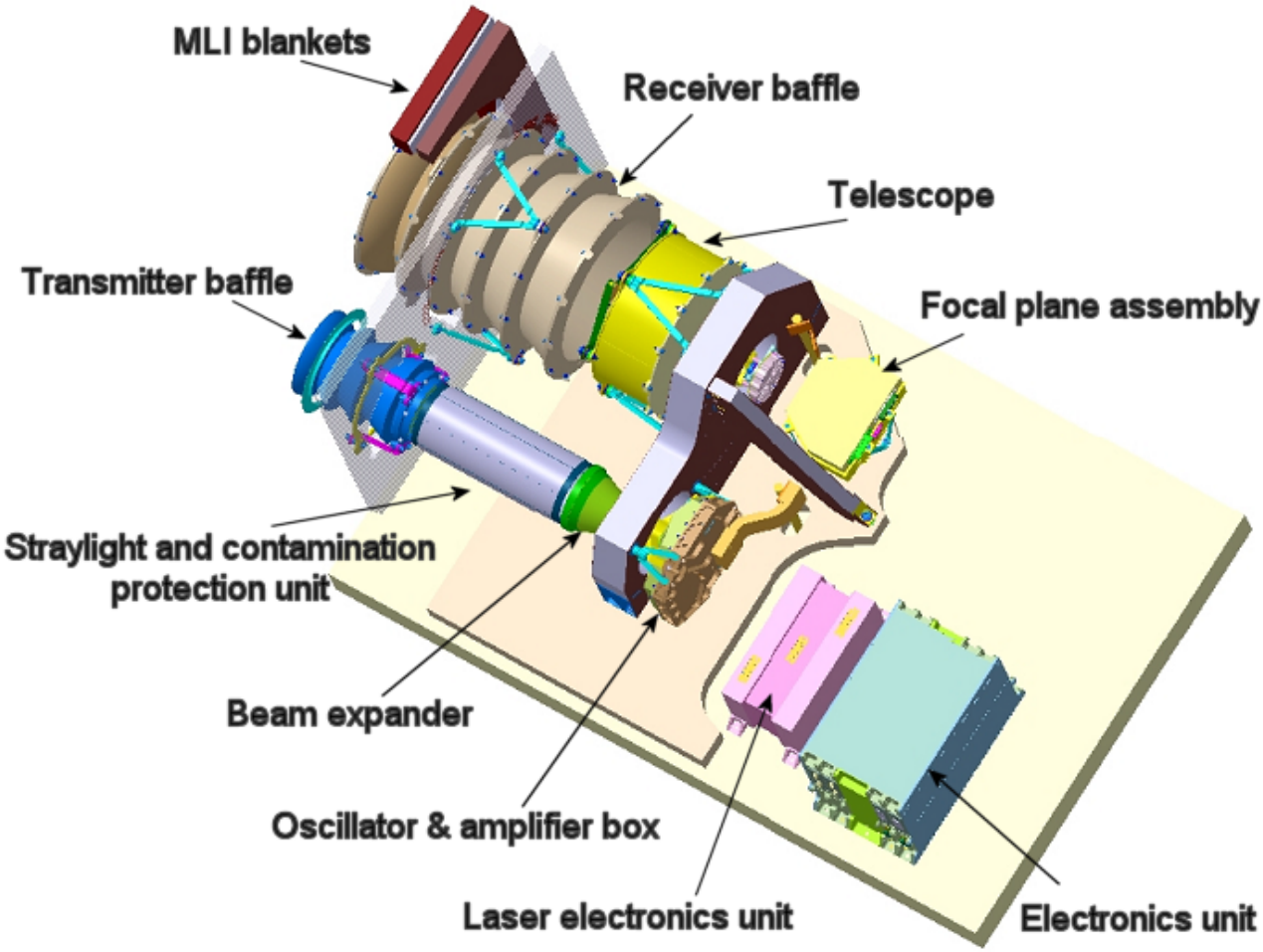

Figure 1-6: BELA schematics [18]

Since laser altimeters are bistatic systems, the transmitter components can be developed separately from the receiver ones [19]. The responsibility for the development of the instrument has been shared between the German Aerospace Center (DLR), which took care of the transmitter, and the University of Bern, responsible for the receiver.

1.3.1 The transmitter

A laser pulse at the wavelength of 1064 nm [17] is generated in the Laser Head Box, then the Beam Expander (the green cone in Figure 1-6) increases the laser beam diameter to the desired value. The laser beam passes then through the Straylight and Contamination Protection Unit (SPU), the pale blue cylinder in the picture. After that, the laser encounters an optical filter, which purpose is to protect the instrument from the IR environmental radiation. The filter, together with the transmitter baffle, is part of the Transmitter Baffle Unit (TBU). The transmitter baffle is the last component that the laser pulse meets before coming out of the instrument; it is represented by the deep blue shape on the left-bottom corner of Figure 1-6.
The laser beam is sent towards the planet surface, where is partially absorbed and partially reflected: most of the reflected share is scattered away and a small part is reflected towards the s/c.

1.3.2 The receiver

The very weak reflected pulse is collected by the Receiver Baffle Unit (RBU), the beige component in Figure 1-6. After that, there is the Receiver Telescope, the yellow cylinder in the picture, which purpose is to focalize the beam to the primary mirror of the Back End Optics: its purposes are to filter the incoming signal and to perform a wave front correction. Finally, the detector and the analogue electronics collect the beam and the signal is processed by the electronics units.

1.4 The Transmitter Baffle Unit (TBU)

The purpose of the TBU is to minimize the environmental heat fluxes entering the instrument through the transmitter aperture. The proximity of the Sun and the low altitude of the s/c orbit around Mercury, which surface experiences very hot temperatures, lead to the need to implement dedicated systems to reduce the environmental heat load.

There are three main sources of heat radiation: the Mercury IR emission, the albedo and the direct sun light. The first two components are aligned with the instrument axis, because the s/c always presents a nadir pointing attitude. Since it is not possible to obscure the laser clear aperture [20], an optical filter has been introduced in order to reflect or absorb as much as possible the albedo and the Mercury IR emission, guaranteeing a very high transmissivity at the laser wavelength.

The sunlight is instead always slanted with respect to the instrument axis: the minimal angle experienced through the whole mission lifetime is 38° [21]. Therefore, a rejecting baffle can be introduced to eliminate off axis sunlight between 38° and 90° from the boresight, or at least to reduce it as much as possible. The presence of a reflective baffle is one of the main differences in the laser altimeter design compared to the MLA.

1.4.1 The baffle body

A baffle has the function to protect the entrance of the instrument from direct light illumination, usually sunlight, in a specified aspect angle range with regard to the optical axis. The requirements for the TBU baffle, related with the environmental radiation, are the following:

BEL-REQ-7601: A baffle for the transmitter shall be implemented which shall limit sunlight entering the instrument to <1% of the flux at the aperture when the Sun is in the range 35° to 90° from the instrument line of sight. [20]

BEL-REQ-7602: The transmitter baffle shall reject, on average along an orbit, >90% of the environment fluxes (IR, albedo, and sunlight) striking it. [20]

It has to be noted that there are no requirements concerning the baffle shape or its working principle. Usually, the unwanted light may be indifferently reflected or scattered on diffuse black surfaces and eventually trapped within the baffle. In this case, the amount of power trapped within the baffle is severely constrained: the MPO s/c has to cope with as much as ten times the solar constant compared to Earth orbit, and furthermore an unavoidable high thermal flux is already entering the instrument: the planetary flux. In order to reduce the device temperature, the amount of trapped radiation should therefore be reduced.

The design of the baffle body is focused mainly on three parameters: the shape, the material and the optical coatings.

1.4.2 The narrow-band-pass filter

The filter should present a narrow bandpass around the laser wavelength (1064 nm), while blocking all the other wavelengths mainly by means of reflection. Different companies have presented their proposal: the chosen filter would be produced by MSO Jena, which developed a dielectric filter capable of achieving a transmissivity peak around the laser wavelength greater than 95 %, as specified by requirements [20]. The spectrum of the MSO Jena filter is shown in Figure 1-7.

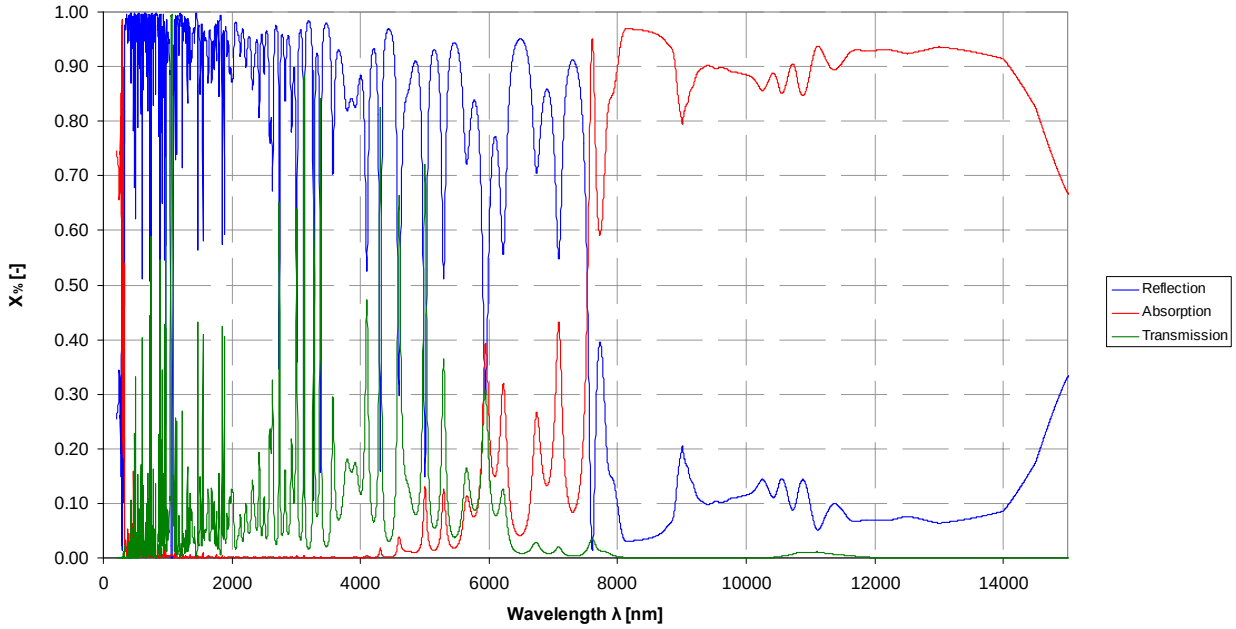

Figure 1-7: The spectrum of the filter

Sapphire (Al_2O_3) has been selected as the substrate material for its relatively high thermal conductivity, with respect to fused silica substrates. A high value of thermal conductivity allows for small temperature gradients on the filter, and hence lower deformations and optical aberrations. Furthermore, sapphire presents a coefficient of thermal expansion close to that of Titanium, which is the material chosen for the filter mount: this reduces the thermally induced stresses and consequently the distortion of the laser beam. Finally, the melting point of sapphire is very high [22]. MSO Jena guarantees the filter functionality up to 400 °C [23]. Unfortunately, sapphire present a very high mass density (about 3980 $kg \cdot m^{-3}$ [22]), and this entails a very high mass.

1.5 The Straylight and contamination Protection Unit (SPU)

The SPU is composed mainly by a cylindrical body, placed between the TBU and the beam expander. Its purposes are to protect the instrument for the residual straylight and to protect both filter and beam expander front lens against contaminations. A schematic of the SPU can be seen in (Figure 1-8).

The SPU cylinder consists in an Aluminum structure on which one or two thin MLI foils are wrapped around. The outer surface of the MLI foils is coated using Vapor Deposited Gold (VDG) in order to reduce the heat exchange with the s/c interior; the inner side is made of Black Kapton, used to absorb the residual straylight which went through the filter. The SPU cylinder is supported by a Carbon Fiber Reinforced Plastic (CFRP) structure.

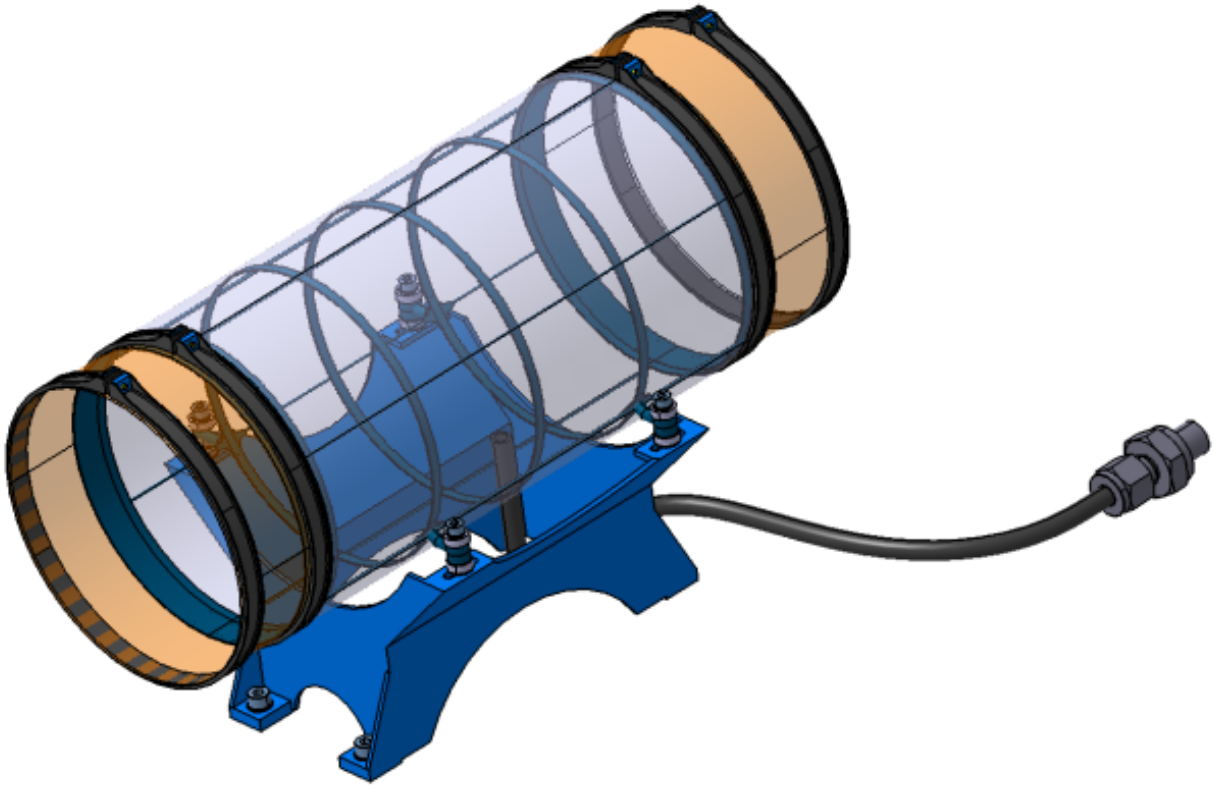

Figure 1-8: The SPU

1.6 Opened issues

At the moment of the beginning of this work, the general architecture of the system had already been decided, leaving the option of the choice of the best baffle shape and strategy.

The main goal was the development of the thermal model of both the TBU and SPU units and their surrounding elements. The following step was the execution of detailed thermal analyses in order to understand the system thermo-optical functioning; many sensitivity analyses have also been performed to understand the key parameters of the system and how to improve the device performances. There were some iterations, to take into account for mechanical updates and changes that revealed to be necessary after the first thermal results. This process has been executed for two different baffle architectures.

The study of the Mercury environment, the MPO orbit and the calculation of the environmental fluxes was also necessary. The comprehension of the orbital conditions was necessary for the following step, the choice of suitable materials and optical coatings. The study of the MPO orbits during the whole mission lifetime was a key factor in the determination of the worst cases to be analyzed and to pick out the critical conditions, like the entrance into and exit from the eclipses. The calculation of the environmental radiation served to impose the boundary conditions of the thermal problem of the system.

In parallel, a study of the possible materials and especially of the possible optical coatings was performed. The purpose was to identify the adoptable and most suitable materials and coatings, to optimize the thermal behavior of the device and to minimize the absorbed environmental load.

Finally, a comparison of the two strategies adopted for the instrument was performed, with the consequent decision on the best solution to be adopted for the instrument.

2 Baffle selection

2.1 Introduction

The first step is the choice of the baffle shape. Many possible solutions have been investigated by Contraves Space: the Radovich [24] configuration, the Modified Radovich [25], the Greynolds [26], the Stavroudis [27],[28],[29], the Linlor [30],[31], the Winston Compound Parabolic Concentrator (CPC) [32] and the Vanesse [33] concept. Contraves Space focused on the research of the most performing and reliable system, which resulted to the Stavroudis concept. The receiver unit of the BELA, which has very strong performances requirements and good mass budget allocation, selected this configuration as the most suitable. Unfortunately, the Stavroudis solutions resulted to be also very complex, heavy and difficult to build and to integrate. These problems are particularly relevant for the transmitter unit, which baffle is significantly smaller and therefore all the issues concerning accuracy of construction, alignment and reliability are amplified. A parallel research for a simpler solution has therefore been carried out.

A simple cylinder can operate as a rejection baffle, with a lower efficiency but with significant advantages in terms of weight, simplicity of construction and maintainability, reliability, possibility to apply optical coatings. This solution entails however higher absorbed environmental fluxes and higher temperatures.

The system has been developed taking into account for two possible solutions: a cylindrical baffle, which is expected to be less efficient, but simpler and less resources consuming, and the Stavroudis concept, which proved to be the most efficient design. All the others solutions proposed by Contraves Space, which performances resulted halfway between the two adopted concepts, have not been taken into account.

2.2 Cylindrical baffle

2.2.1 Description

The simplest version of a transmitter baffle consists in a cylinder. The simplicity of this shape allows for low mass, simplicity and inexpensiveness of construction, and most of all reliability. This solution is even the best concerning the possibility of applying optical coating: its simplicity and uniformity allows for a wide number of different application techniques. On the other hand, the cylindrical baffle is expected to be less efficient and to achieve very high temperatures.

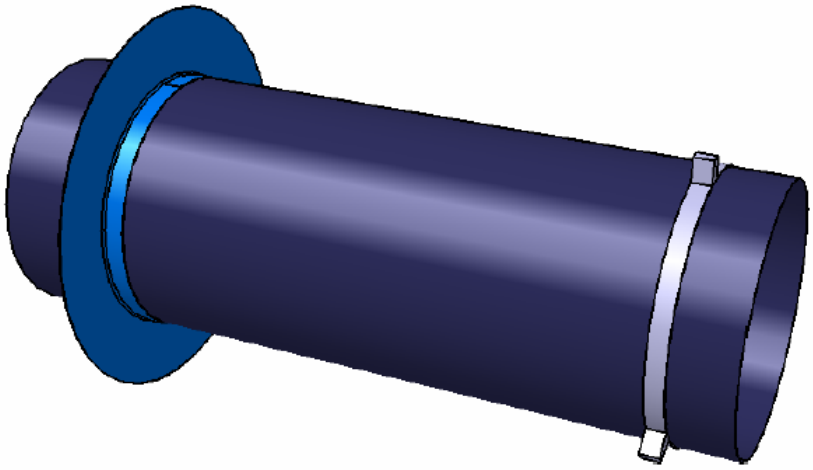

Figure 2-1: The cylindrical baffle

In Figure 2-1 it is possible to see a CAD model to the cylindrical baffle: on the front, the metallic disc used as MLI spacer is clearly visible, and in the back a metallic ring used to connect the baffle to the s/c is present.

2.2.2 Material selection

The material to be used for the cylindrical baffle should comply with the following requirements:

- Resistance to high temperatures
- Low density
- High thermal conductivity (to avoid high thermal gradients)
- Good mechanical strength and stiffness
- Not outgassing in vacuum and at high temperatures
- Possibility to apply optical coatings *or*
- Good thermo-optical properties of the uncoated material

Unfortunately, a material capable to satisfy all the listed requirements does not exist.

Composites materials and plastics were immediately discarded, as a consequence of their outgassing behavior, especially at high temperatures. Outgassing would be particularly harmful due to the presence of optics.

Also ceramics cannot be used: whereas these materials are very suitable to withstand high temperatures, they present inadequate mechanical properties. In particular, ceramics are too fragile and cannot be machined; furthermore, the low fracture point prevents the realization of very thin walls, causing even the issue of a mass increase.

As a consequence, metals are the only class of material that can be used. The best candidates after the first selection were aluminum, titanium and nickel. The physical and thermal properties of these metals are listed in the Table 2-1.

Metal	Thermal conductivity [$W \cdot m^{-1} \cdot K^{-1}$]	Density [$kg \cdot m^{-3}$]	Ultimate Yield strength [MPa]	Melting temperature [°C]
Al 6061	167	2700	310	660
Al 7075	130	2800	570	660
Nickel	88.5	8900	790	1453
Ti 6242	7.78	4500	1050	1667

Table 2-1: Material selection for the cylindrical baffle [34]

There are other relevant thermal parameters which can be analyzed in order to select the best candidate. The first one is the heat capacity, which expressed the propensity of a material to absorb heat. Another fundamental parameter, not always reported in datasheets, is the thermal diffusivity, defined as:

$$\alpha = \frac{k_{COND}}{\rho \cdot c_P} \qquad \textit{eq. 2-1}$$

It expresses the ratio between thermal conductivity and heat capacity, and is measured in square meters per second. The last described thermal parameters for the selected materials are reported in Table 2-2.

Metal	Thermal conductivity [$W \cdot m^{-1} \cdot K^{-1}$]	Specific heat [$J \cdot kg^{-1} \cdot K^{-1}$]	Thermal diffusivity [$10^{-5}\ m^2 \cdot s^{-1}$]
Al 6061	167	917	6.75
Al 7075	130	917	5.06
Nickel	88.5	452	2.20
Ti 6242	7.78	610	0.28

Table 2-2: Thermal parameters for the selected materials

Since the thermal conductivity expresses the propensity of a material to transmit heat by means of conduction and the thermal capacity represents the amount of energy which the material is able to

accumulate for unit of volume, the thermal diffusivity can be seen as the ratio between heat transmitted by conduction and absorbed heat.
The cylindrical baffle, due to its low efficiency, is expected to become very hot. Preliminary numerical simulations showed the cylinder can reach temperatures up to 400 °C, near the melting point of the metal. Since the expected temperatures are not far below the melting point, the mechanical properties listed in Table 2-1 cannot be considered reliable. As a consequence, aluminum cannot be used.
Both nickel and titanium can withstand very high temperatures without compromising their mechanical properties. Nonetheless, titanium is significantly lighter than nickel and has better mechanical properties. Furthermore, titanium is more suitable for the application of optical coatings, which have already been tested and used for space applications [35],[36],[37]. On the other hand, titanium shows a significantly smaller thermal conductivity.
In consideration of the higher application temperature and mechanical properties and the lower mass required, it has been decided to use titanium for the cylindrical baffle.

2.2.3 Manufacturing

Another advantage of the cylindrical baffle is the easiness of manufacturing: a single sheet of titanium foil, with a thickness of 0.2 mm, can be cut and eventually polished or treated without particular problems. The titanium foil would than be bended and electrosoldered.
This process entails a very quick, economic and reliably way to produce the baffle shape; it also allows to polish or to treat the surface while the baffle is still a plain foil, with the consequents advantages in terms of easiness of application of the coating and accuracy of the operation.

2.3 Stavroudis baffle

2.3.1 Description

The Stavroudis baffle would be much more complex than the cylindrical baffle. Its shape is optimized to reflect as much as possible the solar radiation outside the instrument [25], and it is composed by a series of frustums with elliptical and hyperbolical profiles. The Stavroudis concept was first described in 1994 [28], and this solution has been adopted for other units of the BELA and instruments of the BepiColombo MPO: the Receiver Baffle Unit (RBU) [17] and the baffle of the MERTIS instrument [38].
Despite of his high efficiency, the Stavroudis baffle entails some issues: the required volume is larger than the one require by simple baffles; the construction procedure is very complex (especially the intersection between ellipses and hyperbolas) and the device requires high accuracy to guarantee a proper functioning; the construction and integration phase is more expensive; the application of coatings in the internal surface is hampered by the complex shapes and a specific process should be developed for that.
The complexity of the shape entails a clever choice of the material, and the design of a proper system to mechanically and thermally connect the baffle body to rest of the instrument. A schematic of the Stavroudis baffle can be seen in Figure 2-2.

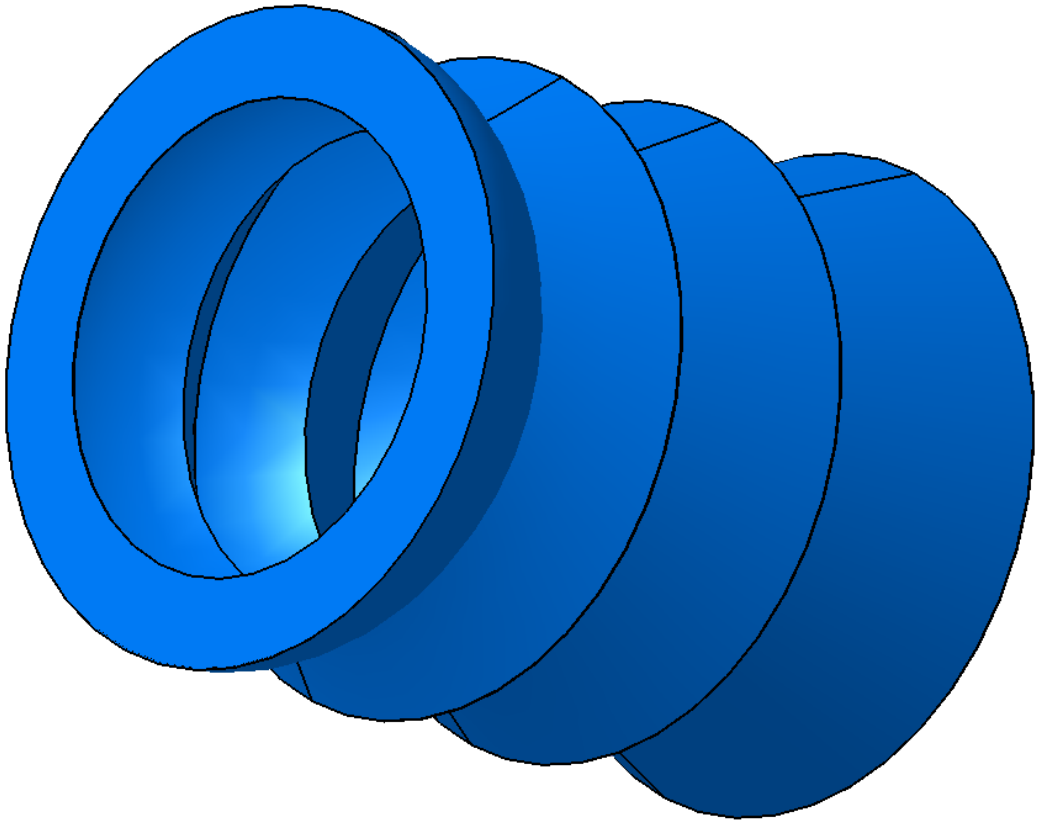

Figure 2-2: The Stavroudis baffle

The ellipsoids face the environment and the hyperboloids the inner side of the instrument. The front side of the baffle presents a disc (on the left in Figure 2-2), which has the same internal radius of the baffle. The purpose of this disc is to limit the environmental fluxes coming from the axial direction, since the baffle is not optimized to reflect the radiation coming from this direction (see §2.3.2). In particular, the front disc of the baffle would continuously be subjected to planetary radiation. It is necessary to protect this part from the environmental radiation, adding an additional front ring, which purpose is to avoid reaching too high temperatures on the front disc and to transmit too high heat fluxes to the baffle.

2.3.2 Mathematical definition

The Stavroudis concept is a completely reflective baffle: no light trapping technique is used, and therefore this makes the Stavroudis baffle particularly desirable for application in hot environments, like the orbit around Mercury is.

The Stavroudis design takes advantage from some peculiar properties of specific conic sections of revolution: the oblate spheroid, or ellipsoid, generated by rotating an ellipse around its minor axis, and the hyperboloid, obtained rotating a hyperbola around its conjugate axis. The foci of these shapes are also rotated about the axes of the conics, drawing a circle.

The reflective baffle is composed by a succession of vanes whose outward facing surfaces are ellipsoids and whose backward facing surfaces are hyperboloids. An annular section is placed at the baffle aperture, so that the focus ring lies exactly at the edge of the baffle's aperture.

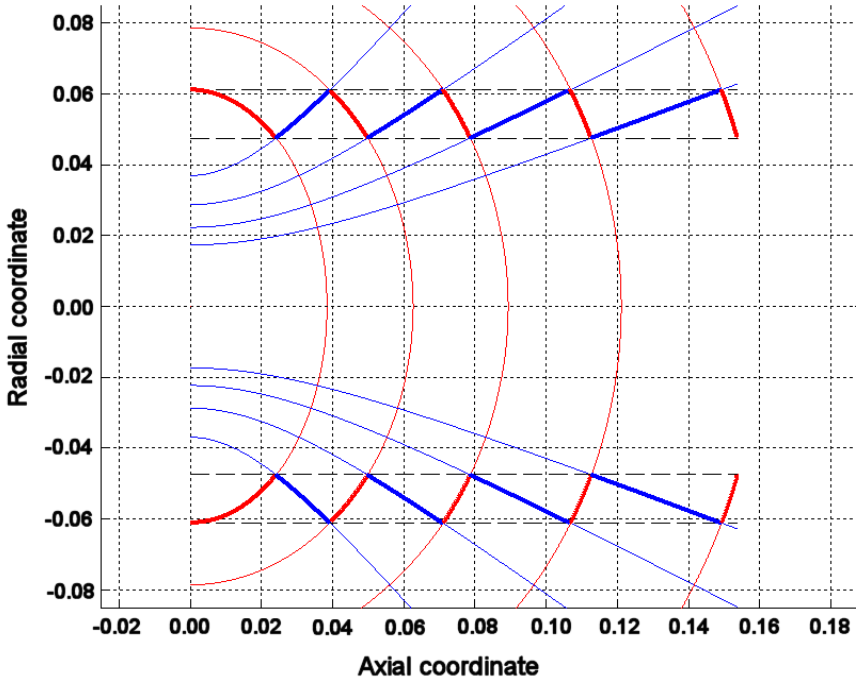

Figure 2-3: Stavroudis shape generation

A fundamental property of the ellipse, which is the key functioning of the Stavroudis baffle, is that the surface normal vector at all points on the ellipse always points between the two focal points. This implies that every ray intersecting any point of the ellipse from between the two focal points will be reflected on a trajectory which passes through the two foci. The hyperbola presents a similar property: any ray directed towards between the focal points, will be reflected passing again between the two focal points.

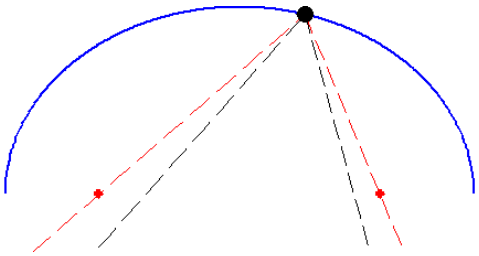

Figure 2-4: Ellipse

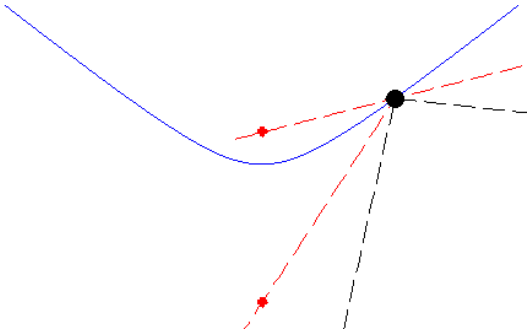

Figure 2-5: Hyperbola

From the preceding sentences, we can infer that any ray entering the baffle aperture (which coincides with the focus ring), and lying in a plane containing the axis of revolution, which strikes an outward surface (an ellipsoid), will be reflected toward the baffle aperture, without intersecting any other surface.

If on the contrary the ray is intercepted by a backward surface (a hyperboloid), whose focus ring coincides with that one of the ellipsoid, the ray is reflected toward the previous ellipsoids [28], from which it will be reflected toward the aperture.

Hence, any ray lying in a plane containing the rotation axis that strike the baffle surface is rejected from the device with one or maximum two reflections. Rays with an angle of incidence below the minimal rejection angle, which is determined by the baffle inner radius and length, pass through the baffle and reach the back aperture (the blue surface in Figure 2-6).

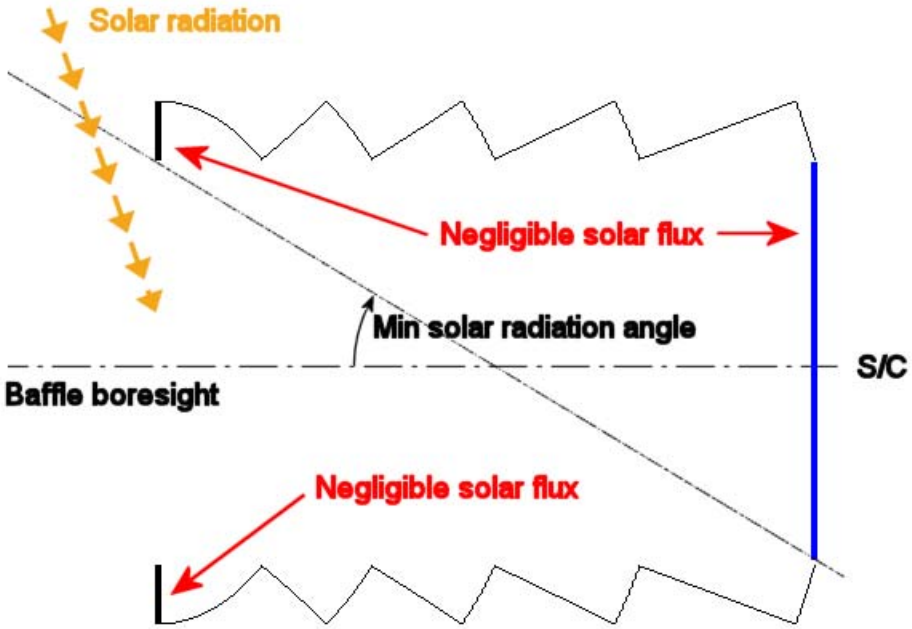

Figure 2-6: Range of angles of the incident radiation which is rejected

From a purely geometrical point of view, the Stavroudis baffle is determined by three parameters: the internal and external diameters, and the length of the instrument, which is determined by the minimal aspect angle of the radiation that the requirements prescribe to reject.

The perfect rejection (assuming perfect specular reflectance) of the Stavroudis baffle for incident radiation beyond the minimal angle is mathematically demonstrated in two dimensions, using the cross section of the baffle. Surprisingly, this desirable behavior has been numerically confirmed also for the three dimensional situation, which takes into account for the slanted beams, which lay outside the plane that contains the baffle boresight [28]. In the tridimensional case the average number of reflection before the expulsion of the incident beam is <1.3 [39], which is an indicator of the excellent performance of the system. The real surface, indeed, cannot present an absorptance equal to zero, and the amount of absorbed heat fluxes is proportional to the average number of reflections.

2.3.3 Material selection

The material suitable for the construction should comply with the same requirements for the cylindrical TBU:

- Low density
- High temperature resistance
- Good thermal conductivity (to avoid high thermal gradients)
- Discrete mechanical properties
- Possibility to apply optical coatings *or*
- Good thermo-optical properties of the uncoated material

With an important addition: the manufacturing process should guarantee a high accuracy in terms of shape, thickness homogeneity and surface polish.

Possible candidates were titanium, aluminum and nickel. Titanium was not suitable for its hardness, which would make the manufacturing process too problematic; furthermore, it has quite high density and low thermal conductivity. Aluminum was a better choice: the building process is easier, the thermal conductance higher and the weight lower.

The solution that has been chosen is nickel: instead of machining the baffle by turning, as for aluminum, it is possible to use the electroforming technique, which guarantees higher levels of shape accuracy and surface smoothness.

2.3.4 Manufacturing

The Stavroudis baffle is produced by electroforming, which guarantees all the three requirements for the baffle: accuracy, thickness homogeneity and surface polish. The company selected for the process is NiCoForm Inc., based in New York, USA. The NiCoForm process implies the use of a particular nickel alloy, named NiColoy®.

Property	Value
Composition	Nickel – 95% Min Cobalt – balance
Density	~8900 $kg \cdot m^{-3}$
Thermal conductivity	~90 $W \cdot m^{-1} \cdot K^{-1}$
Specific thermal capacitance	444 $J \cdot kg^{-1} \cdot K^{-1}$
Maximal temperature rating	316 °C
Yield strength	827 ÷ 1280 MPa
Ultimate yield strength	1030 ÷ 1450 MPa
Modulus of elasticity in bending	152 ÷ 165 GPa
Shear modulus	57.9 ÷ 63.4 GPa

Table 2-3: NiColoy® properties [40],[41]

Electroforming is a highly specialized process of metal components fabrication which makes uses of electrodeposition in a plating bath form. The desired object is synthesized by controlling the electrodeposition of the specific metal passing through an electrolytic solution onto a metal form. The chemical bath and the details of the process depend upon the desired metal and the specific characteristics which are required.

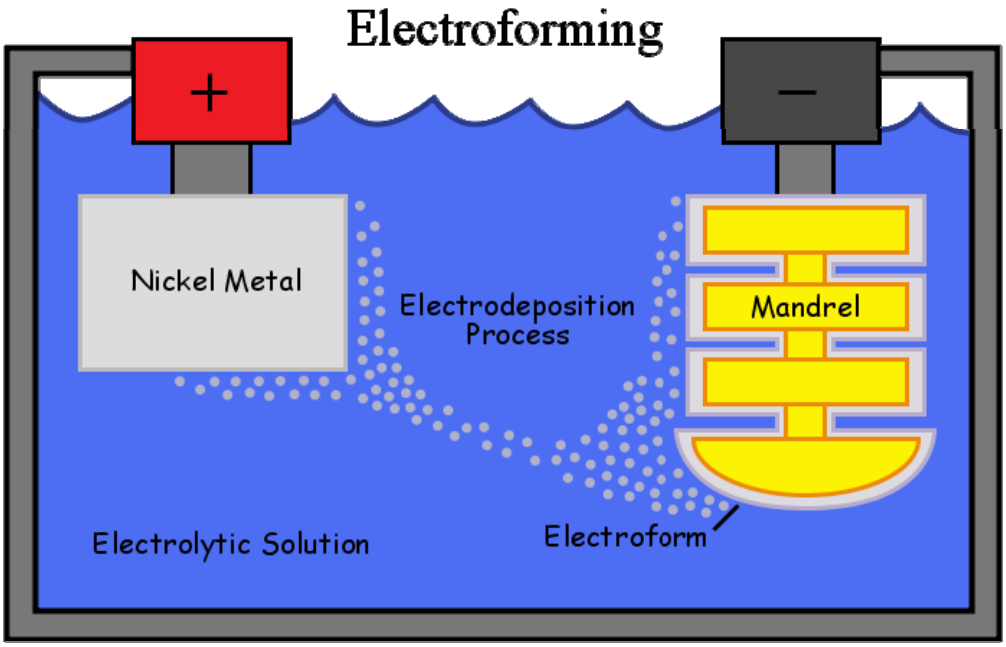

Figure 2-7: The electroforming process [42]

The advantage of the electroforming process is that it reproduces the form or mandrel to within 1 μm without the shrinkage and distortion associated with other metal forming techniques such as casting, stamping or drawing. Further, since the mandrel is machined as an outside surface, close dimensional tolerances and high surface finishes can be held and maintained on complex interior configurations.

A relevant drawback is that thermo-mechanical treatments should be applied after the electroforming. Since the resulting shape is required to be very thin, the mentioned treatments may represent an issue for nickel body. Also the application of vapor or chemical deposition coatings should be applied after the electroforming, and the complex Stavroudis shape makes the operation more complex.

3 Mercury environment

3.1 Mercury

Mercury is the innermost planet of our solar system, and one of the less explored. It features a high inclined and eccentric orbit very close to the Sun. The rotation of the planet about its own axis is very slow, and as a consequence the solar day, the duration of time during which a single point on the surface is illuminated, is longer than the hermean year: 176 days with respect to 116 days.

Mercury's size is between the Moon and Mars, and it is the smallest planet of solar system. Its exceptional density and the presence of a magnetic dipole fields suggest the presence of a large liquid iron core. The atmosphere is very tenuous, and it mostly consists of particles which have been trapped by the magnetic field: charged particles from the solar wind or small molecules ejected from the surface.

Figure 3-1: The planet Mercury

Mercury is locked in an orbital resonance: the spin angular velocity is 1.5 times the orbital mean motion: for this reason, the Mercury's orbital period is 1.5 times the planet's rotational period. This situation is shown in Figure 3-2.

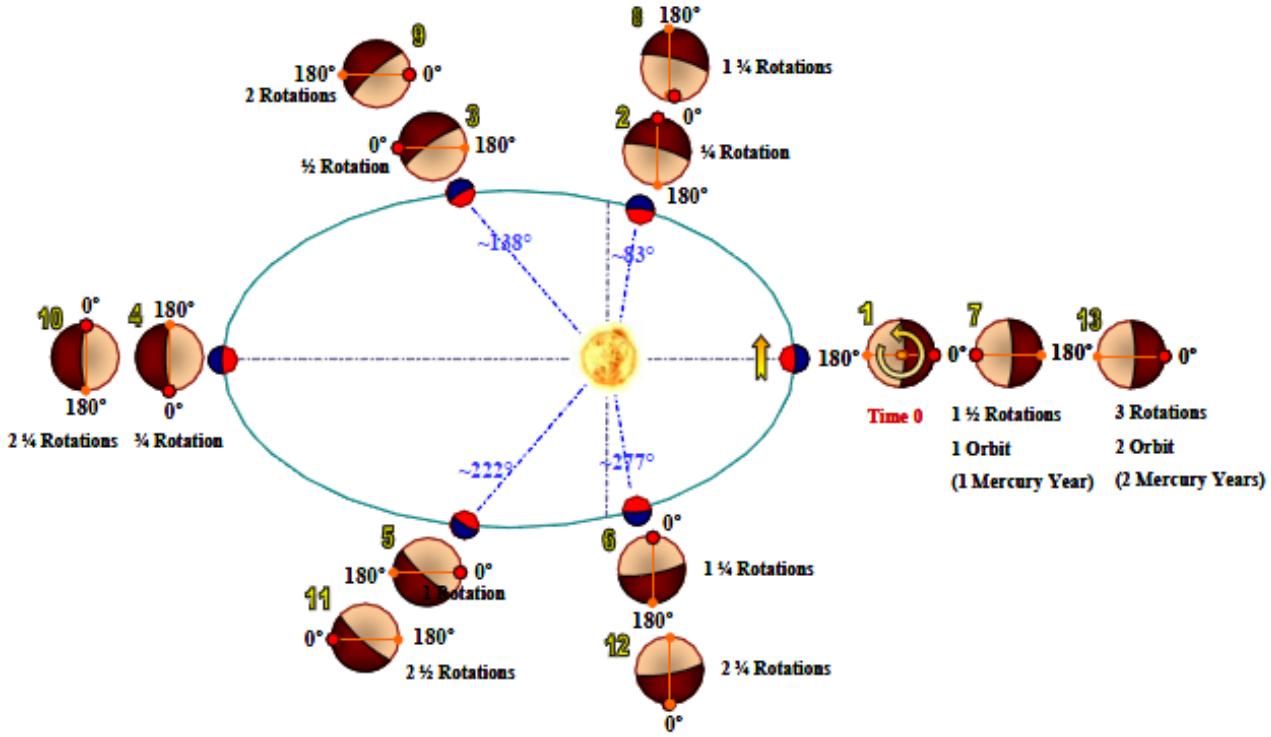

Figure 3-2: Mercury's orbital resonance [43]

The proximity of the Sun, together with the long duration of the hermean day, causes the surface of Mercury to reach the highest temperature in the solar system: up to 725 K [44]. Another consequence of the orbital resonance is the long night period experienced by the surface, which can cause a minimal temperature of 90 K [44].

A summary of Mercury's orbital and bulk properties is given in Table 3-1 and Table 3-2.

Parameter	Value
Perihelion	$46.001 \cdot 10^6$ km
Aphelion	$69.817 \cdot 10^6$ km
Semi-major axis	$57.909 \cdot 10^6$ km
Orbit eccentricity	0.205632
Orbit inclination	7.004986°
Longitude of the ascending node	48.3309°
Longitude of the perihelion	77.4561°
Sidereal orbit period	87.97 days
Sidereal rotation period	58.646 days
Synodal period	115.88 days
Length of the solar day	175.94 days

Table 3-1: Mercury orbital parameters (J2000) [45],[46],[47]

Parameter	Value
Mass	$0.3302 \cdot 10^{24}$ kg
Volume	$6.083 \cdot 10^{10}$ kg
Mean density	5427 kg·m^{-3}
Equatorial radius	2439.99 km
Polar radius	2439.99 km
Planet eccentricity	0.0000
Bond albedo	0.119
Visual geometric albedo	0.138
Surface maximal temperature	90 K
Surface minimal temperature	725 K
Black body temperature	442 K
Estimate J_2	$(60 \pm 20) \cdot 10^{-6}$

Table 3-2: Mercury bulk properties [45],[46]

3.2 MPO orbit evolution

The s/c orbit has been selected so that, when Mercury is at the perihelion and therefore its illuminated side experiences the maximal temperature, the MPO minimal altitude (the periherm) is over the night side of the planet. In this way, it is possible to reduce the IR heat load, which would be in addition combined with the solar flux.

The gravity field local anomalies and the environmental perturbation will slightly modify the MPO orbit after its insertion: the periherm argument shall change from the initial value of 16° to 344° after one year and 312° after 2 years [48] (extended mission); also the altitude of the periherm and of the apoherm shall undergo some minor changes. A representation of the MPO's orbit evolution is depicted in Figure 3-3; a summary of the orbit changes is given in Table 3-2.

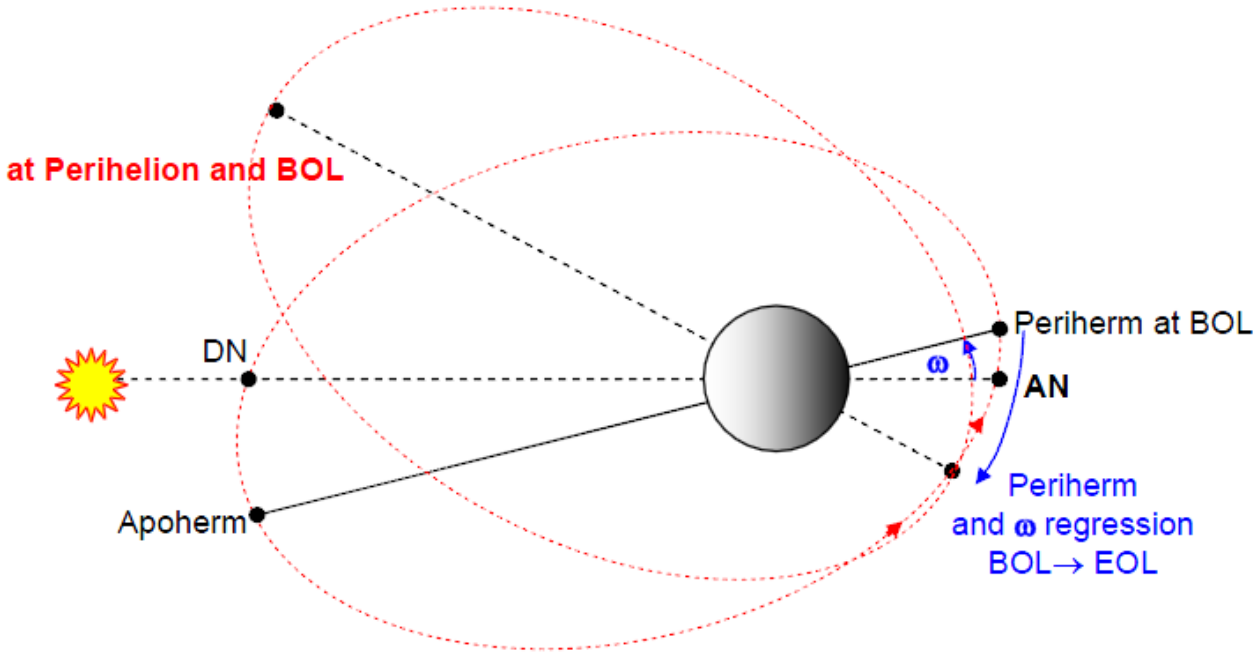

Figure 3-3: MPO's orbit evolution [48]

	Nominal (NOM)	Insertion (BOL)	After 1 year (EOL)	After 2 years (EEM)
Altitude of the periherm [km]	400	400	400	400
Altitude of the apoherm [km]	1508	1508	1508	1481
Periherm argument [deg]	0	16	344	312

Table 3-3: Orbital parameters evolution [48]

3.3 Environmental fluxes

In order to assess the environmental fluxes and the critical conditions that the MPO s/c will withstand through the whole mission lifetime, many simulations have been performed along the whole Mercury's orbit considering its evolution. The purpose is the calculation of the environmental fluxes: their maximums and minimums, both at single time instants and as average values, give an indication of the most severe conditions the s/c will experience.

The environmental heat loads have been calculated numerically, using the same software which will be used for the real model (ESARAD v6.2, see §5.1.4); since the purpose is not the solution of a thermal network for a system, but only the calculation of the environmental radiation, the model has been replaced by a black body disc, with the baffle clear aperture diameter and oriented in the same way of the real device. A simulation of the MPO orbit around Mercury has been run for each position of the planet along its orbit around the Sun: using an angle step of 3.75°, a total of 96 orbits have been simulated. Along the revolution of Mercury around the Sun, the orbital elements of the s/c have been considered constants. The environmental fluxes have been calculated for the BOL, EOL and for the extended mission orbits.

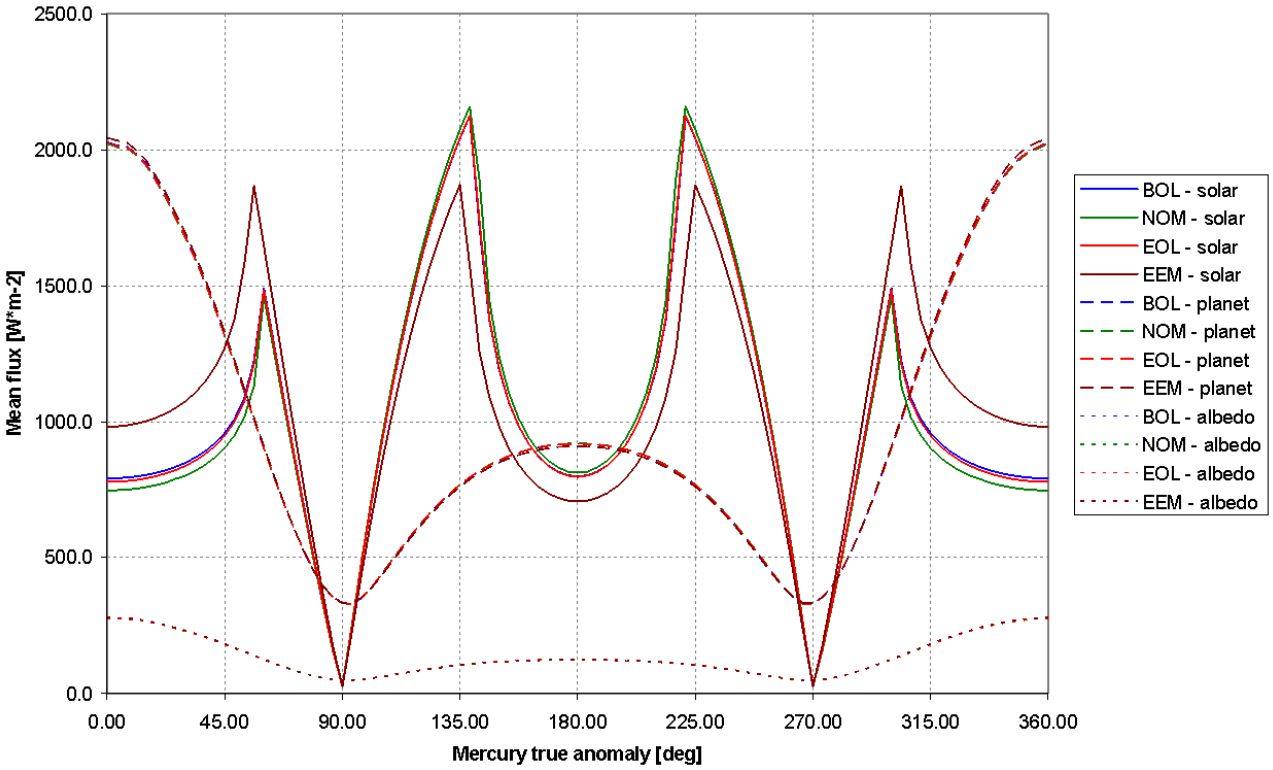

Figure 3-4: Average environmental heat fluxes along an MPO orbit, for different anomalies of MPO periapsis

In Figure 3-4 it is possible to see the results for the nominal orbit (NOM), the BOL, EOL and EEM orbits: the results shown in the picture are the fluxes averaged along one orbit of the s/c around Mercury. The

previous chart is intended to provide for information about the amount of energy which is absorbed by the s/c on the long period, for different position of the planet around the Sun.
The solar fluxes are represented using continuous lines, the IR planetary fluxes using a dashed line and the albedo fluxes using a dotted line. Both planetary and albedo fluxes show almost no differences between the different orbits; instead, the orbit evolution influences the solar fluxes: while for the nominal, BOL and EOL orbit the solar fluxes are very similar, a big difference arises when the EEM orbit is considered.
The maximums of albedo and planetary average fluxes always occur when Mercury is at the perihelion (see Figure 3-6), as expected: in this position, the distance from the Sun is the minimal one (and then, the highest albedo fluxes), and the planet surface temperature is the highest (hence, the highest IR fluxes). The fluxes coming from the planet, both albedo and IR emission, decrease as Mercury moves along its orbit, reaching a minimum in the "spring/autumn" position, in which the Mercury true anomaly is 90° (see Figure 3-7); after that, the fluxes rise again to a local maximum when Mercury is at the aphelion: in this position, the s/c periherm is over the illuminated side of the planet, and this causes the local maximum. However, since at aphelion the distance from the planet is strongly higher that at perihelion, the solar radiation is weaker and the planet is colder: hence, the local maximum of the planetary fluxes is lower than at perihelion. The rest of the graph is symmetrical.
The solar flux shows a more complex trend. While the attitude towards the planet is always constant (nadir pointing), the attitude towards the Sun is variable, and the solar fluxes depend on the orientation of the satellite with respect to the Sun and the eclipse time duration. When Mercury is at the aphelion, the solar fluxes are at a local minimum. When the planet proceeds along its orbit, the exposure to the solar radiation increases till a local maximum, after which there is a rapid decrement: when the true anomaly of Mercury is 90°, the s/c attitude is so that the instrument panel is always perpendicularly oriented with respect to the Sun, and hence the solar radiation is null. The solar radiation reaches another maximum when the true anomaly is 138.75°: in this position, the s/c never enters into the eclipse area, and its average attitude with respect to the Sun presents a low aspect angle (see Figure 3-8). The local minimum when Mercury is at aphelion is caused by the long eclipse period that the s/c experience.
The sum of the environmental fluxes presents a more irregular trend, with two equivalent maximums at about 3100-3400 $W \cdot m^{-2}$ (for all the orbits): the first occurs when the planet is at perihelion, the second one when the Mercury's true anomaly is 138.75° (for the nominal, BOL and EOL orbits) or 52.5° (for the EEM orbit, see Figure 3-9). The minimum instead always occurs in the "spring/autumn" position, when the true anomaly is 90°, where the only significant radiation is the planetary IR emission.
The average fluxes along the MPO orbit are important for the long period dynamics: for the short period temperature peaks, it's also important to analyze of the environmental radiation peaks along one MPO orbit.
As can be seen in Figure 3-5, the solar environmental radiation has its absolute peak when Mercury is at the perihelion; the position of the s/c along the satellite orbit cannot be inferred from the chart. The minimum of the maximal radiation along one orbit is zero, and it occurs when Mercury is in the "spring/autumn" position, since the instrument panel of the s/c is oriented perpendicularly with respect to the Sun. There is a lower local maximum, which arises for a true anomaly of 138.75°.
The planetary IR fluxes and especially the albedo fluxes proved to be less dangerous for the s/c, in particular for the short period dynamics: therefore, the fluxes peaks charts for albedo and IR emission were not considered during the definition of the thermal worst cases.

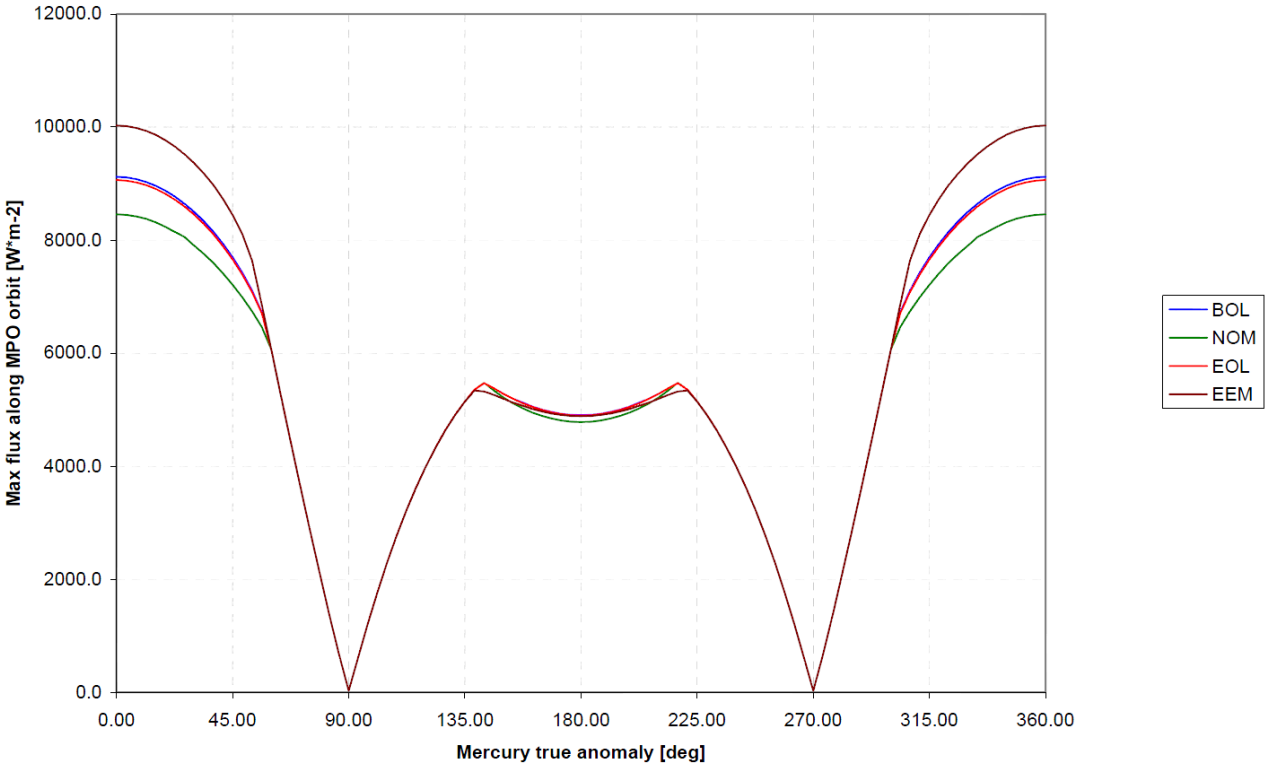

Figure 3-5: Peak Sun flux for different anomalies of MPO periapsis

3.4 Worst cases

On the basis of the previous analysis, it is possible to identify the worst hot and cold cases that the instrument should face for the BOL, EOL and EEM orbits. These worst cases are in terms of s/c orbits: the functioning of the device would be analyzed for a whole orbit around Mercury in each of the defined cases.
Considering the BOL orbit, the first worst case, Hot Case 1, occurs with Mercury at perihelion: in this position, the IR, albedo and total average fluxes have their maximum; further, even the solar flux peak occurs here.

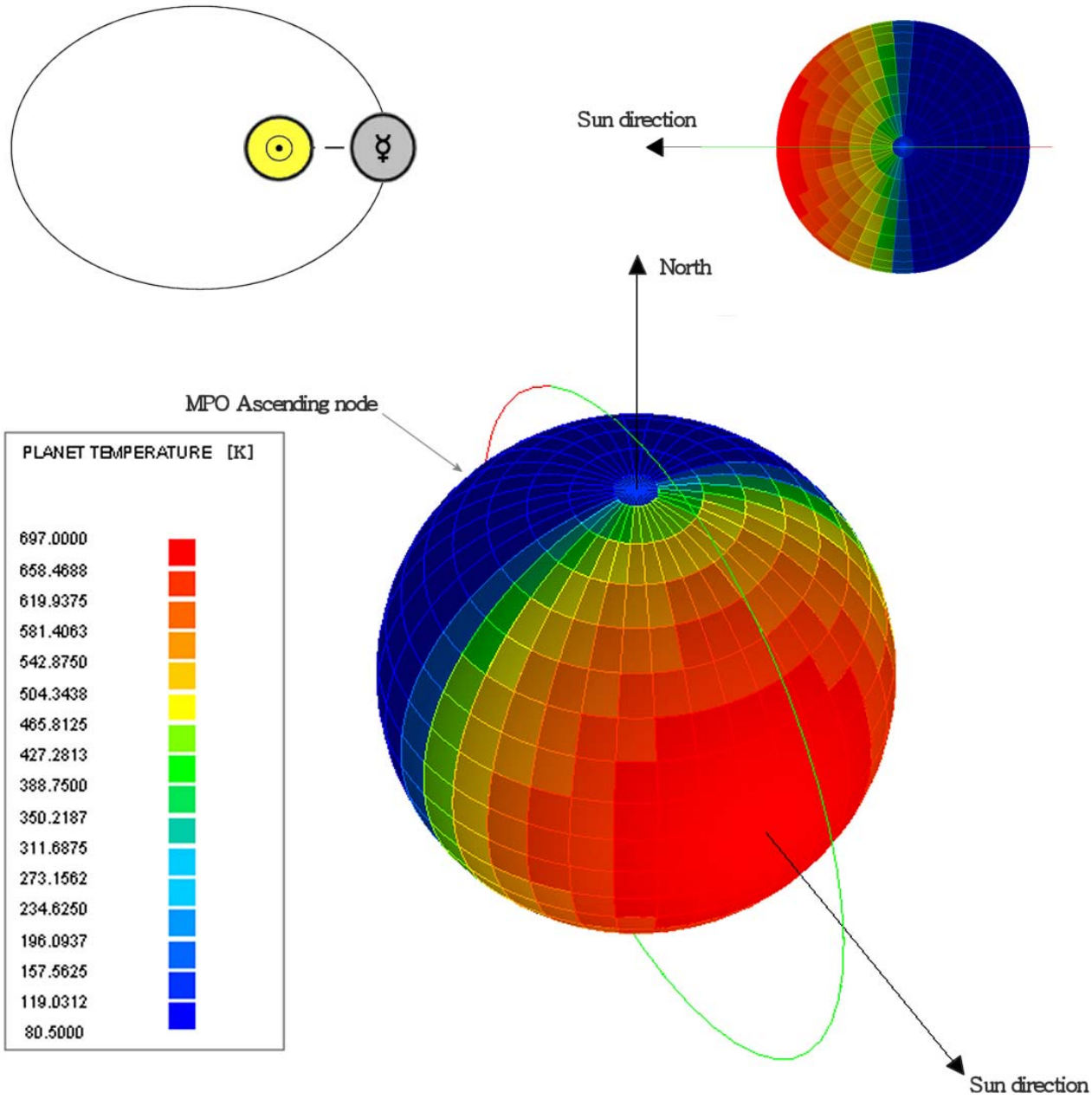

Figure 3-6: Hot Case 1

When the true anomaly of Mercury is 90°, the planet is in the "spring/autumn" position: this position entails the minimum of all the environmental fluxes, both averaged and as peaks.

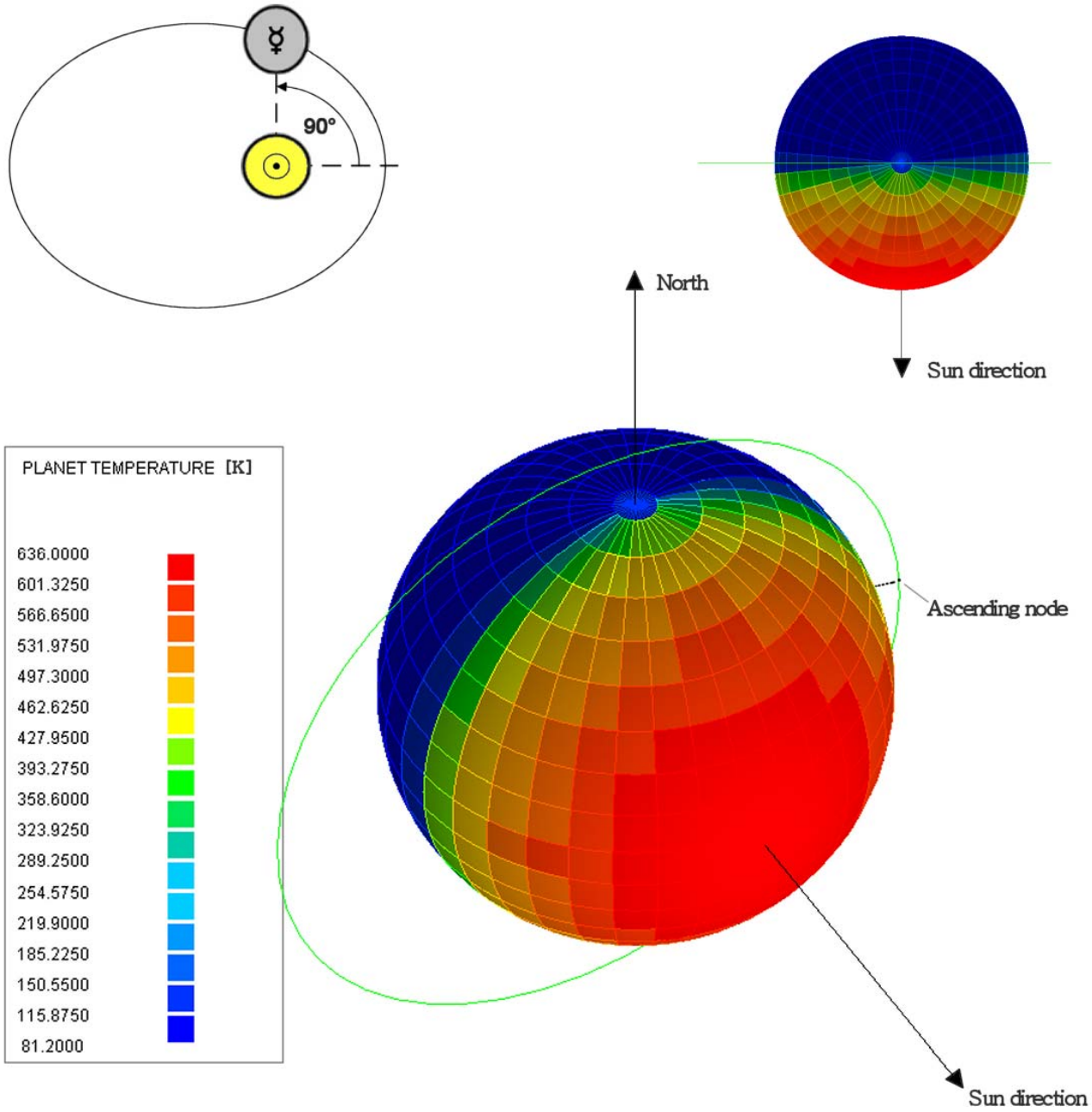

Figure 3-7: Cold Case 1

When the planet is in the position which corresponds to a true anomaly of 138.75°, there is another maximum. The solar average flux is at its maximum, and even the sum of all the averaged environmental radiation is almost equal to the first maximum, which occurs when Mercury is at perihelion.

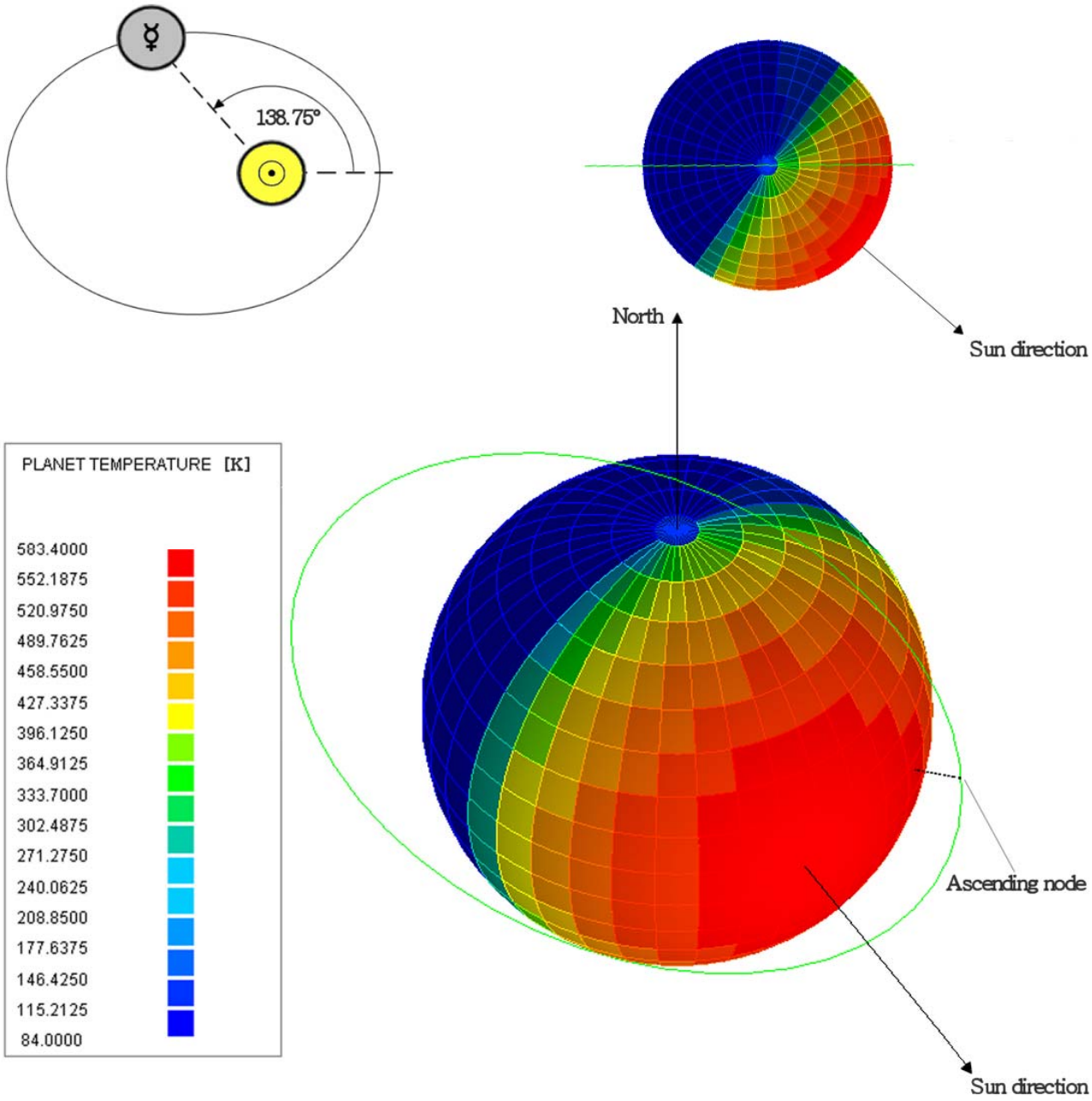

Figure 3-8: Hot Case 2

Considering the EOL orbits, the situation is qualitatively the same: the worst cases Hot 3, Cold 2 and Hot 4 occur at the same positions of Hot 1, Cold 1 and Hot 2. Due to the small difference of the argument of the periherm, the environmental fluxes result slightly different from the BOL orbits; the pictures of Hot Case 3, Cold Case 2 and Hot Case 4 are not depicted, since they are qualitatively identical to those of the BOL orbits. Analyzing the EEM orbits, it can be observed again that Hot Case 5 and Cold Case 3 occur are almost identical to Hot Case 1 and Cold Case 2; however, the peak of the solar averaged radiation is no more at 138.75° but it occurs for a true anomaly of the planet of 5.5° (see Figure 3-4). Hot Case 6 is therefore different from Hot Case 2 and Hot Case 4.

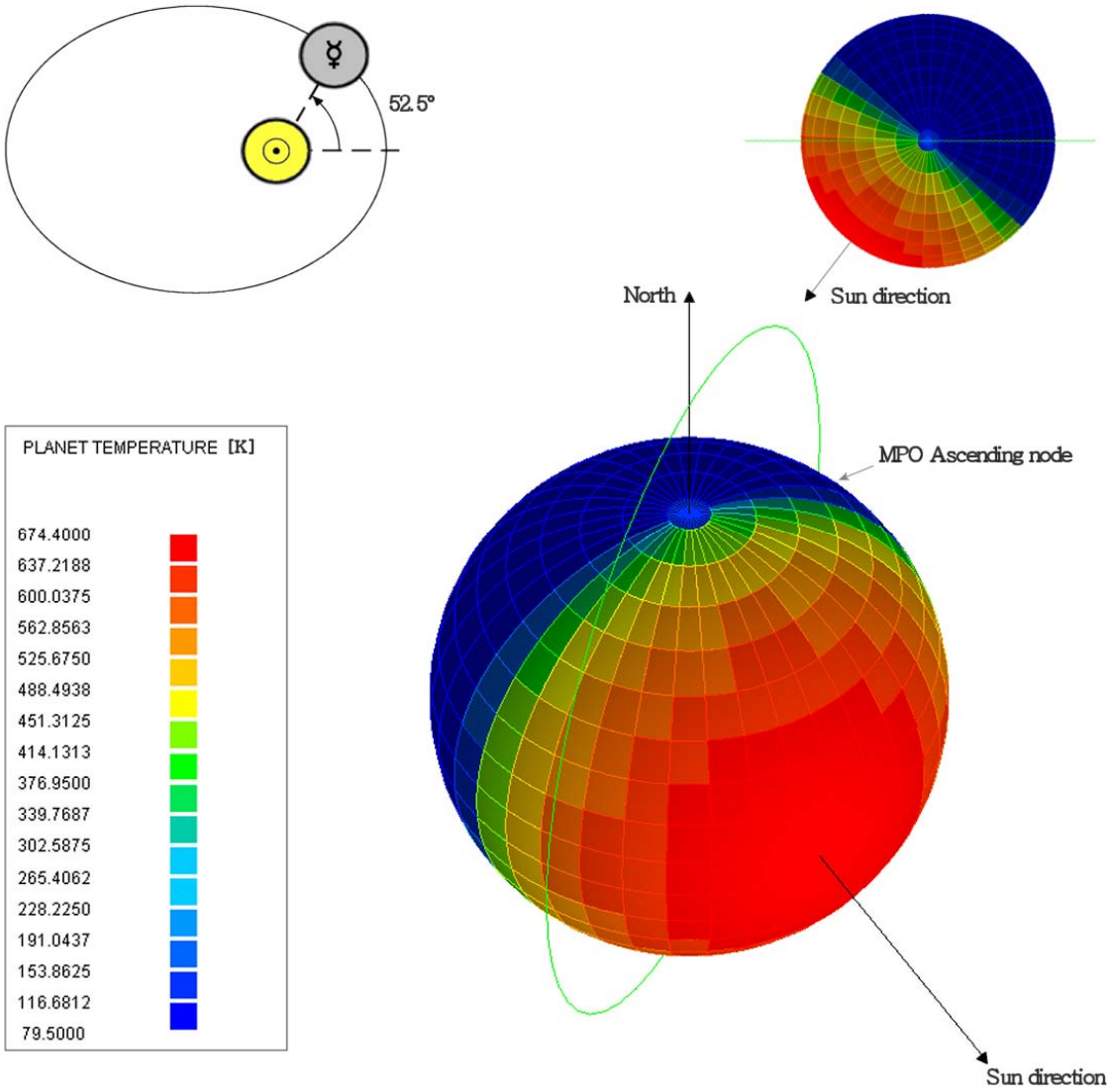

Figure 3-9: Hot Case 6

A summary of the Worst Cases parameters is given in Table 3-4, the average fluxes for each orbit are given in Table 3-5.

Case	Orbit	Mercury anomaly [deg]	Sun distance [10^6 km]	Periherm [km]	Apoherm [km]	MPO periherm argument [deg]
Hot 1	BOL	0	46.001	400	1508	16
Cold 1	BOL	90	61.089	400	1508	16
Hot 2	BOL	138.75	67.507	400	1508	16
Hot 3	EOL	0	46.001	406	1502	334
Cold 2	EOL	90	61.089	406	1502	334
Hot 4	EOL	138.75	67.507	406	1502	334
Hot 5	EEM	0	46.001	434	1474	312
Hot 6	EEM	52.5	63.505	434	1474	312
Cold 3	EEM	90	61.089	434	1474	312

Table 3-4: Worst Cases definition

Case	Solar [W•m^{-2}]	Albedo [W•m^{-2}]	Mercury IR [W•m^{-2}]	Total [W•m^{-2}]
Hot 1	791.48	276.75	2002.14	3070.37
Cold 1	26.16	49.97	341.01	417.14
Hot 2	2124.06	109.11	871.18	3104.35
Hot 3	816.12	276.63	2001.24	3093.99
Cold 2	26.16	50.03	341.48	417.67
Hot 4	2106.89	109.02	870.44	3086.35
Hot 5	1139.26	281.01	2032.90	3453.17
Hot 6	2252.28	155.43	1137.73	3545.44
Cold 3	26.16	50.33	343.21	419.70

Table 3-5: Worst Cases environmental averaged fluxes

The average total environmental radiation for the first four Hot Cases (BOL and EOL mission) feature almost the same value of about 3100 W·m^{-2}; in the same way, the Cold Cases for BOL and EOL mission are almost identical, with an average total heat flux of about 417 W·m^{-2}. The EEM orbit instead proved to be slightly hotter: for Hot Case 6, an average total environmental radiation of 3500 has been estimated; nonetheless, the thermal design should be performed taking into account only for the BOL and EOL parameters, while the EEM orbits is used only to provide for some extra information about the possibility of the instrument to survive a longer mission.

3.5 Harmful characteristics of the Mercury orbit

The Mercury orbit represents a very harsh environment for any spacecraft. The proximity of the Sun and the very high temperatures that the planet experiences may lead to unacceptable high temperatures of the satellite or of some components of it.

The environmental flux in the solar waveband can be particularly dangerous for the instrument, degrading the optical coatings or damaging the laser generator. The direct solar flux in the Mercury orbit varies between a minimal value of 6272 W·m^{-2}, when Mercury is at aphelion, and 14448 W·m^{-2} when Mercury is at perihelion [44]. The albedo flux should also be taken into account, considering an estimated average albedo factor of 0.12 [44].

In order to assess the degradation of the materials and the optical coating used for the instrument, the total amount of solar energy striking the instrument during the whole mission can be calculated. However, it's very difficult to determinate the spatial distribution of this fluxes. The back part of the instrument will be shaded by the front part, and it will have a smaller view factor with respect to the environment: hence, it will receive less environmental fluxes. The total amount of solar energy entering the instrument aperture during the whole nominal mission (1 year) has been calculated to be $1.77 \cdot 10^8$ J: $1.49 \cdot 10^8$ J (84.1 %) coming directly from the Sun and $2.82 \cdot 10^7$ J (15.9 %) from the planet as albedo. Using a black body disc to simulate the baffle aperture, the total Equivalent Sun Hours (ESHs) have been calculated to be 13147.

In Mercury's orbit the s/c will also withstand a high IR flux (see Figure 3-4), which is usually not particularly dangerous for materials and coating, in addition to UV and V-UV radiation [1]. The last radiations can be harmful, especially for optical coatings. Common space-certified paints and ceramic coatings, such as the AZ Technologies white paints, the Z93 series coating of Alion and the PSB white paints of MAP, proved to be subjected to unacceptable degradation of the thermo-optical properties after a smaller number of ESHs of UV radiation [49].

Another harmful characteristic of the Mercury's orbit is the presence of charged particles, especially high-energy protons [1],[50]. These particles mainly come from the solar wind, and are trapped by the Mercury magnetic field. Charged protons proved to be even more dangerous than the UV and V-UV radiation.

On the contrary, the commonly experienced problem of cold trapping is not present at this distance from the Sun. Usually, outgassed material and contaminants may settle on the instrument surfaces when the s/c is cold, normally in the eclipse period. These contaminants can interfere with the device functioning, especially with the optical elements. Due to the very high expected temperatures of the instrument, any volatile substance which could settle on the baffle or on the filter, will be evaporated or sublimated and eventually rejected outside the instrument.

4 Surface finishes and degradation of the thermo-optical properties

4.1 Introduction

Radiation plays a major role in the thermal design of space system. Although it is of a minor importance for terrestrial systems, the absence of convection and conductive sinks and the very high temperatures that satellites experience make radiation a critical aspect in the thermal design of spaceborne systems.
For the case which is analyzed, the influence of radiation is even more important than usual. The peculiar Mercury's orbit entails very high levels of environmental fluxes (see §3.3): it is therefore mandatory to reduce as much as possible the heat absorption from the environment. Since many instruments need a clear aperture, it is unavoidable to experience a large dose of radiation striking the outer elements of these instruments. A clever selection of the surface finishing and coating may result in a better reflection or rejection of the environmental fluxes. For each unit of the BELA, and in particular for the protective baffles, the choice of the proper materials, treatments and coatings are a key factor in the thermal design.
Further, considering the Stavroudis option (see §2.3), the thermal functioning of the baffle is strongly coupled with the optical functioning. A very high level of specula reflectance, with respect to the diffuse reflectance, is necessary to make the Stavroudis baffle working properly.

4.2 Coatings degradation

A critical issue that must be taken into account is the degradation of the thermo-optical properties during the mission lifetime. Most of the commonly used materials and coatings used in thermal control, even if space qualified, proved to be subjected to a modification of the IR emissivity and of the visible absorptance after the exposure to the space environment.
The modification of the thermo-optical properties should be assessed considering the environmental conditions of the Mercury's orbit, and the variation should be taken into account in the thermal design. Any device should be able to fulfill the requirements both at begin of life and at end of life. Additional simulations for the extended mission should be performed, in order to assess the possibility of the s/c to continue the planned mission, but the results have not influence on the thermal design.

4.2.1 UV radiation

The Ultra Violet radiation is the electro magnetic radiation beyond the visible waveband, which wavelengths are between 200 nm and 400 nm [51]. This radiation presents higher energy than the visible light, which has a waveband of 390 ÷ 750 nm [51], and can therefore be more dangerous for the exposed surfaces. The energy per photon of the UV radiation is between 3.10 and 4.43 eV [51], depending on the wavelength.
The incident photons may cause chemical degradations, especially of organic and polymeric material. But also more stable forms of chemical compounds, such as non-metallic bonds or oxidized molecules can be destroyed by a large dose of radiation, causing some atoms to break the bond with the surrounding elements.
This type of degradation source is expected to be less dangerous for metals: the removal of some atoms from the surface does not change the chemical composition and therefore the resulting optical properties should not be significantly changed.
The only relevant source of UV radiation is the Sun, due to the very high temperatures which are required to thermally emit this kind of radiation. Other sources, such as Mercury or the interstellar radiation, can be considered negligible in comparison with the much stronger solar radiation.

4.2.2 V-UV radiation

The Vacuum-Ultra Violet radiation represents the electromagnetic radiation at higher frequencies with respect to the UV radiation (from 100 nm to 200 nm [51]). The Earth's atmosphere filters the solar and

interstellar radiation in this waveband, which is consequently strongly softened on the Earth's surface. Since this radiation is present only outside the atmosphere and that the wavelength are very close to the UV radiation, it is called Vacuum-Ultra Violet. The frequency of the V-UV radiation is higher, thus its specific energy is higher: the energy per photon is between 6.20 and 124 eV. The V-UV radiation can be therefore more dangerous than the UV radiation, due to its energy which can be up to 40 times higher. Nonetheless, the amount of power radiated by the Sun in this waveband is significantly smaller than the amount of power radiated in the UV waveband (26 $W \cdot m^{-2}$ vs. 1867 $W \cdot m^{-2}$).
V-UV radiation is expected to be critical for organic and polymeric materials, and a possible issue for chemical compounds and complex molecules. As for the UV radiation, metals are expected to be more resistant.
The observed degradation of space proof paints caused by V-UV radiation is the main reason of why white paints, such as the MAP PSNB and the Alion Z93 and YB71P have been discarded during an early selection. White coatings present the best optical behavior in the solar waveband, offering high values of IR emissivity versus low values of solar absorptance. After a specific investigation by the Materials Physics and Chemistry Section of the ESA-ESTEC, during which some sample have been subjected to 52000 ESHs of V-UV rays, the mentioned paints presented a strong increment of the solar absorptance and, most important, physical damages on the surfaces such as cracks and detachment of small particles [49].
Also for the V-UV beams, the only significant source of radiation is the Sun.

4.2.3 Atomic oxygen

Atomic oxygen (AO), and in lesser degree atomic nitrogen, hydrogen and helium, are present in the higher layers of the Earth's atmosphere. AO has been shown to produce considerable damage to orbiting spacecraft in the Low Earth Orbit (LEO) [52]. At the high velocity which characterizes s/c orbits (8000 ÷ 25000 km/h), AO impacts the surface of the s/c with an approximate energy of 5 ÷ 7 eV [52]. AO is highly reactive and can therefore destroy the chemical compounds of the stricken surfaces, or cause undesired oxidation. The high energy of the impact can simply damage the exposed surface by means of the physical impact, removing some atoms from the surface.
Mercury has a very this atmosphere [1], which does not contain oxygen and does not represents a problem for the exposed material. Nonetheless, the s/c will be exposed to the terrestrial atmosphere for some weeks before the lunch. In order to prevent undesired contamination, especially on other optical surfaces, like the filter of the baffle unit, the whole instrument will be sealed, kept in a constant controlled atmosphere of pure nitrogen. After the launch, the unit will be purged to remove all the residual gas.
Therefore, AO do not represent an issue concerning the degradation of the thermo-optical properties.

4.2.4 Thermal stresses

It is expected the unit will be subjected to strong temperature variations. The difference from the night side and the day side of the planet is up to 630 K (see §Table 3-2). Therefore, strong variations are expected also on the device. The thermal expansion may represent an issue for some coating, inducing structural stresses and damaging the surface. This is especially true for thin layers coatings, or for elements which are in contact with components which present different coefficients of thermal expansions (CTE).
Thermal stresses are particularly harmful for deposited coatings, namely vapor or chemical deposited thin layers. The most common representatives of this class, such as Vapor Deposited Gold (VDG), Vapor Deposited Aluminum (VDA) and Vapor Deposited Silver (VDS) have CTE which mostly differ from the possible substrates (titanium for the cylindrical baffle and NiColoy® for the Stavoudis concept). This fact may not be a problem in case of small thermal excursions, but must be considered for elements which experience a wide range of temperatures.
A comparison of the different values of CTE is reported in Table 4-1.

Material	Purpose	CTE [10^{-6} K^{-1}]
Titanium	Substrate	9 ÷ 13
NiColoy®	Substrate	12 ÷ 17
Aluminum	Coating	21 ÷ 25
Gold	Coating	13 ÷ 14
Silver	Coating	18 ÷ 20

Table 4-1: Coefficients of thermal expansion for vapor deposition material (at room temperature) [34]

4.2.5 Charged particles and solar wind

The Mercury's orbit presents a high level of charged particles, consisting mainly in solar cosmic rays, trapped by the Mercury's magnetosphere, and galactic cosmic rays [50]. Most of the charged particles consist in protons, with a lesser presence of free electrons and heavy ions. Peaks fluxes of protons exceed 10^{10} protons·m^{-2}·s^{-1} [53]. Protons range in energy from 1 to 200 MeV, electrons from 0.3 to 10 MeV [54]. Protons are therefore more harmful, in consideration of their predominance in terms of quantity and energy.

Charged particles are particularly problematic for any type of surface, since their impact energy is very high and this eases the detachment of atoms from the stricken surface. Coatings which present chemical compounds or complex molecules are most vulnerable to this threat.

4.3 Achievable optical properties for the cylindrical baffle

Due to the difficulty of coatings application, and to the very high temperatures expected during the operational life of the baffle, only mechanical, thermal and chemical conversion treatments are considered reliable for the baffle.

Mechanical treatments consist basically in a modification of the surface roughness, by means of polishing using abrasive materials. Thermal treatments instead take advantage of a chemical modification of the surface of the metal, promoting oxidation through a temperature increment. Finally, chemical conversion treatments are intended to change the chemical and crystalline structure of the surface, forcing oxygen absorption and modifying the shape, the orientation and the size of the oxide crystals in order to achieve the desired optical properties.

4.3.1 Polishing

The polishing operation is the simplest and most reliable. Some possible ways to increase (or decrease) the surface smoothness make use of sandpaper, abrasion using metallic powder, metallic and non-metallic beads.

Sandpaper polishing represents the simples and more economic solution. The grit size of the sandpaper determines the final surface roughness in terms of average and maximal roughness. A high grade corresponds to a low average particle diameter, which results in a smoother polished surface; low grades sandpapers are instead use to intentionally achieve rough surfaces. Table 4-2 reports the CAMI (Coated Abrasive Manufacturers Institute, now part of the Unified Abrasives Manufacturers' Association) grades and the mean particle diameter for a range of grit sizes.

The polishing operation, for relatively small components and for complex shapes, is usually made by hand, wiping the sandpaper till the desired smoothness is achieved. This process introduces some inaccuracies and usually results in a lack of homogeneity into the final result, with respect to mechanized techniques.

A similar solution makes use of metallic powder to wipe the surface. The only remarkable differences with respect to the previous method are the lack of a monolithic substrate and the possibility to use very fine powders, below the limits of common commercial sandpapers. As a consequence of the smaller abrasive particles, metallic powder polishing usually allows obtaining smoother and especially more homogeneous surfaces; the drawback are a more complex operation and a higher temporal and economical cost.

CAMI grit designation	Average particle diameter [μm]
40	425
50	348
60	265
80	190
100	140
120	115
150	92
180	82
220	68
240	53
320	36
360	28
400	23
500	20
600	16
800	12.6
1000	10.3

Table 4-2: CAMI grit standard [55],[56],[57]

Polishing using metallic or non-metallic (usually glass) beads it is possible to achieve very homogeneous surfaces. This quite recent technique proved to be a good solution to achieve the desired optical appearance in the solar waveband. Due to the relative high dimensions of the beads, adopting this method it is not possible to achieve levels of roughness below a fixed value.
The choice of the best polishing techniques depends upon the selected material, the desired mean and maximal roughness and consequently the desired thermo-optical properties in the IR and solar waveband. The presented treatments have been applied to some titanium samples, the details and the results in terms of roughness and thermo-optical properties are reported in §4.6. In this section some values of thermo-optical properties for polished titanium, found in literature, have been reported:

Source	IR emissivity [-]	Solar absorptance [-]
Polished titanium [58]	0.20	n. a.
Sandpaper ASTM grade 2 polished [59]	0.27	0.80
1 μm Al powder polished [59]	0.21	0.57
TiN/Titanium, polished [36]	0.11	0.52

Table 4-3: Optical properties of polished titanium founded in literature

Since polishing and other mechanical surfaces modify only the microscopic shape of the surface, but not its chemical or crystalline composition, no environmental degradation is expected for this type of treatments.

4.3.2 Oxidation

The oxidation process is a thermal treatment. It forces the metallic surface to capture some atoms of oxygen in order to form a thin layer of oxide. This chemical reaction is helped by a high temperature of the substrate and/or of the oxidizing fluid.
Oxidation allows achieving a thin layer of oxide with specific thermo-optical properties, without changing the structure of the material and without making the whole element subjected to mechanical stresses (such as the polishing operation). Beyond improving the optical behavior of the surface, metals oxides are expected to

be more immune to thermal and environmental conditions [59]. This is particularly important for the BepiColombo project, since the s/c will operate in an environment which presents critical issues from a thermal point of view.
There are two commonly used methods to oxidize metals so that to achieve the desired optical properties: standard thermal oxidation and air-plasma oxidation.
Thermal oxidation consists in placing the metallic components in a proper oven, where high temperatures (usually above 500 °C) can be reached. The oxidizing fluid is normal still air. Leaving the components for a selected time, it is possible to achieve the desired percentage of final oxidation, and thus to achieve the desired optical properties.
Air-plasma oxidation makes use of an ionized flow of hot air. The presence of ionized atomic oxygen eases the oxidation process and allows using lower temperatures. The element to be oxidized is attached to the cathode of a capacitive glow discharge system, inside the process chamber. The temperature of the element is raised up (a typical temperature is 350 °C), then a low pressure and hot air flow is allowed to enter the chamber. The air flow can have a pressure between 1 Pa and 100 Pa, and its temperature is usually the same of the component to be oxidized. In order to ionize the flux, a radio frequency signal is applied between anode and cathode. Examples found in literature make use of a power density of 1000 $W \cdot m^2$ and of a frequency of 14 MHz for the signal [59].
Standard thermal oxidation is easy and economic, but usually results in a less efficient oxidation with respect to air-plasma oxidation. The latter one is instead more complex and expensive, but more effective. Further, the very high temperatures used for thermal oxidation can damage the component to be oxidized or compromise its functionality.
In Table 4-4 some values of thermo-optical properties for oxidized titanium, found in literature, have been reported:

Source	IR emissivity [-]	Solar absorptance [-]
Air oxidation at 500 °C, 30 min [59]	0.26	0.85
Sandpaper ASTM grade 2 polished + air oxidation at 500 °C for 30 min [59]	0.07	0.95
Al powder 1 μm polished + air oxidation at 500 °C for 30 min [59]	0.20	0.78

Table 4-4: Optical properties of oxidized titanium founded in literature

The oxidation modifies the chemical composition of the external layer of the substrate, and it is therefore supposed to be a less stable treatment with respect to polishing. Nonetheless, oxidized metals proved to be very stable even if subjected to thermal stress and strong environmental radiation [60].

4.3.3 Anodizing

Anodization is another way to obtain a thin layer of oxide on a metallic surface. Differently from oxidation, which is a thermo-chemical process, it is an electrochemical process. It is widely used to protect the metallic components from atmospheric corrosion, to reduce the friction between sliding surfaces, to create decorative finishing and, relevant to this topic, to provide passive thermal control.
The component to be coated is cleaned and dipped in an electrolytic bath, which makes use of different acids depending on the metal of the element. The component is than connected to an electrical circuit, of which it will be the anode. The anodized layer is grown by passing a direct current through the electrolytic solution. As a consequence, the cathode releases hydrogen and the surface of the metallic anode releases oxygen, creating a build-up of metallic oxide. The voltage of the direct current varies depending on the anodized metal, the selected acid and the desired thickness of the oxide layer, usually between 1 V and 300 V.

Anodizing titanium presents an interesting feature: the resulting color of the surface, and therefore the thermo-optical properties in the visible waveband, can be selected by means of the thickness of the oxide layer. This parameter can be achieved controlling the voltage of the electrical circuit during the anodizing. The process generates an array of different colors without dyes, which proved to be permanent and stable. An approximated correlation of the resulting colors with respect to the applied voltage can be seen in Figure 4-1.

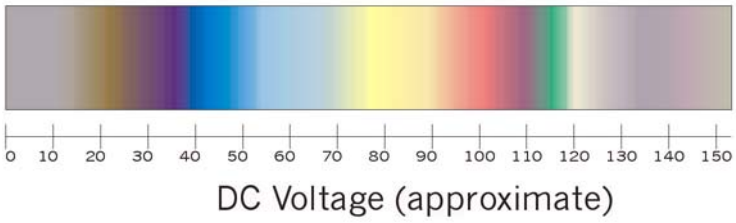

Figure 4-1: Color of anodized titanium vs. voltage [61]

The unusual coloration of anodized titanium is caused by multiple beam interference phenomena [62]. If a white beam strikes the anodized surface, the reflected beam is the sum of the first reflection (from the outer surface) and of the multiple beams which are reflected by the deeper titanium surface (see Figure 4-2). The resulting color will be the one reinforced by the interferences and will thus be the complementary of the extinguished color. The extinguished wavelength, and therefore its complementary, is determined by the thickness of the oxide film [63],[64],[65].

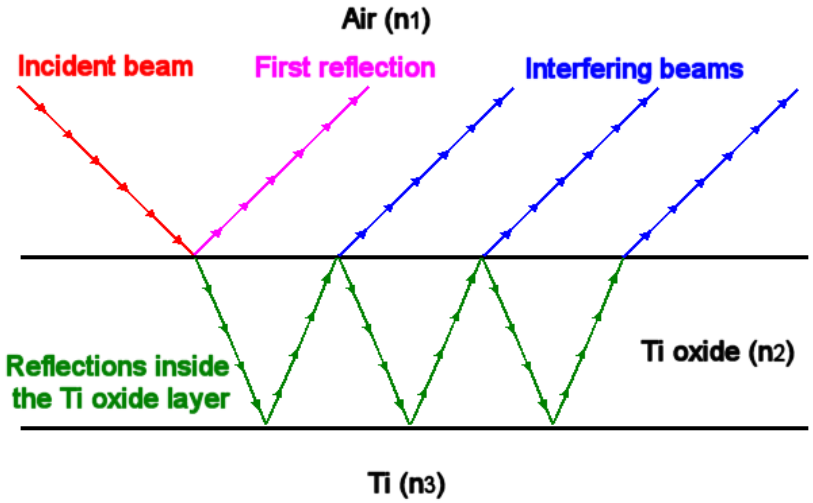

Figure 4-2: Multiple beams interference in anodized titanium

Some commercially available coating processes have been found in literature. Table 4-5 reports the affirmed optical properties for the best products.

Processing and source	IR emissivity [-]	Solar absorptance [-]
Blue anodize foil, 1 mil [60]	0.13	0.70
Anodized foil [66]	0.10	0.70
TIODIZE® Type I bare [67]	0.89	0.62
Galvanized sheet [36]	0.44 ÷ 0.48	0.84 ÷ 0.86

Table 4-5: Optical properties of anodized titanium founded in literature

The treatment is a quite simple and economic process, it can be performed at room temperature without complex hardware.
As for the oxidation, it involves a chemical modification of the surface and it is therefore supposed to be less stable than simple mechanical treatments, such as polishing. Nonetheless, anodizing of many metals has been found suitable for space application [35] and has already been used in space missions [35],[36],[37]. In particular, anodized titanium, which is the selected material for the cylindrical baffle, has been widely used in space applications [35],[36],[37] .
No reliable sources have been found concerning the resistance of anodized titanium under harsh conditions. Even if it has been used in the Earth's orbit, its capability to operate in the more harsh Mercury's environment has to be tested and certified.
The behavior of anodized metals can be analyzed in order to assess the stability of the anodizing process. Anodized Aluminum proved to be immune to AO corrosion and V-UV radiation [52], showing no variations of the thermo-optical properties after 8300 ESHs of V-UV radiation and a flux of $1.3 \cdot 10^{20}$ oxygen atoms$\cdot m^{-2} \cdot s^{-1}$ for 64 days. The loads were applied both alone and in combination.
The resistance to charged particles has been tested at least for anodized aluminum and anodized tantalum. Both the coatings were subjected to a flux of $4.9 \cdot 10^{10}$ protons$\cdot m^{-2} \cdot s^{-1}$, with a proton energy of 2.0 MeV, for 6 hours. Anodized tantalum experienced no variations of the thermo-optical properties, whereas the aluminum sample experienced a small shift on its emissivity spectra, without changing the total absorptivity [50]. This test was conducted for a short time and on other metals, therefore cannot be considered representative of the anodized aluminum. Nonetheless, it provides indications of the good resistance of the anodizing process to the expected environmental conditions.

4.4 Achievable optical properties for the Stavroudis baffle

The material selected for the Stavroudis baffle is the nickel alloy NiColoy®. The desired set of thermo-optical properties should offer:

- low solar absorption
- high specular / diffuse reflectance ratio in the solar waveband

The last requirement is due to the peculiar behavior of the Stavroudis concept (see §2.3.1). As for the cylindrical baffle, in consideration of the harsh and partially unknown environment in which the instrument will work, the Mercury's orbit, paints, vapor and chemically deposited coatings have been considered not reliable. Therefore, only chemical conversions, mechanical and thermal treatments can be considered.
Unfortunately, the very complex shape of the baffle and the manufacturing techniques prevented the use of mechanical polishing: this treatment would damage the thin electroformed shape.
In a similar way, thermal treatments can induce thermally-induced stresses which modify the very sensitive surface. Chemical conversion treatments were also discarded in consideration of the modification of the mechanical properties and to avoid mechanical stresses during the operation and the handling.
Only the bare electroformed NiColoy® surface has been considered as an acceptable finishing.

4.4.1 Thermo-optical properties of the bare baffle

Fortunately, the electroformed nickel presents very low values of absorptivity, both in the IR and in the visual waveband. NicoForm Inc., the producer of the electroformed shape, declared to be able to achieve a very smooth surface, with consequent very high levels of specular reflectance. No measurements of the specular / diffuse reflectance have been performed to verify this declaration. The producer provided for the IR emissivity and the visible absorptance of a tested electroformed sample. The values are reported in Table 4-6.
The presented values have been measured on a simple plain sample. It is possible that the thermo-optical properties are different on complex curved surfaces. A better estimation on a sample representative of the real geometry should be performed, determining also the percentage of specular reflectance.

Coating	IR emissivity [-]	Solar absorptance [-]
Sapphire + silica (sample 1)	0.10	0.07

Table 4-6: Declared IR emissivity and solar absorptance of a NiColoy® sample

4.4.2 Expected degradation

Bare metal is not expected to encounter degradation in the Mercury's environment; anyway, qualification tests on this peculiar material should be performed to certify its usability for the BepiColombo mission.

4.5 Achievable optical properties for the front ring

The front ring, introduced in §2.3.1 and described in §7.1, is the interface between the instrument and the environment. It has a large area ($1.48 \cdot 10^{-2}$ m^2), and a very high view factor towards both Mercury and the Sun. It will therefore experience the highest thermal load on its surface, and this leads to very high temperatures. It is therefore necessary to optimize the environmental fluxes rejection through a clever selection of the coating.

The selected material of the front ring is titanium, as a consequence of its resistance to high temperatures, its moderate density (see Table 2-1) and the possibility of applying different coatings.

The achievable thermo-optical properties and their degradation were assessed in single campaign. The tests were performed by the European Space Research and Technology Centre (ESTEC), part of ESA, together with EADS Astrium Friedrichshafen (ASD), using ESTEC's facilities at Noordwijk, in the Netherlands. Two different coatings have been analyzed:

- Sapphire (Al_2O_3) + silica (SiO_2)
- Yttria stabilized zirconia ($ZrO_2 + Y_2O_3$)

Eight samples were used during the test. The solar absorptance and the IR emissivity were measured for these samples at room temperature (about 25 °C). Results are reported in Table 4-7.

Coating	IR emissivity [-]	Solar absorptance [-]
Sapphire + silica (sample 1)	0.81	0.24
Sapphire + silica (sample 2)	0.81	0.27
Sapphire + silica (sample 3)	0.80	0.26
Sapphire + silica (sample 4)	0.81	0.28
Yttria stabilized zirconia (sample 1)	0.77	0.28
Yttria stabilized zirconia (sample 2)	0.77	0.27
Yttria stabilized zirconia (sample 3)	0.76	0.25
Yttria stabilized zirconia (sample 4)	0.76	0.27

Table 4-7: IR emissivity and solar absorptance of the ceramic coatings before the test

4.5.1 Measured degradation

Four of the eight sample (two with sapphire-silica coating and two with yttria stabilized zirconia) were subjected to a large dose of environmental radiation in order to simulate the operation environment effects (see §3.5). The samples were irradiated by 8 halogen lamps producing UV radiation in the range of 200 to 400 nm as well as 4 Deuterium lamps producing V-UV radiation in the range of 115 to 200 nm. The test lasted for 610 hours (for the combined UV and V-UV radiation) with an additional 20 hours of UV radiation only. The environmental flux power was simulated to a value of 11 SC (about 15070 $W \cdot m^{-2}$) for the UV radiation and of 10 SC (about 13700 $W \cdot m^{-2}$) for the V-UV radiation. 11 SC is the maximal solar flux

expected in the Mercury's orbit. Extensively, the test reproduced an environmental radiation of 7000 ESHs for the UV radiation and 6000 ESHs for the V-UV radiation. These values are below 50 % of the expected environmental radiation received during the mission lifetime, and therefore cannot assure that the achieved degradation level is the maximal the coatings can experience through the whole mission. Nonetheless, the most evident degradation occurred during the first half of the test, and it can therefore be assumed that the materials have reached a good level of stability.
In addition to the simulated environmental radiation, the samples were subjected, for the whole duration of the test, to very high temperatures, in order to reproduce as much as possible the real operational conditions. During the test, the sample temperatures were kept constant to temperatures between 290 °C (for the coldest sample) to 430 °C (for the hottest one).

Coating	Temperature [°C]	IR emissivity [-]	Solar absorptance [-]	Solar selectivity [-]
Sapphire + silica (sample 1)	300 °C	0.80	0.39	0.49
Sapphire + silica (sample 2)	430 °C	0.81	0.46	0.57
Yttria stabilized zirconia (sample 1)	290 °C	0.76	0.40	0.53
Yttria stabilized zirconia (sample 2)	400 °C	0.75	0.44	0.59

Table 4-8: IR emissivity and solar absorptance of the ceramic coatings after the test

Coating	Δ IR emissivity [-]	Δ Solar absorptance [-]	Δ solar selectivity [-]
Sapphire + silica (sample 1)	-1 %	+62 %	+65 %
Sapphire + silica (sample 2)	0	+70 %	+70 %
Yttria stabilized zirconia (sample 1)	-6 %	+43 %	+45 %
Yttria stabilized zirconia (sample 2)	-7 %	+63 %	+67 %

Table 4-9: Difference between the optical properties after the simulated operational life with respect to the BOL values

The accuracy of the measurements is ±0.02, the accuracy of the percentage degradation is ±8%.
The IR emissivity measured after the test is very close, slightly smaller, than the values measured before the test. In particular, the solution which makes use a sapphire + silica coating shows a maximal decrement of the emissivity of 1 %, whereas the yttria stabilized zirconia coating presents a stronger decrement down to 7 %.
On the contrary, the solar absorptivity is greatly increased after the test. The minimal values are achieved by the samples which have been subjected to lower temperatures. The sample 2 of sapphire + silica and sample 2 of yttria stabilized zirconia, which experienced temperatures of respectively 300 °C and 290 °C, caused values of solar absorptance of 0.39 ÷ 0.40. The samples subjected to higher temperatures caused a solar absorptance between 0.44 and 0.46.
The behavior of the coating in the solar waveband is more critical than the behavior in the IR waveband, because the front ring can only absorb but not re-emit in this waveband. It is therefore mandatory to minimize this parameter, whereas the optimal value of IR absorptivity depends upon the balance between absorption and re-emission. This last parameter, called solar selectivity, is expressed by eq. 4-1 and reported in Table 4-8.

$$S = \frac{\varepsilon_{IR}}{\alpha_{VIS}} \qquad \textit{eq. 4-1}$$

Where:

Variable	Physical meaning
S	Solar selectivity [-]
ε_{IR}	emissivity in the IR waveband [-]
α_{VIS}	absorptance in the visible waveband [-]

Table 4-10: Parameter of eq. 4-1

4.6 Measurements of Ti optical properties

The determination of the thermo-optical properties with a high level of accuracy is important for both the baffle concepts: the functioning of the device is strongly based upon the optical properties in the IR and solar waveband. This is especially true for the Stavroudis concept (see §2.3), but unfortunately it this quite difficult and long to obtain some samples of NiColoy®.

Titanium samples are instead easy and economically available on the market. Furthermore, it is possible to easily perform mechanical polishing and thermal treatments. Hence, a campaign to evaluate the different thermo-optical properties achievable for the titanium cylinder has been planned and performed.

4.6.1 Samples and treatments

The German company Astro- und Feinwerktechnik Adlershof GmbH has been selected to provide for the titanium samples and to perform the thermo-mechanical finishing. A small number of mechanical smoothing processes have been selected, trying to cover a large range of surface roughness values:

- Sandpaper CAMI Grit 40 (coarse)
- Sandpaper CAMI Grit 500 (smooth)
- Sandpaper CAMI Grit 1000 (very smooth)
- Al power 15 μm
- Glass beads

Concerning the oxidation, the only available solution was to perform air thermal-oxidation. A process which already showed interesting results [59] consists in oxidizing the Ti sample at the temperature of 500 °C for 30 minutes in a normal industrial oven.

Chemical conversion is probably the most interesting treatments, but unfortunately the process requires quite expensive facilities and trained personnel [35]. Therefore, the analyses of anodized sample have been at present postponed.

A total of twelve Ti 6242 samples have been ordered, with the following treatments:

Sample number	Mechanical polishing	Thermal Oxidation
01	None	None
02	None	500 °C for 30 min
03	Sandpaper 40	None
04	Sandpaper 40	500 °C for 30 min
05	Sandpaper 500	None
06	Sandpaper 500	500 °C for 30 min
07	Sandpaper 1000	None
08	Sandpaper 1000	500 °C for 30 min
09	Glass beads	None
10	Glass beads	500 °C for 30 min
11	Al power 15 μm	None
12	Al power 15 μm	500 °C for 30 min

Table 4-11: Ti samples list

The samples are discs with a radius of 50 mm and a height of 10 mm, their mass is 356.5 g.

4.6.2 Surface roughness

The surface roughness of the sample has been measured by the supplier in order to assess the treatment effect: these values will be used to correlate the results of the thermo-optical measurements. The roughness measurement has been performed using a Hommel Tester T8000, produced by Hommelwerke GmbH. The device has a Class 1 accuracy according to DIN 4772, and a measuring range / resolution ratio of ± 8 µm / 1 nm.

The company reported the average roughness, the mean roughness depth and the maximal roughness depth of the first ten samples; no measurements have been provided for the Al powder polished samples. The previous parameters are defined by the standards DIN EN ISO 4287, DIN EN ISO 4288 and ASME B46.1. The average roughness (R_a) represents the arithmetic average of the absolute values of the roughness profile ordinates. It is depicted in Figure 4-3. The mean roughness depth (R_m) is the arithmetical mean value of the single roughness depths of consecutive sampling lengths, where the single roughness depth is the vertical distance between the highest peak and the deepest valley within a single sampling length. This concept is shown in Figure 4-4. Finally, the maximal roughness (R_{max}) depth is the largest single roughness depth with the evaluation length.

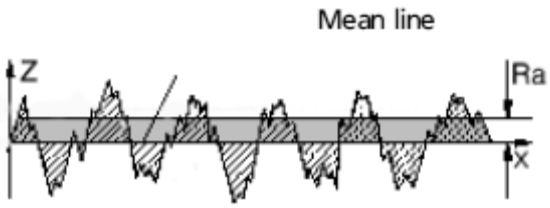

Figure 4-3: Average roughness

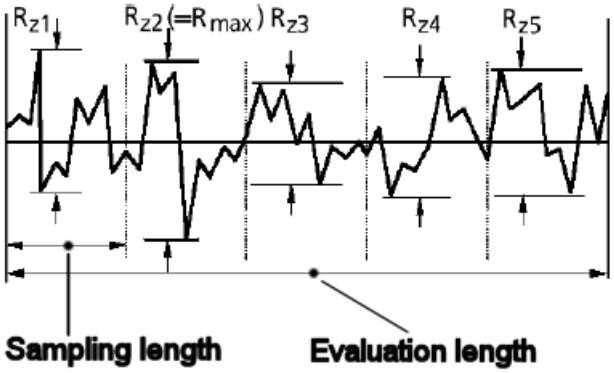

Figure 4-4: Mean and maximal roughness depth

The results of the roughness measurement are reported in the following pictures.

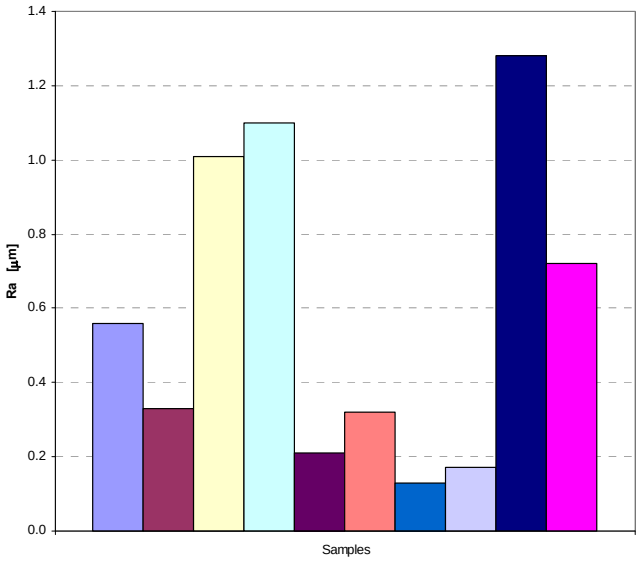

Figure 4-5: Average roughness measurement

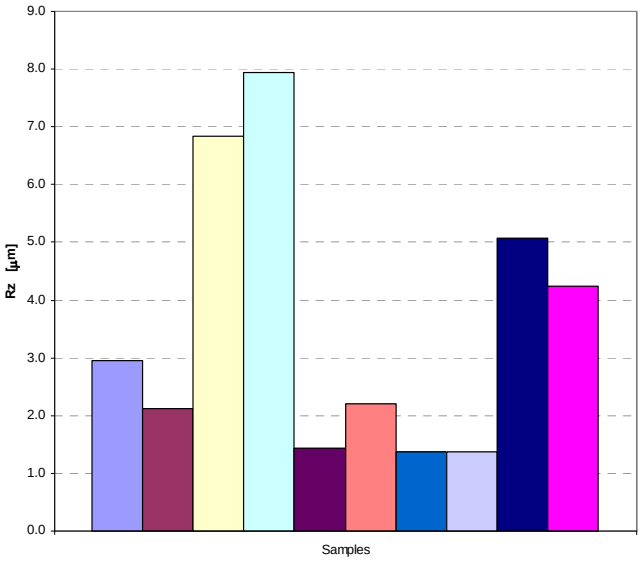

Figure 4-6: Mean roughness depth measurement

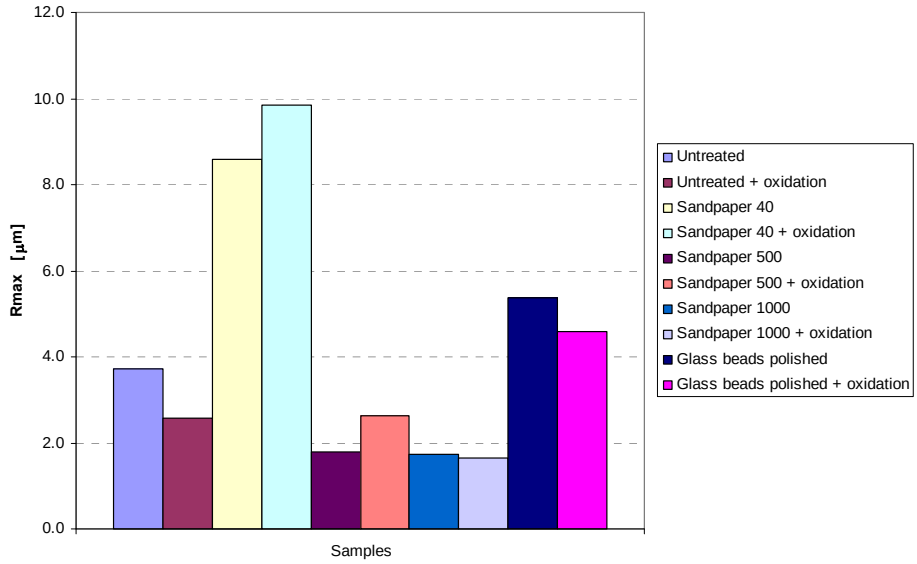

Figure 4-7: Maximal roughness depth measurement

It is interesting to note how, for the untreated samples, the oxidation process causes a decrement of all the three measured index of roughness. As expected, the coarsest sandpaper (CAMI grit 40) produced an increment in the roughness. The thermal oxidation seems to have an opposite effect in comparison with the untreated samples: the oxidized sample is rougher than the corresponding non oxidized one, again for all the three roughness parameters.

The polishing with sandpaper of grits 500 and 1000 caused smoother surfaces with respect to the untreated samples. The increment is more marked for the grit 1000 in a significant way only for the average roughness: considering the mean or the maximal roughness depths, the difference is small or nonexistent. Another relevant note about this class of sandpaper polishing is the influence of the oxidation on the roughness: if for the 500 grit there is the same trend of the 40 grit (the oxidation increases the roughness), for the 1000 grade the effect of the thermal treatment is less relevant and contrasting with respect to the different roughness parameters. It is possible that beyond a smoothness level, the thermal oxidation is not able to significantly change the surface roughness.

The polishing performed using glass beads provided for a non oxidized sample which showed surprising reflective effect. The disc showed a mirror behavior significantly better than the samples polished using sandpaper or untreated. This is supposed to be a consequence of the different ratio between specular and diffuse reflectivity. Even if this parameter will not be measured in the following test, it must be kept in mind for the numerical simulations. The glass beads caused a high surface roughness, especially of the average roughness. This is a consequence of the large size of the abrasive elements (the glass beads), which produced large lack of homogeneity between different areas of the discs, but moderately shallow scratches of short width. It is possible that this is the cause of the strong mirror effect of the non oxidized sample. These samples followed the same tendency of the non polished discs, presenting an increment of the smoothness after the thermal oxidation.

4.6.3 IR emissivity

The IR emissivity has been measured using the Planetary Emissivity Laboratory (PEL) at DLR.

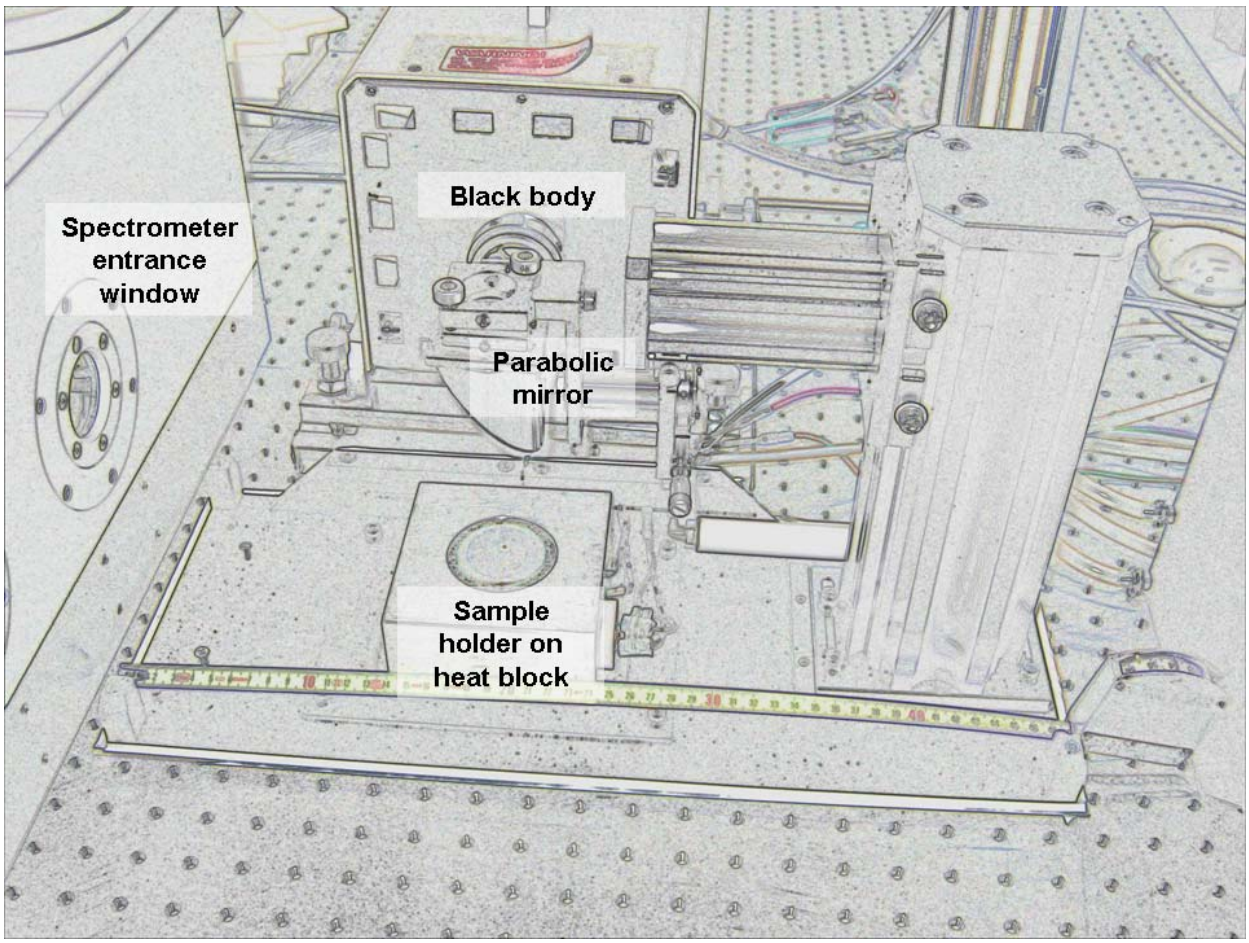

Figure 4-8: PEL chamber schematic

For the test a Fourier transform infrared spectrometer (Bruker IFS 88), purged with dry air and equipped with a liquid-nitrogen-cooled detector has been used [68]. The device measures the thermal emission from the samples, which are placed in a black chamber, in a narrow cone centered on the surface normal. Measuring the heat flux irradiated by the sample and its surface temperature, it is possible to determine the IR emissivity using the eq. 4-2.

$$q = \sigma \varepsilon_S \varepsilon_R A_S F_{SR} \left(T_S^4 - T_R^4\right) \quad \rightarrow \quad \varepsilon_S = \frac{q}{\sigma \varepsilon_R A_S F_{SR} \left(T_S^4 - T_R^4\right)} \qquad \textit{eq. 4-2}$$

Where:

Variable	Physical meaning
q	Heat flux [W] (measured)
σ	Stefan-Boltzmann constant ($\sigma = 5.670 \cdot 10^{-8}$ J·K^{-4}·m^{-2}·s^{-1} [69])
ε_S	IR emissivity of the sample [-] (unknown)
ε_R	IR emissivity of the receiver [-] (know)
A_S	Radiative area the sample [m^2] (known)
F_{SR}	View factor between sample and receiver [-] (known)
T_S	Temperature of the sample [K] (measured)
T_R	Temperature of the receiver [K] (known)

Table 4-12: Parameter of eq. 4-2

The heat flux is measured by the spectrometer for each wavelength, permitting the measurement of the emissivity spectrum over a wide waveband.
In order to achieve higher thermal emission, and therefore lesser numerical errors and uncertainties, the samples have been heated up to the temperature of 137 °C. The Ti discs have been taken inside a small oven and placed inside the black chamber immediately before the measurement. To keep the temperature constant during the process, a small heater was placed just below the samples. Not only the emission spectrum changes as a function of the temperature, according to the Planck's law, but often even the integrated value of the emissivity varies with the surface temperature. This means that the measurement should be done for a wide range of temperatures, trying to reproduce the foreseen environmental conditions. The measurement process is highly time-consuming, but fortunately a literature review about titanium behavior showed that this metal is not very sensible to temperature variation. Therefore, a single measurement has been considered sufficient. Another advantage of implying a high temperature is that most of the baffle radiation occurs at high temperature, and therefore the measured values are more consistent with the operational life.
The surface temperature has been measure using an IR camera. An example of a heated sample is reported in Figure 4-9.

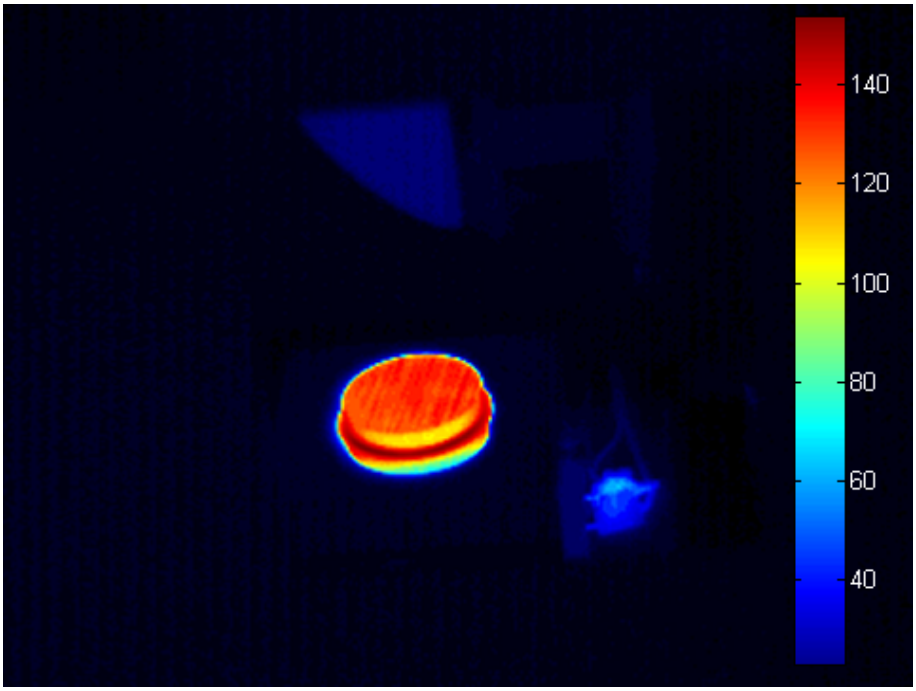

Figure 4-9: Sample #04 surface temperature

The measured spectra in the waveband of 2.5 ÷ 16.5 μm are reported in Figure 4-10, the integrated values in Figure 4-11.

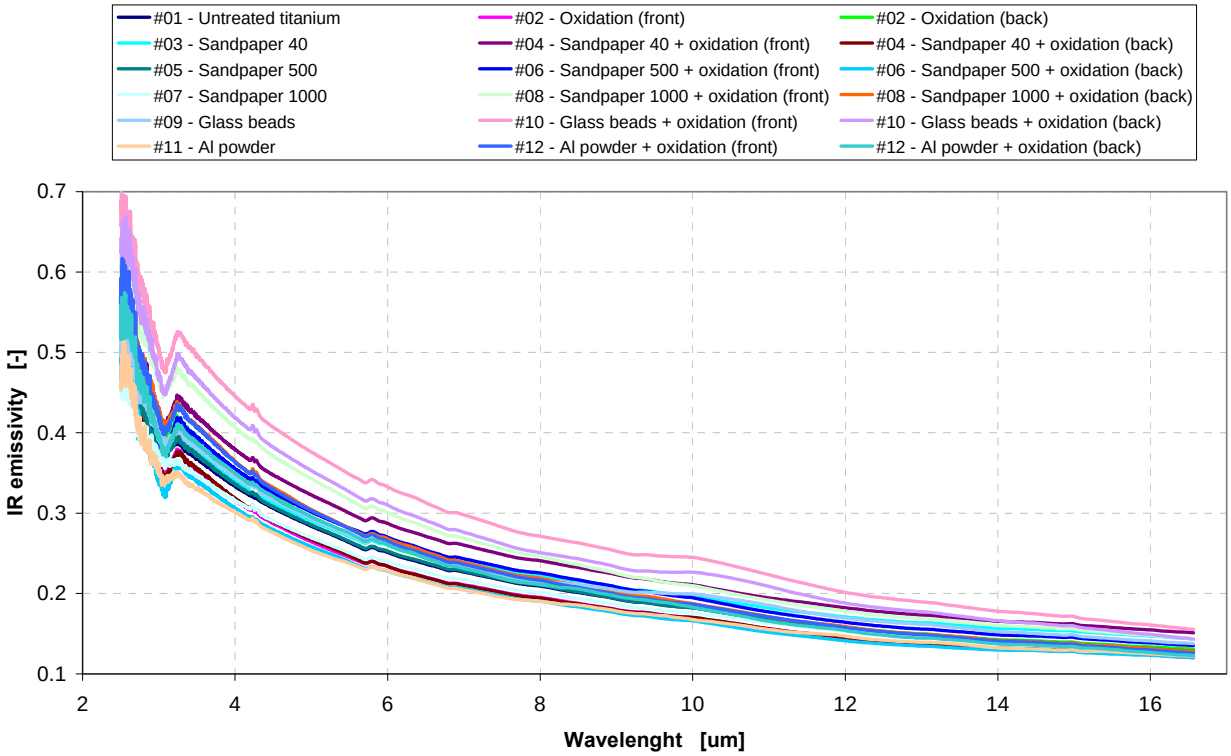

Figure 4-10: Ti samples IR emissivity spectra

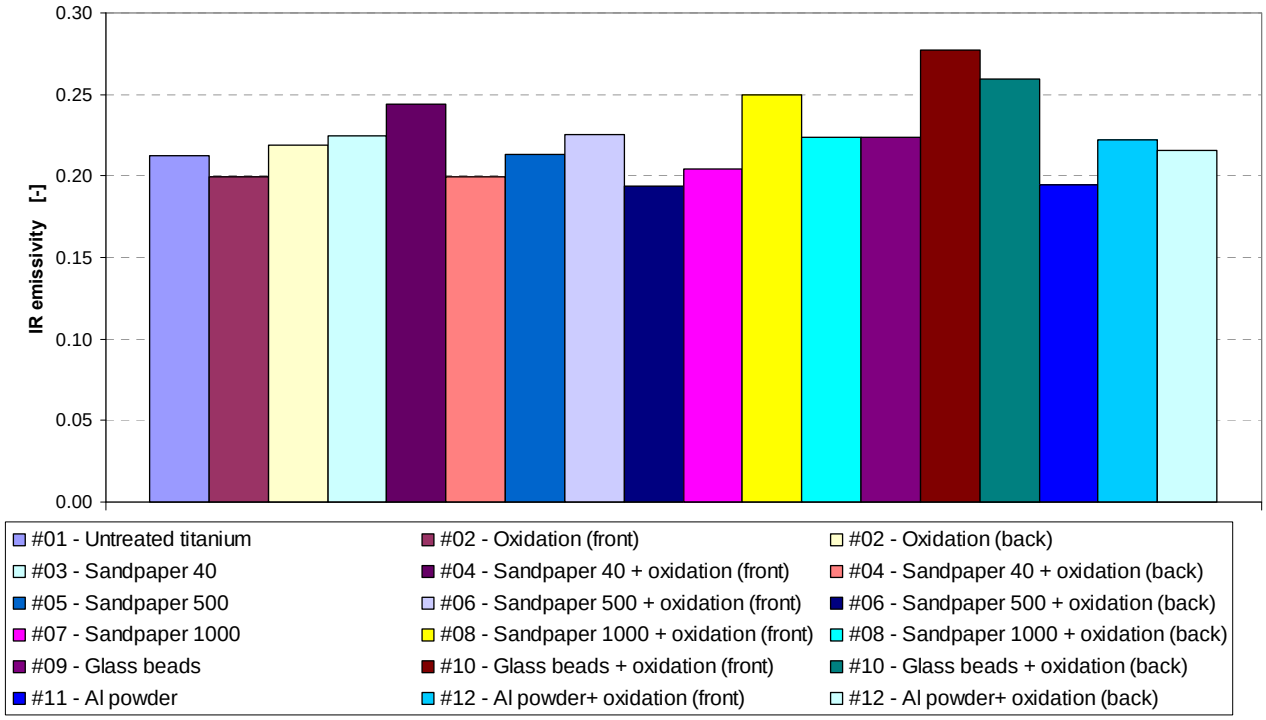

Figure 4-11: Ti samples integrated IR emissivity

As can be seen in Figure 4-11, the performed treatments do not significantly change the IR emissivity of the samples. An important consideration that can be done is that, for all the polished discs, the oxidation slightly increases the IR emissivity. This is more evident for the smoother surfaces. On the contrary, the unpolished samples show the opposite behavior.

Trying to correlate the surface roughness reported in Figure 4-5, Figure 4-6 and Figure 4-7 with the IR emissivity of the non oxidized samples, no relations have been highlighted. This suggests a scarce influence of the polishing process on the emissivity in the IR waveband.

4.6.4 Solar absorptance

The absorptance in the solar waveband was measured again at DLR, but using another facility. The spectrometer used for the test is the Perkin Elmer Lambda 19 UV/VIS/NIR, the spectra were analyzed in the waveband between 300 nm and 2500 nm, covering 30 nm per minute.

The solar absorptance spectra of the 12 Ti samples are reported in Figure 4-12; the spectra have been integrated on a black body curve using an equivalent temperature of 5880 K to simulate the Sun spectrum. The integral values are reported in Figure 4-13.

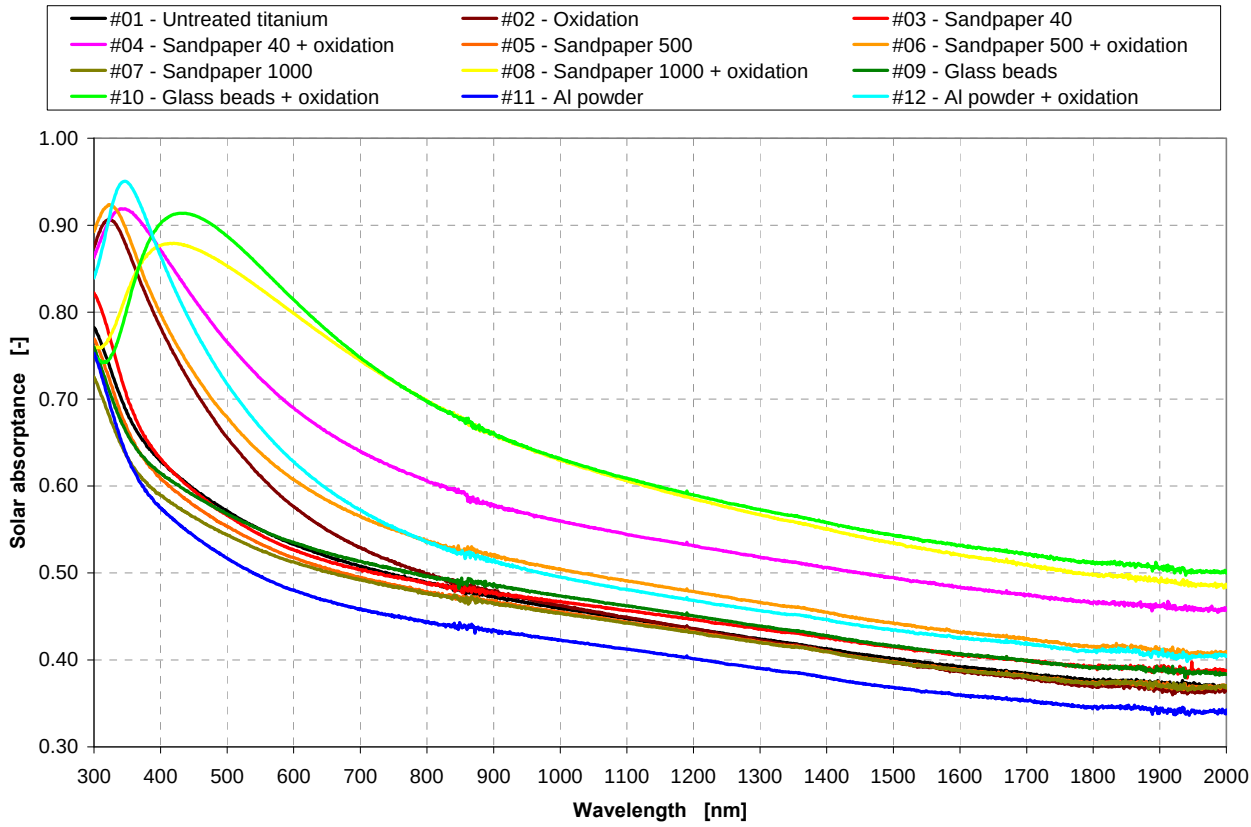

Figure 4-12: Ti samples solar absorptance spectra

Some considerations can be done about the chart reported in Figure 4-13.

All the polished surfaces show about the same value of visible absorptance between 0.47 and 0.52. These values are lower than the absorptance of the untreated sample (0.57). Surprisingly, it is not possible to determine a relation between the surface roughness and the variation of this optical property. It is possible that the solar absorptance is determined not by the surface roughness only but by other parameters also, which have been modified by the polishing process. This hypothesis is reinforced by the fact that the thermal oxidation has no effects on the untreated samples.

For all the polished surfaces, the thermal oxidation strongly increases the solar absorptance. Again, it is not possible to determine a relation between the surface roughness and the absorptance. But differently from the non oxidized samples, in this case the solar absorptance cannot be considered constant but varies between 0.60 and 0.74.

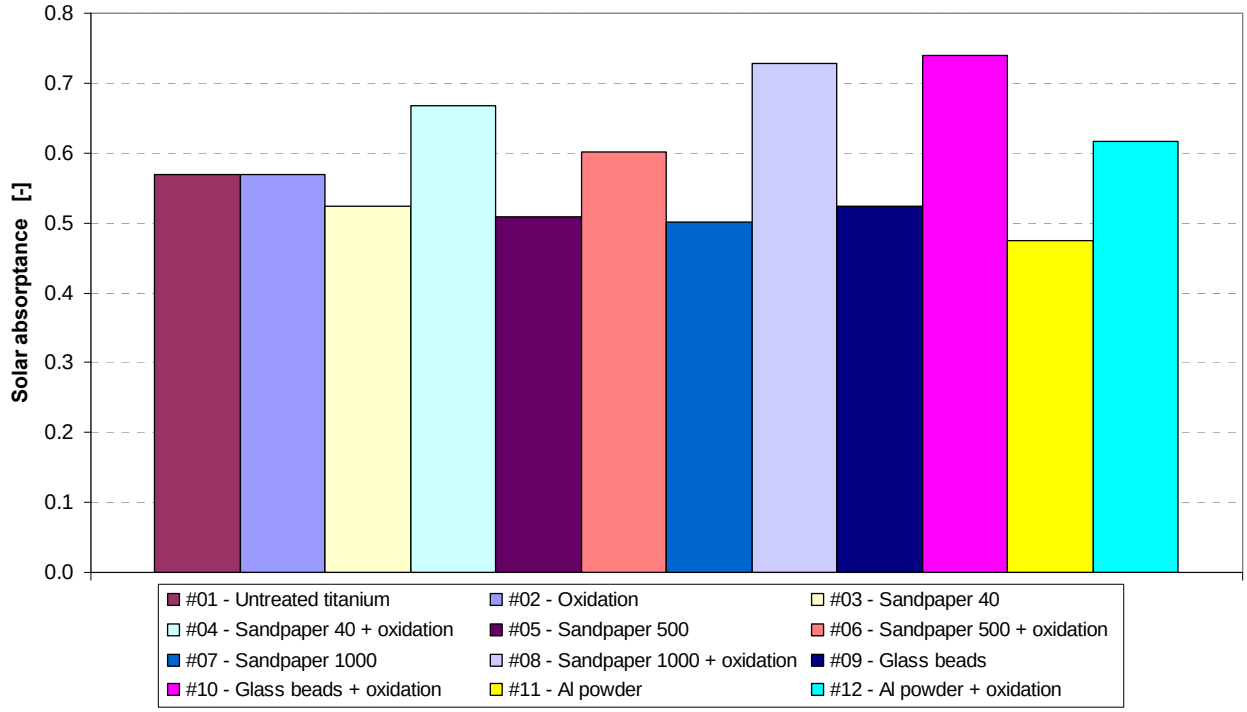

Figure 4-13: Ti samples integrated solar absorptance

The increment of the absorptivity in the solar waveband is a strongly negative effect. Since it is not compensated by a strong increment of the IR emissivity (see Figure 4-11), so that to avoid to increment the solar selectivity (reported in eq. 4-1), this test establishes the inappropriateness of the thermal oxidation of the titanium surfaces.

4.6.5 Summary of the results

The summary of the thermo-optical properties for the twelve titanium samples is reported in Table 4-13.

Sample	Treatments	IR emissivity [-]	Solar absorptance [-]	Solar selectivity [-]
01	None	0.21	0.57	2.71
02	Oxidation	0.20	0.57	2.85
03	Sandpaper 40	0.22	0.52	2.36
04	Sandpaper 40 + Oxidation	0.24	0.66	2.75
05	Sandpaper 500	0.21	0.51	2.43
06	Sandpaper 500 + Oxidation	0.23	0.60	2.61
07	Sandpaper 1000	0.20	0.50	2.50
08	Sandpaper 1000 + Oxidation	0.25	0.73	2.92
09	Glass beads	0.22	0.52	2.36
10	Glass beads + Oxidation	0.28	0.74	2.64
11	Al power 15 μm	0.19	0.47	2.47
12	Al power 15 μm + Oxidation	0.22	0.62	2.82

Table 4-13: Summary of the thermo-optical properties of the titanium samples

The performed surface finishing do not provide significant improvement of the bare Aluminum samples. The minimal value of solar absorptivity is achieved for the sample polished using glass beads without oxidation.

5 Thermal analyses

5.1 Description

5.1.1 Purposes

Thermal analyses can be performed both numerically and analytically. Due to the large number of unknown parameters of a typical space system, and to the mathematical difficulty implied in the radiative problem, usually the first approach is the preferred one.

The purposes of the thermal analyses can be summarized as follow:

- Preliminary investigation of the system
- Determination of the key parameters/elements
- Optimization of the system
- Correlation with the results of the tests conducted on the real hardware

The preliminary investigation about the thermal behavior of the systems is carried out before the realization of the real device. In this way it is possible to determine the temperatures and the heat fluxes that the system will experience. In this phase, the design may still radically change and the results are subjected to large uncertainties.

The determination of the critical components and parameters of the systems allows identifying the weak point of the thermal design and studying different solutions.

The optimization of the systems consists in a review of the first design, modifying the key elements in order to achieve better results in terms of instrument functioning with respect to the defined parameters, such as performances, requirements, efficiency and weight. Numerical analyses consent the simulation of different solutions without the realization of a real model.

Finally, the hardware of the final design will be tested. The results from the tests should be correlated with the numerical model in order to correct the some parameters, obtaining a more accurate thermal model. Typical parameters which are affected by large uncertainties are, for instance, the conductive conductance of the joints, the precise value of the thermo-optical properties and the thermal conductance inside elements with complex shapes or honeycombs.

The first step of the thermal analyses consists in calculating the environmental fluxes which strike the instrument: these heat fluxes are implemented as boundary conditions in the solution of the thermal problem. In order to evaluate the environmental fluxes, all the parameters concerning the orbit and the environment should be provided. This includes the temperature map of the surface of Mercury, the position and the attitude of the s/c with respect to the Sun and the planet.

Results from the radiative analysis are implemented in the thermal network model. The environmental fluxes are used as boundary conditions, whereas the effects of the radiative exchange are coupled with the temperature solution. Details about the thermal problem are explained in the following paragraph.

Finally the post-processing operation is used to retrieve all possible data from the system. The solution of the thermal problem produces the list of the temperatures of the system, from which it is possible to calculate all the radiative fluxes.

5.1.2 Mathematical background

The solution of the thermal problem consists in the determination of the temperatures and the heat fluxes inside a continuous system as a function of time. The process may be described by the following equations [70].

$$\frac{\partial}{\partial t}\rho u = -\nabla \cdot q'' + q''' \qquad \textit{Energy conservation equation} \qquad \textit{eq. 5-1}$$

$$q'' = -k\nabla T \qquad \textit{Heat conduction (Fourier's Law)} \qquad \textit{eq. 5-2}$$

$$q'' = -\frac{q}{A}$$ *Relation between the heat flux and the heat transfer rate* *eq. 5-3*

$$q_{1-2} = \sigma A_1 F_{1-2}\left(T_1^4 - T_2^4\right)$$ *Heat radiation* *eq. 5-4*

Variable	Physical meaning
t	Time [s]
ρ	Density [$kg \cdot m^{-3}$]
u	Internal energy [J]
q´´	Heat flux [$J \cdot s^{-1} \cdot m^{-2} = W \cdot m^{-2}$]
q_{1-2}	Heat transfer rate between body 1 and body 2 [$J \cdot s^{-1} = W$]
q´´´	Heat flux of the sources [$J \cdot s^{-1} \cdot m^{-3} = W \cdot m^{-3}$]
K	Thermal conductivity [$W \cdot m^{-1} \cdot K^{-1}$]
A	Area [m^2]
σ	Stefan-Boltzmann constant ($\sigma = 5.670 \cdot 10^{-8}$ $J \cdot K^{-4} \cdot m^{-2} \cdot s^{-1}$ [69])
A_1	Radiative area of body 1
F_{1-2}	View factor between body 1 and body 2
T	Temperature [K]

Table 5-1: Parameters of eq. 5-1, eq. 5-2, eq. 5-3 and eq. 5-4

Like many differential problems, the analytical solution is possible only for very simple geometries and conditions. Therefore, an approximation of the equations or/and of the system is necessary. In order to create a computer model of the problem, the geometry and the time should be discretized: the main advantage, from a computational point of view, is that a continuous system obeys differential equations, whereas a discretized model obeys a system of algebraic equations. In a continuous system, the variables present a spatial and time distribution: their values can be numerically calculated only for some points in space and for some time steps, but the analytical distribution would remain unknown. A system of algebraic equations can be solved in a finite number of variables using standard computer science techniques.

There are different ways to discretize the problem, each one which its own advantages and disadvantages: some of the best known are the Finite Elements representation and the Lumped Parameter (or Network Analogy) method. The last one has found many applications for the solution of thermal problems: it has its origins in the analogy between thermal and electrical problems. The success of the Network Analogy lies in its simplicity and in the possibility of using the same conceptual and mathematical tools of the early developed electrical engineering. The Lumped Parameter method entails the modeling of a continuous medium as a network of discrete nodes, connected by bi-directional conductors. The nodes are used to represent single massive parts of the system: a thermal capacitance is associated to them, and their state is described only by their temperature; the conductors are used to model the heat fluxes between different parts of the system. Considering the electrical analogy, the temperature equates with the voltage and the heat flow with the current flow.

Another advantage of the Lumped Parameter method is the intuitive plausibility of the physical representation. Some complex pieces of mechanism can be difficult to be accurately modeled from a thermal point of view, and very often this is even not necessary. In these cases, it is possible to replace the whole component using only one node and the conductors to link it to the rest of the model. The temperature distribution and the heat fluxes inside the piece cannot be calculated, but often this is not required, since it may be insignificant for the solution of the whole thermal problem; anyway this detailed calculation would entail a very high computational and programming time. Summarizing, the Lumped Parameters method offers the possibility to build thermal models from complex real geometries, whereas other methods, such as the Finite Elements representation, are often less suitable.

Considering only solid bodies, eq. 5-1 can be rewritten, considering that the internal energy *u* depends on the temperature only (eq. 5-5). Always considering incompressible solids, eq. 5-6 states the identity between the specific heats at constant pressure or constant volume.

$$du = c \cdot dT \qquad \textit{eq. 5-5}$$

$$c = c_p = c_v \qquad \textit{eq. 5-6}$$

$$\frac{\partial}{\partial t}(\rho u) = \rho \frac{\partial u}{\partial t} = \rho \left(\frac{\partial u}{\partial T} \right) \frac{\partial T}{\partial t} = \rho c_p \frac{\partial T}{\partial t} \qquad \textit{eq. 5-7}$$

In eq. 5-7 the derivative part of eq. 5-1 has been rewritten as a function of the density, of the specific heat and of the temperature. It is finally possible to write the energy conservation equation as:

$$\rho c_p \frac{\partial T}{\partial t} = \nabla \cdot k \nabla T + \nabla \cdot \left[\sigma \; A \; F \; \nabla \left(T^4 \right) \right] + q''' \qquad \textit{eq. 5-8}$$

Where:

Variable	Physical meaning
ρ	Density [kg·m^{-3}]
c_p	Specific heat at constant pressure [J·kg^{-1}·K^{-1}]
T	Temperature [K]
t	Time [s]
k	Thermal conductivity [W·m^{-1}·K^{-1}]
σ	Stefan-Boltzmann constant (σ = 5.670·10^{-8} J·K^{-4}·m^{-2}·s^{-1} [69])
A	Area [m^2]
F	View factor
q´´´	Heat flux of the sources [J·s^{-1}·m^{-3} = W·m^{-3}]

Table 5-2: Parameters of eq. 5-8

Mathematically, the Lumped Parameter method consists in a first-order finite-difference approximation of the governing differential equation. Once the model has been discretized into a finite number of nodes *n*, it is possible to write *n* Lumped Parameter equations:

$$C_i \frac{dT_i}{dt} = \sum_{i \neq j} K_{ij} \left(T_j - T_i \right) + \sum_{i \neq j} R_{ij} \left(T_j^4 - T_i^4 \right) + Q_i \qquad \textit{eq. 5-9}$$

The meaning of the variables is reported in the following table.

Variable	Physical meaning
T	Temperature
C	Thermal capacitance
Q	External heat load
K_{ij}	Linear conductance between node *i* and node *j*
R_{ij}	Radiative exchange constant between node *i* and node *j*

Table 5-3: Parameters of eq. 5-9

It's important to note that T is not the average temperature over the node cell, but an approximation of the temperature at the nodal point.

The term on the left of the equal sign implements the thermal capacitance: this part is null in the steady state case. For each node, and for each time step, it is necessary to provide for the thermal capacity *C* and the

external incident heat fluxes *Q*. Furthermore, the linear and the radiative conductances should be defined. All the parameters can be time dependant: in this case, an iterative matrix solution is required.
In order to perform transient solutions, it is also necessary to apply a finite difference to the time variable: both explicit and implicit methods are suitable, with their own advantages and disadvantages. In particular, explicit formulations are usually more quickly solved, but since they are only conditionally stable, there is a minimal time step that can be applied in the solution of transient analyses. If the user set a time step of the solver smaller than this value, the software automatically reset the time step to 0.95 times the value of the minimal time step for stability and provides a warning in the output.
Considering only conduction, eq. 5-9 can be rewritten as

$$\frac{dT_i}{dt} - \sum_{i \neq j} \frac{K_{ij}}{C_i}\left(T_j - T_i\right) = \frac{Q_i}{C_i} \qquad \textit{eq. 5-10}$$

From which:

$$\frac{dT_i}{dt} - \left(\sum_{i \neq j} \frac{K_{ij}}{C_i}\right) T_i = F_i \qquad \textit{eq. 5-11}$$

Which has as solution:

$$T_i = A_i \cdot \exp\left\{-\left(\sum_{i \neq j} \frac{K_{ij}}{C_i}\right) t\right\} + B_i \qquad \textit{eq. 5-12}$$

The meaning of the variables is reported in the following table.

Variable	Physical meaning
T_i	Temperature
K_{ij}	Linear conductance between node *i* and node *j*
C_i	Thermal capacitance
Q_i	External heat load
F_i	External forcing
A_i	General constant
B_i	General constant
t	Time

Table 5-4: Parameters of eq. 5-10, eq. 5-11 eq. 5-12

The term inside the brace brackets in eq. 5-12 is the stability criterion, and its reciprocal is referred as *CSGMIN* in the software and in the documentation. It depends upon the sum of the linear conductances and the thermal capacitance of the node. It is influenced mainly by small elements of the systems, which present small capacitances and high thermal conductances (low resistances) with the surrounding nodes. If the *CSGMIN* is smaller than the timestep selected by the user, this may indicate that the thermal mesh is not correctly defined, in particular that it is too fine. If this is the case, the uses is trying to take into account for too small elements, which temperature is very close to that of the surrounding elements, and which can therefore be merged with them.
In addition to very small elements, issues may arise from elements which have very high thermal conductances (such as metallic parts), and therefore small thermal gradients, or which present very low (but not null) capacitances. In the latter case, often a good solution consists in simply setting the thermal capacitance of these elements to zero, neglecting the very fast transients than these components would have and that the explicit solver is not able to properly reproduce without a drastic increment of the computational time.

Coming back to eq. 5-9, the linear conductances between the nodes can be implemented to represent heat conduction inside solids, and also as an approximation of physical processes like convection, condensation and evaporation. The value of the linear conductance is derived analytically by direct integration of the Fourier Law:

$$\vec{q} = -K \nabla T \qquad \textit{eq. 5-13}$$

Where:

Variable	Physical meaning
$\vec{q}$	Density flux vector [$W \cdot m^{-2}$]
K	Linear conductivity [$W \cdot m^{-1} \cdot K^{-1}$]
∇T	Gradient of the temperature [$K \cdot m^{-1}$]

Table 5-5: Parameters of eq. 5-13

The radiative conductances represent the non-linear term of the Lumped Parameter equations. The formula describing the radiative heat exchange between the node *i* and the node *j* is the following:

$$q_{ij} = \sigma \varepsilon_i \alpha_j A_i F_{ij} \left(T_j^4 - T_i^4\right) = R_{ij} \left(T_j^4 - T_i^4\right) \qquad \textit{eq. 5-14}$$

The meaning of the parameters of the equation is:

Variable	Physical meaning
q_{ij}	Heat flux [W]
σ	Stefan-Boltzmann constant ($\sigma = 5.670 \cdot 10^{-8}$ $J \cdot K^{-4} \cdot m^{-2} \cdot s^{-1}$ [69])
ε_i	Emissivity of the node *i*
α_j	Absorptivity of the node *j*
A_i	Radiative area of the node *i*
F_{ij}	View factor between node *i* and node *j*
R_{ij}	Radiative exchange constant between node *i* and node *j*

Table 5-6: Parameters of eq. 5-14

The view factor F_{ij} between node *i* and node *j* is expressed by the formula:

$$F_{ij} = \frac{1}{\pi A_i} \int_{A_i} \int_{A_j} \frac{\cos \beta_{ij} \cos \beta_{ji}}{r^2} dA_i \, dA_j \qquad \textit{eq. 5-15}$$

Where:

Variable	Physical meaning
F_{ij}	View factor between node *i* and node *j*
β_{ij}	Angle subtended by dA_j and the normal to dA_i at dA_i
r	Distance from dA_i to dA_j
A_i	Radiative area of the node *i*
A_j	Radiative area of the node *j*

Table 5-7: Parameters of eq. 5-15

This integral can be analytically evaluated only for very simple geometries, which are not of interest for real devices. Therefore, it is necessary to calculate the view factor numerically. There are two ways to do that: numerically integrating the expression or using a ray-tracing stochastic method.

The stochastic approach allows modeling the thermal radiative behavior of the system without introducing any assumption concerning the geometry, the shapes and the thermo-optical properties: diffusive and specular reflection, transmission, absorption and emission are modeled exactly. The Monte Carlo method is a stochastic method based on a ray tracing procedure. Ray tracing methods are based on the tracing of the path of light, where the single rays are absorbed or reflected statistically in accordance with the specified thermo-optical properties and the angles of incidence of the rays: every single ray is traced, including the multiple reflections, till the absorption point. The Monte Carlo method considers the individual history of a large number of rays, from the point of emission to the point of absorption, estimating the radiative coupling averaging the obtained results. Being essentially a statistic method, the Monte Carlo approach needs to fire a large number of rays from each surface of the model: the higher the number of rays, the lower the maximal error. It is not possible, indeed, to calculate the real error of the method: it is only possible to say that the estimated value is converging towards the theoretical solution, and that the real error is within a band whose width is inversely proportional to the square root of the numbers of rays fired (see Figure 5-1).

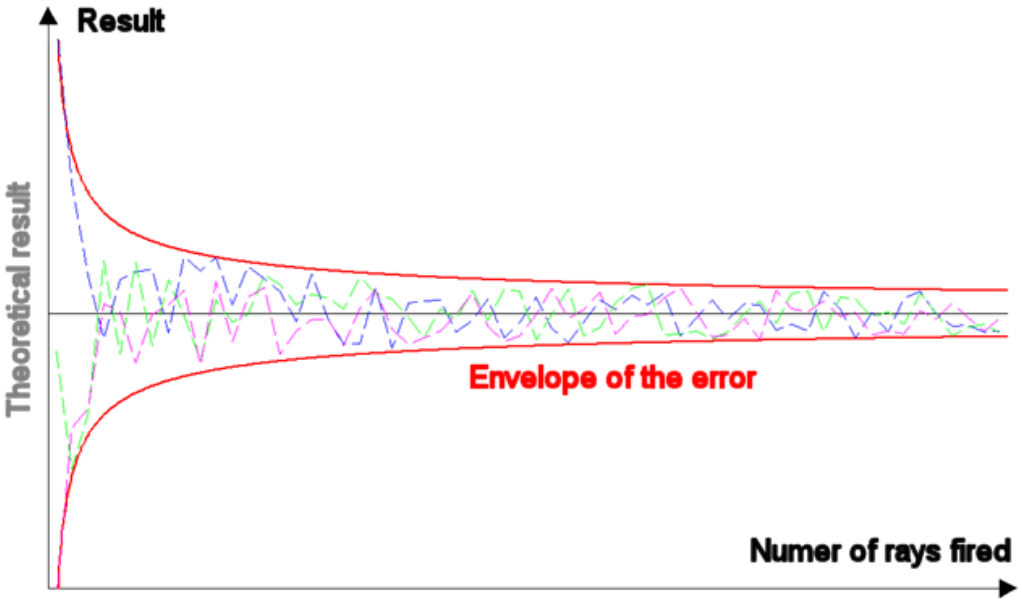

Figure 5-1: Stochastic error versus number of rays fired

The maximal error can be described by the following formula:

$$\varepsilon_{MAX} = \propto \pm e^{\frac{k}{\sqrt{N}}} \qquad \textit{eq. 5-16}$$

Where:

Variable	Physical meaning
ε_{MAX}	Maximal error
k	Constant of proportionality
N	Numbers of rays fired

Table 5-8: Parameters of eq. 5-16

The disadvantage of the Monte Carlo method is that it tends to be highly time consuming, especially for systems with low absorption optical properties: in these cases, the average number of multiple reflection is very high, and therefore even the computational time dedicated to each ray and to each surface.

5.1.3 Procedure

In order to describe the s/c orbit and mission, it's necessary to specify the 5 Keplerian orbital elements which determine the orbit: the eccentricity, the semimajor axis, the orbit inclination, the longitude of the ascending node and the argument of the periapsis (see Figure 5-3).

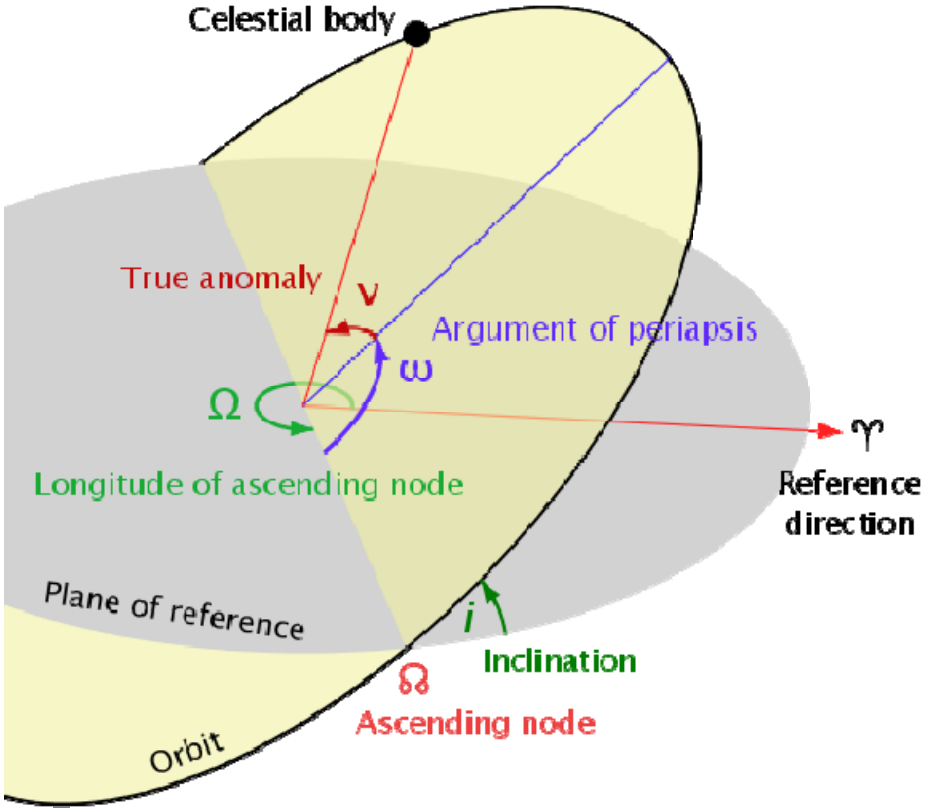

Figure 5-2: MPO orbital elements [71]

The reference values for the nominal orbit of the MPO are reported in the following table:

Parameter	Value
Eccentricity e	0.163229709
Semimajor axis a	3947.99 km
Inclination i	90°
Longitude of the ascending node Ω	68°
Argument of the periapsis ω	0°

Table 5-9: MPO orbital elements [44]

The s/c attitude should be defined for each time step of the simulation.

In addition, the planet and the Sun radii should be defined, such as the Sun temperature and the planet temperature map. This last parameter is very important for the calculation of the planetary IR fluxes, which can represent a large part of the environmental heat load. The planet temperature map can be calculated assuming the Mercury surface as a grey body and calculating the heat balance of the whole planet. This method produces only one temperature to reproduce the whole surface, and it is therefore too inaccurate, especially in consideration of the strong thermal gradients Mercury experiences (see Table 3-2 and Figure 3-6). A more precise method consists in implementing a user defined temperature map, which can be created assuming a predefined distribution law (for instance, a cosine law with respect to the subsolar point) or

creating a model for the Mercury soil. An example of a temperature map calculated with this last method is reported in Figure 5-3. The longitude of the map, in compliance with the ESARAD convention, is set zero over the subsolar point; the latitude is zero at the equator of the planet. It can be noted that the highest temperature is not achieved exactly over the subsolar point but slightly after it (with respect to the planet rotation): this is an effect of the soil thermal inertia, which has been considered in model and that cannot be present assuming a simpler cosine law temperature distribution.

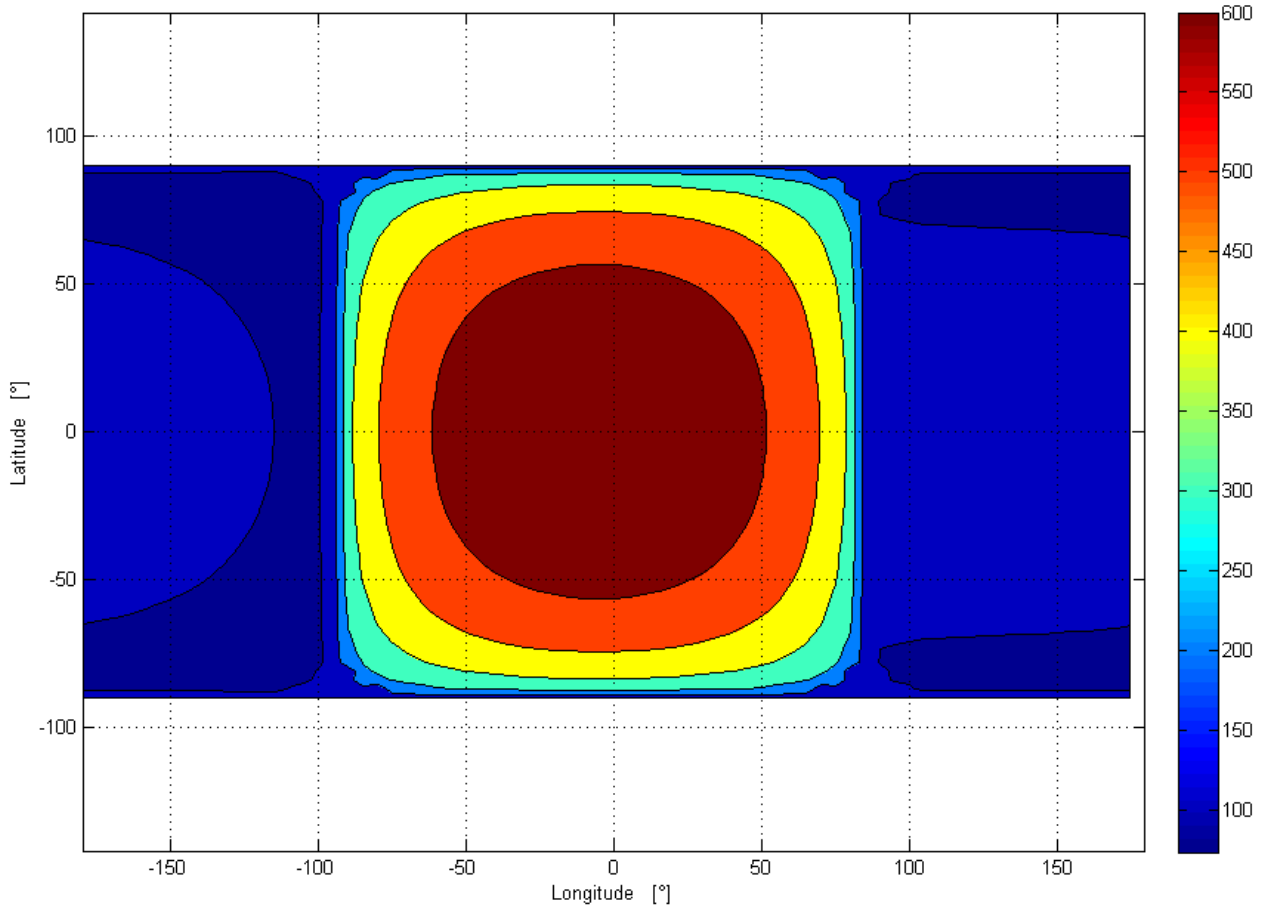

Figure 5-3: Mercury temperature map

5.1.4 Software

The European Space Agency required the use of ESARAD v.6.2 and ESATAN v10.2 for the thermal numerical simulation (requirement #3101 of the Instrument Requirement Document [54]).

ESARAD is a powerful tool, developed by Alstom Aerospace (now ITP-Alstom), which allows modeling and analyzing the radiative aspects of the thermal design. The main key features of the software are:

- Possibility to create a geometrical model for radiative purposes
- Possibility to define different orbits, non-orbital paths and attitudes
- Calculation of the geometrical view factors and of the radiative exchange factors
- Calculation of the solar, albedo and planetary fluxes
- Calculation of some of the linear conductances inside the defined geometry

The radiative analysis using ESARAD is usually the first step of a complete thermal analysis (see §5.1.1).

Peculiar characteristics of ESARAD v6.2 (or above) are the possibility to implement a temperature map to represent the planet surface and the possibility to represents the finite size of Sun (lower part of Figure 5-4) in the calculation of the environmental fluxes. These features, not often implemented into radiative software, are of great importance in the representation of the orbit around Mercury, and have been implemented into the software just to make it suitable for the BepiColombo mission.

The surface of the planet experiences strong thermal gradients, and the representation of the surface using a fixed homogeneous temperature would jeopardize the calculation of the planetary fluxes, in particular of the peaks.
Avoiding a punctiform representation of the Sun, it is possible to take into account for the solar slanted rays. At 0.38 AU from the Sun, the star cannot be modeled as a single point source at infinite distance (upper part of Figure 5-4) without introducing considerable errors in the calculation of the solar fluxes.

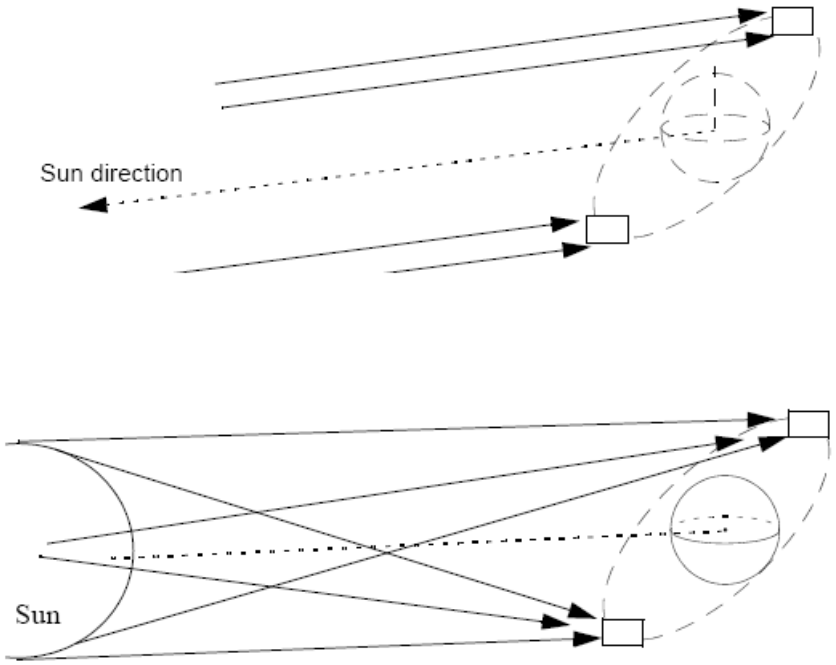

Figure 5-4: Different modeling of the Sun in the radiative analyses [72]

ESARAD v6.2 has also some drawbacks: for instance, it is not possible to implement temperature-dependant thermo-optical properties, and to model different behaviors of the surfaces with respect to different wavelengths of radiation. Further, ESARAD v6.2 does not allow modeling complex 3D surfaces, such as ellipsoids and hyperboloids: therefore, a proper approximation to model the Stavroudis baffle should be implemented (see §7.2).
The thermal network expressed by eq. 5-9 is solved using ESATAN, again from Alstom Aerospace. ESATAN is a software package for the prediction of temperature distributions in thermal systems, which makes use of the thermal network representation. From the calculated resulting temperatures, it is possible to determine the heat fluxes between components or between a single component and the environment. ESATAN is written in Fortran 77, and it is basically a compiler of the same language. The thermal model must be written as numerical code following the Fortran 90 / Mortran rules, listing the thermal nodes and its properties, the conductive and radiative conductances between them (which have been calculated using ESARAD), the boundary conditions, the environmental heat fluxes (again from ESARAD) and the solution routine. ESATAN creates an executable file of the model and tries to solve the thermal system. The results may be outputted only for a few parameters or for the whole systems. For large models and transient analysis, it is possible to achieve very large output files, above 1 Gb.
The results have been analyzed using ThermNV, the last software from the Alstom package. Using this calculation and visualization tool, it is possible to determine the heat fluxes from the nodal temperatures, to plot temperature distributions and fluxes in flexible representations.
In February 2009, ITP-Alstom released ESATAN-TMS, a new package in which ESARAD and ESATAN have been merged together. The software performs basically the same operations of the previous versions, with a couple of minor improvements. In particular, now it is possible to use a single Graphic User Interface

for both the radiative solver and the thermal network modeling; nonetheless, the core and the mathematical part of the software is still the same and ESATAN-TMS provides the same results of ESARAD and ESATAN.

5.2 Indexes of performance

In order to evaluate the performances of the different models, five parameters have been taken into account: the purpose of the thermal design is to optimize these values.
The functioning of the device is actually characterized by many values and by many indexes: however, in order to perform a design optimization, only the most important of them have been analyzed: some of them are related to the device ability to resist the environmental conditions avoiding failures and damages, others provide for information about the system efficiency. Even if the secondary parameters have not been taken into account for the design optimization, they have anyway been checked for each selected design: the exceeding of the acceptable margins leaded to the discard of the chosen configuration, even if it has been proved to be suitable concerning the primary parameters.
Some of the primary indexes of performance are actually requirements from the University of Bern and are clearly defined; some others derive from technical requirements from other components or from technological limits.
As it would become clearer afterwards, some indexes of performance present opposite trends, and therefore it is impossible to optimize them all together. A trade-off between different necessities and different requirements tried to find the best achievable solution, assigning different weights and different priorities to the different indexes of performance.

5.2.1 Rejection efficiency

The rejection efficiency is the main parameter to describe the performances of the device. It expresses the ratio of the heat load rejected towards deep space to the total received environmental heat load.
This value is a requirement prescribed by the University of Bern in the Instrument Requirement Document:
BEL-REQ-7602: The transmitter baffle shall reject, on average along an orbit, >90% of the environment fluxes (IR, albedo, and sunlight) striking it. [20]

5.2.2 Fluxes to the BEX

As described in the previous paragraph, the device should minimize the heat load absorbed by the environment. This flux can be dumped into the instrument through the laser beam expander (BEX) or into the s/c. There are no specific requirements concerning the distribution of the fluxes or the maximal allowable heat flux to be dumped into one specific sink. However, analyses on the functioning of the laser generator highlighted possible problems: during the operational phase, too high values of heat fluxes reaching the BEX can interfere with the laser pumping, increasing the signal to noise ratio; furthermore, even during the non-operational phase, too high heat fluxes entering the BEX can damage the instrument.
There are no well defined upper limits to the total heat fluxes entering the BEX: therefore, one goal of the thermal design optimization is to minimize, as much as possible and being all of a piece with the optimization of the other parameters, the heat fluxes entering the BEX. It has to be noted that the goal is to minimize the total heat flux, comprehensive of both direct environmental fluxes and re-emitted IR radiation from the device.

5.2.3 Fluxes to the s/c

As already described, the absorbed environmental heat fluxes can be dumped either into the instrument or into the s/c. Even if the s/c environment is not part of the instrument, it is desirable to minimize the heat load on this sink in order to prevent any problem to other units of the instrument and to the s/c.
There is not a defined upper limit for this parameter: the thermal design optimization has been performed in order to reduce this value. The results of the trade-off with the other parameters should be evaluated by the

thermal architect of the instrument and the thermal architect of the s/c: if they consider this parameter too high, the found solution should be discarded and a new trade-off would be performed.

5.2.4 Maximum baffle temperature

There are no prescribed limits to the maximal baffle temperatures. Anyway, it's clear a limit should be imposed to this value: a too high temperature on the baffle would indeed entail serious issues.
The maximal temperature achievable by the baffle is one of the primary indexes on which choosing the baffle material: it should withstand the maximal temperature without melting or achieving excessive deformations, which can jeopardize the optical behavior or obstruct the laser beam. Excessive deformations can also damage the optical coating (if present), and this value determines also which classes of coatings can be applied to the structure: many coatings do not withstand high temperatures, or changes their thermo-optical properties above the prescribed temperature limits.
A very hot baffle also entails very high heat fluxes re-emitted towards the spacecraft and/or to the instrument inner side: therefore, optimizing this parameter helps also in the optimization of the previous two indexes of performance.
The physical and technological limits which limit the baffle maximal temperature also apply to each component which is connected to the baffle: not only the baffle structure should withstand the maximal temperature achieved, but it is also necessary to guarantee that all the surrounding components are able to withstand the consequently high temperatures and the received heat fluxes. Particular relevance has in this context the s/c MLI blankets, which in some models can directly touch the baffle surface.

5.2.5 Maximum filter temperature

There are some requirements even on the filter maximal temperature: the melting point of the sapphire is very high and consequently it doesn't arise any problem concerning the physical and structural integrity of this component. Nevertheless, the filter has a very important and sensible optical behavior: therefore, it is mandatory to minimize the thermal distortions, which can jeopardize the optical functioning of the device.

5.2.6 Secondary parameters

As already mentioned, there are many other parameters which could be used to evaluate the performances. The following indexes have been considered anyway less important than the previously described ones. Therefore, the thermal design optimization has been performed without the attempt to minimize them; at the end of each thermal optimization, these parameters have been assessed in order to avoid achieving too high (or too low) levels.
In the following list there are also some requirements from the University of Bern: since they proved to be quite easily achievable, they have not been included into the indexes of performance, but their compliance has also been checked for each thermal design.

5.2.6.1 Maximal sunlight entering the instrument

BEL-REQ-7601: A baffle for the transmitter shall be implemented which shall limit sunlight entering the instrument to <1% of the flux at the aperture when the Sun is in the range 35° to 90° from the instrument line of sight. [20]

5.2.6.2 Clear aperture obscuration

BEL-REQ-7603: The transmitter baffle shall not obscure the beam expander clear aperture. [20]

5.2.6.3 Maximal mass

BEL-REQ-5401: The TBU mass is max. 0.16 kg without margin.[20]

This requirement proved to be not achievable, for thermal and structural reasons. Therefore, the thermal design tried to reduce, as much as possible, the total mass, always considering the indexes of performance and without assigning a too high performance weight on this parameter.

5.2.6.4 Thermal gradients on the filter and on the baffle

In order to avoid jeopardizing the optical function of the sapphire filter, it's important to limit the thermal deformation of the filter disc, which is caused by the thermal gradient on its surfaces and between the front and the back surfaces. After a first rough evaluation, a maximal difference of 1°C on the filter surface has been allowed.

To prevent excessive thermal deformation on the baffle, the thermal gradient on the baffle has been kept under control and checked for each configuration. This value is important especially for the Stavroudis configuration, in which the optical functioning of the baffle is more relevant.

5.3 Wavelength dependant thermo-optical properties

For a give surface temperature, the monochromatic emissivity, absorptance, transmissivity or diffusivity are a function of the wavelength only. Therefore, the amount of heat power which is exchanged or received by the elements of the system can be calculated on the bases of the wavelength of the incoming/outcoming radiation and of the surface temperature.

In most thermal software, including ESARAD, the wavelength dependency of the thermo-optical properties is reduced to the definition of only two different sets: one for the solar-UV waveband and one other for the IR waveband. No dependency upon the temperature of the surfaces is usually taken into account. In these software, the set of thermo-optical properties in the solar waveband is used to calculate the environmental fluxes coming from the Sun (direct solar flux and albedo); the latter set is used both for the calculation of the IR planetary environmental fluxes and for the internal radiative coupling.

For most surfaces the wavelength dependency of the optical properties can be neglected, and the reduction of the spectrum to two sets of properties is adequate. In some other cases, when the thermo-optical properties significantly vary with the wavelength and when the temperature of the emitting and/or receiving body presents some variations, it is not. The baffle unit contains an optical filter, which main purpose is to reflect the planetary fluxes (see §1.4.1), and which spectrum is strongly wavelength dependant (see Figure 1-7). In addition, Mercury experiences extreme temperature variations (see Table 3-1), and thus also the emitted radiation. It is therefore necessary to develop a method to implement dynamic thermo-optical properties into ESARAD, in order to properly simulate the filter's behavior.

The direct solar flux and the albedo flux are originated from the Sun, which surface temperature can be considered constant over time. Therefore, the wavelength dependency of the thermo-optical properties can be neglected for these heat fluxes. In this section, only the planetary IR fluxes, which are originate by bodies which surface temperature may vary over a wide range, are considered. Two different aspects should be taken into account:

- The different behavior of the optical surfaces with respect to different wavelengths of the environmental radiation
- The modification of the thermo-optical properties with the variation of the surface temperature of the receiving body

The first aspect implies that, even if the system is kept at a constant temperature, its optical properties and the consequent heat load absorption may vary with the waveband of the environmental radiation (and then with the temperature of its source).

The thermo-optical properties of any optical surface should then be "weighted" upon the spectrum of the planetary radiation, which depends on the surface temperature. The spectrum of the planetary radiation can be represented with a good approximation [68],[73] using the Planck's law of a black body radiation:

$$I(\lambda,T)d\lambda = \left(\frac{2\cdot h\cdot \lambda^3}{c^2}\right)\cdot\left(e^{\frac{h\cdot\lambda}{k\cdot T}}-1\right)^{-1} d\lambda \qquad \textit{eq. 5-17}$$

Where:

Variable	Physical meaning
I(λ,T)	Intensity of the radiation in the wavelength range between λ and $d\lambda$ [W·m^{-3}]
λ	Wavelength [m]
T	Temperature of the black body [K]
h	Planck constant (6.62606896·10^{-34} J·s [74])
c	Speed of light in vacuum (2.99792458·10^{-8} m·s^{-1} [74])
k	Boltzmann constant (1.3806504·10^{-23} J·K^{-1} [74])

Table 5-10: Parameters of eq. 5-17

A representation of eq. 5-17 is depicted in Figure 5-5.

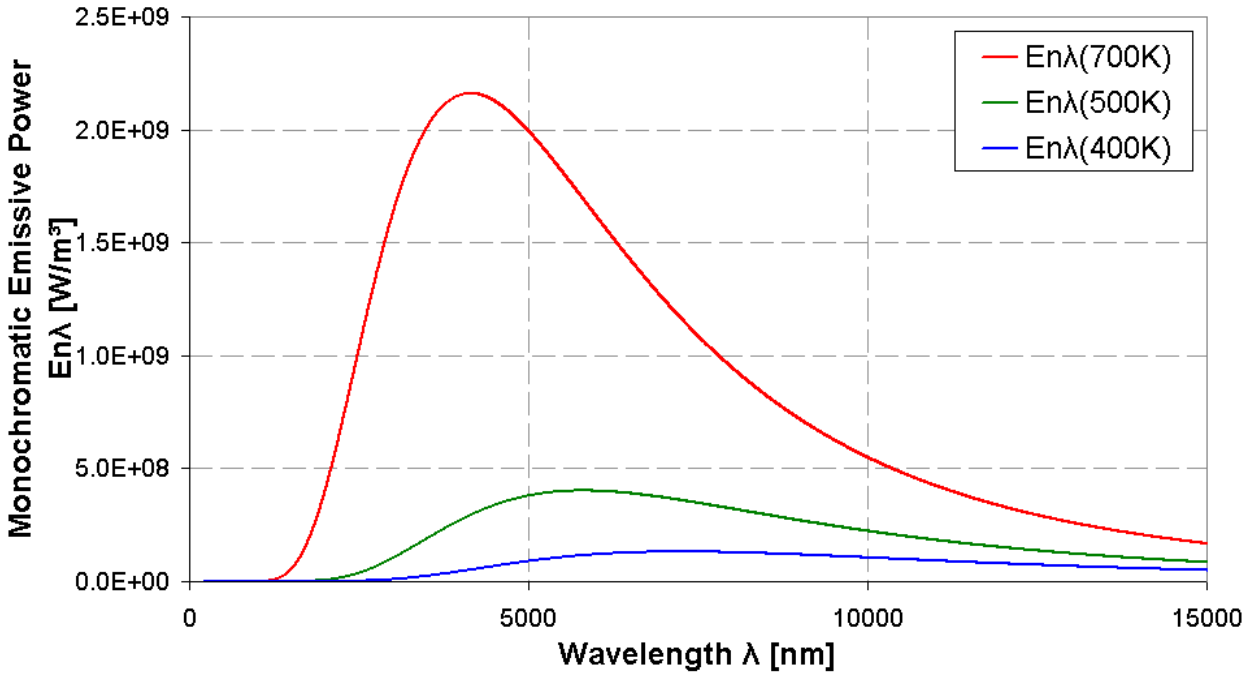

Figure 5-5: Black body emission spectrum for different temperatures

As can be noted from eq. 5-17, the intensity of the radiation at the desired wavelength depends only on the temperature of the emitting source. But the surface temperature of a planet cannot usually be considered homogeneous. Therefore, an equivalent temperature, used to generate the radiation spectrum, should be defined and calculated. A possible solution consists in using the equivalent homogeneous temperature that the planet should have to cause the same density of power of the actual environmental radiation. This last parameter can be analytically calculated, or, for complex problems, it can be numerically determined performing a simulation with the real geometry and every surface set as black body. Thus, it is possible to express the calculated radiation power as:

$$q = \sigma\cdot\varepsilon_{PLANET}\cdot\alpha_{BODY}\cdot F_{PLANET-BODY}\cdot T_{EQ}^4 \qquad \textit{eq. 5-18}$$

Where:

Variable	Physical meaning
q	Heat flux
σ	Stefan-Boltzmann constant ($\sigma = 5.670 \cdot 10^{-8}$ $J \cdot K^{-4} \cdot m^{-2} \cdot s^{-1}$ [69])
ε	IR hemispherical emissivity of the planet
α	IR absorptance of the body
F	View factor between the planet and the body
T_{EQ}	Equivalent temperature of the planet

Table 5-11: Parameters of eq. 5-18

Both the heat power and the view factor can be calculated, analytically or numerically; the absorptivity of the body is 1, if a black body has been implemented, in any case it is known; the emissivity of the planet is taken from the applied model: hence, it is possible to calculate T_{EQ}. This represents the equivalent temperature, for each orbital position and for each attitude of interest, which should be used to calculate the emission spectrum of the planet using eq. 5-17. The emission spectrum characteristic of each of these conditions is used to weight the thermo-optical properties spectrum of any desired surface, using the formula:

$$\eta\left(T_{EQ}, T_{BODY}\right) = \frac{\int_0^\infty I\left(\lambda, T_{EQ}\right) \cdot \eta\left(\lambda, T_{BODY}\right) d\lambda}{\int_0^\infty I\left(\lambda, T_{EQ}\right) d\lambda} \qquad \textit{eq. 5-19}$$

The meaning of symbols used in eq. 5-19 is reported in the table below.

Variable	Physical meaning
η	Generic thermo-optical property
T_{EQ}	Equivalent temperature of the planet
T_{BODY}	Temperature of the stricken body
I	Intensity of the radiation in the frequency range between λ and $d\lambda$ [$W \cdot m^{-3}$]
λ	Wavelength [m]

Table 5-12: Parameters of eq. 5-19

The presence of the body's temperature in eq. 5-19 requires the solution of the thermal network, which is not necessary for the pure radiative analysis. Therefore, some iterations using the radiative solver and the thermal solver are required. A long computational time is expected following this method. Furthermore, the variation of the spectrum upon the body's temperature is often unknown, compromising the possibility of using eq. 5-19.

Fortunately, for a large class of materials the variation of the spectrum upon the temperature is not very sharp. The expected temperature range for a spacecraft is also much narrower than the temperature variation of most radiation sources (especially for the inner planets), reducing the influence of the T_{BODY} in comparison to the T_{EQ} in eq. 5-19. Neglecting the influence of the surface temperature, that is considering the thermo-optical properties constant upon the body's temperature, it is possible to write:

$$\eta\left(T_{EQ}\right) = \frac{\int_0^\infty I\left(\lambda, T_{EQ}\right) \cdot \eta\left(\lambda\right) d\lambda}{\int_0^\infty I\left(\lambda, T_{EQ}\right) d\lambda} \qquad \textit{eq. 5-20}$$

It is therefore possible, for each orbital position and attitude of interest, to calculate the planet's equivalent temperature. If the optical spectrum of the body is known, this curve can be weighted on the planet's radiation spectrum (not necessarily a black body radiation) and integrated on the relevant waveband in order to calculate the total hemispherical optical properties to be implemented for the calculation of the planetary heat radiation.

This procedure involves the use of the radiative solver only. If the dependency of the thermo-optical properties on the body's temperature is not negligible, some iterations using the thermal solver are unavoidable.

The weighing of the thermo-optical properties on the planetary black body radiation is graphically represented in Figure 5-6. Integrating the resulting curves and dividing them for the integral of the black body curve, it is possible to obtain the scalar values to be implemented in the software.

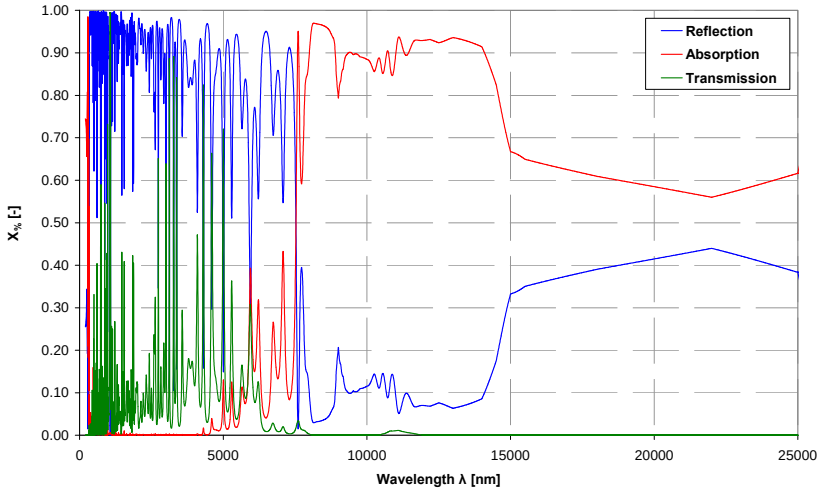

X

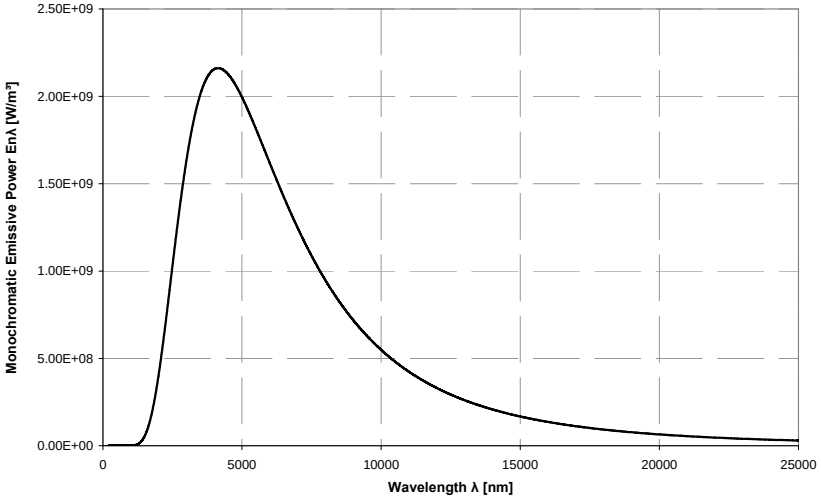

=

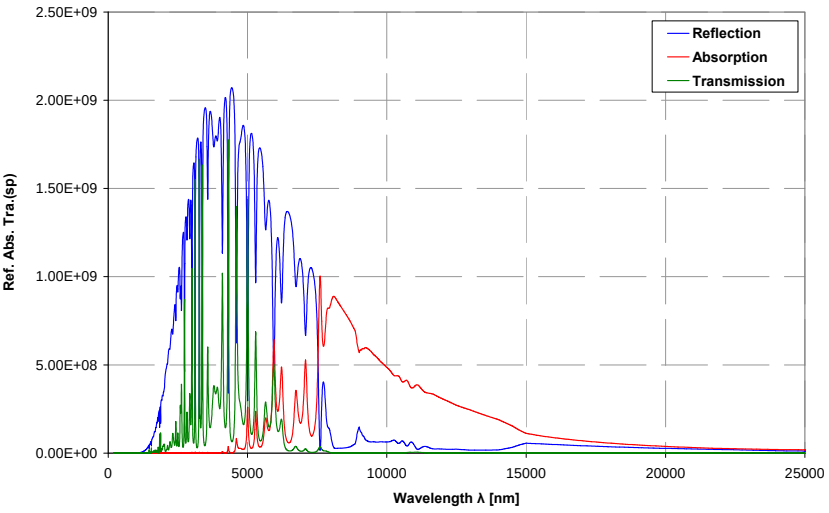

Figure 5-6: Thermo-optical properties weighing

6 Cylindrical TBU: models and analyses results

6.1 Model description

6.1.1 Mechanical model

A CAD model of the cylindrical TBU, integrated into the BELA environment and alone, can be seen in the following pictures:

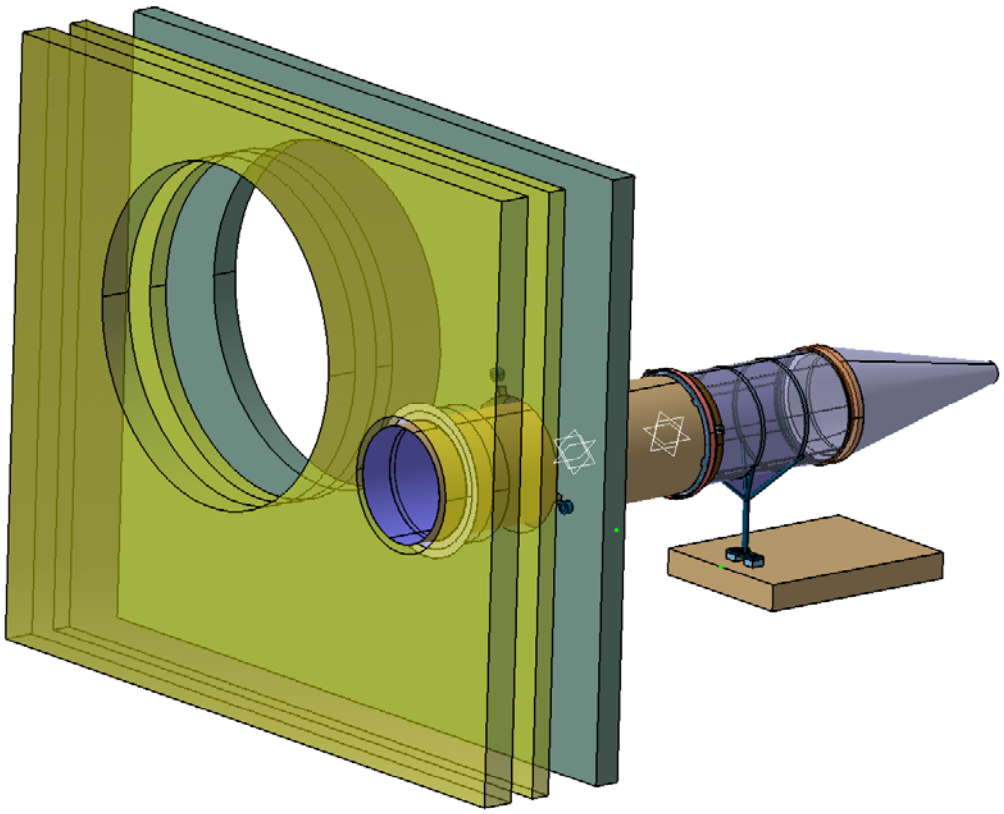

Figure 6-1: Cylindrical TBU, SPU and environment – CAD model

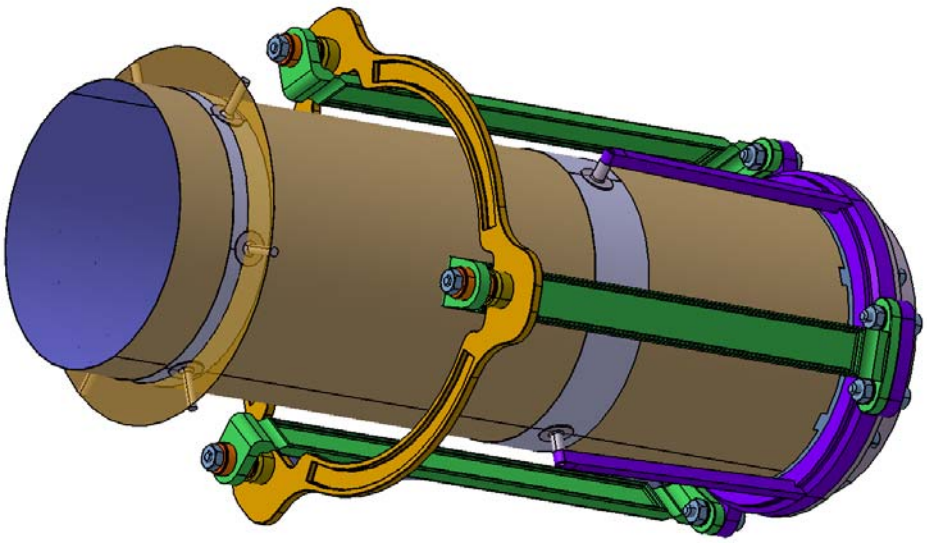

Figure 6-2: Cylindrical TBU – CAD model

The cylindrical TBU is connected to the filter mount with three aluminum arms (violet in Figure 6-2); the filter mount is then connected to the BSP mounting ring (orange in the picture) through three aluminum isostatic mounts (green color). The BSP mounting ring is made of aluminum and is directly glued on the BSP, representing therefore the boundary between the TBU unit and the BELA instrument. There is no direct connection between the baffle cylinder and the filter mount; only a small MLI foil should be fastened in order to prevent for undesired radiation coming inside the instrument.
A small titanium ring, sustaining a MLI foil, is placed in front of the cylinder, between the s/c HT-MLI and the s/c Std-MLI: its purpose is to stop the residual environmental radiation coming through the gaps between the s/c MLI blankets and the baffle body. It is not possible to avoid this gap, leaving the s/c touching the cylinder, mainly for two reasons: the thermal dilatation of the elements can induce inadmissible mechanical stresses, and the heat conduction between the baffle and the MLI blankets may lead to unacceptable high temperatures and decrease the insulation efficiency.
The sapphire filter is set between the two filter mount parts, both made of aluminum. In order to reduce the mechanical stresses, especially the thermally induced ones, the filter is pinned between two Room-Temperature Vulcanization (RTV) rubber rings. This material is suitable for space applications, even in proximity of optical devices, since it does not outgas and it can withstand high temperatures [75]. The rubbish rings are represented in Figure 6-3 by the two lavender ellipses, between which the sapphire filter is placed. Furthermore, three radial spacers of the same material are placed between the lateral side of the filter disc and the filter mount: one of these components, depicted as a lavender rectangle, can be seen in the upper side of Figure 6-3.

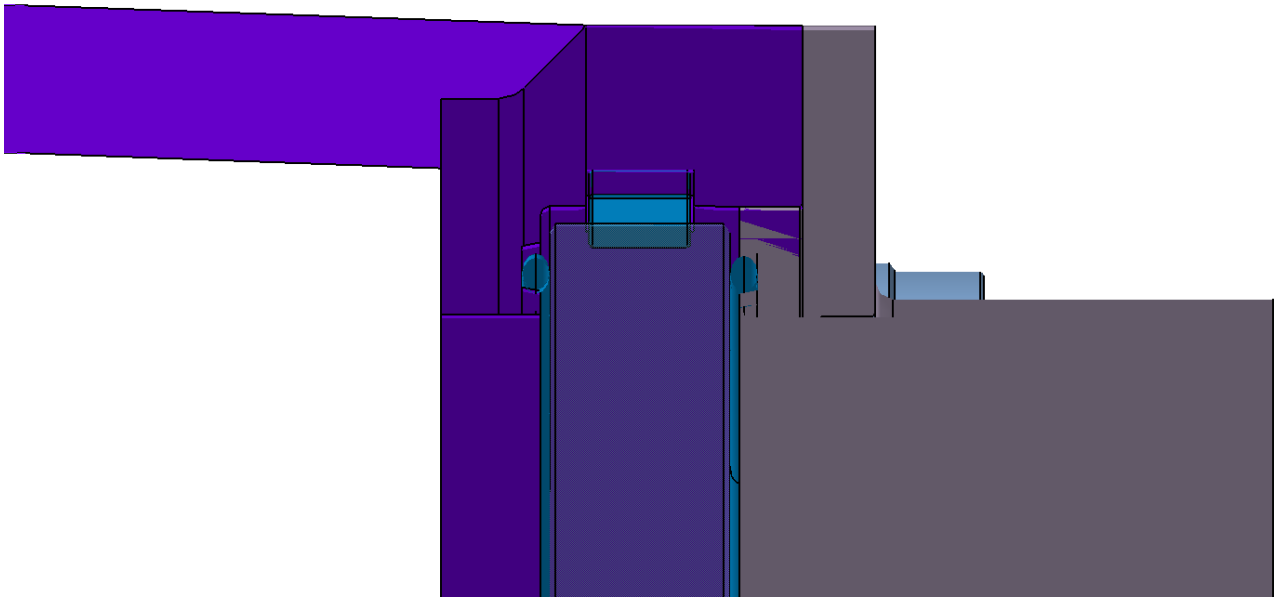

Figure 6-3: Filter mount and filter – CAD model

On the right side of the TBU, the SPU is also visible in Figure 6-1: it is the semi-transparent cylinder just before the grey cone, which represents the beam expander. The SPU lean on the optical bench, a component of the s/c which is schematically represented as a parallelepiped.

6.1.2 Geometrical Mathematical Model

The Geometrical Mathematical Model (GMM) of the cylindrical TBU, including the SPU and the MPO environment, is show in Figure 6-4.

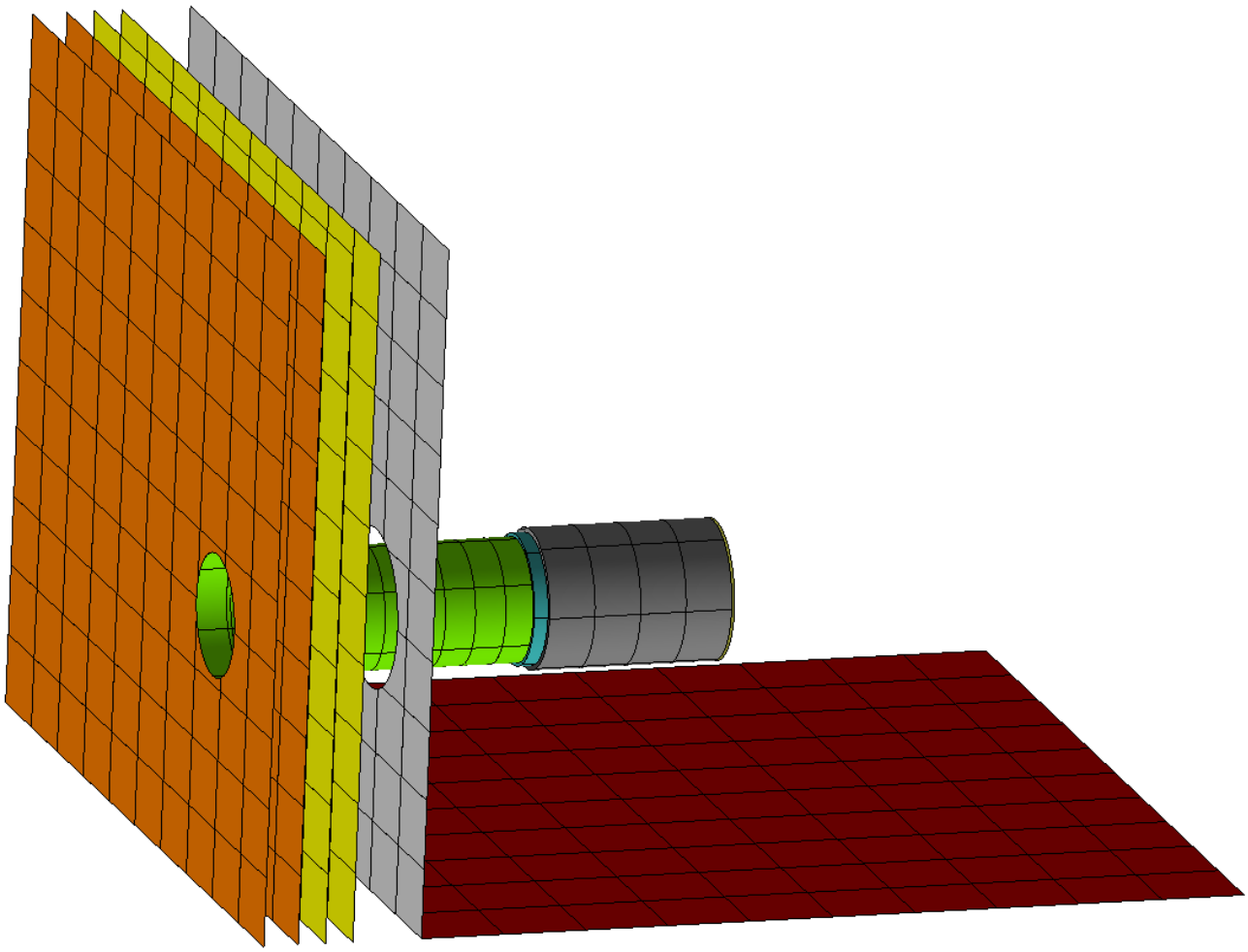

Figure 6-4: Cylindrical TBU, SPU and environment – GMM

The baffle has been implemented using a cylinder, divided into 60 faces and nodes. The filter mount is placed just after the cylindrical shell, and it is represented by its external surface: a squat cylinder and an annulus; surrounded by the filter mount, the filter has been implemented using a disc divided into 18 faces/nodes (Figure 6-5).

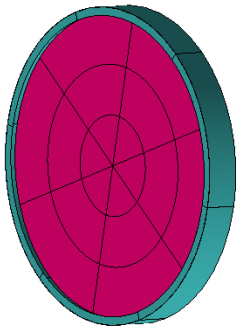

Figure 6-5: Filter and filter mount – GMM

The SPU is represented by the grey cylinder in Figure 6-3; the beam expander has been implemented using a simple black body disc at the end of the SPU cylinder.

The modeling of the beam expander and of the laser head box is liability of another company, and at the moment of the model development a detailed GMM of the device was not ready. Therefore, a simplified model of the LHB has been implemented and the equilibrium temperature of the front lens has been calculated. This value has been applied to the black body disc in the real analyses.

6.1.3 Thermal Matemathical Model

The TMM of the Stavroudis baffle is composed by the following nodes:

Element	Number of nodes	Material
Baffle	60	Ti 6242
Filter	18	Sapphire
Filter mount	6	Al 7075
SPU cylinder	24	Al 7075
Total	*108*	

Table 6-1: Nodes of the cylindrical TBU TMM [44]

The conductive conductances inside the TMM are shown in Figure 6-6.

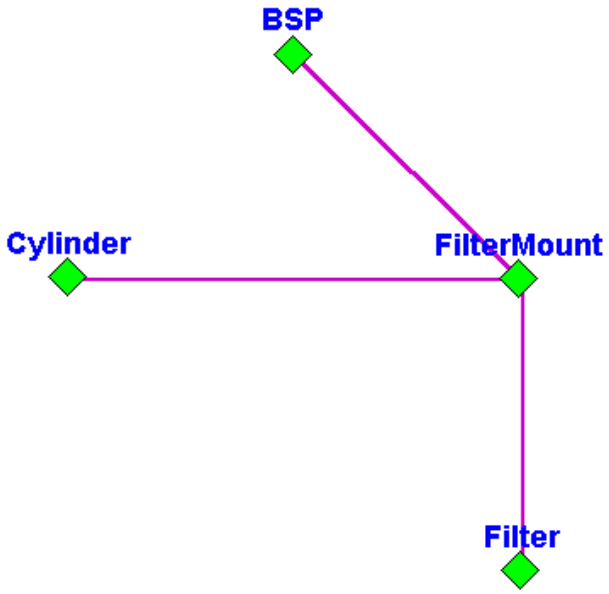

Figure 6-6: Conductive conductors of the cylindrical TBU TMM

6.2 Effect of the thermo-optical properties on the indexes of performance

In order to identify the optimal thermo-optical properties for the TBU cylinder, many simulations have been performed; the results in terms of indexes of performance have been compared to identify the best trade-off. The main purpose of these analyses was to determine the device behavior for different set of optical properties; to determine the influence of the different parameters on the single indexes of performance and to understand the synergy between these parameters and the whole device performance. The correlation between IR emissivity, solar absorptance and the indexes of performances of the TBU was the primary goal. These analyses have been performed for both a completely diffusive reflection and a perfect specular reflection. The actual situation would be intermediate between these two extremes. The ratio of diffusive/specular reflection is strictly correlated with the material intrinsic nature and with the surface roughness [76]; usually very polished metal surfaces, which have high values of total reflectance, exhibit high ratios of specular/diffusive reflectance, whereas coarse materials present a prevalent diffusive reflectance [76]. The cylindrical baffle has been considered divided into two parts, the front and the back, which can be differently coated. The reason of this division is to implement different rejection strategies as a function of the intensity of the environmental radiation (high on the front, lower on the back) and of the possibility to radiate towards the deep space (again high on the front).

The optical properties of the cylinder front and of the cylinder back have been set to a finite number of options: the range of 0÷1 has been divided into 7 point with a step of 0.15 for both α and ε, both for the cylinder front and for the cylinder back. Hence, 2401 cases have been analyzed for the diffusive reflection and the same amount for the specular reflection, covering the most part of the possible optical properties, and more precisely the range between 0.05 and 0.95 for each parameter. It has to be noted that even the unrealistic combinations of optical properties, or the values which represent unusable coatings, have been analyzed.
Each analysis, comprehensive of radiative coupling calculations, solution of the thermal network and post-processing, lasted about 12 min: therefore, the execution of all the 4802 cases required about 960.4 h, more than 40 days of computational time. These analyses have been mostly performed at night capitalizing on distributed parallel computation of unused computers. The simulated system consists of the baffle only, without the SPU and the environment. In this way, it is possible to minimize the influence of other components of the system and the computational time.
The simulated orbit is the Hot Case 1, which is described in §3.4. The resulting charts are reported in Appendix. In each page, 16 charts have been printed, varying the thermo-optical properties (IR emissivity and solar absorptance) of one of the two areas of the cylinder (front or back), and varying the optical properties of the other part inside each single chart. In each chart, it is therefore possible to analyze the trend of one single parameter as a function of the optical properties of only one part of the cylinder, and analyzing the differences between different charts in the same page it is possible to assess the influence of the optical properties of the other part of the baffle.

6.2.1 Rejection efficiency

The rejection task is divided between cylinder and filter. The cylinder shall re-emit most of the solar light and reduce the solar flux toward filter. The filter shall be optimized to reduce the IR transmission. As a matter of fact, the filter reflects better the solar radiation (90%) than the IR radiation (37%). The remaining IR flux is almost entirely absorbed by the filter itself (61%).
Since the filter reflects better the solar light than the IR radiation, it is better to not convert solar light into IR before it strikes the filter.
The TBU operates as following: the cylinder shall reject the most environment radiation as possible. The remaining part don't have to be converted into IR radiation (by absorbing solar light in the back), because the filter reject better solar light than IR radiation.
The analyses performed implementing a perfect diffusive reflection exhibit a minimal efficiency of 0.66 and a maximal one of 0.76, far below the requirement of 0.9 (§5.2.1). Both the front part and the back part of the cylinder have a strong influence on the rejection efficiency. The best results are achieved with low solar absorptance in the baffle front and avoiding very low values of emissivity in the front: in fact, ε doesn't have strong influence on the efficiency, only if very low - ≤ 0.05 – it brings to a decrement of the efficiency.
Specular coatings are generally less efficient than diffusive ones. The highest efficiency is achieved with a front part with high IR emissivity and high solar absorptance: it is indeed better to absorb solar light and re-emit it in the IR wavelengths than reflecting it backwards to the instrument. In case of α in the front is very low (smaller than 0.2), than it is better to have even low values of emissivity in the front. If a large amount of solar light is absorbed in the front, than it is better to maximize the emission. On the contrary if the most part of the solar radiation is reflected backward to the instrument ($\alpha < 0.02$), than is better to reduce also the IR emission. In the back part of the cylinder, to maximize the efficiency are required low values of solar absorptance: if α is low, than most solar light is reflected toward the filter; if instead α is high, than solar light is absorbed and re-emitted towards the filter and into the s/c. The first case entails high solar radiation on the filter; the second, high IR radiation on the same component. Since the filter reflects better solar (90%) than IR (37%) radiation, high solar reflectivity reduces the flux towards the instrument. The IR emissivity of the baffle back has no significant influence on the rejection efficiency.

6.2.2 Fluxes to the BEX

The flux dependency on back and front cylinder optical properties is very low, in case of diffusive reflection. The best solution is low solar absorptance and high IR emissivity in the front (to maximize re-emission to the deep space), and low α and ε in the back (so that the IR emission toward the filter is minimized and the solar light is not converted into IR radiation). The minimum flux achievable considering a perfect diffusive reflection is 1.76 W; the maximum is 2.24 W.

With a perfect specular reflection the fluxes towards the beam expander are much higher than implementing a diffusive reflection: the minimal value is 1.93 W and the maximal one 3.13 W. The best solution is to have high solar absorptance and high IR emissivity in the baffle front: in this way, the most part of the solar radiation is absorbed in the front and the re-emission into the deep space is more efficient; otherwise, the specular reflection entails that the solar radiation is absorbed by the back part of the cylinder (where the re-emission is less efficient because the deep space has a smaller view factor) or by the beam expander. To achieve low fluxes to the BEX, α has more influence then ε. The best coating for the back part of the cylinder is a high IR emission: it is better to absorb IR radiation from the front and re-emit it than reflect it all towards the filter; it is also important to have a low solar absorptance, because the filter reflects better the solar light than the IR radiation.

6.2.3 Fluxes to the s/c

Regarding a diffusive reflection, the best solution to minimize the heat fluxes to the s/c consists in achieving a low solar absorptance and high IR emissivity in the baffle front, to minimize the heat load absorption and to maximize the re-emission to the deep space; the cylinder back should have low solar absorptance and low IR emissivity so that to avoid absorbing the high IR emission from the baffle front. The best value achievable is 2.67 W and the worst 4.19 W.

Considering a specular reflection, the heat fluxes are slightly higher: the minimum is 2.68 W and the maximum 4.93 W. The main parameter is the solar absorptance in the baffle front: high values of α lead to low solar fluxes transmitted towards the baffle back and from there toward the s/c. For the back part of the cylinder, the best is to have low solar absorptance, so that the solar light is not much absorbed and partially emitted towards s/c.

The effect of IR emissivity in the back on the flux to the MPO depends mainly on two things:

- If the solar radiation absorbed in the back is mainly re-emitted towards the s/c and the BEX, then a high ε is better because it implies more emission towards the filter and less towards the MPO
- If the IR flux absorbed from cylinder front is emitted also towards the s/c, then from the MPO point of view it is therefore better to reflect it towards the filter, and hence a low emissivity is preferred. It has to be noted that this solution entails higher heat fluxes on the beam expander.

The first point prevails when solar absorption in the front is low, the second otherwise.

6.2.4 Maximum baffle temperature

The cylinder maximum temperature is one of the most critical parameters: temperatures have to be significantly lower than the titanium melting point [34].

Using a perfect diffusive reflection, the optical properties of the back have almost no influence; the optimal coating of the front has the solar selectivity as low as possible, in combination to very high IR emissivity. The minimum of the maximal cylinder temperatures that is achievable is 214.4 °C, the maximum is 1092 °C, far beyond the titanium melting point [34].

With a specular reflection, the situation is almost identical, with the exception of the case in with the cylinder front coating has low solar absorptance and high IR emissivity, and the baffle back has high α and low ε. In this case, the maximal temperature of the cylinder moves from the front to the back. The minimum of the maximal temperatures using a specular reflecting coating is 209.1 °C, the maximum is 1109 °C.

6.2.5 Maximum filter temperature

In the analyses involving a diffusive reflection, the filter maximum temperature is slightly influenced by the cylinder thermo optical properties: the minimal temperature is 134.5 °C and the maximum is 158.8 °C; the maximal difference is hence ~25 °C. The frontal part of the cylinder has a very low influence on the filter temperature; low values of solar absorptance and especially of IR emissivity slightly decrease the filter temperature.

Adopting a completely specular reflection, the temperatures on the filter result to be higher (minimal 142.8 °C, maximal 175.2 °C); in this case, the optical properties of both the cylinder front and the cylinder back are relevant. The lowest temperatures are achieved for high values of IR emissivity in the front: this causes a better IR-reemission of the cylinder and therefore lower temperatures in the whole device. The solar absorptance in the baffle front has a lower influence than the IR emissivity, but high values of α in the cylinder front cause a small decrement of the filter temperatures: there is less solar radiation on the baffle back, hence a lower baffle back temperature is achieved and then there is a lower IR radiation from the baffle to the filter. High values of solar absorptance in the cylinder back cause a significant increment of the filter temperature, especially for high values of emissivity in the back: they involve higher solar radiation to the baffle back and higher IR fluxes to the filter. Low values of emissivity in the baffle back leads to slightly lower temperature; IR emissivity has anyway less influence than solar absorptance.

6.3 Achievable configurations

The analyses described in §6.2 are relative to the whole spectrum of thermo-optical properties. Unfortunately, only a small part of the analyzed parameters are really feasible for the cylindrical baffle. In particular, it has been proved that the Mercury environment makes impossible the use of paints and dyes [49], mainly due to the presence of strong UV and V-UV radiation. The use of vapor deposited reflecting metals has not been tested, but some elements suggested that their application is not possible. The instrument is expected to be subject of strong thermal gradients, causing very rapid expansions and contraction for thousands of times in the nominal mission of the MPO. This strong structural modification can easily crack and damage the thin vapor deposited metal layer, which, in addiction, presents different coefficient of thermal expansion with respect to the substrate of titanium, emphasizing the mechanical stress induced by the thermal expansion. Lastly, no tests have been done on the resistance of vapor deposited coatings to very high temperatures, presence of charged particles, UV and V-UV radiation. In conclusion, the vapor deposited metal coatings cannot be adopted because not reliable.

Only three possible solutions are left: the used of untreated titanium, mechanical polishing, thermal oxidation and chemical conversion (anodizing, see §4.3). Among the achievable possibilities, the best trade-off has been found to be the application of anodized titanium in the front part of the cylinder, in particular of TIODIZE® Type I bare, and untreated titanium in the back part of the cylinder. The thermo-optical properties are summarized in Table 6-2.

Part	Coating	IR emissivity [-]	Solar absorptance [-]	Solar selectivity [-]
Front	TIODIZE® Type I bare	0.89	0.62	0.70
Back	Untreated titanium	0.28	0.83	2.96

Table 6-2: Best thermo-optical properties set

These values will be adopted for the detailed analyses reported in the following chapter.

6.4 Results

6.4.1 Rejection efficiency

Case	Efficiency [-]
Hot 1	76.18 %
Cold 1	85.30 %
Hot 2	81.06 %
Hot 3	76.28 %
Cold 2	85.39 %
Hot 4	81.35 %
Hot 5	77.24 %
Hot 6	81.07 %
Cold 3	85.31 %

Table 6-3: Cylindrical baffle –Rejection efficiency

As can be seen from Table 6-3, the baffle is never able to comply with the requirement of a rejection efficiency of 90 %. The minimal efficiency highlighted in a thermal worst case is achieved during Hot Case 1, with a value of 76 %. The Cold Cases proved to be less critical than the Hot Cases: it is possible to reach a value up to 85 % of efficiency. Unfortunately, this condition occurs when the environmental fluxes are very low, and therefore when a high efficiency is not useful.

6.4.2 Fluxes to the BEX

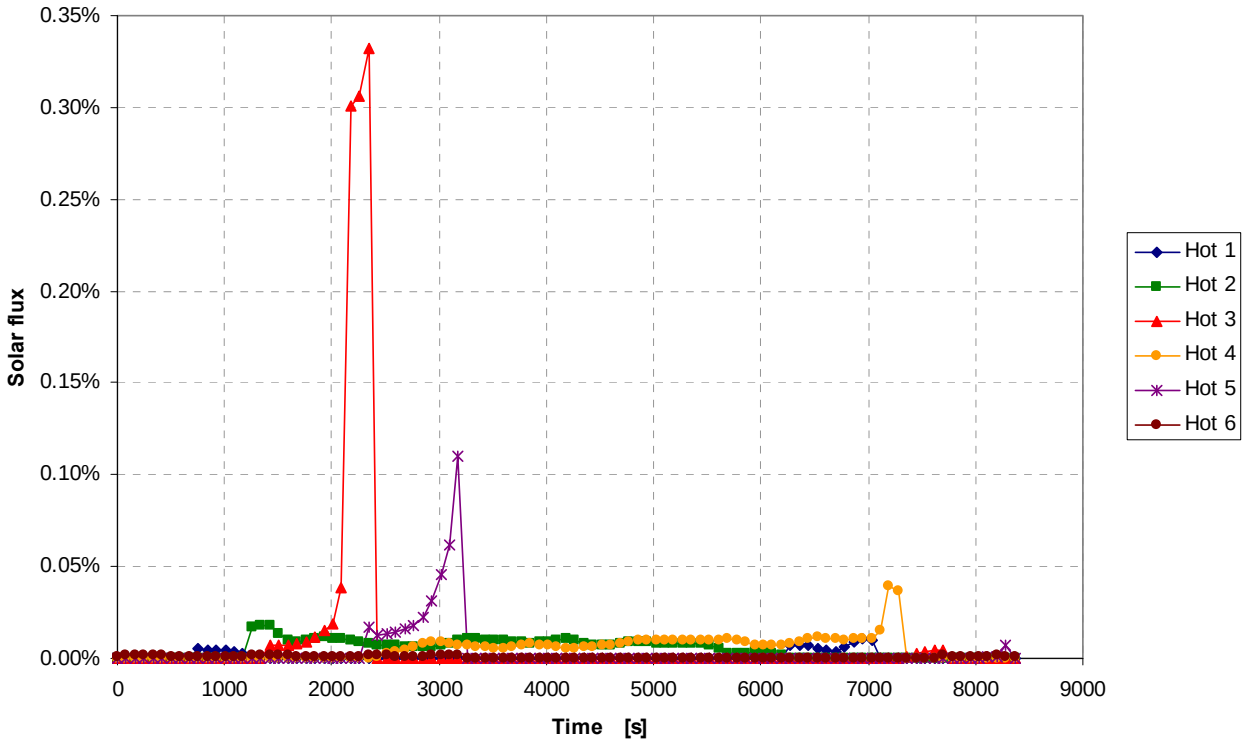

Figure 6-7: Cylindrical baffle – Solar fluxes absorbed by BEX vs. fluxes at the aperture (hot cases)

The solar fluxes entering the beam expander are always below 1% of the fluxes at the aperture, as requested by the Instrument Requirement Document [20]. There are two relevant peaks during Hot Case 3 and Hot Case 5: these high fluxes occur when the s/c exits the eclipse area and faces the Sun with a low aspect angle.

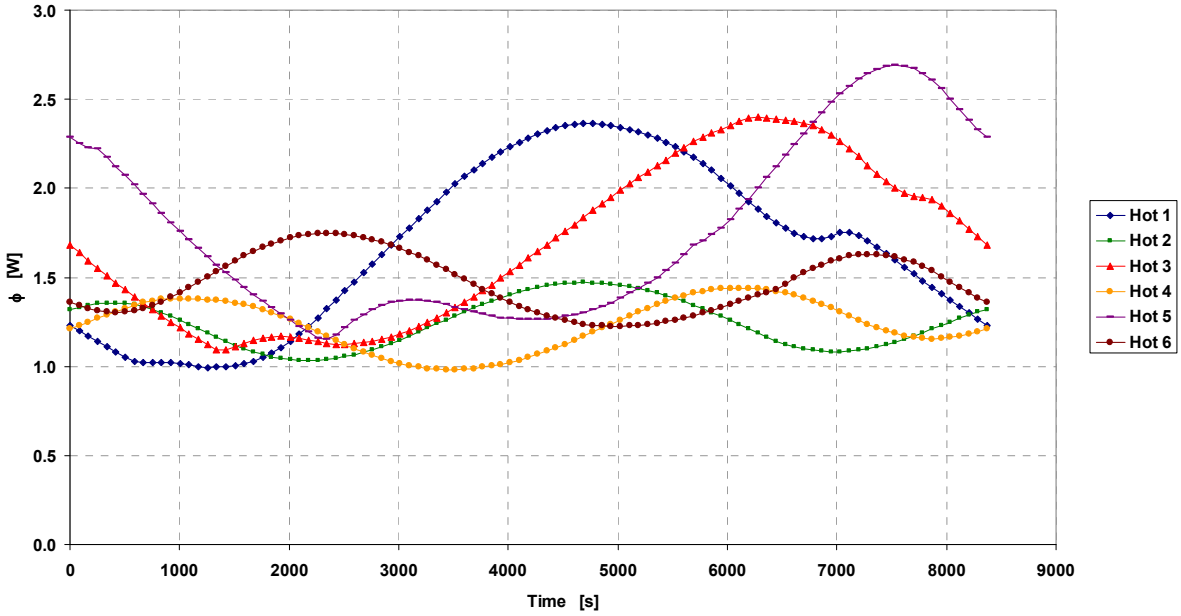

Figure 6-8: Cylindrical baffle – Total heat fluxes in the BEX (hot cases)

During the hot cases (at BOL and EOL), the amount of total heat fluxes (Sun, albedo, Mercury IR emission + re-emission from the device) is between 1 W and 2.5 W when Mercury is at perihelion and between 1 W and 1.5 W when the true anomaly of the planet is 138.75° (Hot Cases 2 and 4). It is therefore possible to infer that the most dangerous load is the (indirect) solar radiation. The value of 2.4 W achieved during Hot Case 1 and Hot Case 2 may represent a critical issue for the laser, and it should be discussed with the developers of this unit.

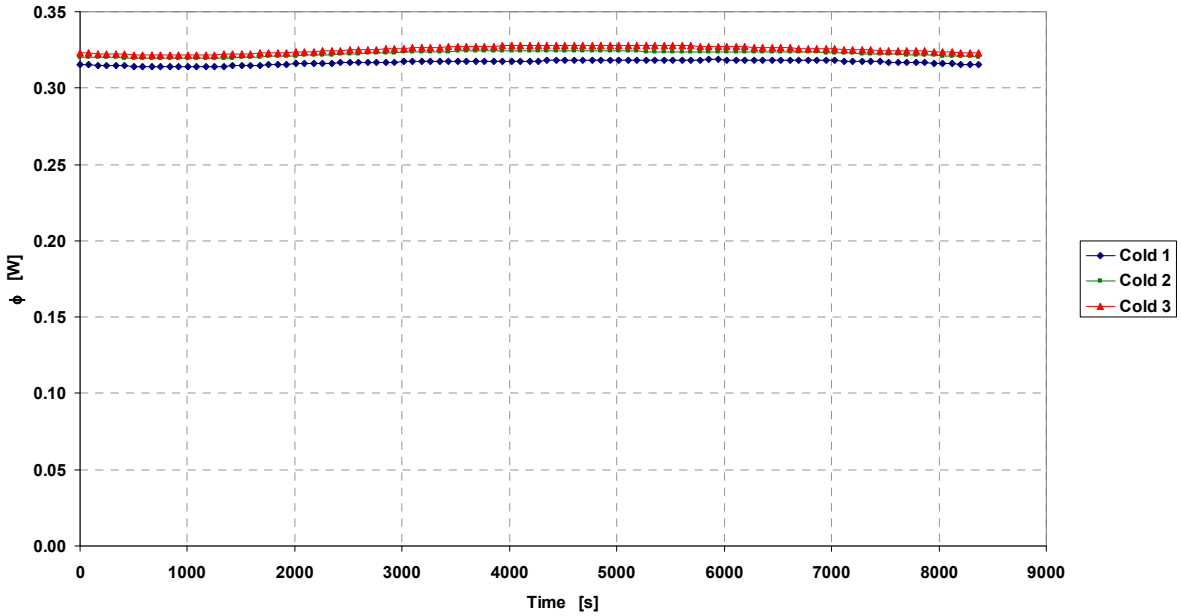

Figure 6-9: Cylindrical baffle – Total heat fluxes in the BEX (cold cases)

The cold cases, on the contrary, provides for a constant low value of heat fluxes striking the BEX of the laser, with a power of about 0.32 W.

6.4.3 Heat fluxes into the s/c

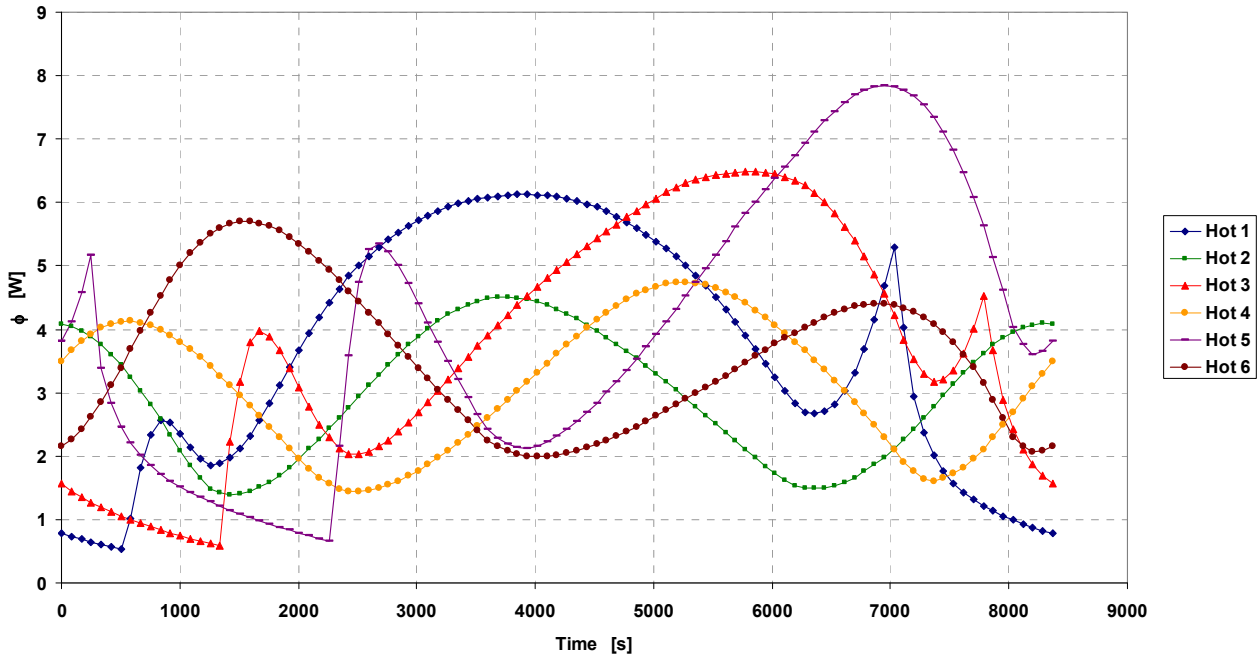

Figure 6-10: Cylindrical baffle – Heat fluxes absorbed by the s/c (hot cases)

The maximal heat absorption from the s/c, during the dimensioning cases (BOL and EOL, not EEM), is about 6.5 W and occurs during Hot Case 3. The other case in which the true anomaly of Mercury is 138.75°, Hot Case 1, has a slightly smaller value.

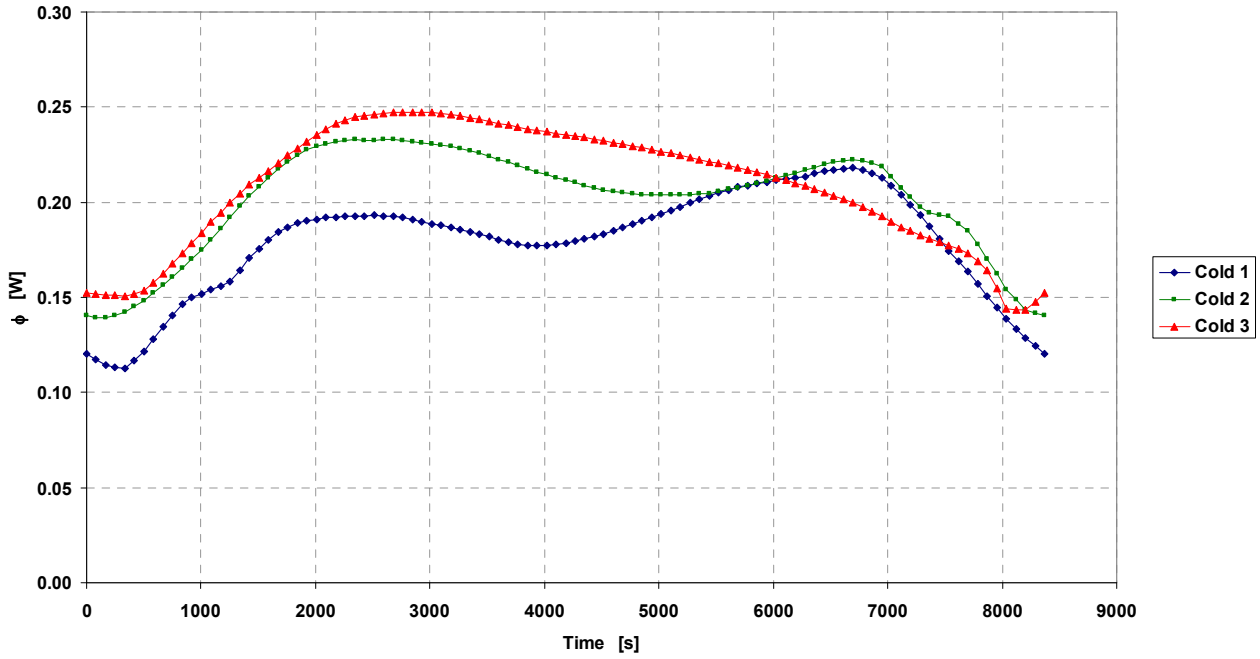

Figure 6-11: Cylindrical baffle – Heat fluxes absorbed by the s/c (cold cases)

Hot Case 2 and Hot Case 4 are significantly colder: these hot cases are related with a high mean solar absorption, whereas the maximal values of Hot Case 1 and Hot Case 3 occur when the s/c is over the subsolar point of the planet. Hence, the planetary radiation is the cause of the highest power absorption.
During the cold cases, the absorption from the s/c is negligible, always below 0.25 W. There are no relevant differences between the three cold cases. As expected, Cold Case 1 is slightly colder, on average, than the others.

6.4.4 Baffle temperatures

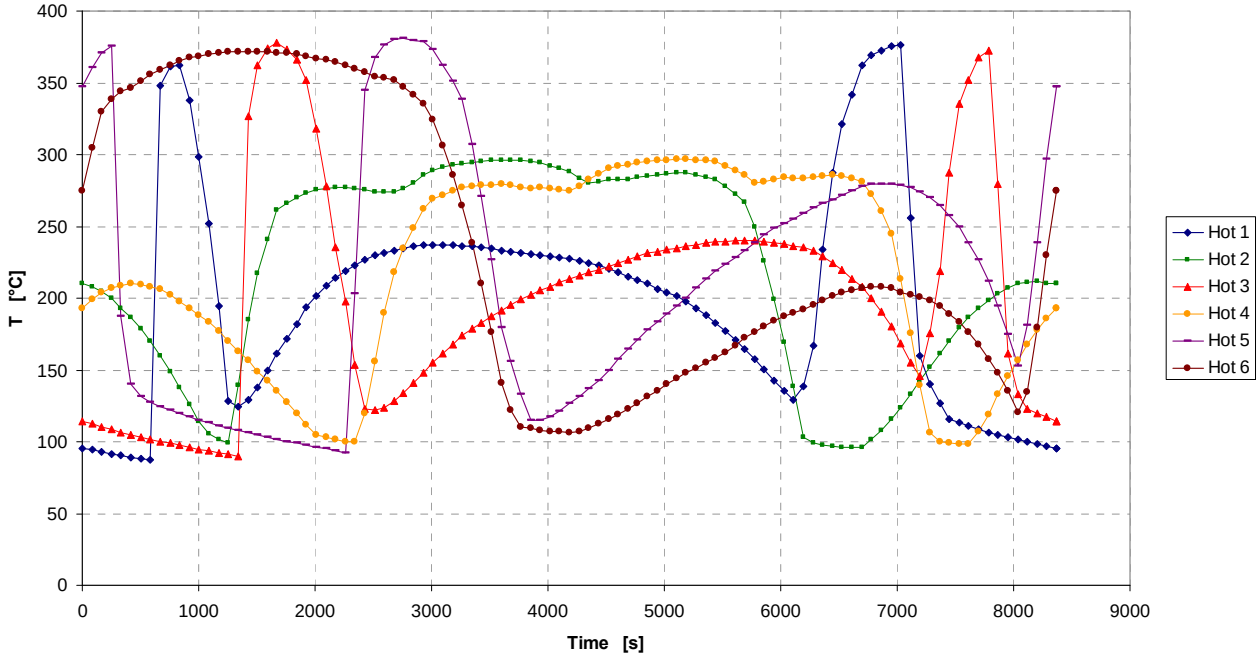

Figure 6-12: Cylindrical baffle – Max baffle temperature (hot cases)

The same mould, shifted, is clearly identifiable for Hot Cases 1, 3 and 5, that is when Mercury is at perihelion. Starting from a cold situation in the eclipse area, the baffle temperature arises when the s/c exits the eclipse cone and faces the Sun with a low aspect angle. In this period the baffle absorbs a high amount of solar energy, but fortunately the orbit has been chosen so that the aspect angle of the Sun quickly decreases, reducing the environmental load and the baffle temperature. After this peak, the temperature rises again to a local maximum when the s/c faces the planet subsolar point: in this region, almost all the environmental radiation is IR emission from the planet. Moving along its orbit, the satellite experiences another peak of the solar radiation just before entering into the eclipse region: this peak of environmental heat load causes another peak of the baffle temperature. Some considerations are possible about these orbits:

- The solar radiation causes higher temperature peaks wrt. the IR radiation
- Solar peaks are relatively short, whereas the local maximum caused by the IR radiation is longer
- The first and the second temperature peaks reach approximately the same temperature
- There are no significant differences between the different orbits (BOL, EOL, EEM)

Hot Cases 2 and 4 occur when Mercury's true anomaly is 138.75°. For these orbital positions, the MPO ascending node lies approximately over the subsolar point: the planet high temperature causes the local temperature maximums. Moving along its orbit, the s/c first experiences a temperature decrement, since the temperature of the observed surface of the planet diminishes, and then a long and stronger temperature increment. These maximums are due to the solar radiation: in these positions, the satellite never experiences eclipses, and its attitude presents a low Sun aspect angle for relatively long time. Concerning Hot Case 2 and 4:

- The solar radiation causes higher and longer temperature peaks wrt. the IR radiation
- There are no significant differences between the two different orbits (BOL & EOL)
- The temperature peak is significantly lower than in Hot Cases 1, 3 or 5

Hot Case 6 occurs at the EEM, when the planet's true anomaly is 52.5°: the mould is the same of Hot Cases 2 and 4, with some relevant differences:

- The solar peak is significantly shifted
- The maximal temperature is comparable with the maximal one in Hot Cases 1, 3 and 5

In all the Hot Cases, the solar radiation proved to be the critical heat source for the baffle maximal temperature.

The temperature peak is 378 °C: this extremely high value may represent a critical issue for the baffle and for the surrounding hardware.

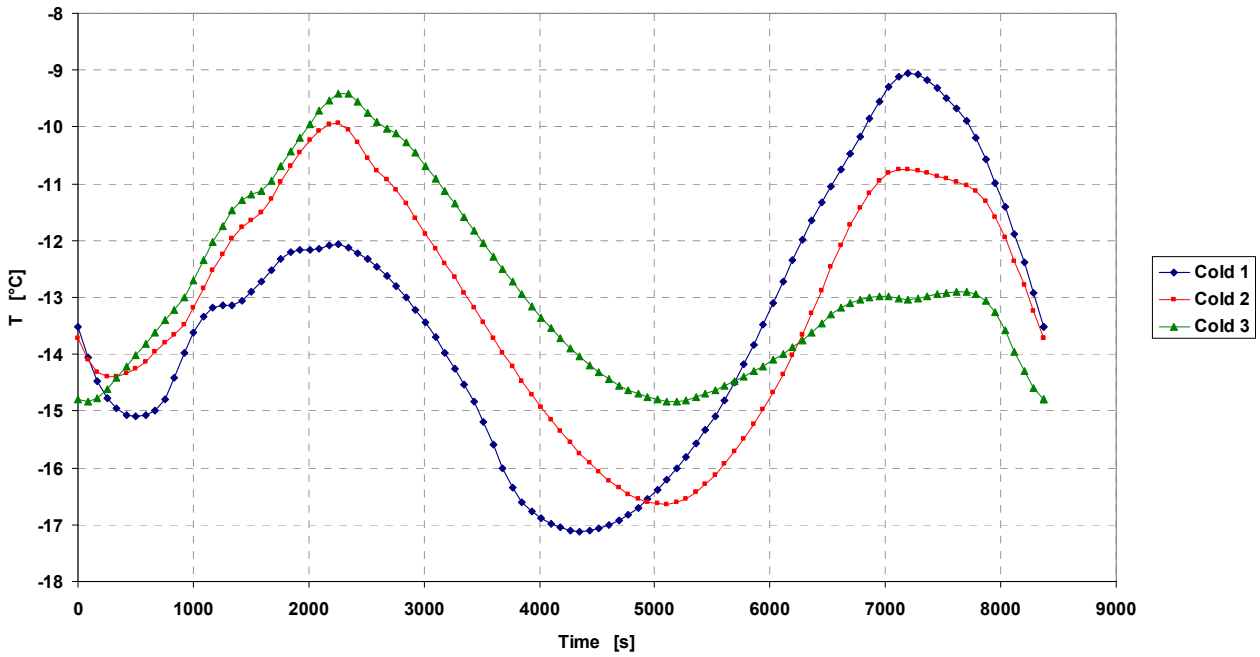

Figure 6-13: Cylindrical baffle – Min baffle temperature (cold cases)

Considering the baffle minimal temperature, there are no significant differences between Cold Case 1, Cold Case 2 and Cold Case 3. The temperature range of the baffle when the s/c is in the spring/autumn position is between -9 °C and -18 °C.

6.4.5 Filter temperatures

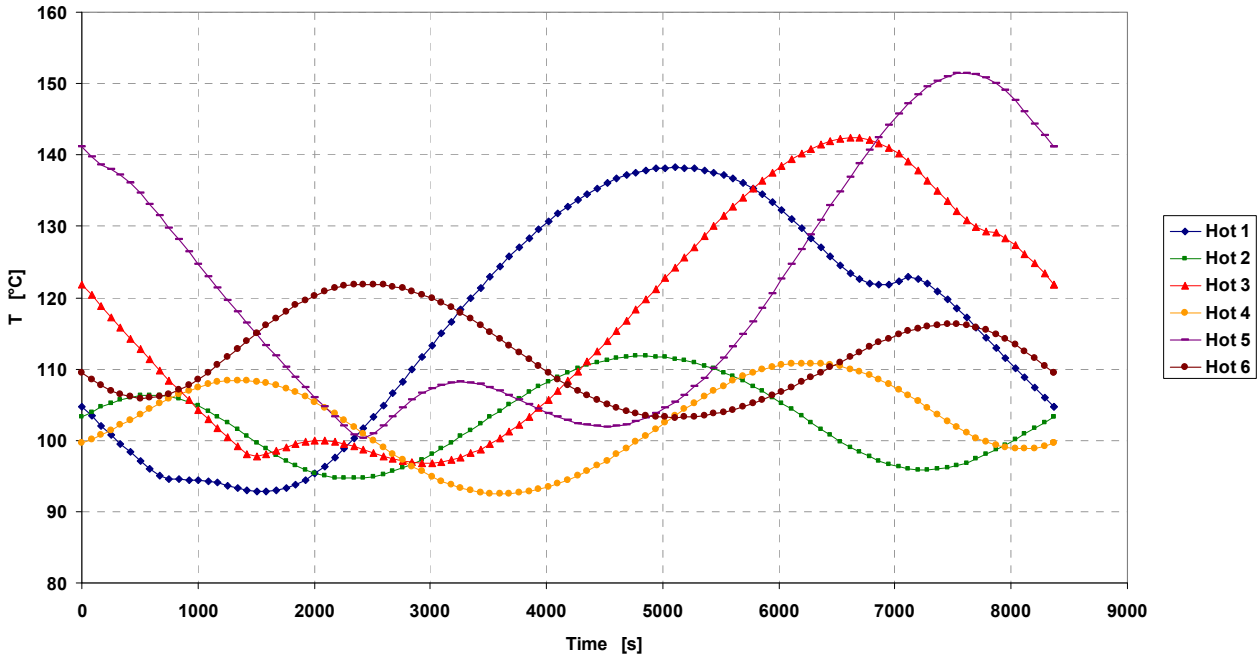

Figure 6-14: Cylindrical baffle – Max filter temperature (hot cases)

The filter temperature presents the same trend for Hot Case 1, Hot Case 3 and Hot Case 5. There is a high temperature peak after the subsolar point, with a significant delay with respect to the correspondent temperature peak of the baffle. The delay is due to the thermal inertia of the baffle, which absorbs the environmental heat flux and re-emits it later, and especially to the thermal inertia of the filter itself. Differently than for the baffle, the maximal temperature of the filter is caused by the planetary flux and not by the solar radiation.

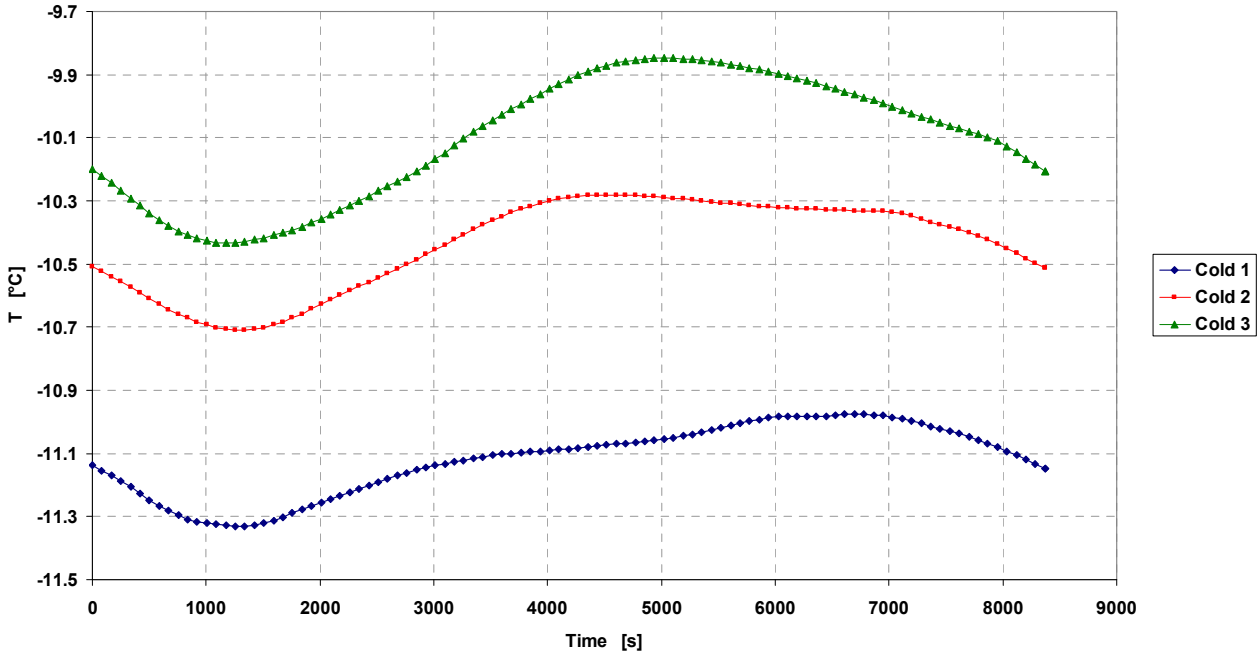

Figure 6-15: Cylindrical baffle – Min filter temperature (cold cases)

Also for Hot Case 2, Hot Case 4 and Hot Case 6, when the s/c receives the maximal solar radiation, the peak of the filter temperature is caused by the Mercury IR emission. The temperatures in these latter cases are on average lower than when Mercury is at perihelion.
The maximal temperature reached by the filter is above 140 °C, which is a limit value for the thermal distortions.
The minimal temperature of the filter presents negligible variations. The lowest peak is -11.3 °C, achieved during Cold Case 1. This temperature is important for the calculation of the thermal stresses to which the filter is subjected: the thermal expansion from a cold case to a hot case causes serious structural issues. Further, the temperature range of the filter is important also because it is used to calculate the optical distortions the lens can produce, and thus the optical performance of the device.

6.4.6 Summary

Case	Efficiency [-]	Fluxes to BEX max [W]	Fluxes to s/c max [W]	Baffle T max [°C]	Filter T max [°C]
Hot 1	76.18 %	2.362	6.126	376.06	138.25
Cold 1	85.30 %	0.319	0.218	35.19	-10.94
Hot 2	81.06 %	1.470	4.505	296.15	111.80
Hot 3	76.28 %	2.402	6.487	377.66	142.41
Cold 2	85.39 %	0.324	0.233	33.73	-10.24
Hot 4	81.35 %	1.440	4.743	296.82	110.81
Hot 5	77.24 %	2.691	7.840	380.89	151.50
Hot 6	81.07 %	1.747	5.698	371.97	121.89
Cold 3	85.31 %	0.328	0.247	32.86	-9.80

Table 6-4: Cylindrical baffle – Summary of the indexes of performance

In Table 6-4 the main indexes of performance are summarized for each thermal worst case.
As already discussed, the cylindrical version of the baffle is not able to comply with the requirement of the minimal efficiency. The solar fluxes absorbed by the laser, as requested, are always below 1 % of the fluxes at the apertures. Nonetheless, other heat fluxes, such as the planetary flux and the IR re-emission, cause a heat load on the beam expander quite high, up to 2.4 W.
The heat fluxes transmitted to the s/c are on average below 3.5 W, even if peaks may cause a heat absorption up to 6.5 W during Hot Case 3.
The baffle temperature is inside the range -17 °C ÷ +378 °C. The extreme temperature variation (almost 400 K) causes several issues concerning the integrity of the baffle and of the surrounding hardware, in addition to the survival of the selected coatings.
Also the filter presents high temperatures and strong variations of the temperature with time. The maximal temperature of 142 °C set problems concerning the thermally induced stresses and the optical distortion the filter may experience.

7 Stavroudis TBU: models and analyses results

7.1 Model description

7.1.1 Mechanical model

The Stavroudis version of the TBU is much more complex than the cylindrical version. In Figure 7-1 it is possible to see a CAD model of the unit, inclusive of the baffle body (blue), the filter mount (violet) and the elements used to connect the TBU to the s/c.

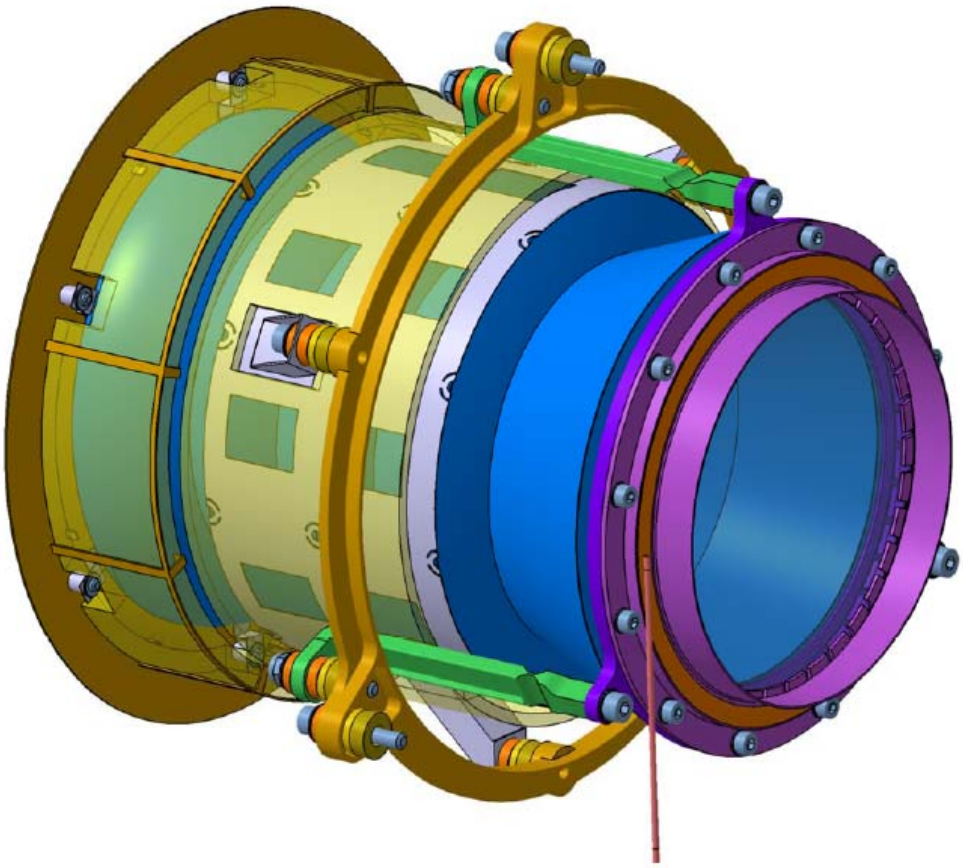

Figure 7-1: Stavroudis TBU – CAD model

In Figure 7-2 the baffle body (blue), the baffle sustaining cylinder (grey) and the BSP mounting ring (ocher) are shown. The baffle and the baffle sustaining cylinder are made of electroformed Nickel. This technique guarantees a very high accuracy of the shape, of the surface roughness and of the thickness uniformity [77]. It also permits to realize a very thin baffle, allowing for a large mass saving. The baffle thickness is indeed only 0.2 mm, the inner diameter is 47.5 mm and the outer diameter 61.1 mm, the axial length is 154.0 mm. The baffle sustaining cylinder purpose is to enable a connection between the baffle and the rest of the instrument. The baffle surface is very complex, and its thickness very low, therefore a mechanical clamping on the baffle surface would damage the Stavroudis body. Introducing a cylindrical shape, made of nickel as well and electrosoldered on the edges of the baffle vanes, a wider surface capable of withstanding structural connections is introduced. Another advantage of the baffle sustaining cylinder is that it increases the device stiffness. The sustaining cylinder has a thickness of 0.2 mm and it is 68.5 mm long.
The baffle sustaining cylinder is connected through three nickel arms to the BSP mounting ring. The purpose of this last element is to interface the TBU to the s/c through the BPS, on which it is screwed.

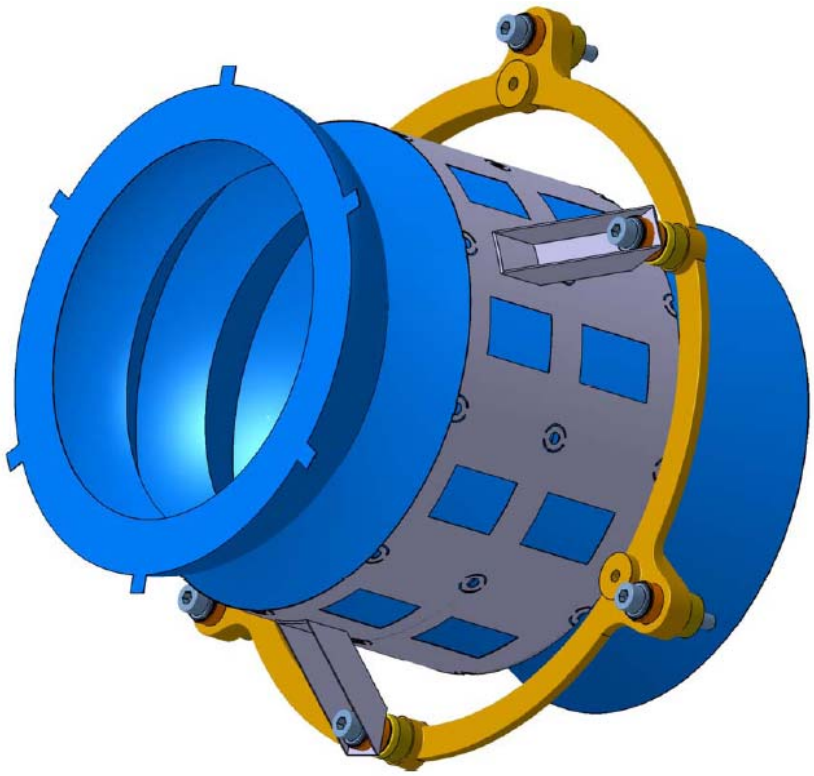

Figure 7-2: Baffle body, baffle sustaining cylinder and BSP mounting ring – CAD model

As for the cylindrical version of the TBU, the filter mount is not connected to the baffle body in order to minimize the heat flux and the filter heating. The connection with the BSP mounting ring is depicted in Figure 7-3.

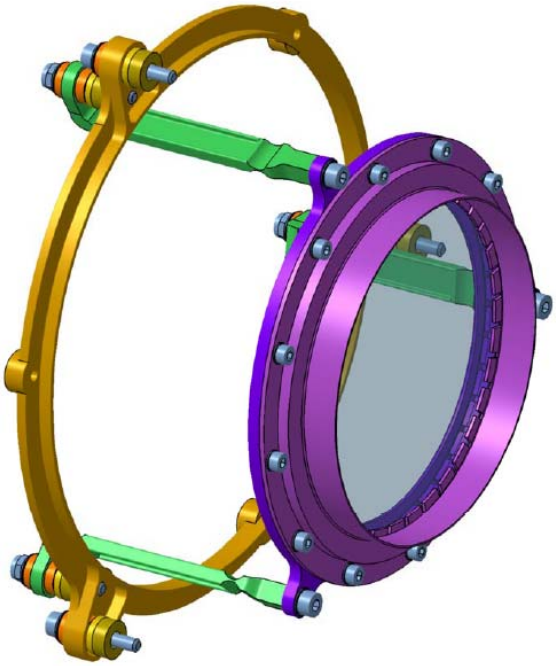

Figure 7-3: Filter mount, filter and BSP mounting ring – CAD model

The filter mount is made of two aluminum components which clamp the sapphire filter. Three isostatic legs made of titanium connect the filter mount to the BSP mounting ring. Due to the different coefficients of thermal expansion of the materials of the filter mount (aluminum) and of the filter substrate (sapphire), a

flexible clamping for the filter is necessary. This is achieved implementing a large number of flexible pads (see Figure 7-4), which are able to compensate for the different CTEs of the two body; these pads are anyway stiff enough and with a large contact area in order to grant a good thermal contact.
Since the filter has a higher view factor with respect to the space environment than the filter mount, when a sudden increment of the environmental fluxes occurs, it could happen that the filter overheats, while the filter mount would remain relatively cold. A good thermal conduction between the filter, which has temperature upper limit requirements, and the filter mount, which does not have any constrain, is therefore necessary.

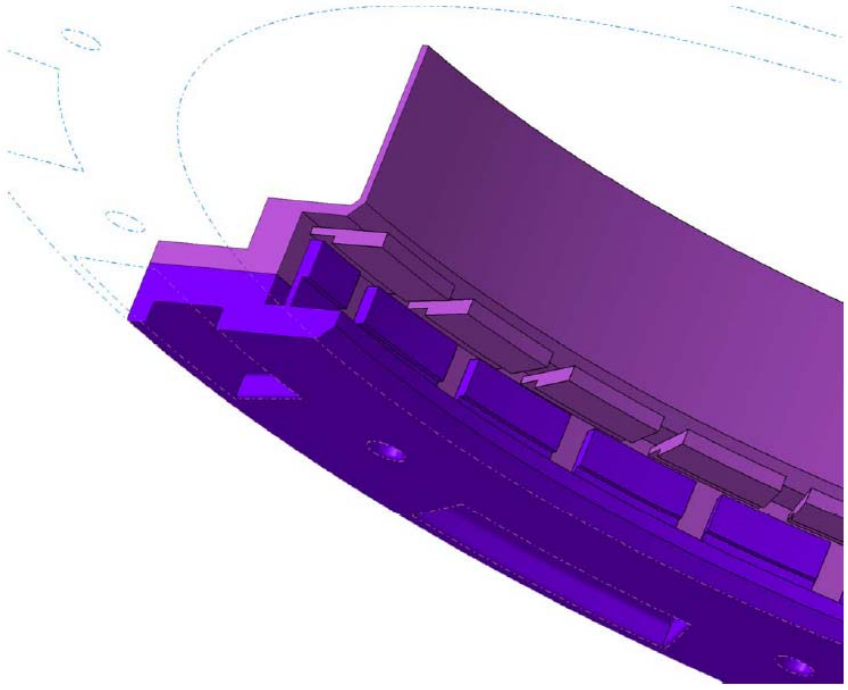

Figure 7-4: Filter mount clamping system – CAD model

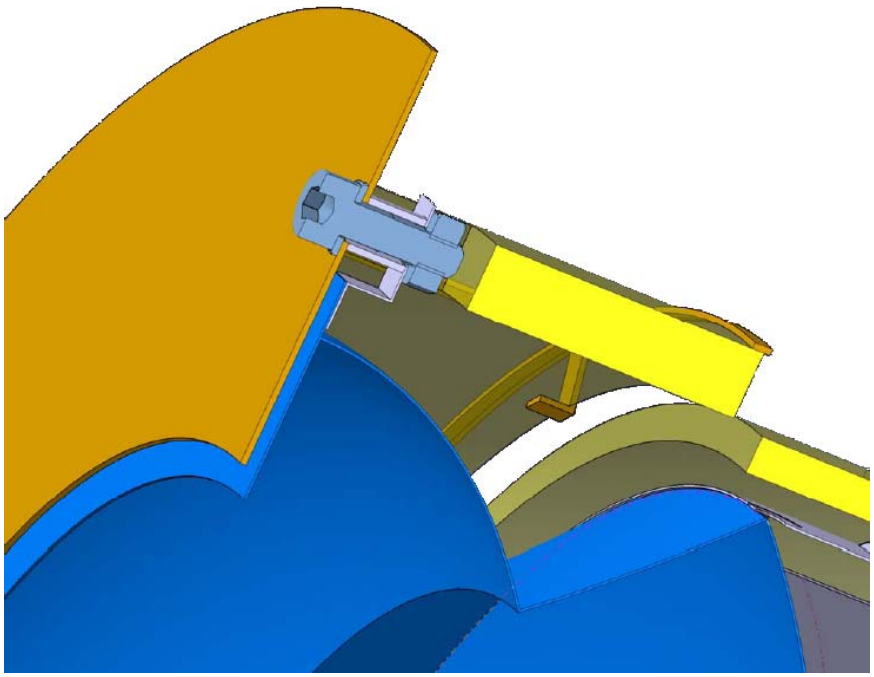

Figure 7-5: Front ring and connection with the baffle – CAD model

In the Figure 7-5 it is possible to see a detail of the front ring and its connection with the baffle. The baffle ring is an annulus made of titanium which serves as interface between the baffle and the outer side of the s/c. Its purpose is not optical, but mechanical and thermal. The mechanical goal is to sustain the s/c HT-MLI, avoiding any contact between the MLI blanket and the baffle body, which may cause mechanical stresses, unacceptable high temperature on the HT-MLI blanket and heat conduction toward the s/c.
The thermal purpose is to provide for a front line against the environmental radiation. The baffle annulus, made of nickel and depicted in blue in Figure 7-5, would otherwise achieve too high temperatures, not tolerable for the baffle. This is unavoidable, since any perpendicular surface at the instrument aperture would present a very high view factor with respect to the environment and would be the first element to collect the environmental radiation. The strategy that has been adopted consists in implementing a non-optical element, made of a material which can withstand very high temperatures (titanium), in order to partially shade the optical components of the device. Since this surface will become unavoidably very hot, the connection with the other TBU elements (the baffle) should be designed in order to minimize the thermal conductivity. In Figure 7-5, a titanium screw connecting the front ring and a small flange of the baffle is depicted in grey. Titanium was the material chosen for the screw as a consequence of its resistance to high temperatures and its low thermal conductivity (7.78 $W \cdot m^{-1} \cdot K^{-1}$ [34]).

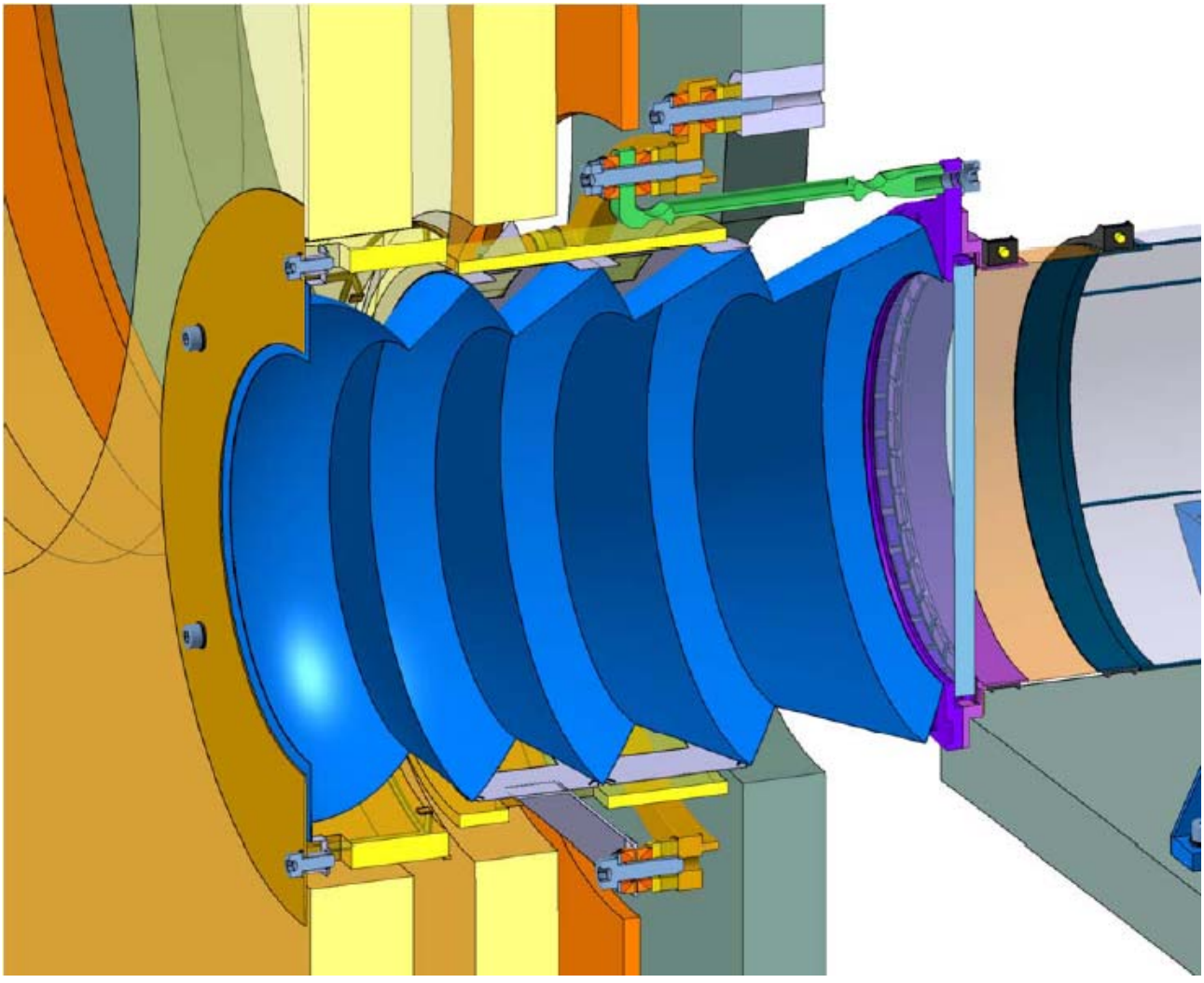

Figure 7-6: Stavroudis TBU integration in the MPO – CAD model

In Figure 7-6 it is possible to see the integration of the whole TBU in the MPO environment. The BSP (the dark grey panel in the right side of the picture) is the element of the s/c which has to hold the baffle body and the filter mount, through the BSP mounting ring. Most of the TBU is surrounded by the s/c MLI blankets: the

HT-MLI and Std-MLI, both represented in light yellow in the picture. The TBU protects itself from these S/C MLI layers by providing two additional MLI packages (dark yellow). The front TBU MLI blanket should withstand higher temperature and is therefore made of more layers; it is fixed on the front ring. The back element of the TBU MLI protection will experience lower temperatures, and it is therefore thinner. It is wrapped around and fixed to the baffle sustaining cylinder.

7.1.2 Geometrical Mathematical Model

The GMM of the Stavroudis baffle, the baffle sustaining cylinder and the BSP mounting ring is depicted in Figure 7-12.

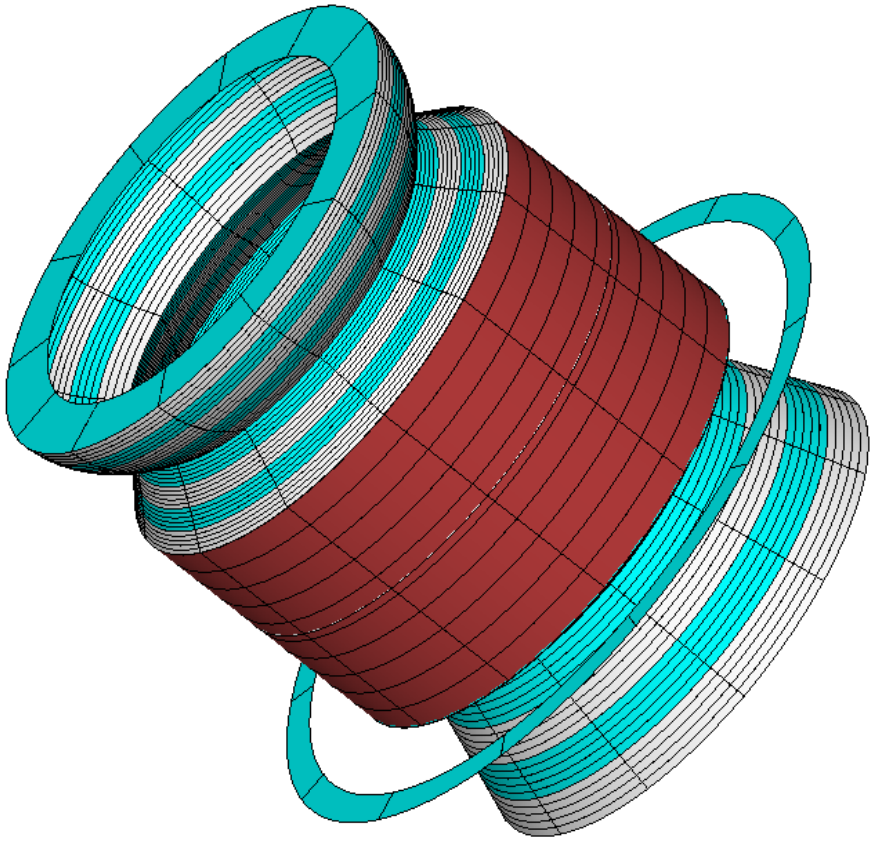

Figure 7-7: Stavroudis baffle, baffle sustaining cylinder and BSP mounting ring – GMM

The baffle sustaining cylinder is the rust brow shape wrapped around the baffle body, the BSP mounting ring is the lavender annulus which surrounds the baffle. The connections between the baffle sustaining cylinder and the BSP ring have not been modeled in the GMM, since its influence on the radiative behavior was assessed to be small.

The MLI blankets, front and back, are shown in Figure 7-8. The TBU front MLI blanket, which should withstand higher temperatures and is therefore thicker, is depicted in blue, while the back MLI, thinner and less critical, is depicted in yellow.

If Figure 7-9 it is possible to see the whole TBU and SPU assembly. The green disc at the front of the instrument is the titanium front ring, which purpose is to interface the unit with the s/c MLI blanket and to endure a large amount of the environmental radiation, keeping the instrument safe. Due to its thermal requirement, the front ring is externally coated using a ceramic layer with yttria stabilized zirconia (see §4.5), achieving simultaneously a good resistance to the harsh environmental condition (see §3.5) and a good IR emissivity / solar absorption ratio. The internal side of the front ring is coated with VDA to minimize the heat transmission between from the hot disc and the baffle.

The filter mount is the dark green body after the baffle; the filter GMM is exactly the same of the cylindrical version of the TBU, since the filter is the same. After the TBU, the Stavroudis version of the SPU is represented. Basically, the SPU GMM in the Stavroudis version is the same of the SPU in the cylindrical version, but it is longer (since the baffle is shorted) and it is supported by a CFRP support. The purple body is the SPU support structure, it lies on the instrument optical bench and it is coated with Vapor Deposited Gold (VDG) to minimize the radiative heat exchange with the SPU.

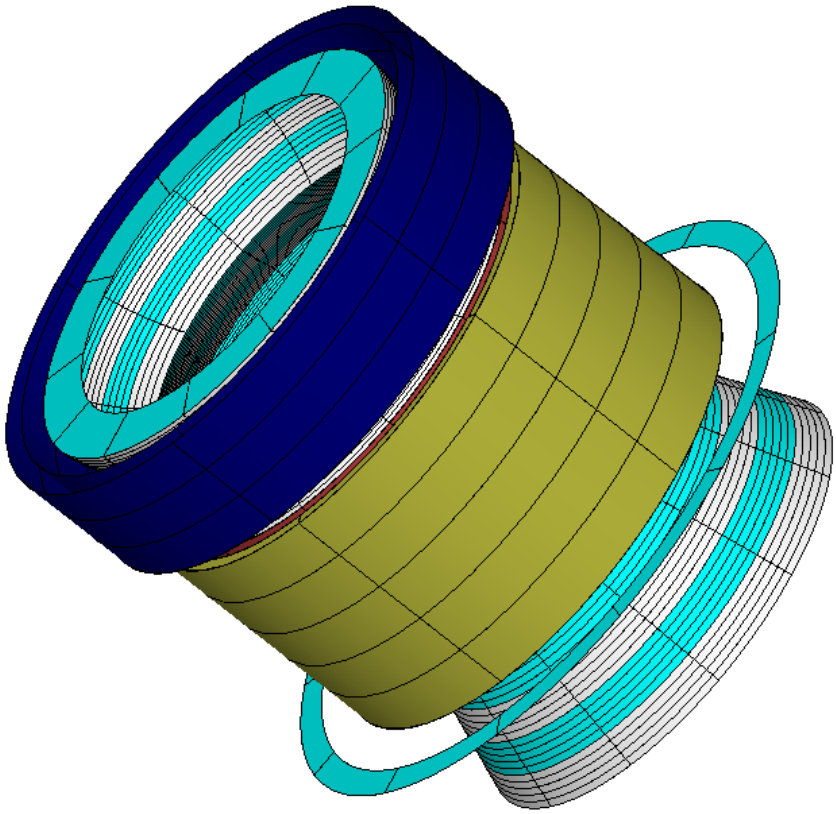

Figure 7-8: The Stavroudis baffle, surrounded by the TBU MLI blankets – GMM

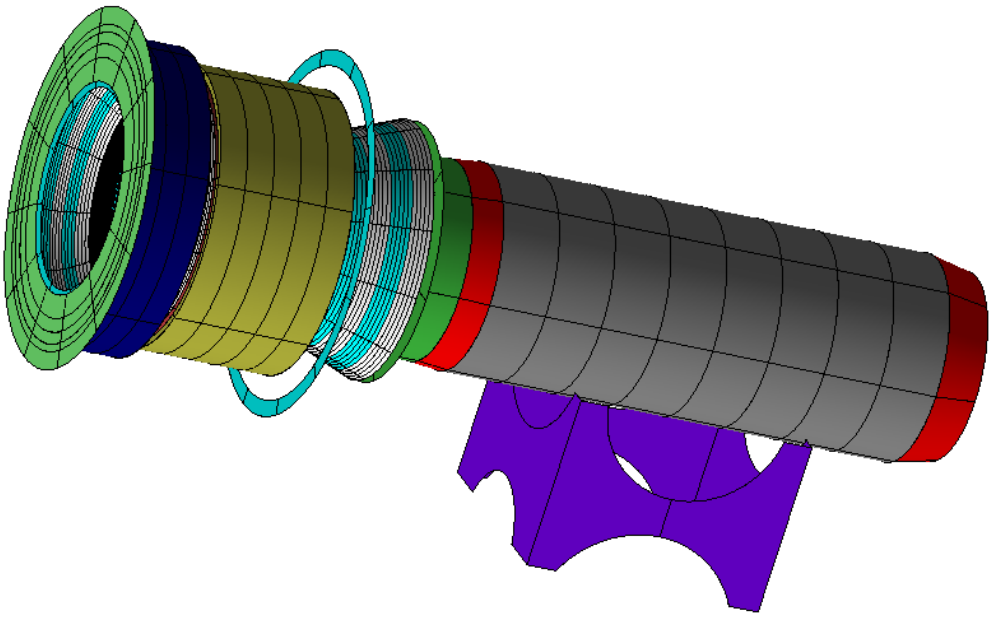

Figure 7-9: Stavroudis TBU and SPU – GMM

The integration of the TBU and the SPU units in the BELA environment is shown in the next picture.

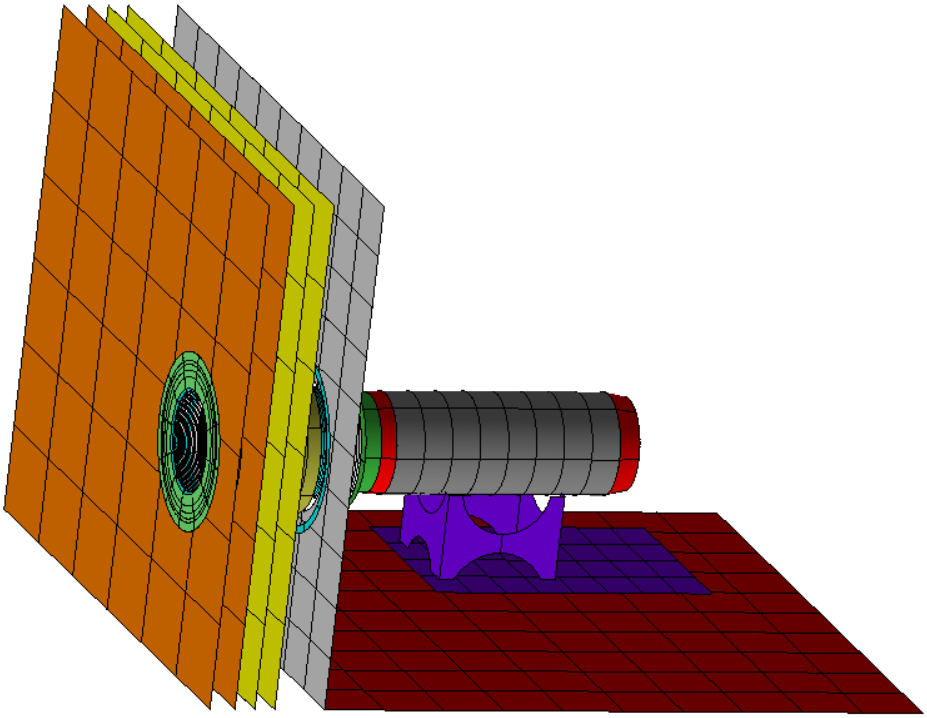

Figure 7-10: Stavroudis TBU and SPU in the BELA environment – GMM

7.1.3 Thermal Mathematical Model

The TMM of the Stavroudis baffle is composed by the following nodes:

Element	Number of nodes	Material
Baffle	324	NiColoy®
Filter	18	Sapphire
Filter mount	6	Al 7075
Baffle sustaining cylinder	120	NiColoy®
Front ring	12	Ti 6242
BSP mounting ring	12	Al 7075
TBU MLI front	42	MLI
TBU MLI back	72	MLI
SPU cylinder	48	Al 7075
SPU MLI connectors	12	MLI foils
SPU support	6	CFRP
Total	*672*	

Table 7-1: Nodes of the Stavroudis TBU TMM [44]

The conductive conductances inside the TMM are shown in Figure 7-11.

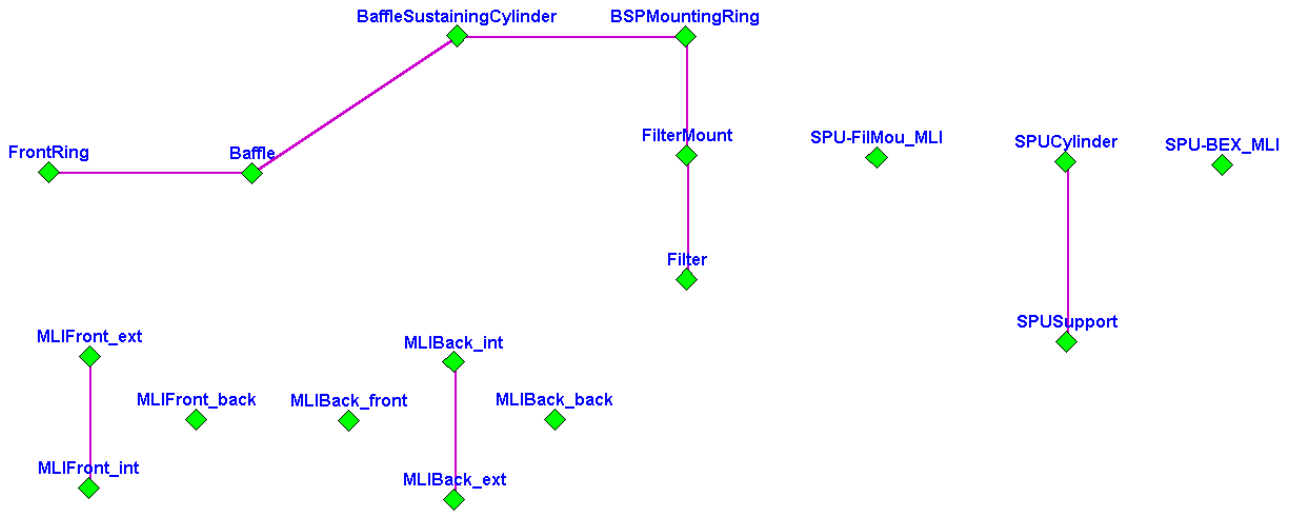

Figure 7-11: Conductive conductances in the Stavroudis TBU TMM

The calculation of the conductive conductances has been particularly difficult for the Stavroudis baffle. The conductances have been numerically calculated using the formulas for the heat conduction inside conical shells, and the results have been compared to more accurate estimations calculated from a structural software, which took into account for the real shape. The difference between the results was always below 3%.

A large uncertainty affects the contact conductances, influencing for instance the thermal conductance between the filter mount and the BSP mounting ring. These parameters should be properly investigated during the test campaign on the prototypes of the hardware.

7.2 Discretization of the Stavroudis shape

As explained in §2.3.2, the Stavroudis baffle is composed by ellipsoids and hyperboloids. Unfortunately, these shapes are not implemented in ESARAD, and therefore an approximation was required. Since the baffle is essentially an optical device, it is mandatory to reproduce with high precision its shape, to guarantee the modeling of the proper optical behavior.

A first attempt was the approximation of the Stavroudis shapes using frustums: each ellipsoid and each hyperbola was modeled using 20 frustums (Figure 7-12).

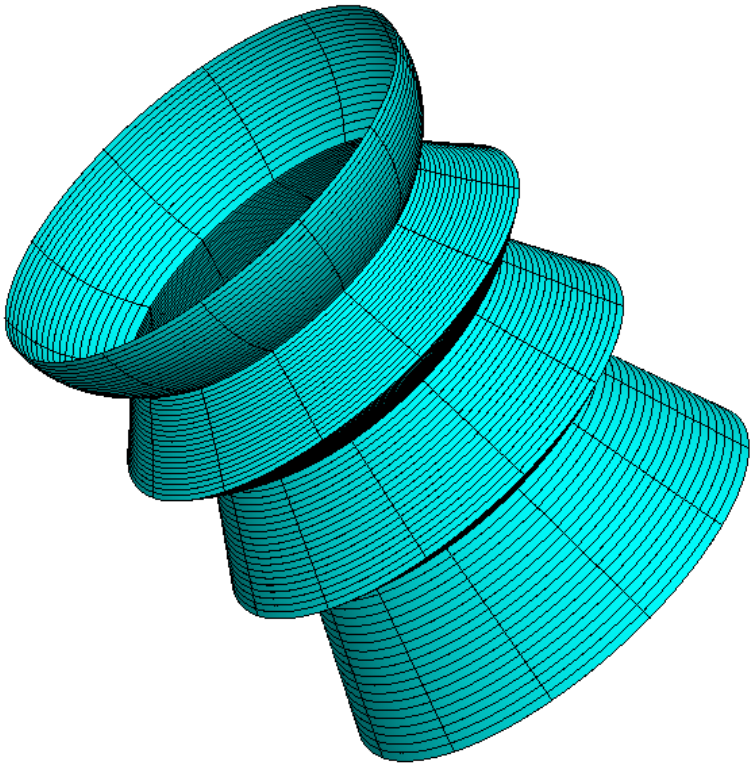

Figure 7-12: The Stavroudis baffle discretized using 20 frustums for each surface

This was the same procedure and the same discretization adopted for the receiver baffle [78], which also adopts a Stavroudis configuration. The University of Bern proved that using frustum to approximate the conics, the RBU baffle results converged to realist values, and that 20 elements for each surface were enough to achieve a good approximation of the converged values. This analysis was accomplished using the THERMICA software.

Anyway, some issues were still opened:

- The study of the University of Bern proved the convergence of the results, but not the convergence to the exact value
- The same study used the fluxes absorbed by the baffle as figure of merit, but did not consider the fluxes transmitted beyond the baffle (for the TBU, to the filter)
- The TBU has different geometrical parameters, and therefore the same discretization may could have inadequate
- The computational time of the GMM was of about 26 hours, limiting the number of simulations which could have been performed

7.2.1 Comparison with an optical dedicated software

The first step was a validation of the results obtained discretizing the baffle with 20 frustums for each surface. Kayser-Threde GmbH, a German company which has some contracts for the BepiColombo project, developed an optical model of the instrument using ZEMAX, a dedicated optical software which is able to exactly reproduce the complex conic shapes and can supply to some ESARAD limitations. ZEMAX indeed takes into account for the angle of incidence of the rays and implements temperature-dependant thermo optical properties, while ESARAD does not.

Two separate radiative analyses have been performed using ESARAD and ZEMAX: the model adopted included only the Stavroudis baffle body, with a completely specular reflection. Due to the difference of the software and some assumption adopted, the conditions were not exactly the same: the differences are shown in Table 7-2.

Parameter	ESARAD	ZEMAX	Possible effects
Mercury surface T	Temperature map from Mercury soil model (includes effects of soil thermal inertia)	Cosine law distribution	Different planetary IR fluxes through baffle aperture
Absorbed fluxes calculation	Stochastically computed	Analytical (numerical integrals)	Numerical approximations Analytical simplifications
Stavroudis geometry	Approximated	Exact	Discordances in baffle efficiency
Wavelength dependent optical properties	Not implemented	Implemented	No effect on solar and albedo fluxes Possible discordances for planetary flux absorbed by the baffle and the filter
AOI dependent optical properties (for the filter)	Not implemented	Implemented	No effect on solar fluxes Possible differences for albedo and planetary fluxes

Table 7-2: Differences between the ESARAD and the ZEMAX models

Since the two analyses use different models for Mercury, only the direct solar radiation has been taken into account. Average transient results for a Hot Case 1 MPO orbit are show in the following table:

ESARAD	ZEMAX	Difference (ZEMAX wrt. ESARAD)	
87.2 W	86.8 W	-0.4 W	-0.45 %

Table 7-3: Absorbed direct solar fluxes for the ESARAD and ZEMAX analyses

As can be seen, the error is very low and this validates the adopted discretization of the Stavroudis shapes. The differences of the results can be ascribed to the differences listed in Table 7-2 and to the stochastic errors in the ESARAD calculation method of the environmental fluxes.
Another simulation has been performed to compare the solar fluxes absorbed by the baffle and the solar fluxes which pass beyond it (and, in the real TBU model, would reach the filter). The results have been calculated for a Hot Case 1 orbit, at the rim of the eclipse shadow: in this situation the solar fluxes are at their peak.

	ZEMAX	ESARAD	Difference (ZEMAX wrt. ESARAD)	
			Δ	%
Absorbed by the baffle	8.5 W	8.2 W	0.3 W	+3.7%
Passed beyond	0.0 W	0.0 W	0.0 W	0.0%

Table 7-4: Direct solar fluxes distribution, edge of the eclipse shadow

The ESARAD model shows a small but significant discordance in the result of solar fluxes absorbed by the baffle body; in particular, the solar fluxes are underestimated with respect to the ZEMAX model. This is unexpected, since the ZEMAX model uses a perfect geometry of the Stavroudis baffle whereas the ESARAD model uses an approximation which should worsen the baffle efficiency.
The filter absorption is exactly 0.0 W in the ZEMAX model, whereas it is 0.013 W in the ESARAD model. Since a perfect specular reflectance has been implemented, the Stavroudis geometry should prevent any solar

ray from reaching the filter: hence, the amount of direct solar fluxes absorbed by the filter can be considered as an index of the error due to the geometrical simplification.
Numerical errors can contribute to the difference between the two models: due to the high computational time required to perform a complete ESARAD analysis, the ray-tracing method accuracy parameters have been relaxed in order to achieve an enough accurate solution, in terms of temperatures, in a shorter time. The selected ESARAD accuracy, despite proved to provide for reliable temperature prediction, might have a major influence on the different absorbed flux between the ESARAD and ZEMAX models.

7.2.2 Optimization of the baffle discretization

Once the reference model was validated, the next step has been the numerical quantification of the errors and the optimization of the baffle approximation with respect to the computational time.

Three possible shells available in ESARAD may be used to approximate the Stavroudis ellipsoids and hyperboloids: cones, paraboloids and spheroids. Due to the fact that hyperboloids are 3D convex shapes, only cones are suitable to approximate them; on the other hand, all the three mentioned shapes may be used to approximate the ellipsoids (Figure 7-13).

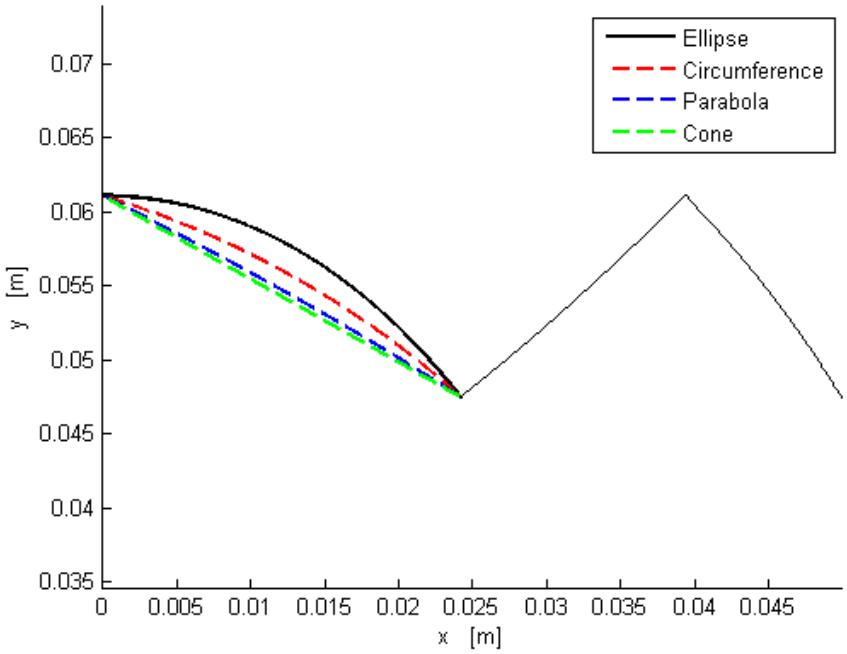

Figure 7-13: Possible approximations of the Stavroudis ellipsoids

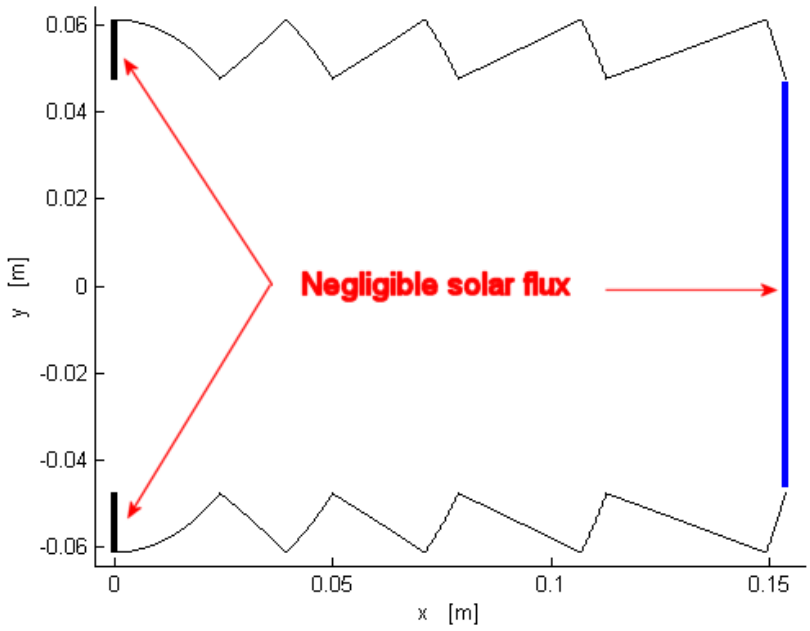

Figure 7-14: Error parameters

The performances of the different discretizations have been evaluated by means of the following parameters:

- The absorbed solar flux on the rear of the baffle front ring
- The solar flux which passes beyond the baffle

For a perfect Stavroudis shape, with 100% of specular reflection, both these parameters (see Figure 7-14) should be zero [28].

The analyzed cases are reported in Table 7-5.

Case ID	1st ellipsoid		Other ellipsoids		Hyperboloids	
	Shape	Segments	Shape	Segments	Shape	Segments
1	Cone	20	Cone	20	Cone	20
2	Cone	20	Cone	20	Cone	1
3	Cone	40	Cone	8	Cone	2
4	Cone	10	Cone	8	Cone	2
5	Cone	10	Cone	4	Cone	4
6	Cone	5	Cone	2 (2nd); 1 (3rd,4th,5th)	Cone	4
7	Sphere	20	Sphere	20	Cone	20
8	Sphere	2	Sphere	1	Cone	20
9	Sphere	1	Sphere	1	Cone	20
10	Sphere	40	Sphere	8	Cone	2
11	Sphere	20	Sphere	4	Cone	4
12	Sphere	10	Sphere	4	Cone	4
13	Sphere	5	Sphere	4	Cone	4
14	Sphere	5	Sphere	2 (2nd); 1 (3rd,4th,5th)	Cone	4
15	Sphere	2	Sphere	1	Cone	2
16	Sphere	2	Sphere	1	Cone	1
17	Sphere	1	Sphere	1	Cone	1
18	Parabola	20	Parabola	20	Cone	20
19	Parabola	2	Parabola	1	Cone	20
20	Parabola	1	Parabola	1	Cone	20
21	Parabola	40	Parabola	8	Cone	2
22	Parabola	20	Parabola	4	Cone	4
23	Parabola	10	Parabola	4	Cone	4
24	Parabola	5	Parabola	4	Cone	4
25	Parabola	5	Parabola	2 (2nd); 1 (3rd,4th,5th)	Cone	4
26	Parabola	2	Parabola	1	Cone	2
27	Parabola	2	Parabola	1	Cone	1
28	Parabola	1	Parabola	1	Cone	1

Table 7-5: Optimization of the discretization: analyzed cases

The analyses results, in terms of solar flux absorbed by the rear side of the baffle front disc, in terms of solar flux passed beyond the baffle (and then intercepted by the filter) and finally in terms of computational time, are depicted in Figure 7-15, Figure 7-16 and Figure 7-17.

The violet areas of the charts depicted in Figure 7-15 and Figure 7-16 are “undesirable zones”, where the approximation errors are high or/and the computational time is high. On the other hand, the green areas represent the target of the optimization, where both the errors and the computational time are low.

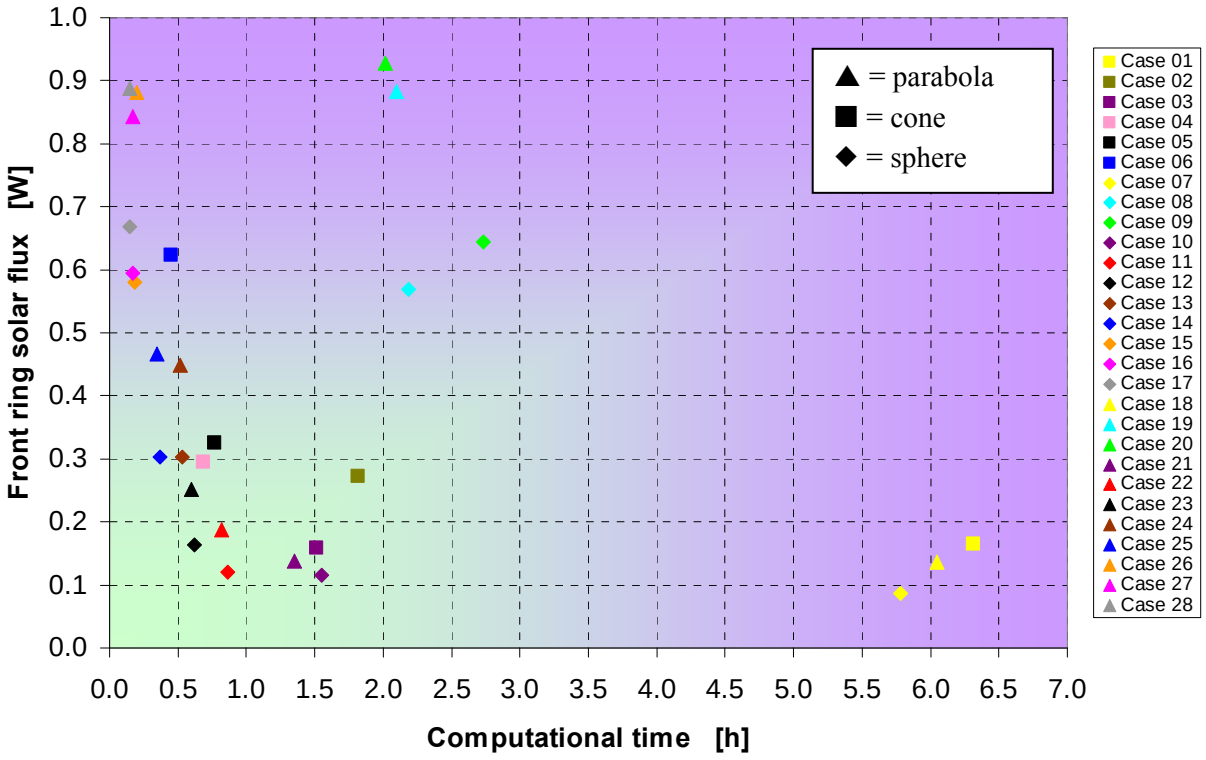

Figure 7-15: Solar flux on the rear of the front ring

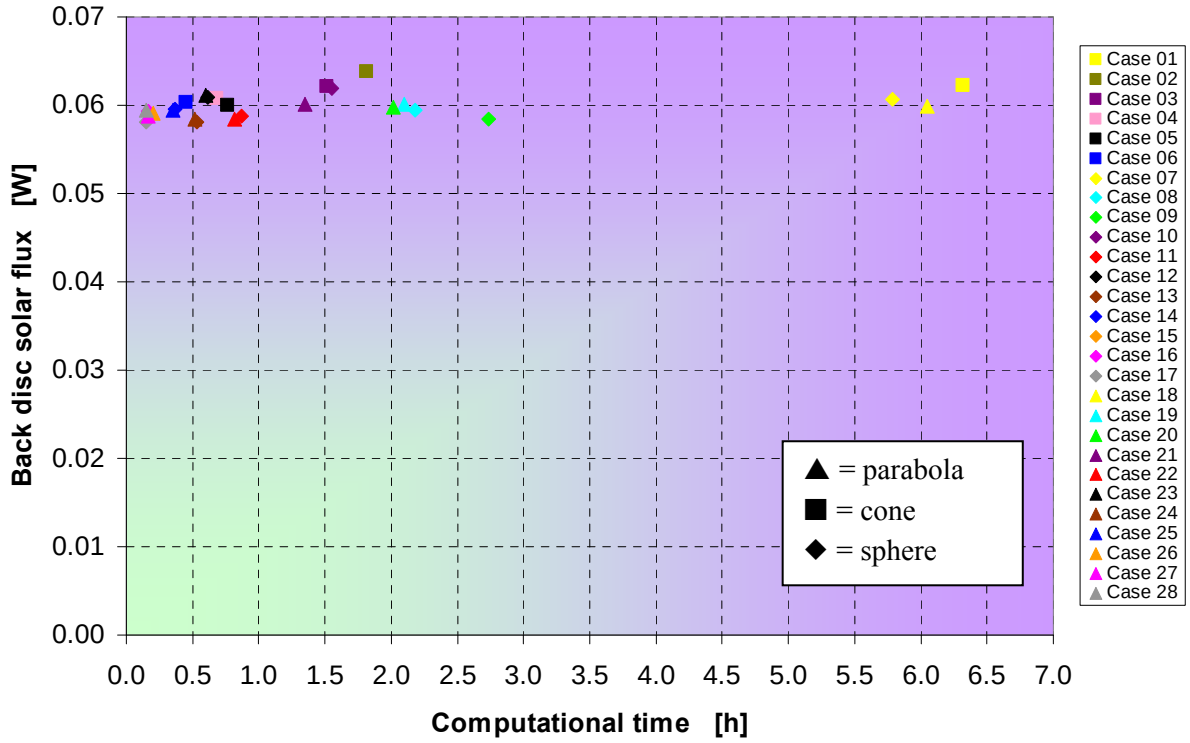

Figure 7-16: Solar flux passed beyond the baffle

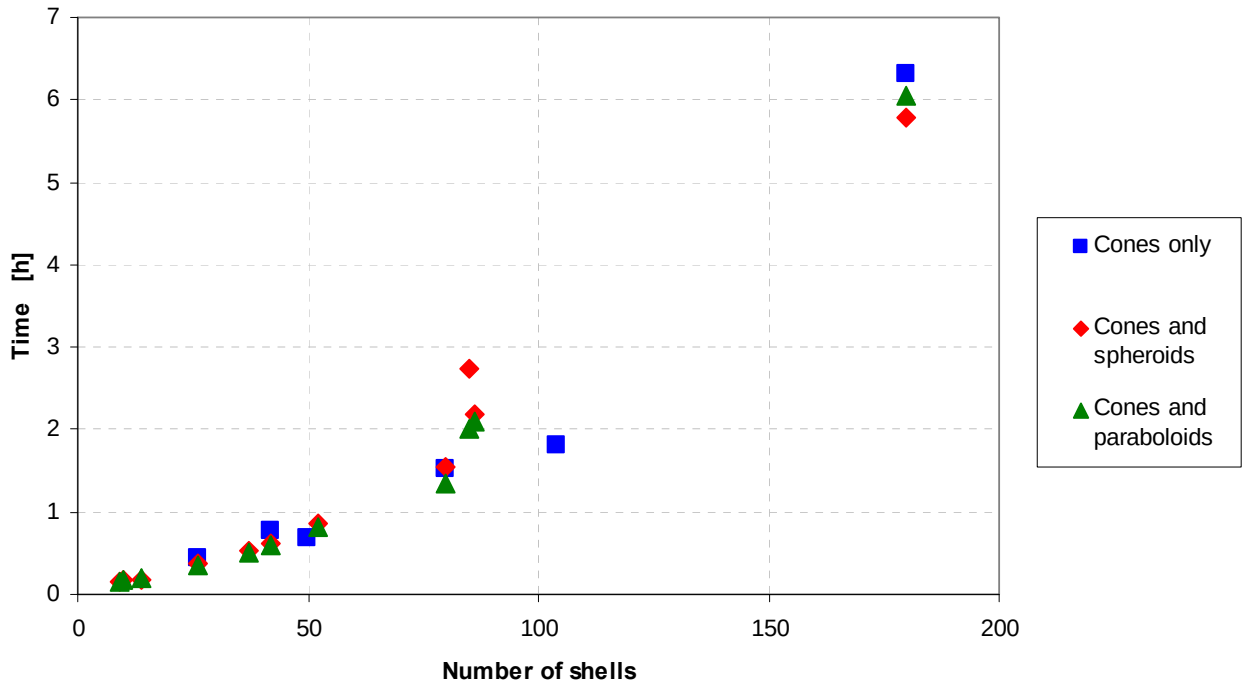

Figure 7-17: Computational time vs. number of shells

7.2.2.1 Results: solar flux absorbed by the rear side of the baffle disc

As shown in Figure 7-15, it is possible to decrease the computational time up to 90% keeping the same error level on the flux absorbed by the rear side of the front ring (Case 12 with respect to Case 01). Even without the implementation of spherical shells, just using a non homogenous discretization of conical shells (Case 03: 80 shells, fine mesh on the front and coarse on the back), it is possible to achieve the same results of a very detailed model (Case 01, 180 conical shells) saving up to 75% of computational time. With a smart use of the spherical shells, it is even possible to decrease the error and at the same time significantly reducing the computational time (Case 10 and Case 11).

The use of parabolic shells seems to only slightly increase the accuracy wrt. the conical models, whereas it always achieves worse results than the spherical shells

7.2.2.2 Results: solar flux passed beyond the baffle

The use of conical, spherical or parabolic shells is almost irrelevant for this parameter, as shown in Figure 7-16, and in the same way the number of shells adopted. The solar flux (which should be zero) is in all analyzed cases constant at about 0.06 W.

It has to be considered that the solar flux passed beyond the baffle (that is, the flux intercepted by the filter in the real device), is strongly lower than the solar flux on the baffle front ring (at least of one order of magnitude), and therefore it is less important for the thermal analyses of the TBU. This parameter could nevertheless be very important concerning the analyses about the laser safety.

7.2.2.3 Optimization of the baffle discretization: conclusions

The use of spherical shells to approximate the ellipsoids and the implementation of non homogeneous discretization lead both to more accurate results and a significant computational time saving.

The best compromise between computational time and numerical accuracy is considered to be a discretization of 20 spherical shells for the first ellipsoid, 4 spheroids for each one of the other ellipsoids and 4 cones for each hyperboloid; it is represented in Figure 7-18.

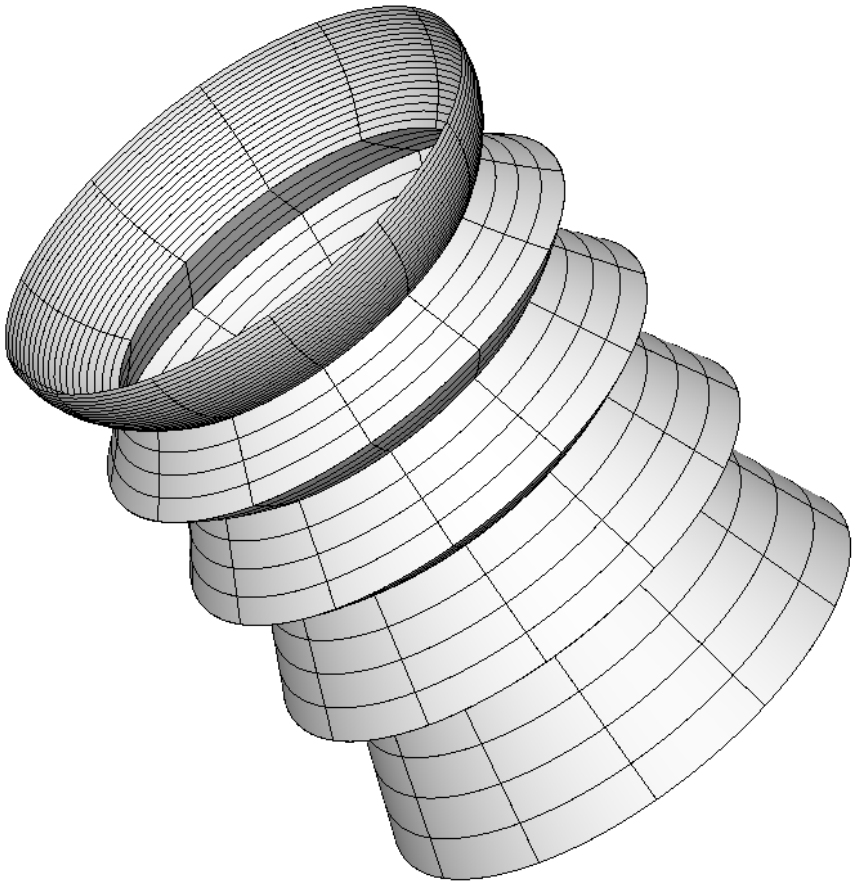

Figure 7-18: The Stavroudis baffle discretized using spherical shells and non-homogeneous discretization

7.3 Analyses results

7.3.1 Rejection efficiency

Case	Efficiency [-]
Hot 1	94.92 %
Cold 1	97.57 %
Hot 2	97.10 %
Hot 3	93.95 %
Cold 2	97.33 %
Hot 4	95.27 %
Hot 5	94.22 %
Hot 6	94.84 %
Cold 3	97.31 %

Table 7-6: Stavroudis baffle –Rejection efficiency

The Stavroudis baffle is always able to comply with the requirement of a rejection efficiency of 90 %. The minimal efficiency highlighted in a thermal worst case is achieved during Hot Case 3, with a value of 94 %. The difference with the cylindrical version is considerable, since the Stavroudis baffle is able to reject 18 % more of the environmental fluxes.

The Cold Cases proved again to be less critical than the Hot Cases, providing for a rejection efficiency above 97 %.

7.3.2 Heat fluxes into the beam expander

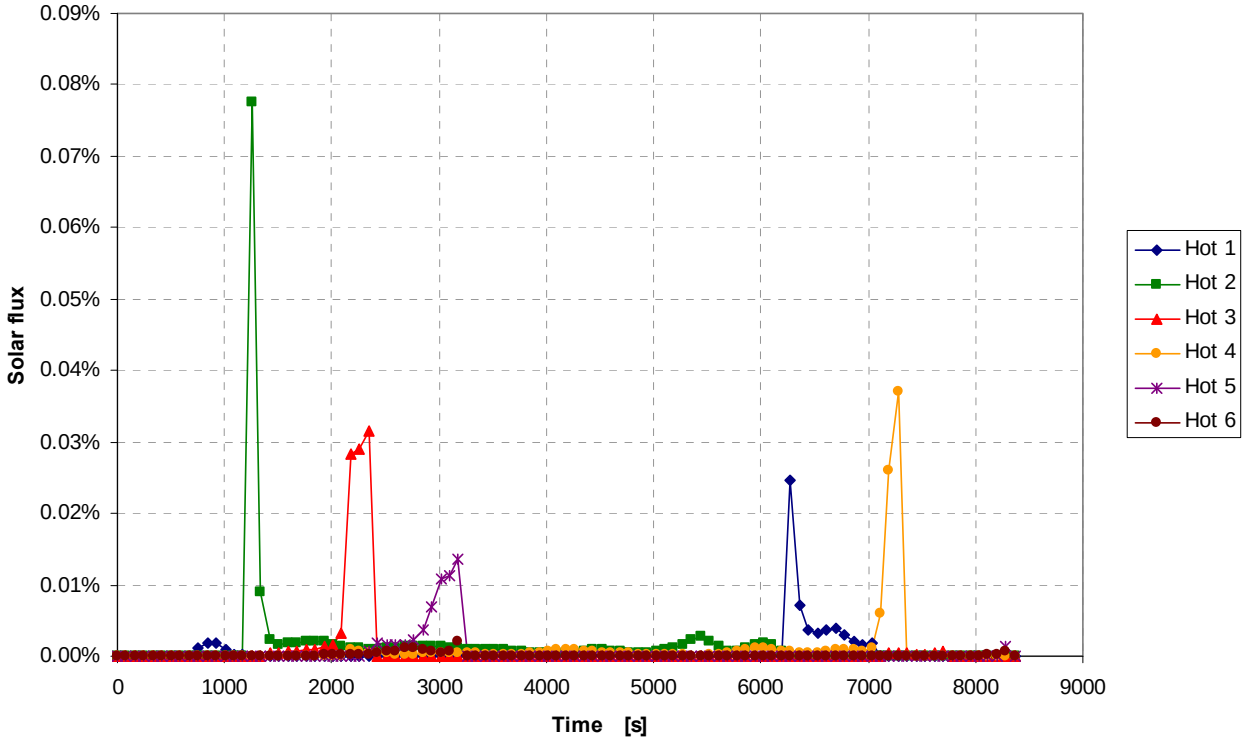

Figure 7-19: Stavroudis baffle – Solar fluxes in the BEX (hot cases)

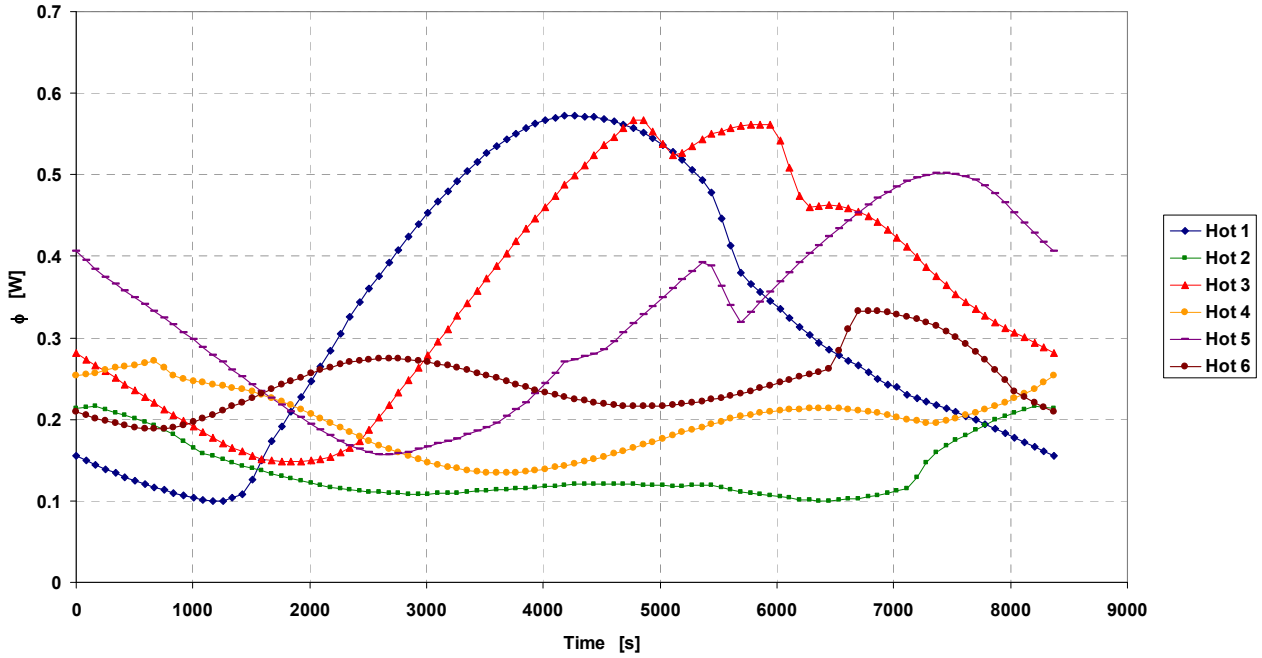

Figure 7-20: Stavroudis baffle – Total heat fluxes in the BEX (hot cases)

The direct solar fluxes entering the laser are, for each thermal worst case, below the prescribed value of 1 % of the fluxes at the aperture. The highest value is 0.08 %, which guarantees for a large margin of safety.
The total heat fluxes are instead always below 0.6 W, a low power which does not arise any problem for the laser safety or functioning. Hot Case 1 and Hot Case 3 proved again, as for the cylindrical baffle, to be the most severe conditions, whereas Hot Cases 2 and 4 are less critical.

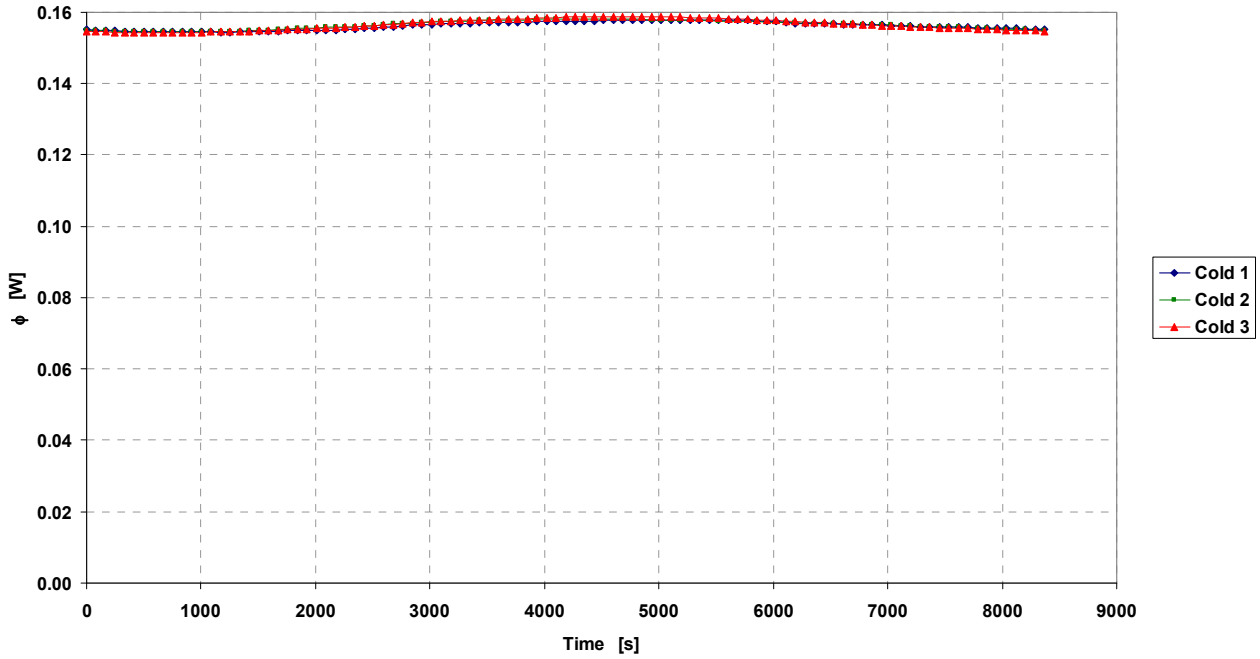

Figure 7-21: Stavroudis baffle – Total heat fluxes in the BEX (cold cases)

7.3.3 Heat fluxes into the s/c

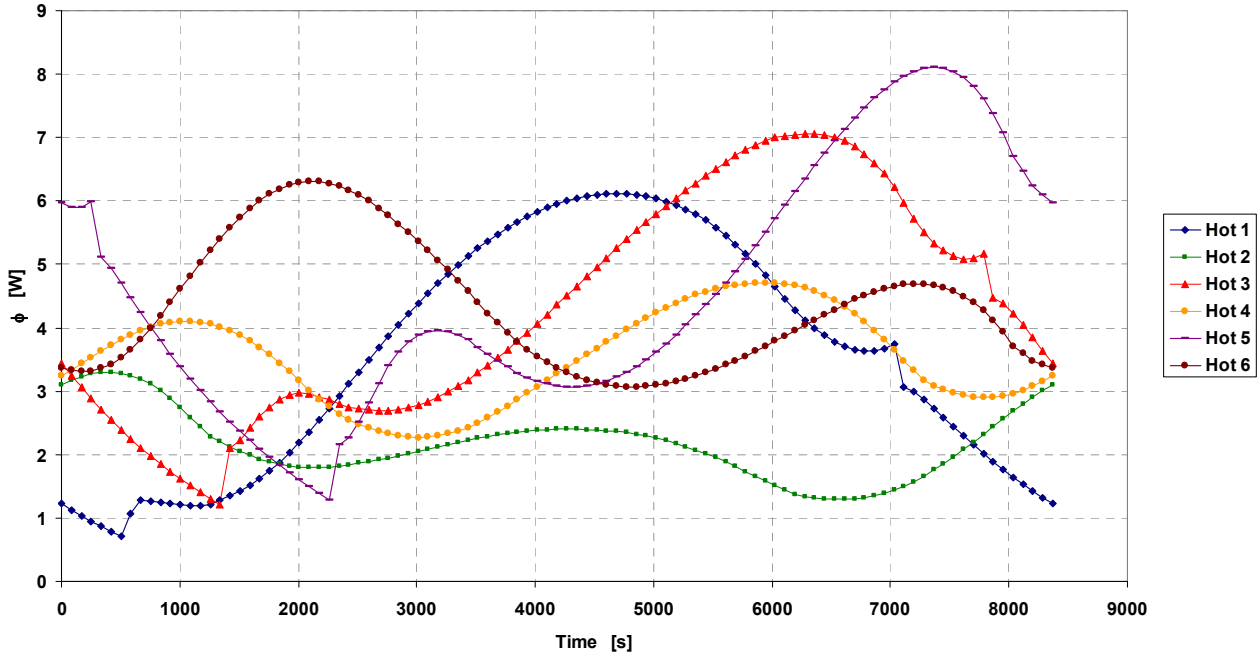

Figure 7-22: Stavroudis baffle – Heat fluxes absorbed by the s/c (hot cases)

The maximal heat absorption from the s/c, during the dimensioning cases (BOL and EOL, not EEM), is about 7 W and occurs during Hot Case 3. The other case in which the true anomaly of Mercury is 138.75°, Hot Case 1, has a smaller value, 6 W. Hot Case 2 and Hot Case 4 are significantly lower. As for the cylindrical baffle, the peaks of heat absorption are due to the planetary IR radiation.
It is interesting to note that the Stavroudis concept, which is supposed to be the best performing, causes a higher absorption peak by the s/c in comparison with the cylindrical version (7 W vs. 6.5 W). Even if the Stavroudis concept is more efficient in rejecting the environmental radiation in percentage, the bigger radiated area causes higher absolute values of absorbed heat fluxes, which are conductively transmitted inside the instrument and there conductively and radiatively transmitted to the s/c. The bigger illuminated area is a consequence of the internal cavities of the baffle and of the large front ring.

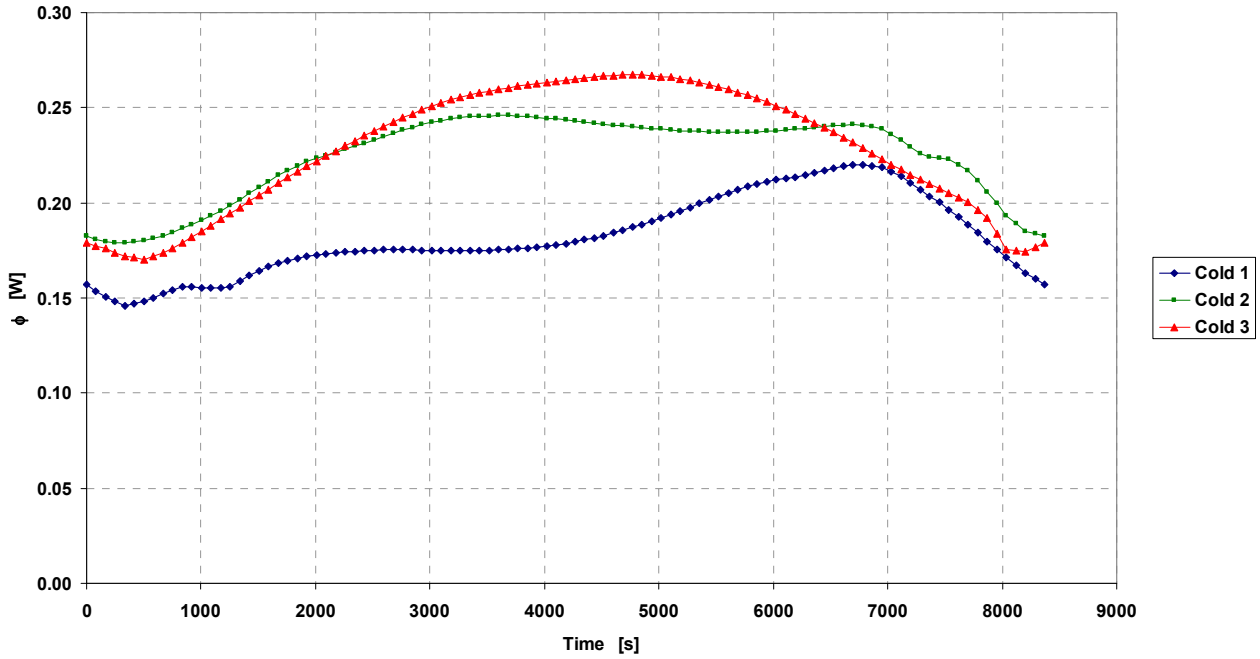

Figure 7-23: Stavroudis baffle – Heat fluxes absorbed by the s/c (cold cases)

The absorbed heat fluxes during the cold cases do not provide significant information. The heat flux transmitted to the s/c ranges from 0.15 W to 0.27 W.

7.3.4 Baffle temperature

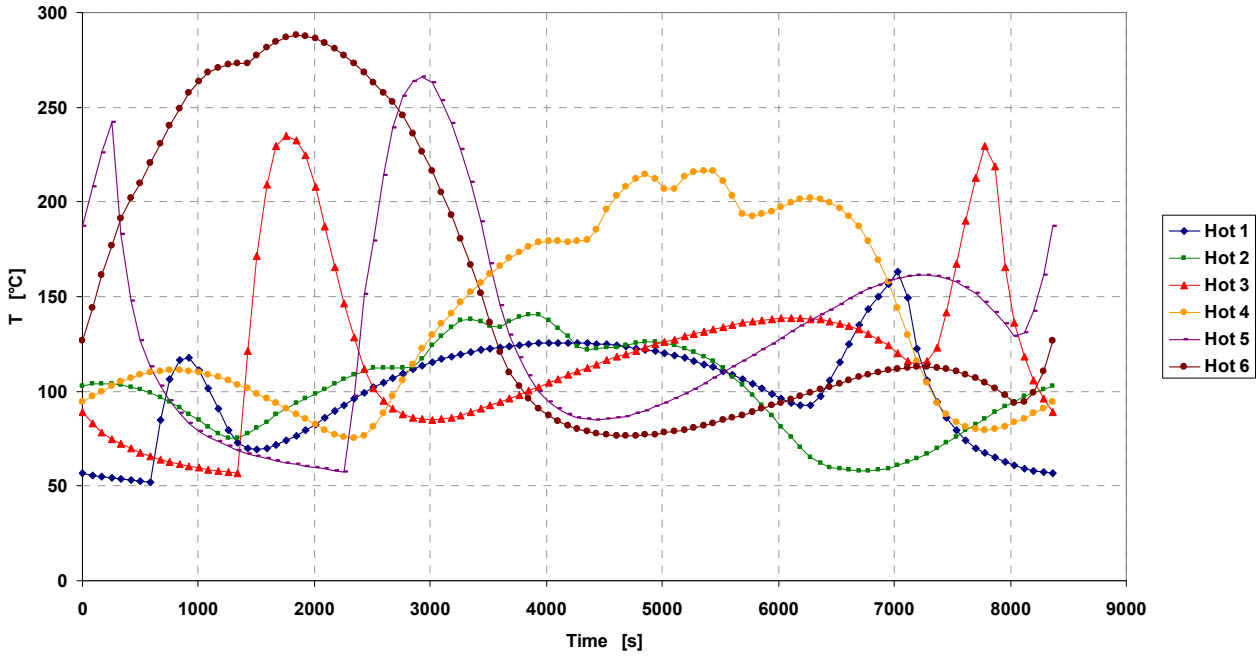

Figure 7-24: Stavroudis baffle – Max temperature (hot cases)

The first consideration that can be done is that the maximal temperatures, as expected, are significantly lower than the results from the cylindrical baffle (see Figure 6-12 and Figure 7-24). The highest temperature experienced by the cylindrical baffle is about 378 °C, during Hot Case 3, whereas for the Stavroudis baffle the maximal temperature occurs again during Hot Case 3 and it approximately 235 °C.
Considering Hot Cases 1, 3 and 5, which correspond to the orbits when Mercury is at perihelion, it is possible to identify the same mould, similarly to what happened for the cylindrical baffle. The trend is almost the same for the three cases, but the orbit evolution shows a shift and an increment of the temperatures. Analyzing the general trend, Hot Cases 1, 3 and 5 begin from a cold point in the eclipse area and then the temperature quickly rises up when the s/c exits from the eclipse and faces the Sun with a low aspect angle. The solar radiation and the temperature drop down as soon as the solar aspect angle decreases, then a temperature local maximum occurs when the satellite faces the enlightened side of the planet. In this area, the Stavroudis baffle behavior significantly differs from the cylindrical one: the local maximum caused by the planetary IR radiation occurs after the subsolar point, as a consequence of the high thermal inertia of the device. Another consequence is that the baffle temperature just before entering the eclipse is strongly higher than the temperature which occurs after the first solar peak. This asymmetry of the temperature brings as a consequence that the second temperature peak is higher than the first one. The amount of energy absorbed from the Sun is the same during both the peaks, but the initial temperature is higher after the local maximum caused by the planetary fluxes and therefore the second temperature peak is more critical. Summarizing the considerations about Hot Cases 1, 3 and 5:

- The solar radiation causes higher temperature peaks wrt. the IR radiation
- Solar peaks are relatively short, whereas the local maximum caused by the IR radiation is longer
- The temperature chart is asymmetrical, as a consequence of the high thermal inertia of the device: in particular, the second solar peak is more critical than the first one
- The orbit evolution causes a shift of the trend and a significant temperature increment, mainly due to the degradation of the thermo-optical properties

Hot Cases 2 and 4, which occur when the planet's true anomaly is 138.75°, present the same temperature curves trend. The first local maximum is due to the planetary IR radiation: for these orbits, the s/c ascending node is approximately over the planet subsolar point. The main temperature peak, for intensity and duration, is due to the low aspect angle about the Sun that the s/c keeps for a long time. A significant difference from the cylindrical version of the baffle is that Hot Cases 2 and 4 are not significantly less dangerous than Hot Cases 1 and 3. Concerning the BOL orbits, Hot Case 2 has smaller temperature peaks than Hot Case 1; regarding EOL orbits, Hot Case 4 is most of the time hotter than Hot Case 3, but presents a lower maximal temperature. About Hot Cases 2 and 4:

- The solar radiation causes higher and longer temperature peaks wrt. the IR radiation
- The orbit evolution causes a shift of the trend and a significant temperature increment, mainly due to the degradation of the thermo-optical properties
- The temperature peak at BOL is lower than in the case when Mercury is at perihelion, but at EOL the peaks are more similar

Hot Case 6, which occurs at EEM when Mercury's true anomaly is 52.5°, presents some relevant differences wrt. Hot Cases 2 and 4:

- The solar peak is high (up to 288 °C) whereas the IR peak is negligible
- The solar and IR peaks are significantly shifted

Hot Case 6 shows a significantly higher maximal temperature, but the device should be sized only considering BOL and EOL missions. Therefore, the reference cases used are Hot Case 3 and Hot Case 4.

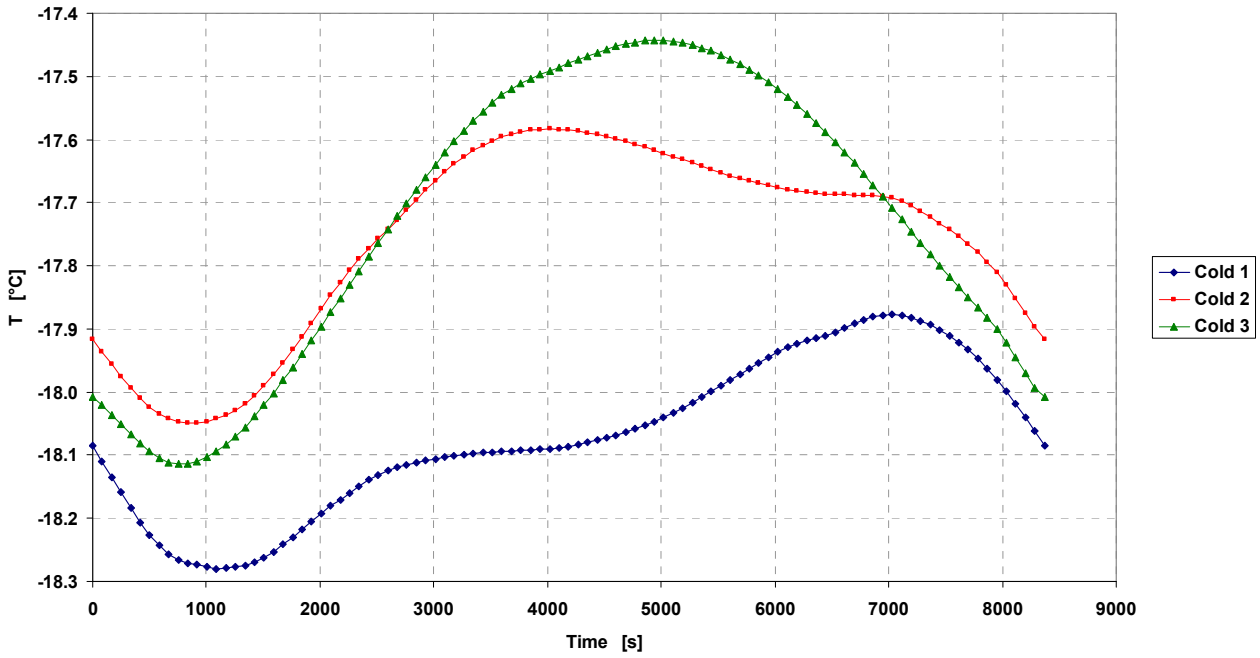

Figure 7-25: Stavroudis baffle – Min temperature (cold cases)

Considering the baffle minimal temperature, there are no significant differences between Cold Case 1, Cold Case 2 and Cold Case 3. The baffle minimal temperature is almost identically constant at -18 °C.

7.3.5 Filter temperature

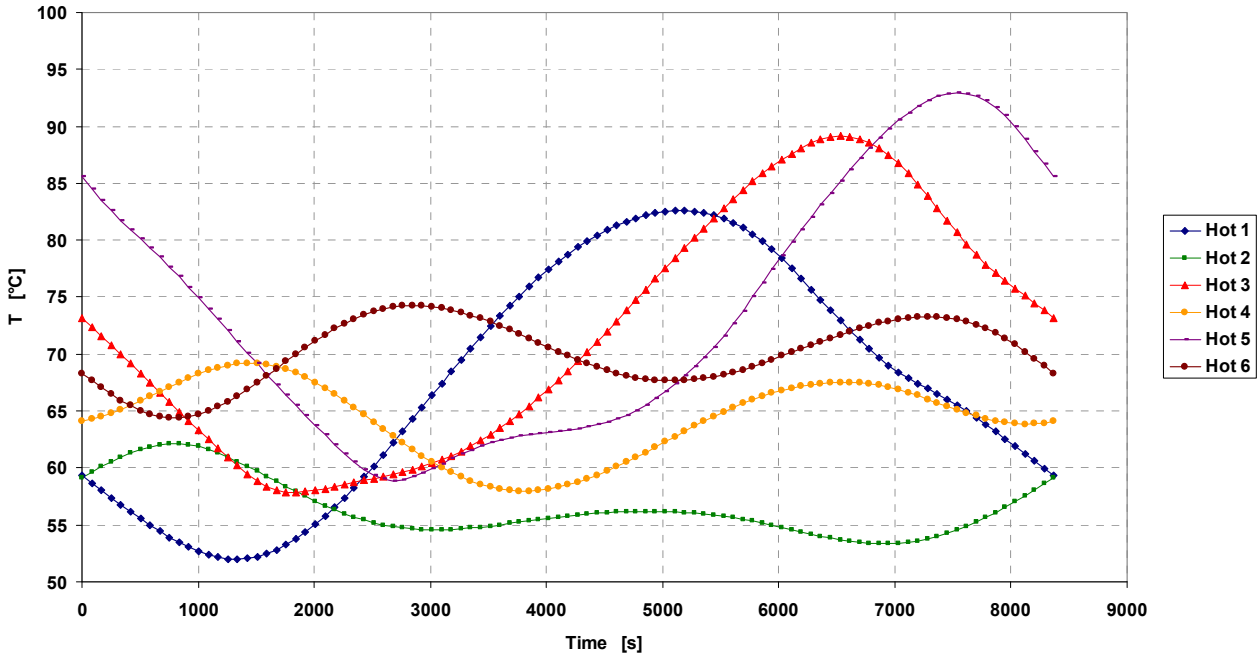

Figure 7-26: Stavroudis baffle – Max filter temperature (hot cases)

The trend of the filter temperature in the Stavroudis TBU is the same than in the cylindrical TBU (see §6.4.5). However, the temperatures are significantly lower (40 ÷ 50 °C). The maximal temperature of the filter is achieved during the Hot Case 3, and it corresponds to 89 °C. At this temperature, the thermal expansion and the deformation of the filter lens do not arise relevant concerns about mechanical stresses, and the optical distortion of the lens is limited and tolerable.

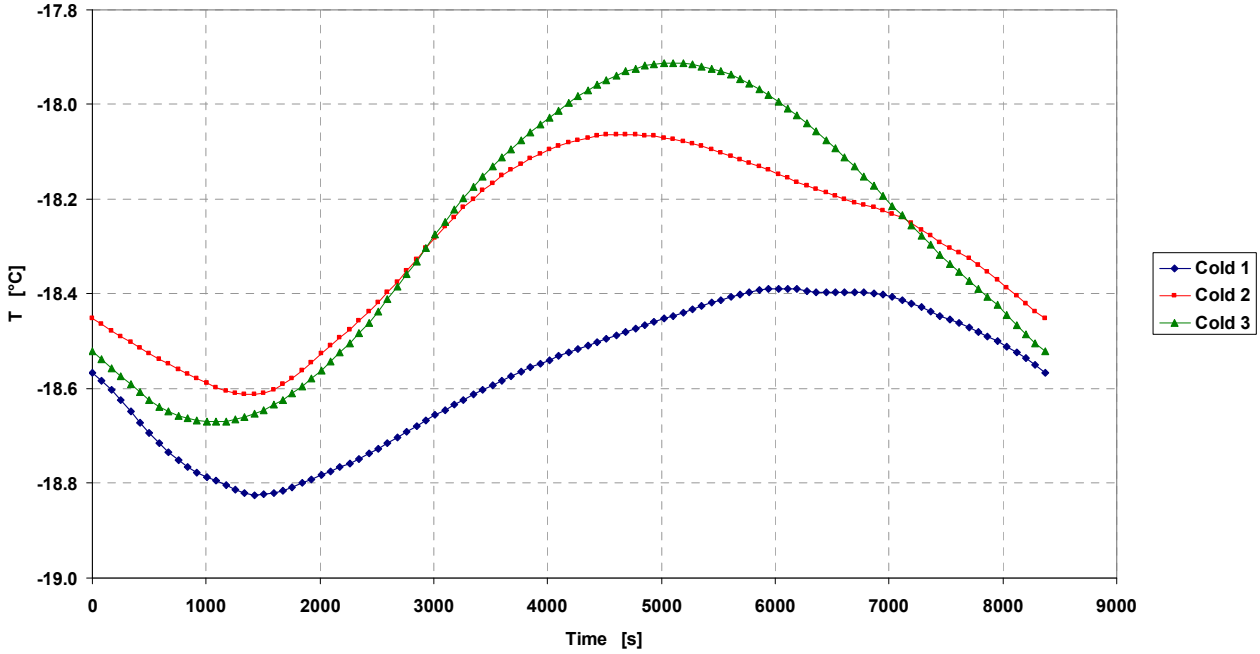

Figure 7-27: Stavroudis baffle – Min filter temperature (cold cases)

The temperature of the filter during the cold cases is very stable and between -18 °C and -19 °C. These values are used in combination with the temperature during the hot cases to calculate the thermal stresses and the modification of the optical performances.
The analysis of the filter temperatures highlighted the significantly better behavior of the Stavroudis baffle in comparison with the cylindrical one.

7.3.6 Summary

Case	Efficiency [-]	Fluxes to BEX max [W]	Fluxes to s/c max [W]	Baffle T max [°C]	Filter T max [°C]
Hot 1	94.92 %	0.573	6.115	163.30	82.58
Cold 1	97.57 %	0.158	0.220	-12.04	-18.28
Hot 2	97.10 %	0.216	3.301	140.73	62.14
Hot 3	93.95 %	0.567	7.053	234.96	89.17
Cold 2	97.33 %	0.158	0.246	-11.45	-17.94
Hot 4	95.27 %	0.271	4.708	216.63	69.19
Hot 5	94.22 %	0.502	8.108	265.89	92.91
Hot 6	94.84 %	0.333	6.311	287.88	74.29
Cold 3	97.31 %	0.159	0.267	-11.92	-17.79

Table 7-7: Stavroudis baffle – Summary of the indexes of performance

As it has already been mentioned, the Stavroudis baffle is able, for each thermal worst case, to achieve a rejection efficiency above 90 %. The first thermal requirement is therefore fulfilled. Also, the solar fluxes reaching the BEX of the laser are always below 0.1 %, fairly below the requirement of 1 %. The peak of the heat fluxes entering the instrument occurs during the Hot Case 1, when 0.573 W strike the front lens of the BEX. These values are limited and do not present an issue for the safety and the functioning of the laser. The heat fluxes absorbed by the s/c are quite high, presenting a maximal value at EOL of 7 W.
The maximal temperature of the baffle foreseen during the operational life is 235 °C (Hot Case 3). This value is not too high to be considered a serious issue for the integrity of the hardware, but it is high enough to lay down conditions concerning the baffle coating. The filter temperature, on the other hand, is always below 90 °C and no significant issues are foreseen for this element.

8 Conclusions

8.1 Comparison of cylindrical TBU vs. Stavroudis TBU

8.1.1 Baffle efficiency

The efficiency for both the cylindrical and the Stavroudis baffle are reported in Table 8-1. This value represents the amount of environmental radiation that the device is able to reject toward the deep space, by means of reflection or re-emission. It has been calculated considering the steady state conditions.

It is immediately recognizable that the efficiency of the cylindrical version is significantly lower than the Stavroudis version one. In particular, the cylindrical baffle never achieves the requirement of 90% stated in the Instrument Requirement Document [54]. Among the Worst Cases, the minimal efficiency of the cylindrical baffle is 76 %, against the 94 % of the Stavroudis device, which is always able to satisfy the prescribed requirement.

Worst Case		Cylinder	Stavroudis
BOL	Hot Case 1	76.18 %	94.92 %
BOL	Hot Case 2	81.06 %	97.57 %
BOL	Cold Case 1	85.30 %	97.10 %
EOL	Hot Case 3	76.28 %	93.95 %
EOL	Hot Case 4	81.35 %	97.33 %
EOL	Cold Case 2	85.39 %	95.27 %
EEM	Hot Case 5	77.24 %	94.22 %
EEM	Hot Case 6	81.07 %	94.84 %
EEM	Cold Case 3	85.31 %	97.31 %

Table 8-1: Comparison of the baffle efficiency

8.1.2 Sunlight entering the instrument

This requirement fixes a limit to the amount of solar energy that can reach the beam expander when the Sun is in the range 35° to 90° from the instrument line of sight. The MPO orbit has been chosen so that the Sun angle is always above 38°; therefore, this requirement is always applicable.

The ratio of the solar fluxes reaching the beam expander with respect to the fluxes at the baffle aperture is show in Figure 6-7 for the cylindrical baffle and in Figure 7-19 for the Stavroudis. It is immediate to note that the requirement is easily fulfilled for both the versions without particular efforts. Anyway, the Stavroudis TBU proved to be much more efficient: the solar fluxes ratio is approximately one order of magnitude lower than for the cylinder.

8.1.3 Fluxes to the BEX and to the s/c

In Table 8-2 the absorption of the heat fluxes by the beam expander of the laser and by the s/c, both as conductive and radiative sink, are summarized for the cylindrical and for the Stavroudis version.

Parameter	Cylinder	Stavroudis
Max fluxes absorbed by the laser BEX [W]	2.402	0.573
Max fluxes absorbed by the s/c [W]	6.487	7.053

Table 8-2: Comparison of the heat fluxes absorbed by the BEX and by the s/c

As expected, the Stavroudis baffle is largely more efficient in preventing the heat fluxes to reach the inner side of the instrument. This is a consequence of the specific design of the Stavroudis baffle, which is

optimized to reject the solar fluxes, and of the lower baffle temperature. A large amount of the 2.4 W that are absorbed by the BEX implementing the titanium cylinder comes indeed from the IR emission of the TBU and SPU, which are significantly hot in the worst cases.
Surprisingly, the cylindrical baffle is slightly more efficient concerning the heat dissipation to the s/c, being able to spare 0.6 W. The reason of the Stavroudis baffle lower efficiency is the larger area that this complex design entails. The baffle vanes present a larger area than the simple cylinder, and the front ring constantly exposes a large surface to the environment. The absorption of the environmental radiation is therefore greater, even if the percentage of rejected radiation (the efficiency) is higher. This absorbed heat load is conductively transmitted inside the instrument and there radiatively and conductively dumped to the s/c.

8.1.4 Temperatures

	Cylinder		Stavroudis	
Parameter	**Value**	**Worst Case**	**Value**	**Worst Case**
Baffle max temperature	377.66 °C	Hot Case 3	234.96 °C	Hot Case 3
Baffle min temperature	-17.12 °C	Cold Case 1	-18.28 °C	Cold Case 1
Baffle max thermal gradient	278.97 °C	Hot Case 1	175.17 °C	Hot Case 3
Filter max temperature	142.41 °C	Hot Case 3	89.17 °C	Hot Case 3
Filter min temperature	-11.33 °C	Cold Case 1	-18.39 °C	Cold Case 1
Filter max thermal gradient	0.23 °C	Hot Case 3	0.71 °C	Hot Case 3
Front ring max temperature	n. a.	n. a.	271.30 °C	Hot Case 3

Table 8-3: Relevant temperatures

An interesting consideration concerns the Stavroudis TBU maximal temperature. The maximal temperature reached by the device is about 270 °C, but it must be noted that this value is achieved on the front ring only: this component is made of titanium and has a special coating with already proved to be able to withstand high temperatures [49]. The maximal temperature experienced by the nickel baffle is instead 235 °C, a lower value: the good insulation of the connections between the baffle body and the front ring allows referring mainly to the front ring the thermal shielding task.
This also implies the chance to have weaker maximal thermal gradients on the baffle body (175 °C with respect to 279 °C): this is vital since the Stavroudis baffle, being essentially an optical device, is much more sensible to the thermal deformations.

8.1.5 Size and mass

The cylindrical baffle results to be 275 mm long, with a maximal external diameter of 133.5 mm (the half-hidden orange ring in Figure 8-1); the baffle mass is 0.062 kg. The total mass of the TBU, considering the cylinder, the filter, the filter mount, the MLI blankets and all the connection components is 0.617 kg.
The Stavroudis version is shorted: the length is 181 mm only, the external diameter of the main body is 174 mm, but the baffle requires also a front ring (purple in Figure 8-2) which external diameter is 200 mm. The bare baffle mass is 0.251 kg, but the total mass of the device proved to be 0.970 kg.
The beam expander clear aperture is never obscured, hence the requirement reported in §5.2.1 is always fulfilled.
The baffle masses represent instead an issue. The requirement of an overall unit weight of 0.160 kg proved to be greatly unrealistic. The mere optical filter weights 0.135 kg, and our team had no control on this component. The cylindrical TBU mass is 0.617 kg (+286% wrt. the requirement), whereas the Stavroudis version of the TBU weights 0.970 kg (+506% wrt. the requirement).

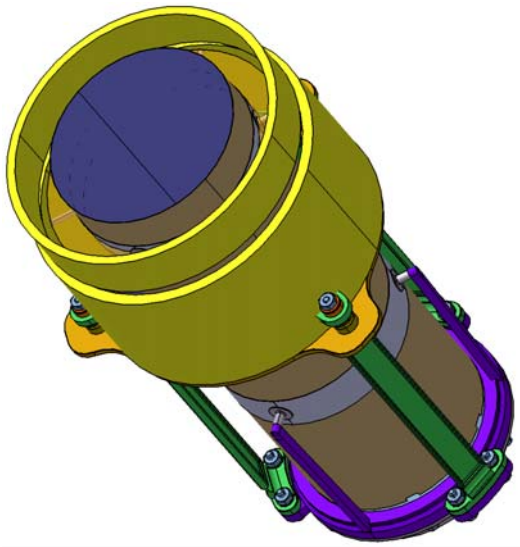

Figure 8-1: Cylindrical TBU

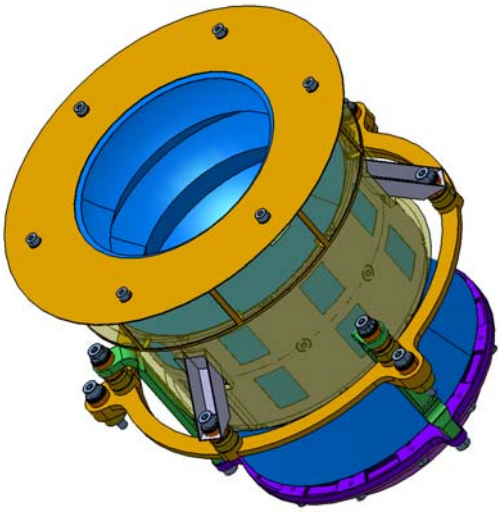

Figure 8-2: Stavroudis TBU

Yet, the whole instrument and even the s/c experienced the same mass budget problems. Therefore, the whole mission design has been reviewed and the initial estimated mass of 250 for the MPO has been incremented to 1000 kg. This implied a heavy mission redefinition, which envisaged the used of a more powerful launcher (an Ariane 5 ECA [2], from the previously envisaged Soyuz/Fregat [3]). The masses of the two versions of the TBU have been discussed with the system engineer and with ESA, and they have been accepted even if they do not satisfy the stated requirement, which is now to be considered obsolete.

8.1.6 Manufacturing and risks

An advantage of the cylindrical version of the baffle consists in its simplicity of construction. The Stavroudis version, on the other hand, requires a very fine surface accuracy in order to be able to properly accomplish its optical task. The required average surface roughness should be lower than 0.5 μm: this strict requirement requires the economical and time expensive procedure of electroforming. The titanium cylinder instead does not require particular operations for its production.

The optical functioning of the Stavroudis baffle causes some issues even concerning the device assembly and its integration into the instrument. The baffle must be properly assembled: this operation must be performed granting the proper alignment. The integration of the baffle should obviously preserve the proper pointing and should not generate mechanical deformation within strict margins. Finally, the Stavroudis baffle requires much more assembling components than the cylindrical baffle, and each of these components has again to be implemented granting that the required alignment accuracy alignment is preserved. Each of these elements should be properly designed, produced and implemented, requiring a further effort in terms of temporal and economical resources.

The proper alignment of the Stavroudis baffle is vital: if the required accuracy is not granted, the foci of the ellipsoids and of the paraboloids which constitute the shape can move outside the baffle clear aperture, completely jeopardizing the device functioning [28]. The cylinder baffle instead is not based upon its optical functioning: therefore, even quite large misalignments or assembly inaccuracies do not cause particular issues. The final alignment accuracy required for the Stavroudis baffle is typically 1 μm, which is hard to be achieved and granted, whereas the same value for the cylinder is 1 mm.

Another relevant difference between the two versions of the baffle is the amount of temporal and economical resources required for their design, development and manufacturing. The thermal model of the cylindrical baffle consists of 109 nodes, and the transient solution of a simulation for a whole orbit around Mercury requires about 0.4 h. The thermal model of Stavroudis version instead consists of 672 nodes, and the computational time rise up to 27 h. It must be noted that about 95% of the computational time in the

Stavroudis case is dedicated to the radiative analysis: the complex geometry and the high reflectance of the shape require long ray-tracing calculations. Similar considerations can be done concerning the mechanical model and design of the device. Considering manufacturing only, the order of magnitude of the devices cost is 10^5 Euro: the Stavroudis version, in particular, is about 2.5 times more expensive than the cylindrical one. The final costs and the cost ratio between the two versions would be further increased if the design and development costs were taken into account.
Others important points to be examined are the system reliability and the device sensitivity to risk. Once again, the optical nature of the Stavroudis baffle makes it more problematic. First of all, even quite small deformations of the baffle can jeopardize the instrument functioning: therefore, the Stavroudis version is much more sensible to mechanical and thermally induced stresses. A completely coupled thermo-optic-mechanical analysis has unfortunately not been performed, due to the lack of reliable software and to the expected extremely high computational time required. Another point is that the high reflectivity of the Stavroudis baffle is sensible to contamination: the very low solar absorptance of the electroformed nickel can quickly increase in presence of even a low amount of contaminants. Small changes in the absolute value of the solar absorptance mean high changes in the percentage of the absorbed solar fluxes, since the nominal absolute value of the absorptance is very low. Small changes in the thermo-optical properties of the titanium cylinder do not instead cause significant variations in the thermal results.

8.2 Conclusions

The Stavroudis baffle has been selected as the best choice, as a consequence of its better mechanical, optical and thermal behaviour. The drawbacks of this concept, such as the greater weight, complexity and economical costs, and the higher heat load dumped in to the s/c, have been considered minor issues in comparison with the other advantages. At the present day, the manufacturing of the prototypes of the TBU and SPU units are on-going processes. It has to be noted that the baffle design has been modified: the current project makes use of an aluminium shape produced with diamond turning.
In this work, the general problematic of the baffling system has been introduced and the environmental conditions of the systems have been determined. Two different solutions have been proposed and analyzed, paying attention to the real feasibility of the options. Thermal analyses have been carried out to determine and to optimize the thermal behaviour of the system.
The cylindrical version is a light, simple and reliable solution, but it proved to be unable to satisfy most of the thermal requirements. The Stavroudis baffle, instead, demonstrated to be able to fulfil most of the requirements, even if not all of them. The mass of the unit and the amount of heat power dissipated inside the s/c are exceeding the prescribed values.
On the base of the results, and considering also the structural, optical and logistic information, the Stavroudis version has be chosen by the system engineer as the unit to be manufactured for the BELA real hardware.

8.2.1 Opened issues

The determination of the precise values of the thermo-optical properties of the baffle and of other elements is a priority in order to achieve a better accuracy of the simulations. More important, the determination of the real degradation of optical properties, expected after a long exposure in the Mercury's orbit, must be carried out.
A complete coupled structural-thermal-optical simulation should be carried out to determine how the thermal loads distort the shape and modify the optical functioning, which consequently affects the thermal and structural behaviour of the device. Unfortunately, no commercial software is known to be able to perform a completely coupled structural-thermal-optical analysis.
Further, the thermal models of the single units of the BELA should be integrated together to simulate the complete thermal system. With this operation, it will be possible to assess how each unit influences the

others. Iterating, it is possible to assemble the thermal models of the different instruments to simulate the complete s/c.
Finally, the thermal models of the units should be correlated with the real hardware during the thermal tests, in order to verify the expected thermal behaviour and to determine the parameters which are affected by large uncertainties.

8.2.2 Spin-offs

At least two different extra results have been achieved during the described work:

- The development of a method to represent complex 3D geometries in ESARAD
- The determination of a procedure to implement wavelength dependant thermo-optical properties in ESARAD

The first work originated from the necessity of modelling the complex Stavroudis shape: the mathematical background to perform and to optimize the discretization of ellipsoids and hyperboloids has been investigated, and numerical software has been developed to automatically create the long code which is necessary for the approximation. The results have been presented at the 23rd Thermal and ECLS Software workshop, which took place in October 2009 in Noordwijk, The Netherlands.
The development of a procedure to implement the wavelength dependency of the thermo-optical properties has been carried out to correctly model the optical filter, which presents a complex spectrum, and to properly take into account for the planetary fluxes, which wavelength significantly vary with time. A paper has been written, in collaboration with the Group Head of the Thermal Engineering & Software Products of ITP-Alstom, to explain the detailed method. This paper will be presented at the 40th International Conference on Environmental System, which will take place in July 2010 in Barcelona, Spain.

Appendix

The charts reported in the following pages are the results of the analyses explained in §6.2. Due to the large amount of data reported, it is suggested to print them in A3 or in a larger format.
Four tables are presented for each index of performance: two of them represent simulations with a perfectly specular reflectance, and the other two with perfect diffusive reflectance. The two charts with the same reflectance provide for the same data, but present the information in a different way. In one of them, the optical properties of the front part of the baffle are the main parameter: each chart of the table corresponds to a specific set of IR emissivity and solar absorptance for the front part of the cylinder; the axes of the chart instead represent the optical properties of the back part. For the other table it is the opposite: the rows and the columns represent the optical properties of the back part, and in each chart the trend of the parameter as a function of the front part only is depicted.

Efficiency of the baffle [%] – Main parameter: front optical properties - Diffusive reflection

Front	α = 0.05	α = 0.20	α = 0.35	α = 0.50	α = 0.65	α = 0.80	α = 0.95
ε = 0.05	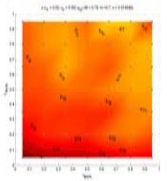	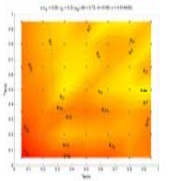	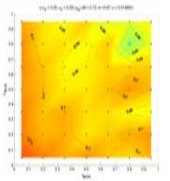	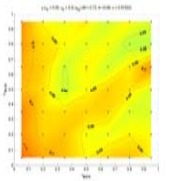	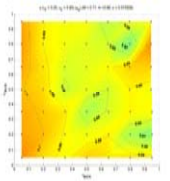	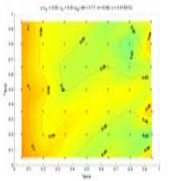	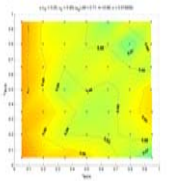
ε = 0.20	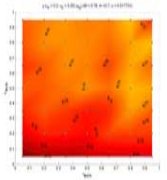	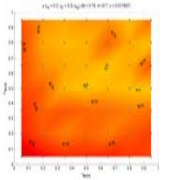	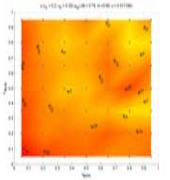	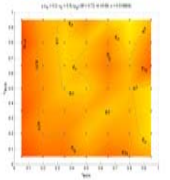	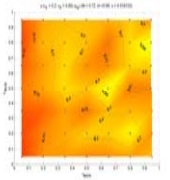	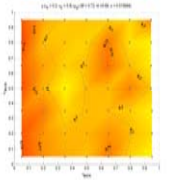	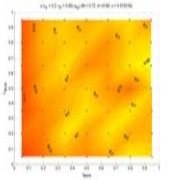
ε = 0.35	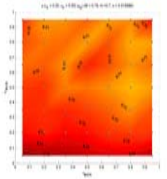	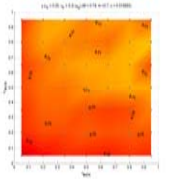	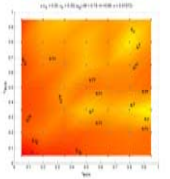	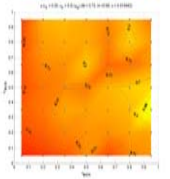	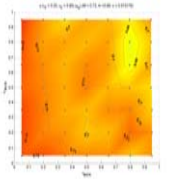	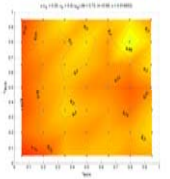	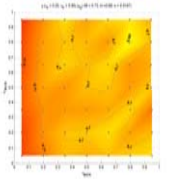
ε = 0.50	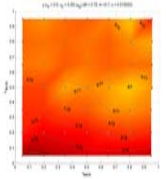	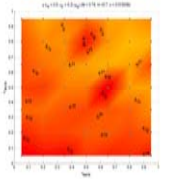	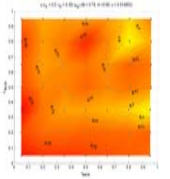	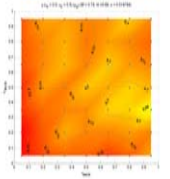	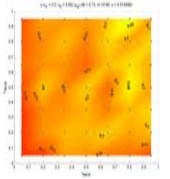	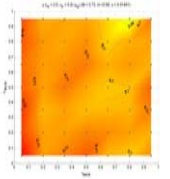	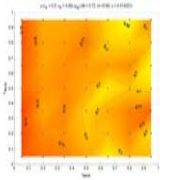
ε = 0.65	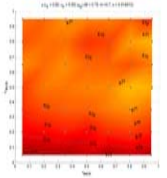	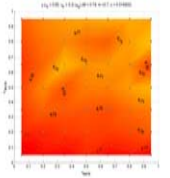	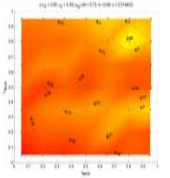	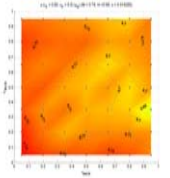	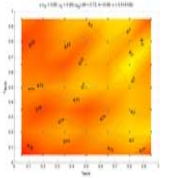	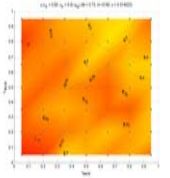	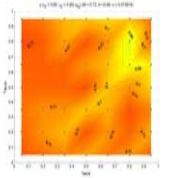
ε = 0.80	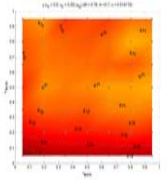	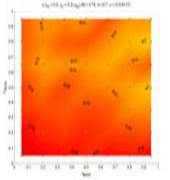	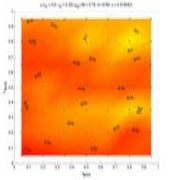	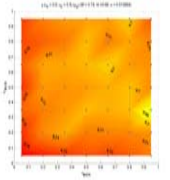	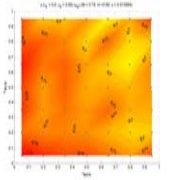	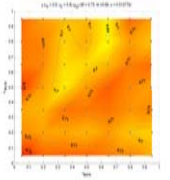	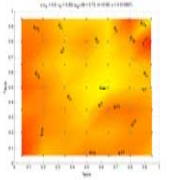
ε = 0.95	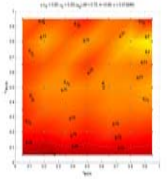	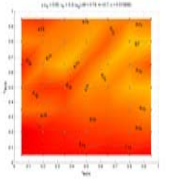	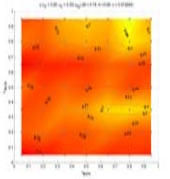	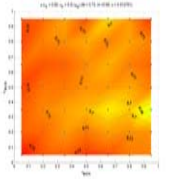	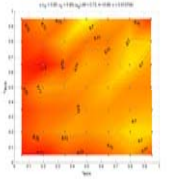	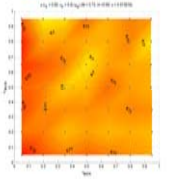	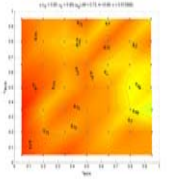

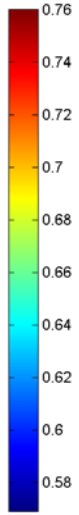

Efficiency of the baffle [%] – Main parameter: front optical properties - Specular reflection

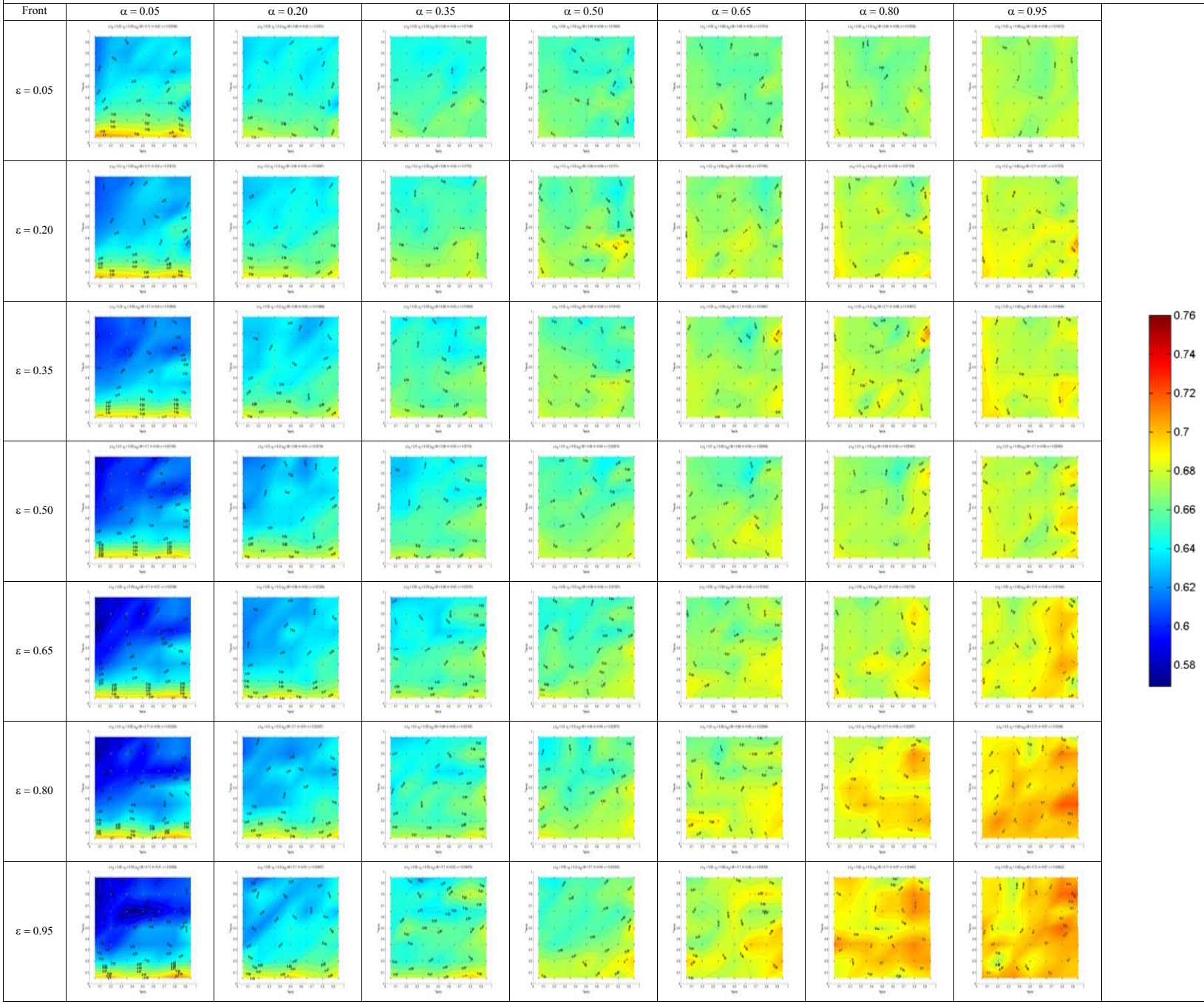

Efficiency of the baffle [%] – Main parameter: back optical properties - Diffusive reflection

Back	α = 0.05	α = 0.20	α = 0.35	α = 0.50	α = 0.65	α = 0.80	α = 0.95
ε = 0.05	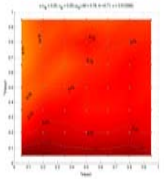	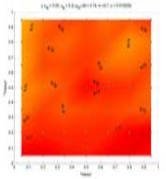	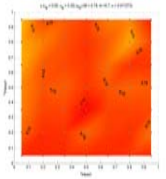	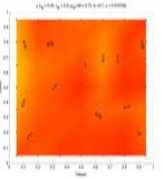	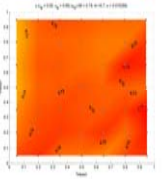	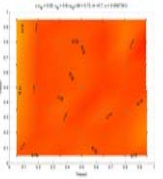	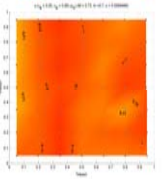
ε = 0.20	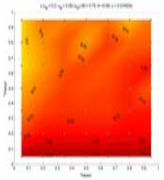	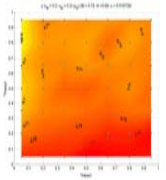	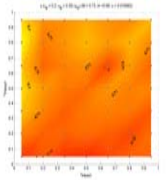	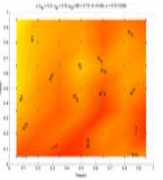	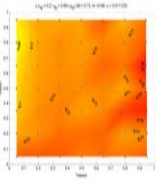	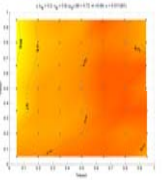	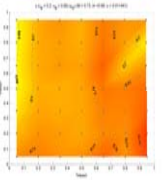
ε = 0.35	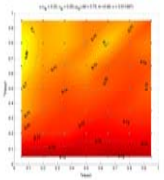	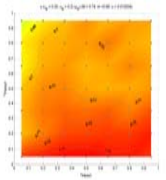	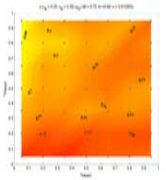	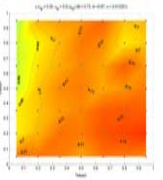	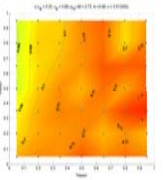	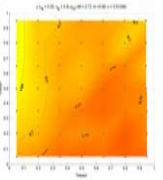	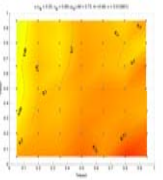
ε = 0.50	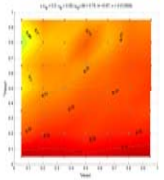	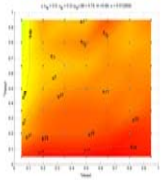	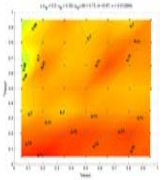	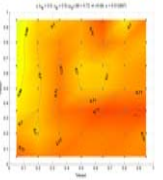	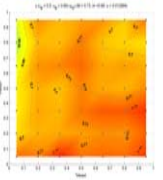	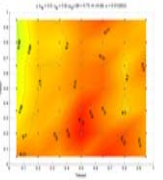	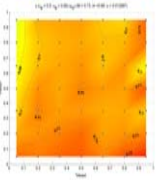
ε = 0.65	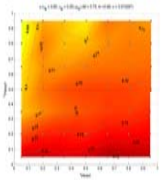	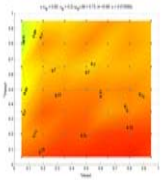	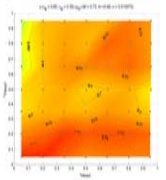	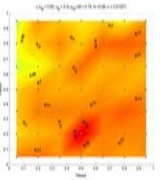	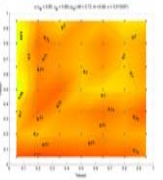	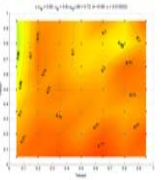	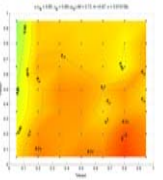
ε = 0.80	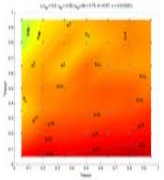	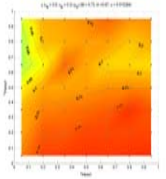	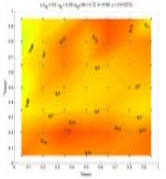	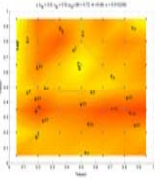	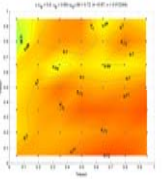	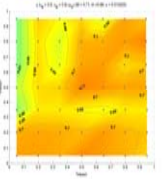	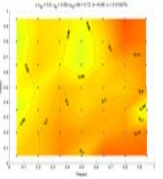
ε = 0.95	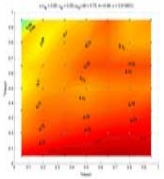	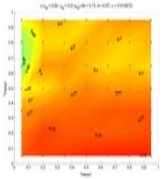	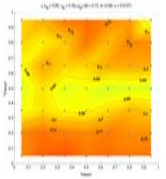	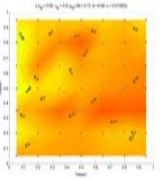	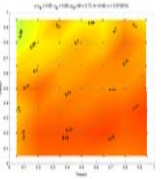	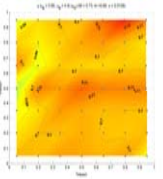	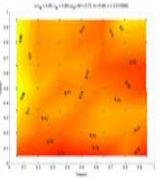

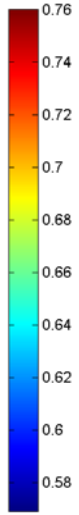

Efficiency of the baffle [%] – Main parameter: back optical properties - Specular reflection

Back	α = 0.05	α = 0.20	α = 0.35	α = 0.50	α = 0.65	α = 0.80	α = 0.95
ε = 0.05	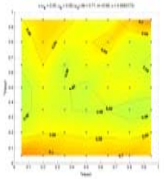	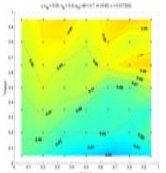	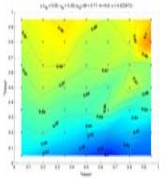	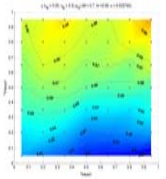	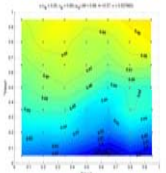	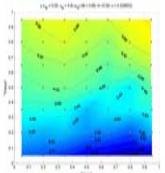	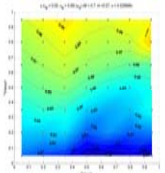
ε = 0.20	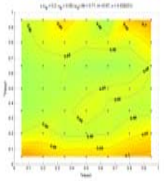	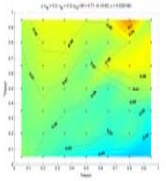	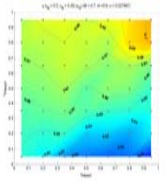	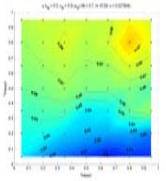	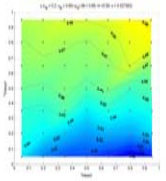	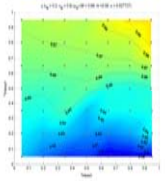	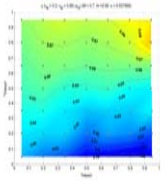
ε = 0.35	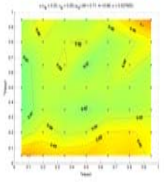	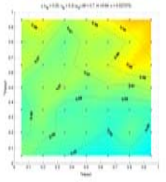	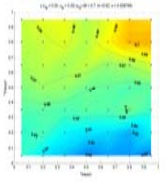	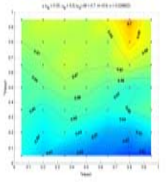	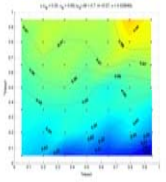	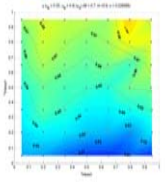	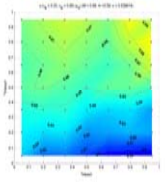
ε = 0.50	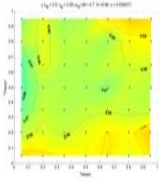	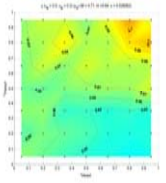	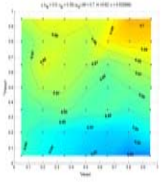	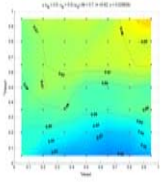	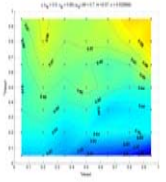	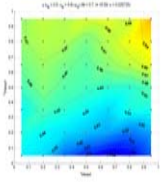	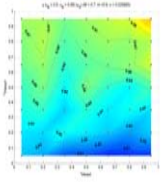
ε = 0.65	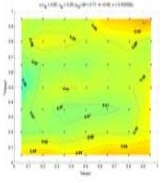	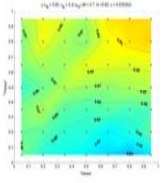	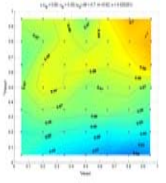	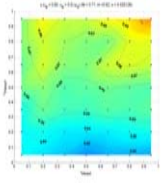	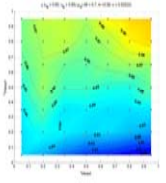	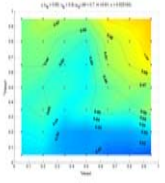	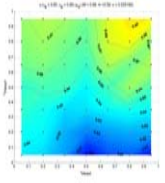
ε = 0.80	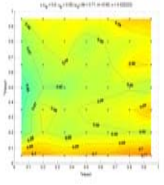	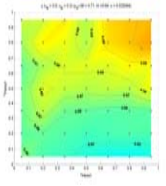	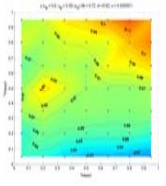	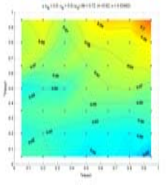	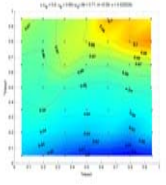	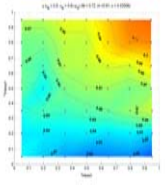	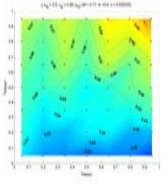
ε = 0.95	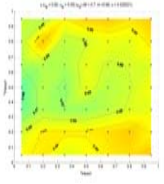	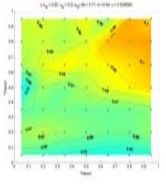	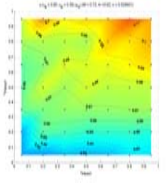	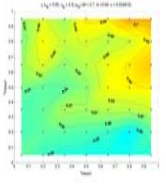	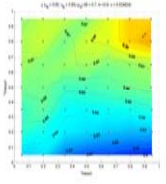	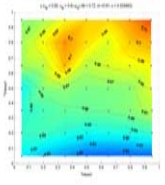	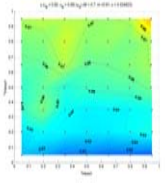

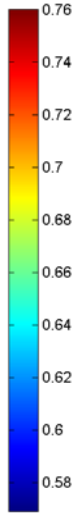

Heat fluxes to the instrument [W] – Main parameter: front optical properties - Diffusive reflection

Front	α = 0.05	α = 0.20	α = 0.35	α = 0.50	α = 0.65	α = 0.80	α = 0.95
ε = 0.05	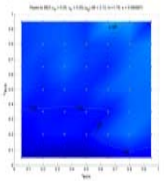	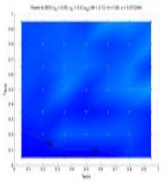	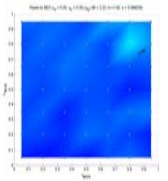	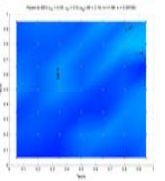	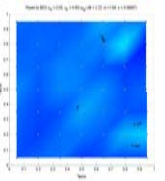	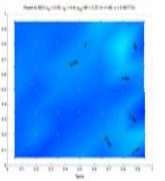	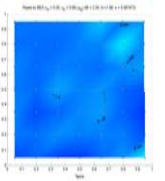
ε = 0.20	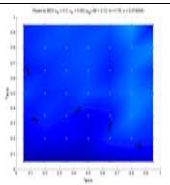	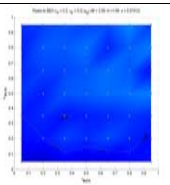	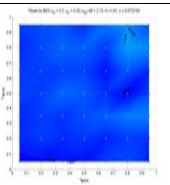	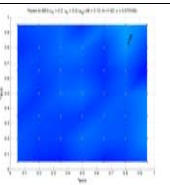	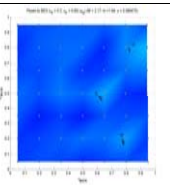	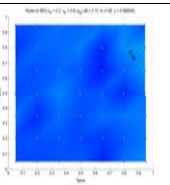	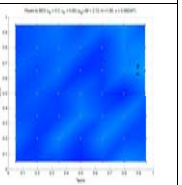
ε = 0.35	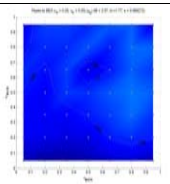	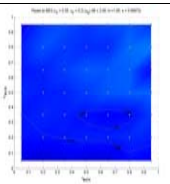	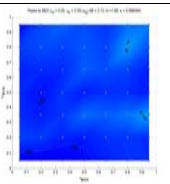	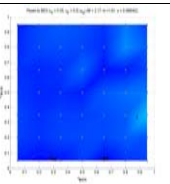	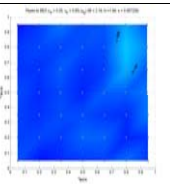	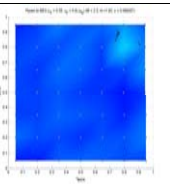	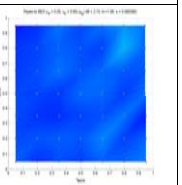
ε = 0.50	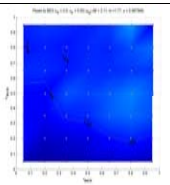	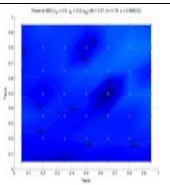	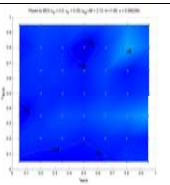	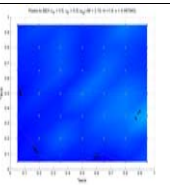	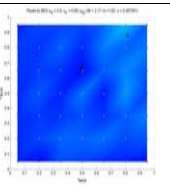	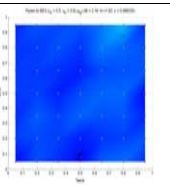	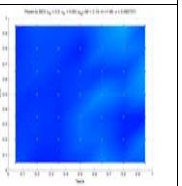
ε = 0.65	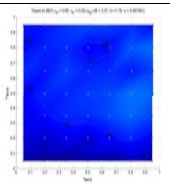	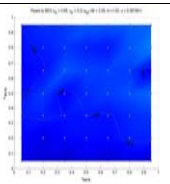	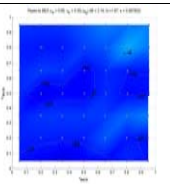	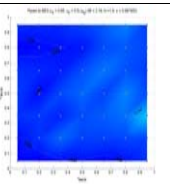	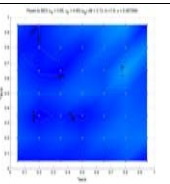	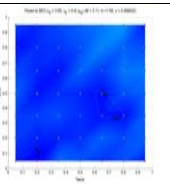	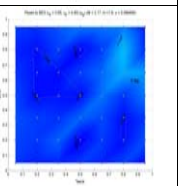
ε = 0.80	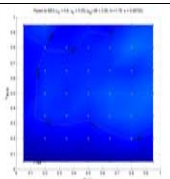	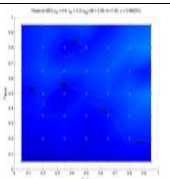	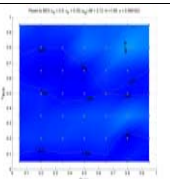	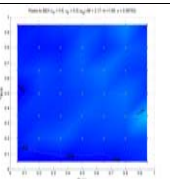	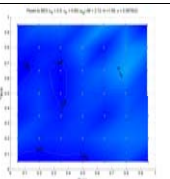	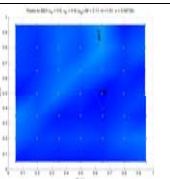	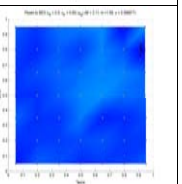
ε = 0.95	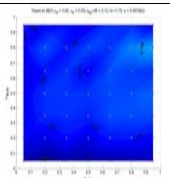	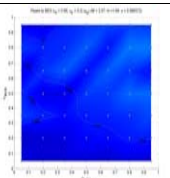	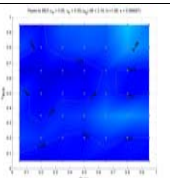	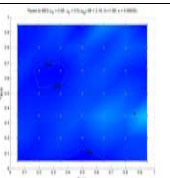	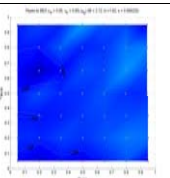	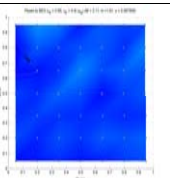	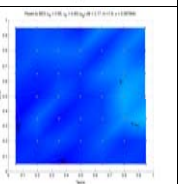

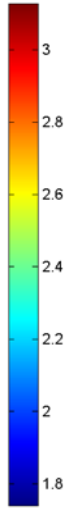

Heat fluxes to the instrument [W] – Main parameter: front optical properties - Specular reflection

Front	α = 0.05	α = 0.20	α = 0.35	α = 0.50	α = 0.65	α = 0.80	α = 0.95
ε = 0.05	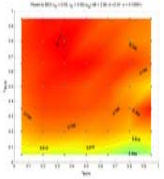	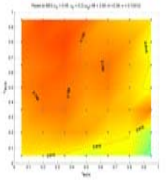	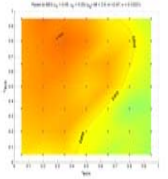	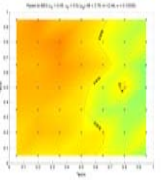	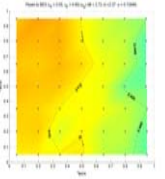	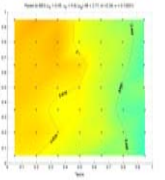	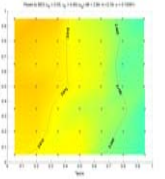
ε = 0.20	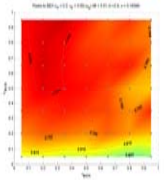	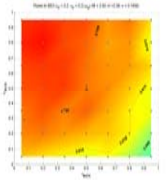	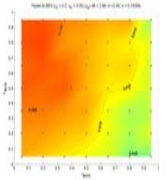	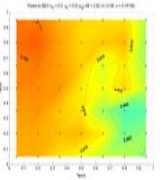	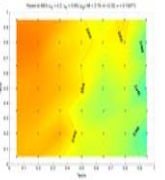	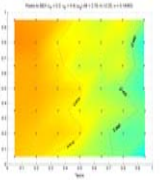	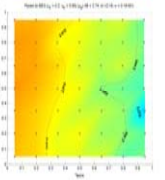
ε = 0.35	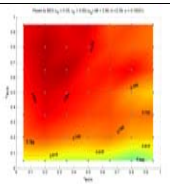	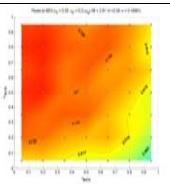	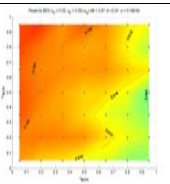	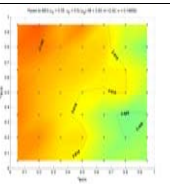	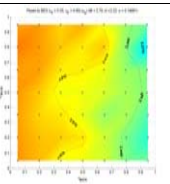	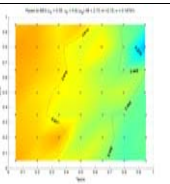	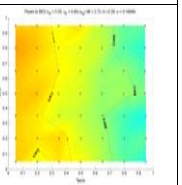
ε = 0.50	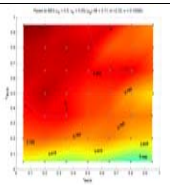	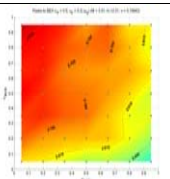	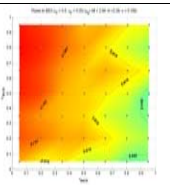	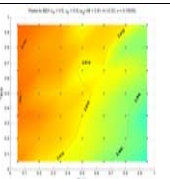	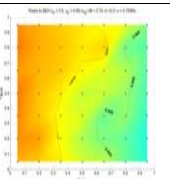	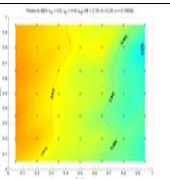	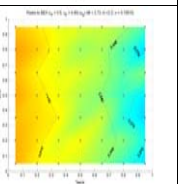
ε = 0.65	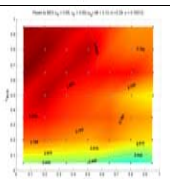	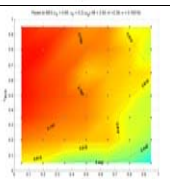	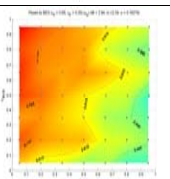	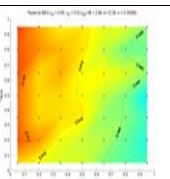	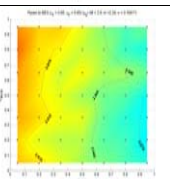	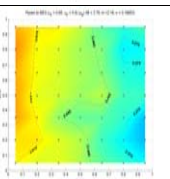	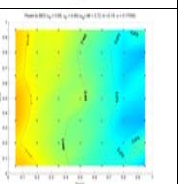
ε = 0.80	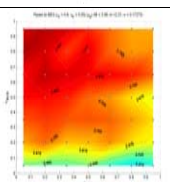	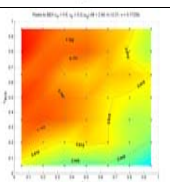	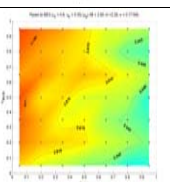	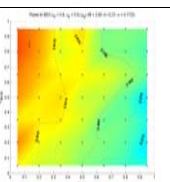	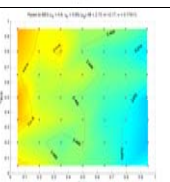	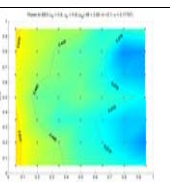	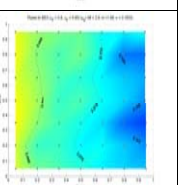
ε = 0.95	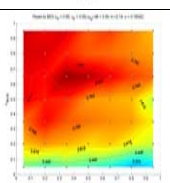	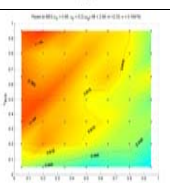	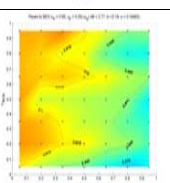	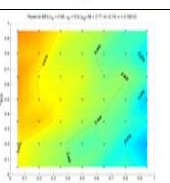	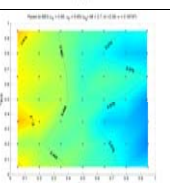	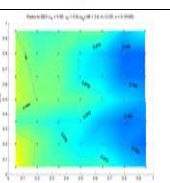	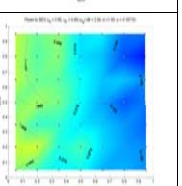

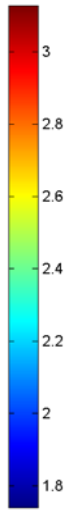

Heat fluxes to the instrument [W] – Main parameter: back optical properties - Diffusive reflection

Back	α = 0.05	α = 0.20	α = 0.35	α = 0.50	α = 0.65	α = 0.80	α = 0.95
ε = 0.05	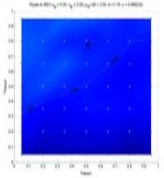	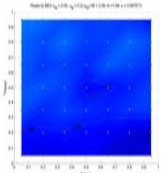	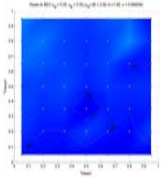			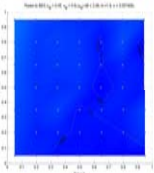	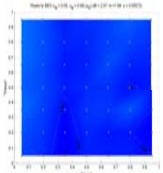
ε = 0.20	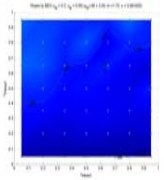	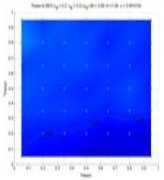	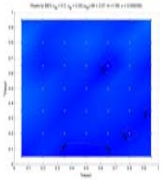	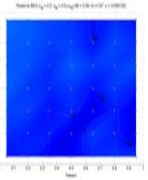	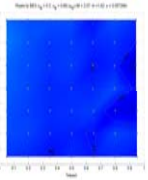	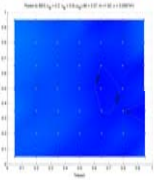	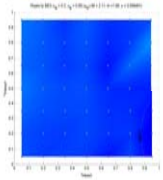
ε = 0.35	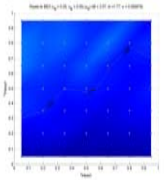	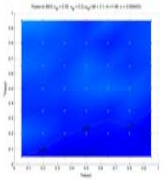	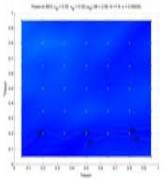	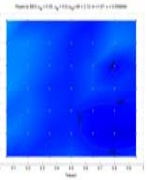	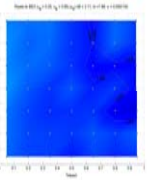	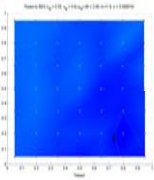	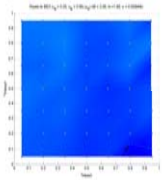
ε = 0.50	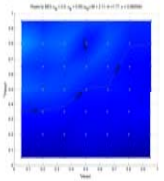	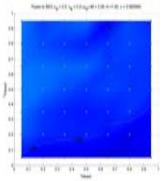	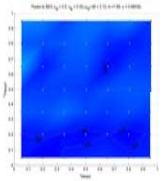	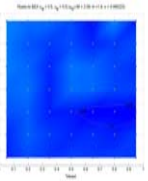	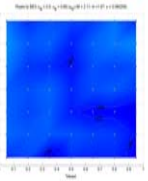	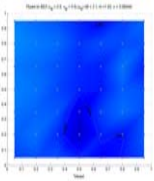	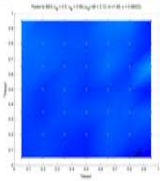
ε = 0.65	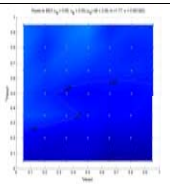	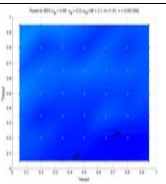	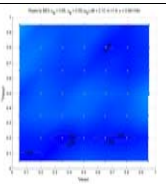	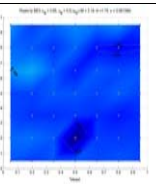	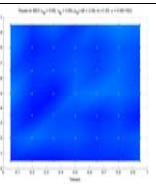	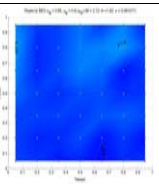	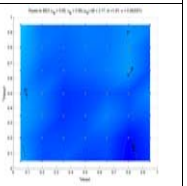
ε = 0.80	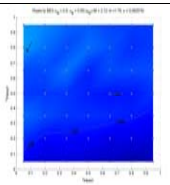	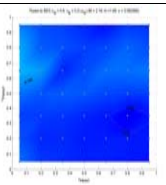	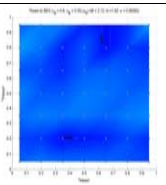	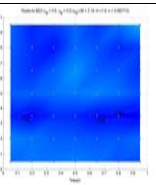	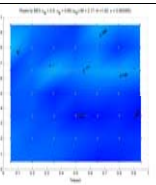	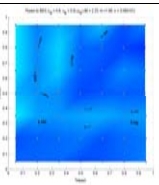	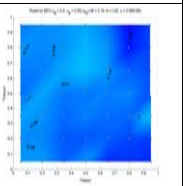
ε = 0.95	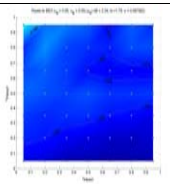	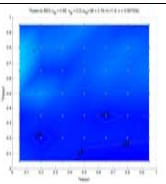	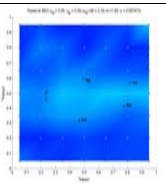	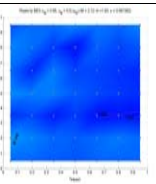	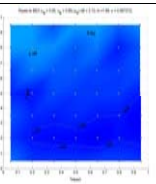	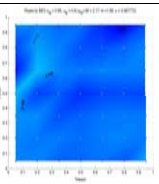	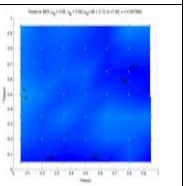

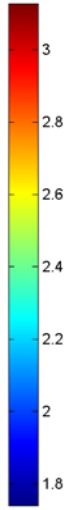

Heat fluxes to the instrument [W] – Main parameter: back optical properties – Specular reflection

Back	α = 0.05	α = 0.20	α = 0.35	α = 0.50	α = 0.65	α = 0.80	α = 0.95
ε = 0.05	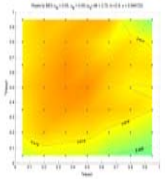	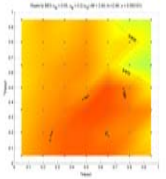	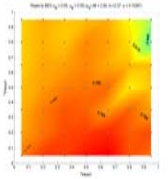	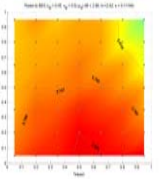	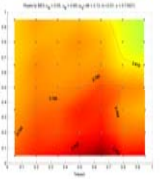	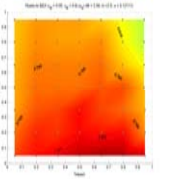	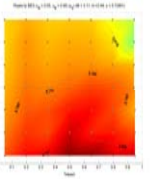
ε = 0.20	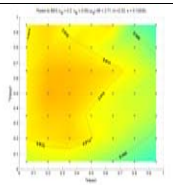	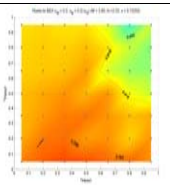	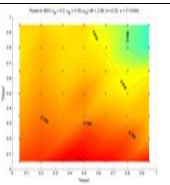	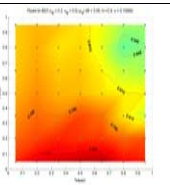	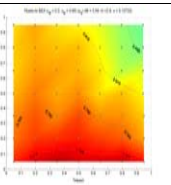	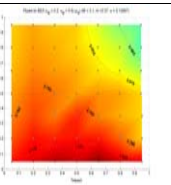	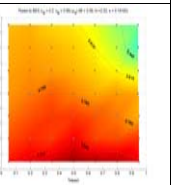
ε = 0.35	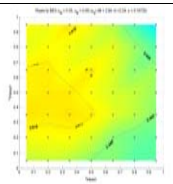	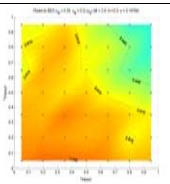	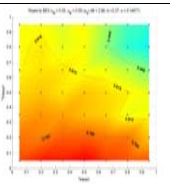	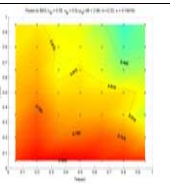	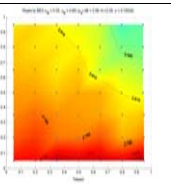	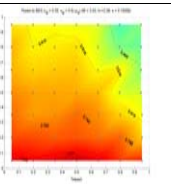	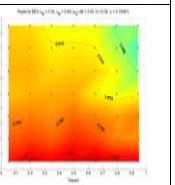
ε = 0.50	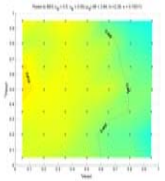	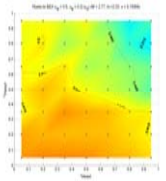	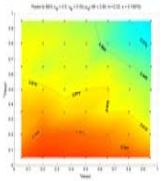	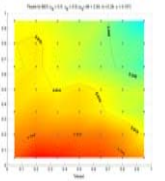	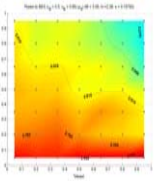	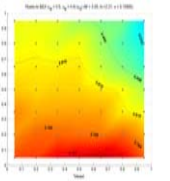	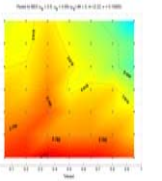
ε = 0.65	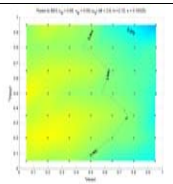	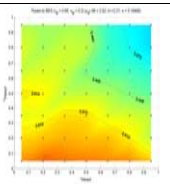	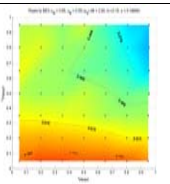	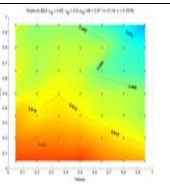	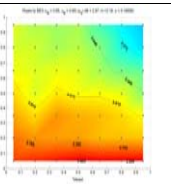	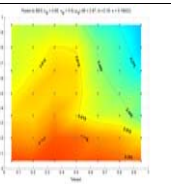	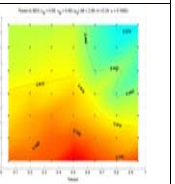
ε = 0.80	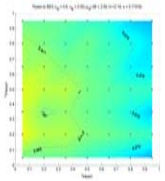	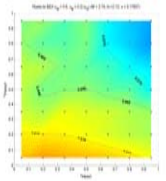	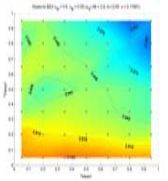	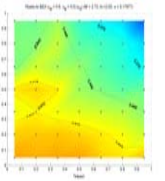	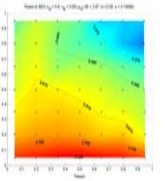	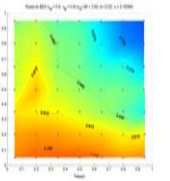	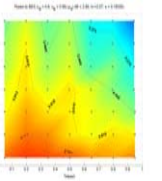
ε = 0.95	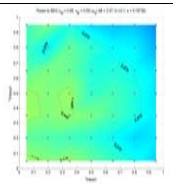	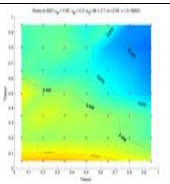	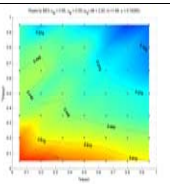	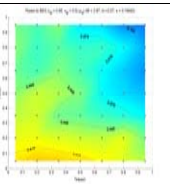	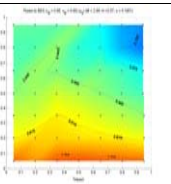	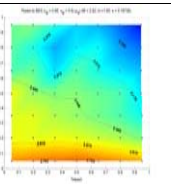	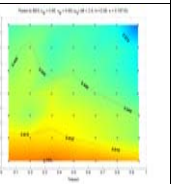

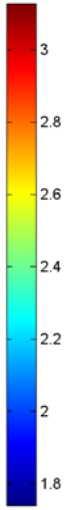

Heat fluxes to the s/c [W] – Main parameter: front optical properties - Diffusive reflection

Front	α = 0.05	α = 0.20	α = 0.35	α = 0.50	α = 0.65	α = 0.80	α = 0.95
ε = 0.05	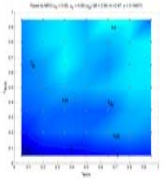	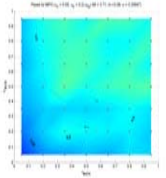	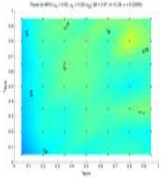	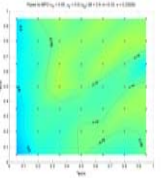	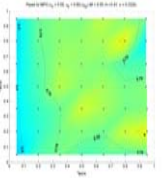	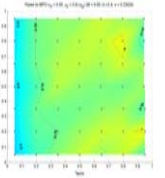	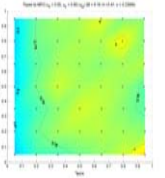
ε = 0.20	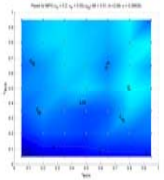	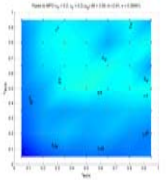	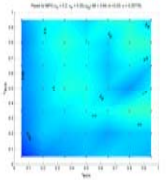	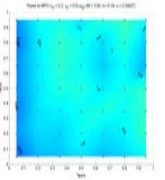	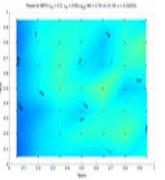	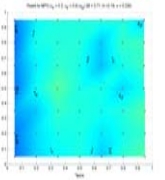	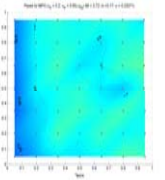
ε = 0.35	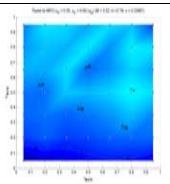	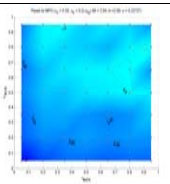	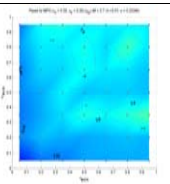	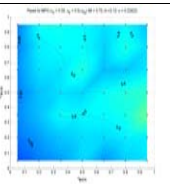	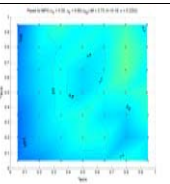	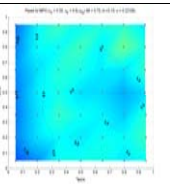	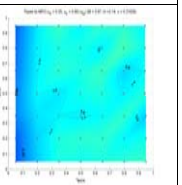
ε = 0.50	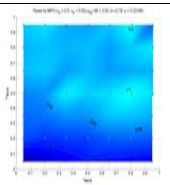	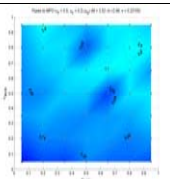	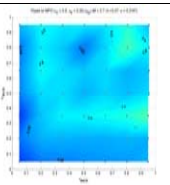	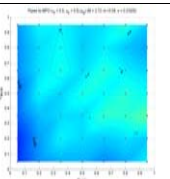	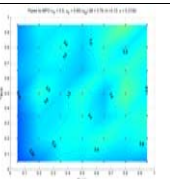	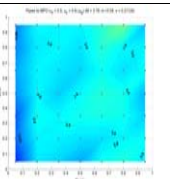	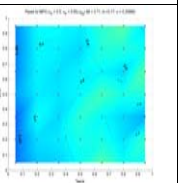
ε = 0.65	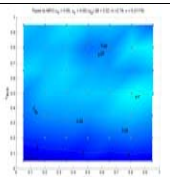	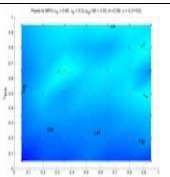	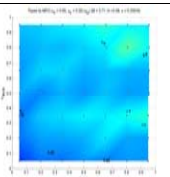	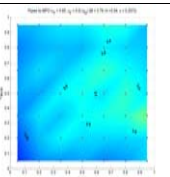	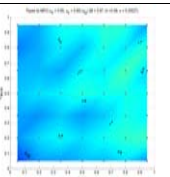	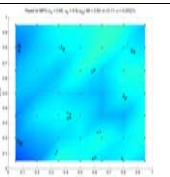	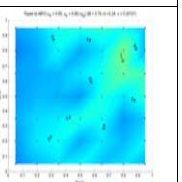
ε = 0.80	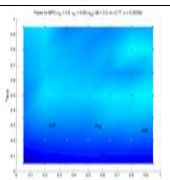	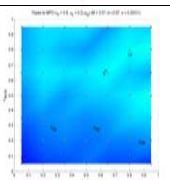	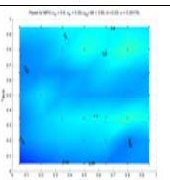	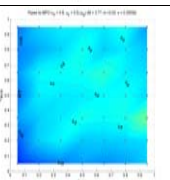	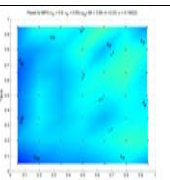	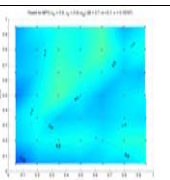	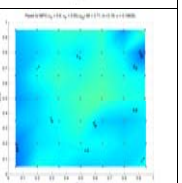
ε = 0.95	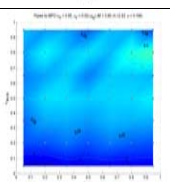	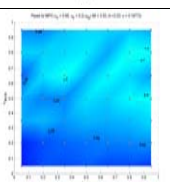	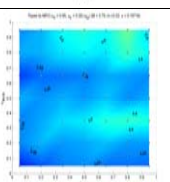	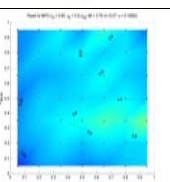	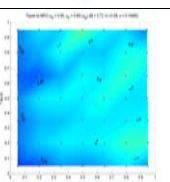	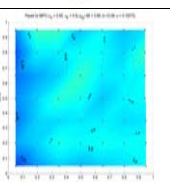	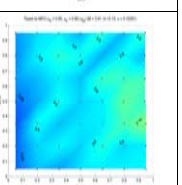

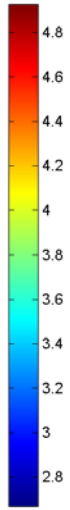

Heat fluxes to the s/c [W] – Main parameter: front optical properties - Specular reflection

Front	α = 0.05	α = 0.20	α = 0.35	α = 0.50	α = 0.65	α = 0.80	α = 0.95
ε = 0.05	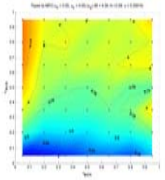	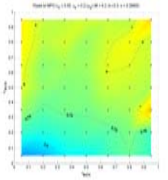	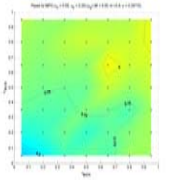	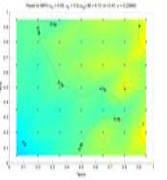	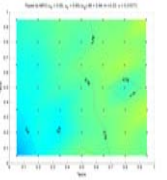	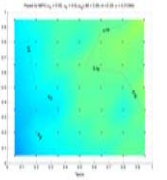	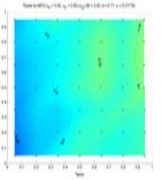
ε = 0.20	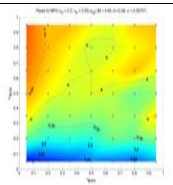	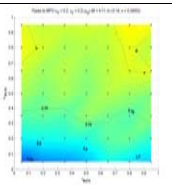	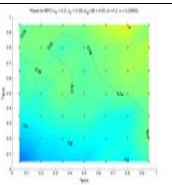	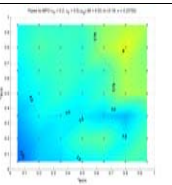	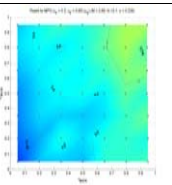	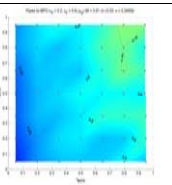	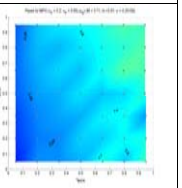
ε = 0.35	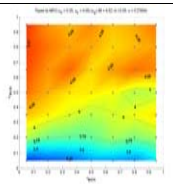	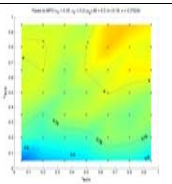	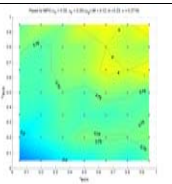	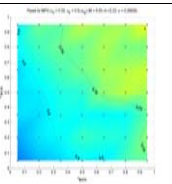	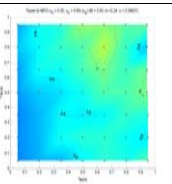	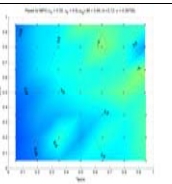	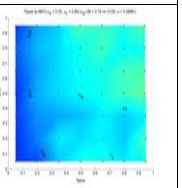
ε = 0.50	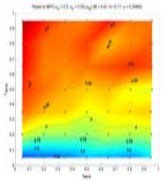	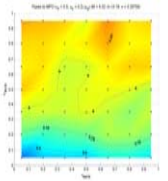	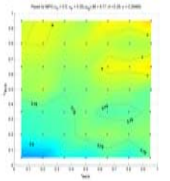	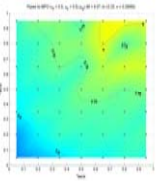	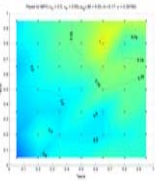	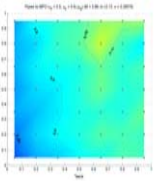	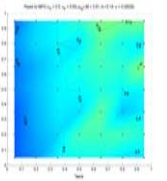
ε = 0.65	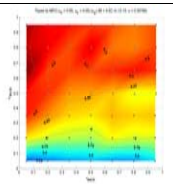	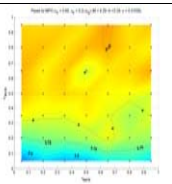	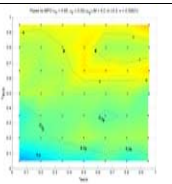	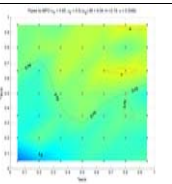	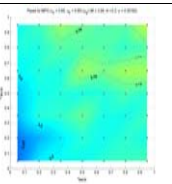	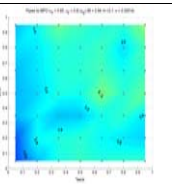	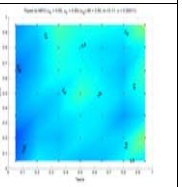
ε = 0.80	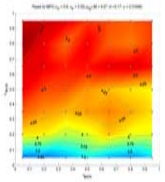	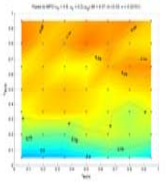	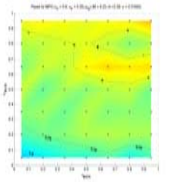	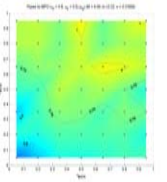	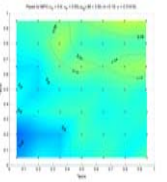	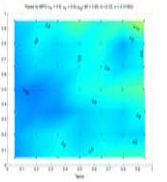	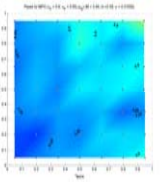
ε = 0.95	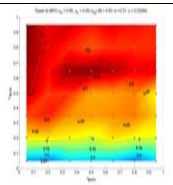	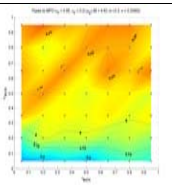	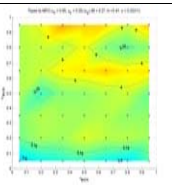	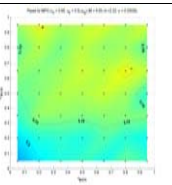	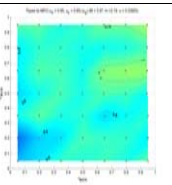	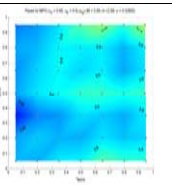	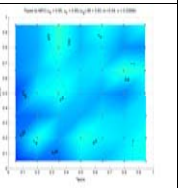

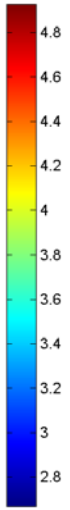

Heat fluxes to the s/c [W] – Main parameter: back optical properties - Diffusive reflection

Back	α = 0.05	α = 0.20	α = 0.35	α = 0.50	α = 0.65	α = 0.80	α = 0.95
ε = 0.05	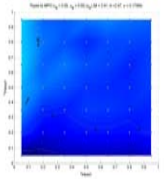	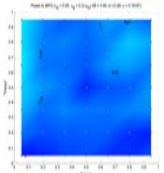	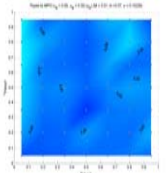	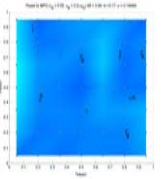	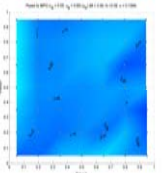	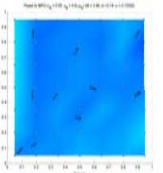	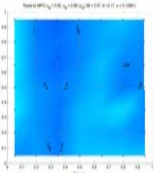
ε = 0.20	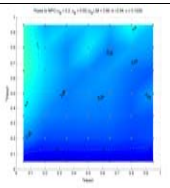	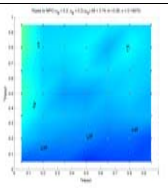	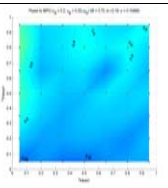	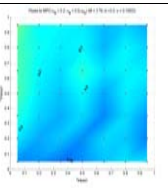	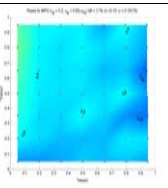	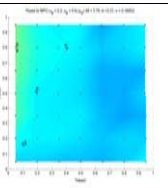	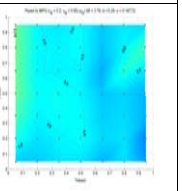
ε = 0.35	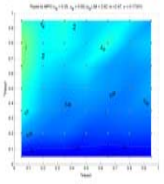	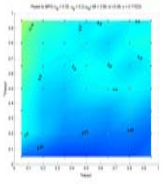	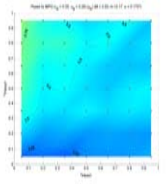	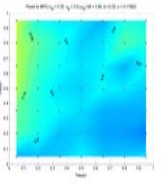	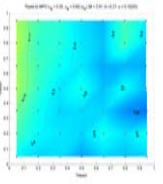	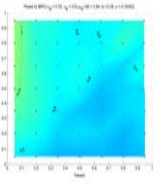	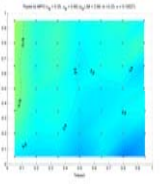
ε = 0.50	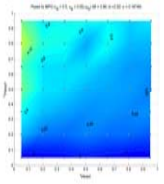	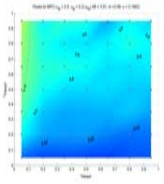	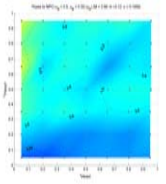	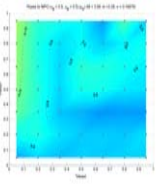	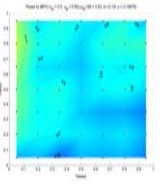	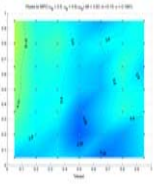	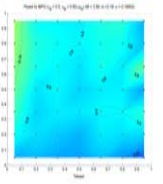
ε = 0.65	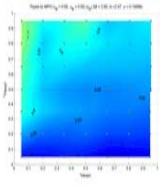	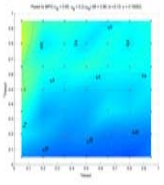	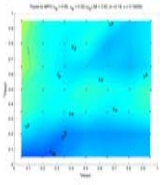	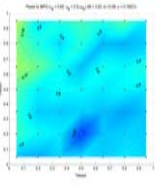	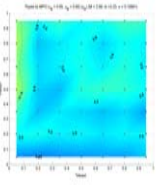	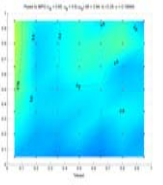	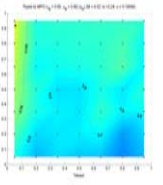
ε = 0.80	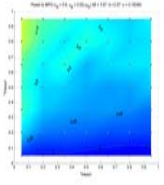	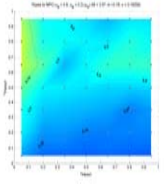	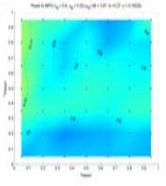	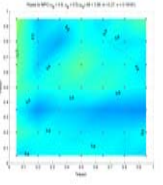	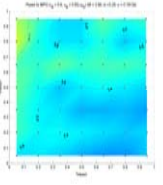	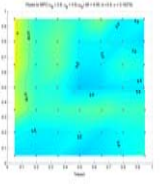	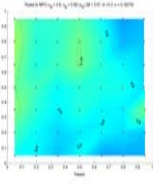
ε = 0.95	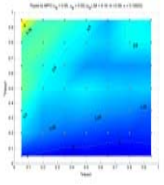	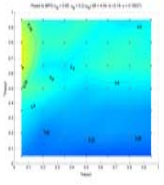	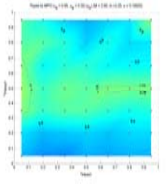	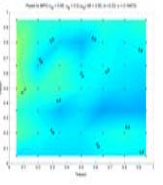	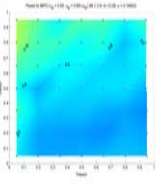	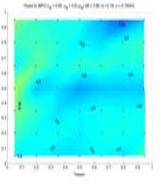	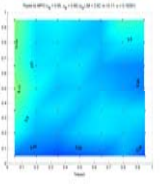

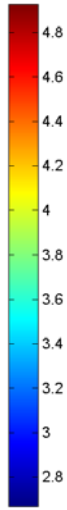

Heat fluxes to the s/c [W] – Main parameter: back optical properties – Specular reflection

Back	α = 0.05	α = 0.20	α = 0.35	α = 0.50	α = 0.65	α = 0.80	α = 0.95
ε = 0.05	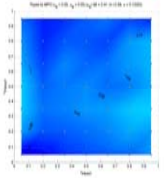	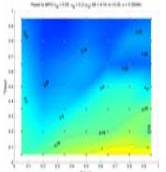	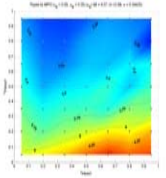	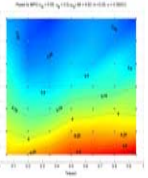	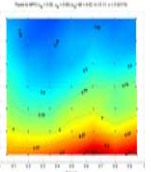	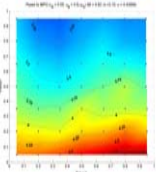	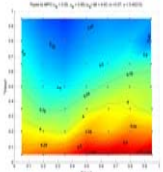
ε = 0.20	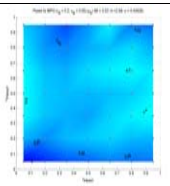	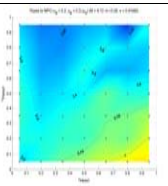	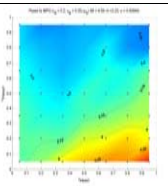	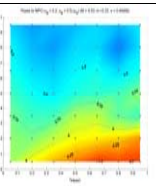	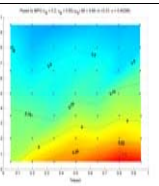	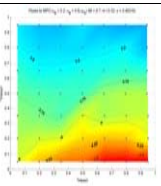	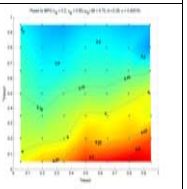
ε = 0.35	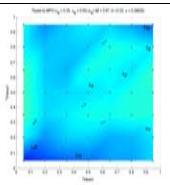	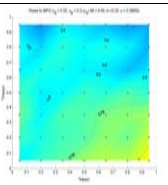	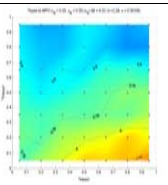	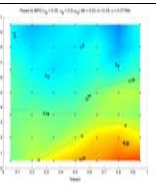	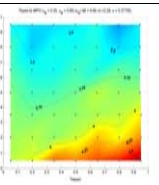	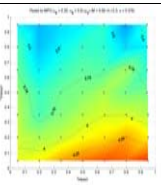	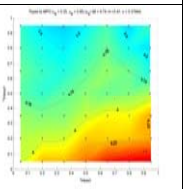
ε = 0.50	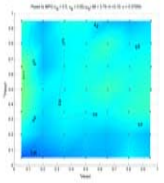	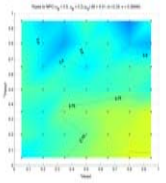	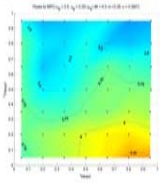	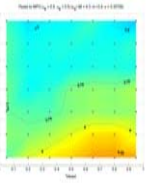	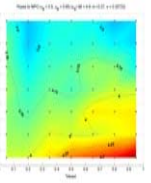	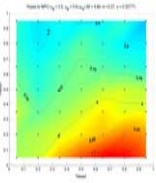	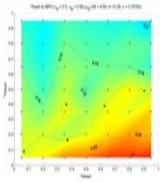
ε = 0.65	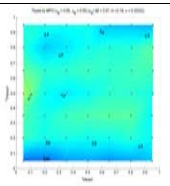	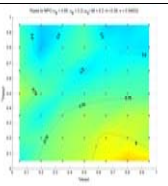	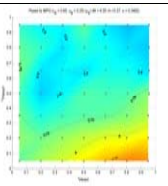	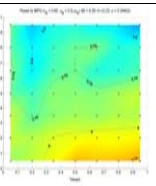	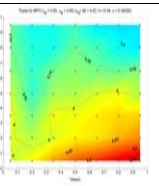	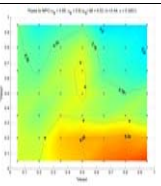	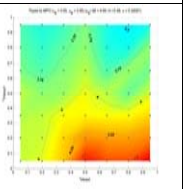
ε = 0.80	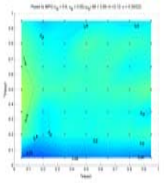	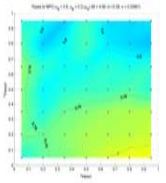	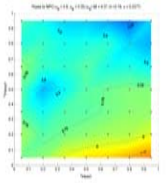	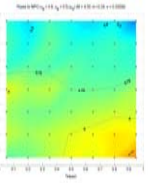	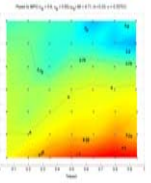	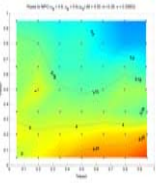	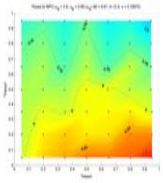
ε = 0.95	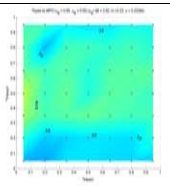	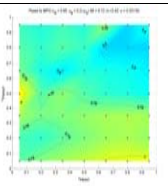	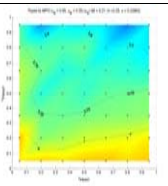	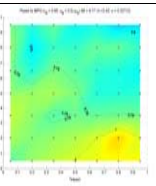	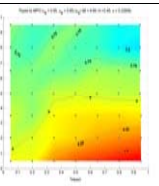	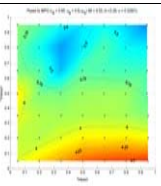	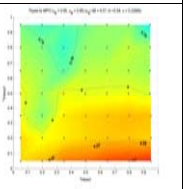

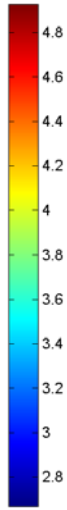

Baffle max temperature [°C] – Main parameter: front optical properties - Diffusive reflection

Front	α = 0.05	α = 0.20	α = 0.35	α = 0.50	α = 0.65	α = 0.80	α = 0.95
ε = 0.05	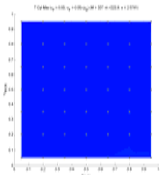	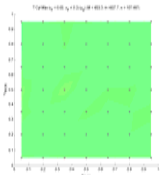	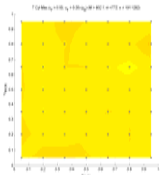	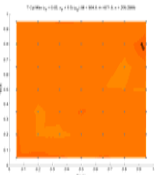	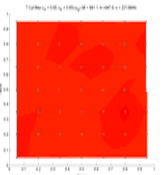	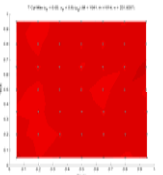	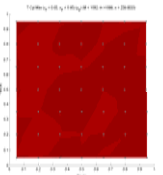
ε = 0.20	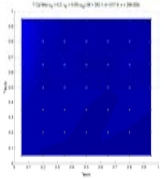	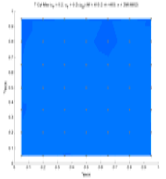	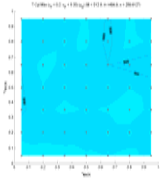	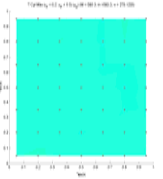	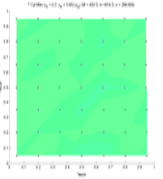	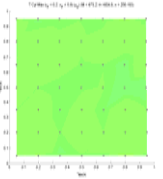	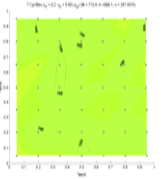
ε = 0.35	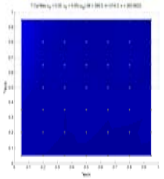	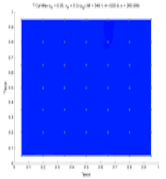	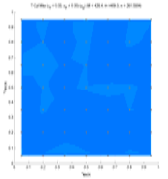	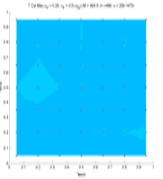	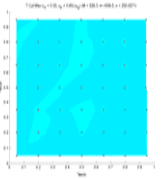	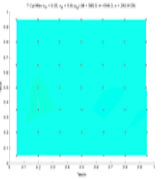	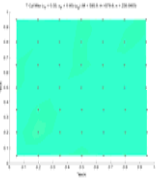
ε = 0.50	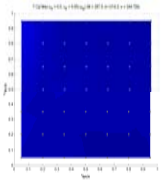	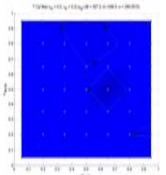	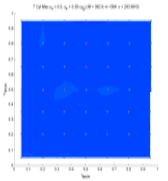	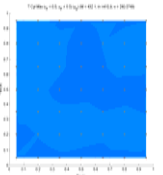	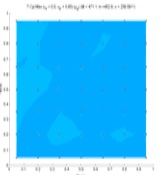	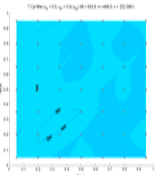	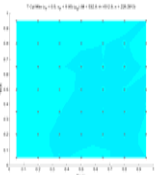
ε = 0.65	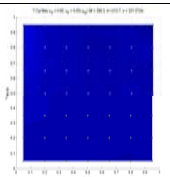	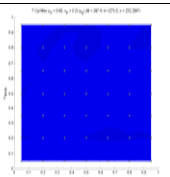	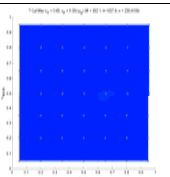	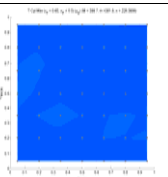	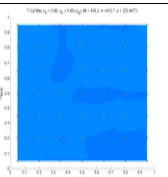	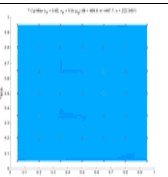	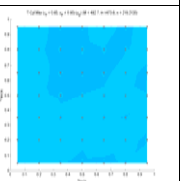
ε = 0.80	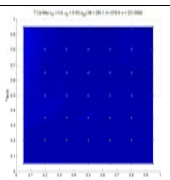	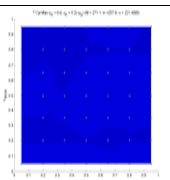	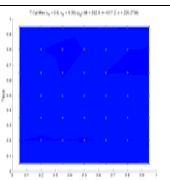	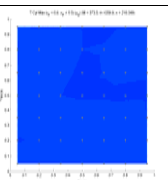	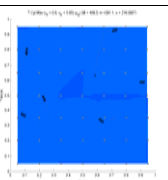	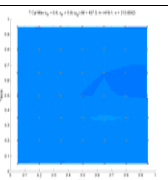	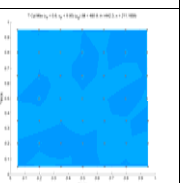
ε = 0.95	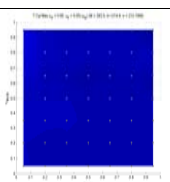	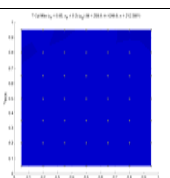	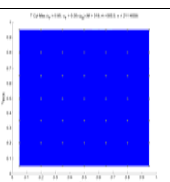	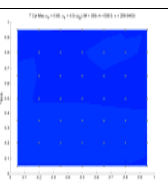	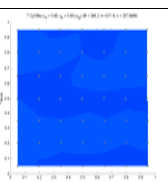	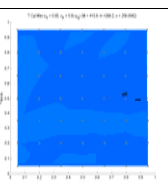	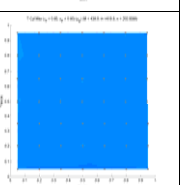

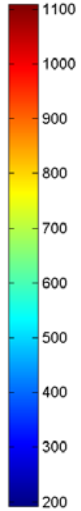

Baffle max temperature [°C] – Main parameter: front optical properties - Specular reflection

Front	α = 0.05	α = 0.20	α = 0.35	α = 0.50	α = 0.65	α = 0.80	α = 0.95
ε = 0.05	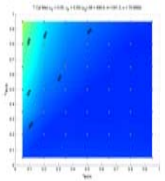	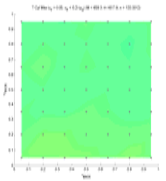	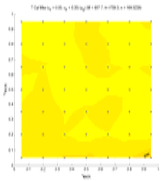	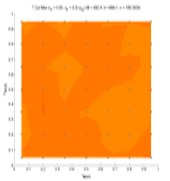	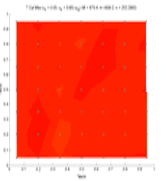	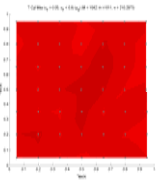	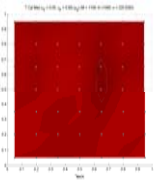
ε = 0.20	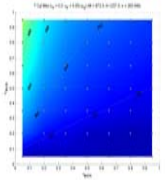	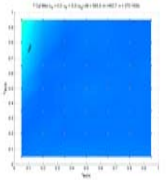	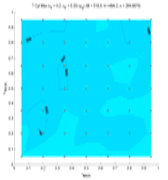	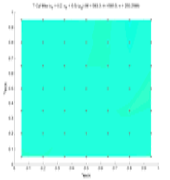	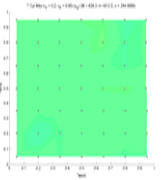	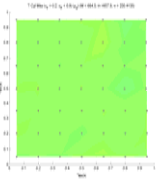	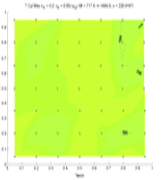
ε = 0.35	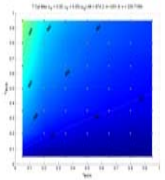	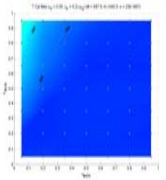	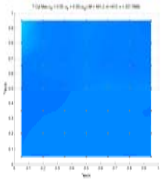	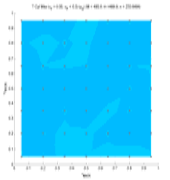	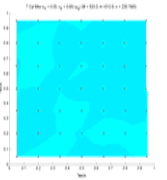	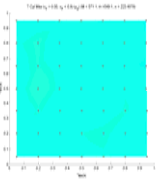	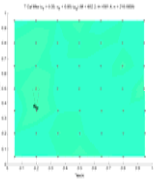
ε = 0.50	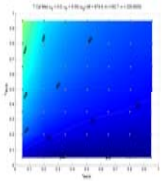	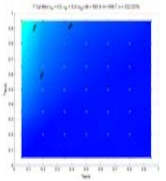	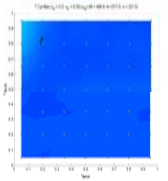	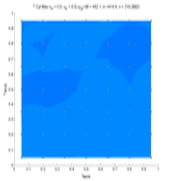	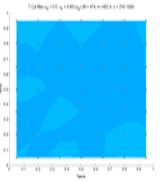	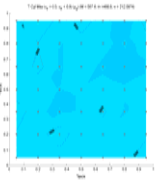	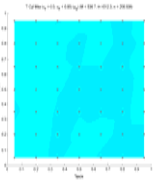
ε = 0.65	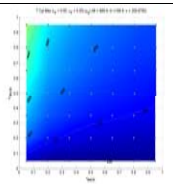	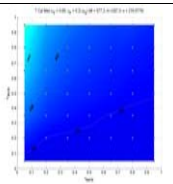	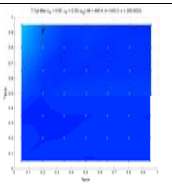	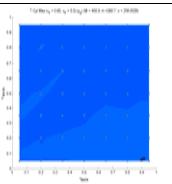	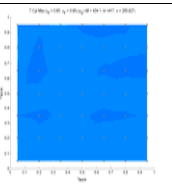	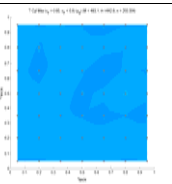	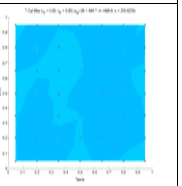
ε = 0.80	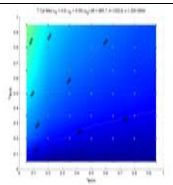	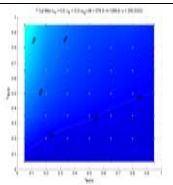	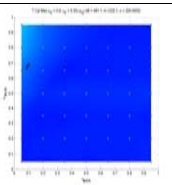	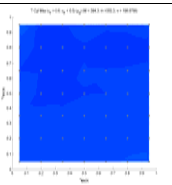	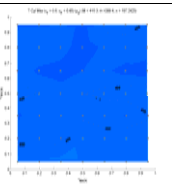	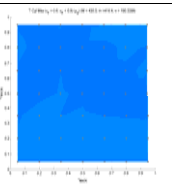	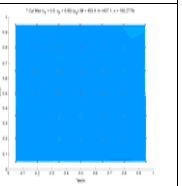
ε = 0.95	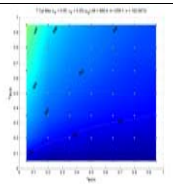	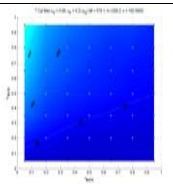	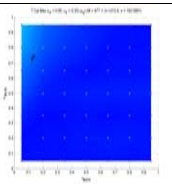	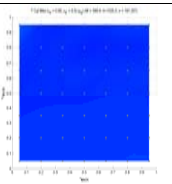	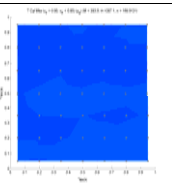	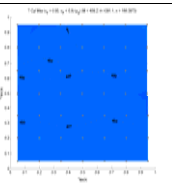	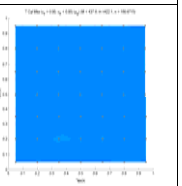

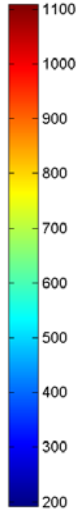

Baffle max temperature [°C] – Main parameter: back optical properties - Diffusive reflection

Back	α = 0.05	α = 0.20	α = 0.35	α = 0.50	α = 0.65	α = 0.80	α = 0.95
ε = 0.05	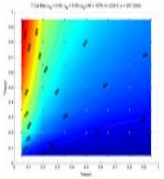	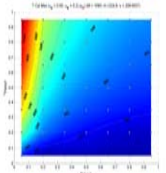	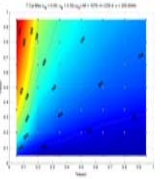	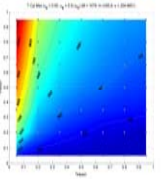	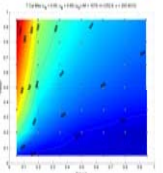	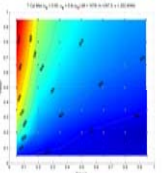	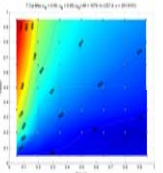
ε = 0.20	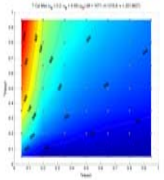	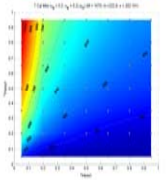	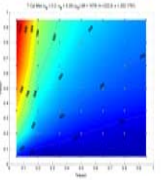	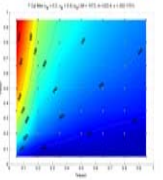	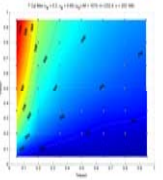	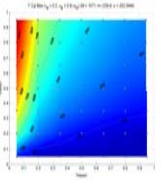	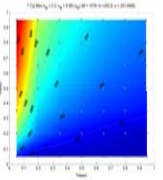
ε = 0.35	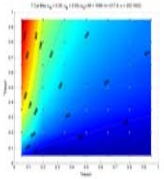	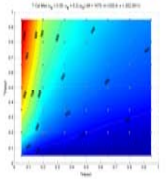	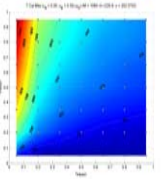	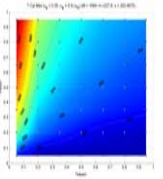	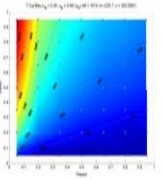	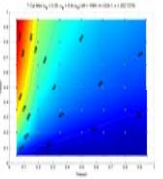	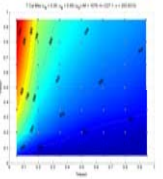
ε = 0.50	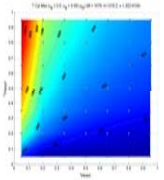	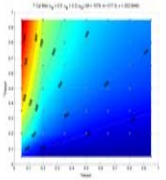	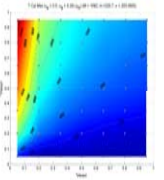	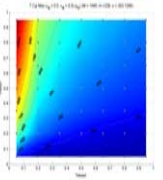	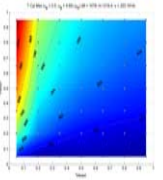	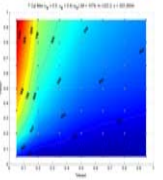	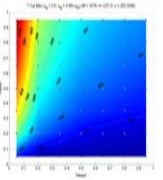
ε = 0.65	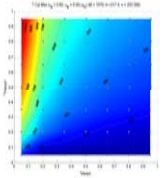	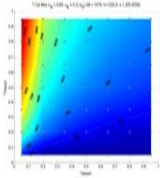	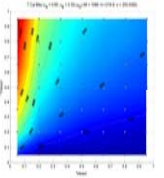	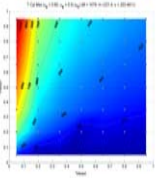	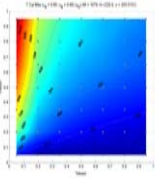	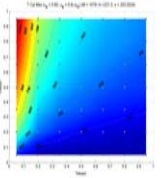	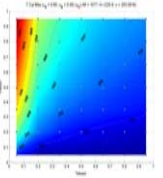
ε = 0.80	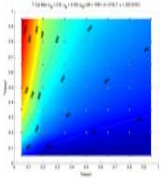	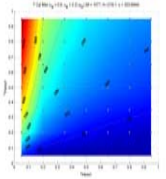	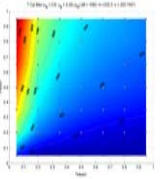	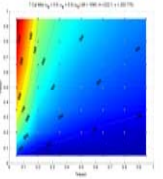	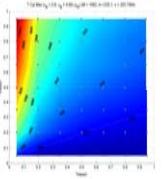	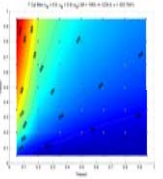	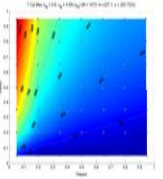
ε = 0.95	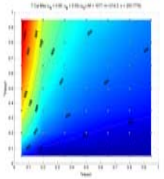	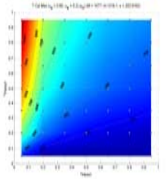	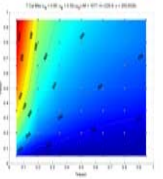	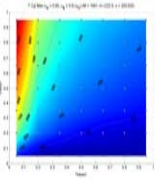	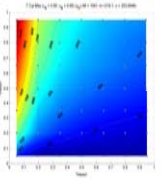	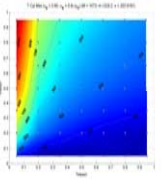	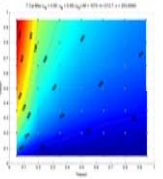

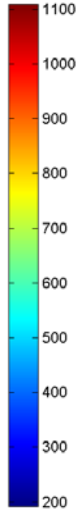

Baffle max temperature [°C] – Main parameter: back optical properties - Specular reflection

Back	α = 0.05	α = 0.20	α = 0.35	α = 0.50	α = 0.65	α = 0.80	α = 0.95
ε = 0.05	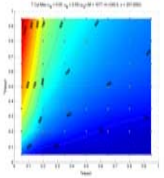	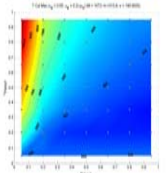	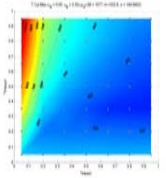	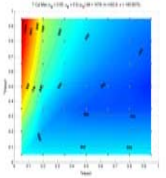	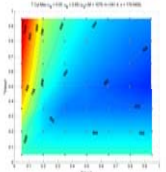	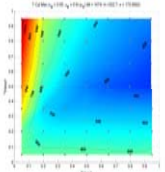	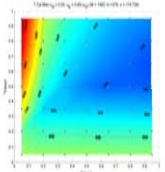
ε = 0.20	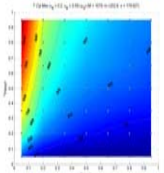	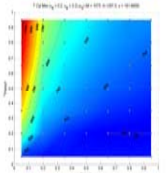	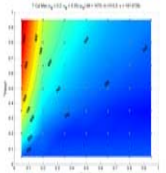	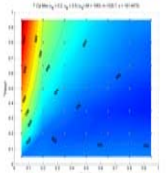	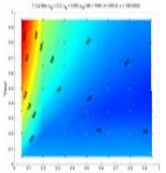	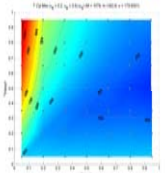	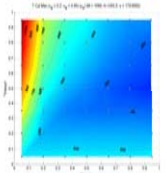
ε = 0.35	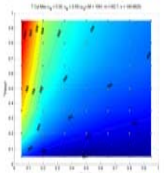	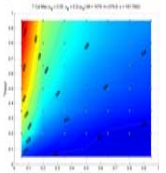	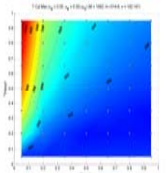	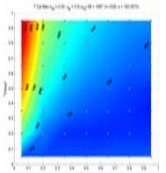	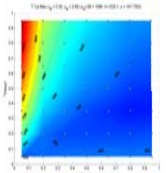	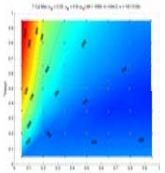	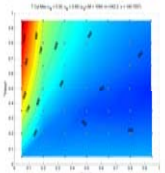
ε = 0.50	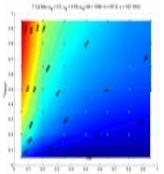	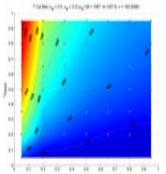	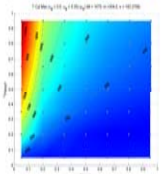	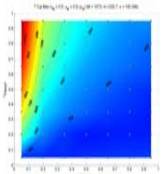	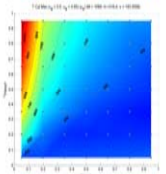	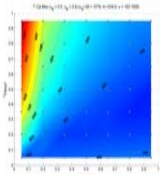	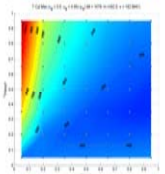
ε = 0.65	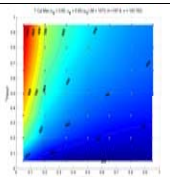	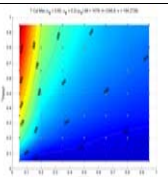	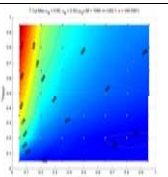	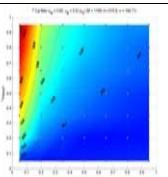	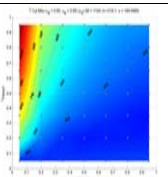	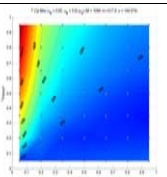	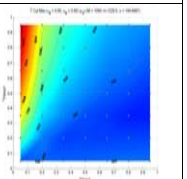
ε = 0.80	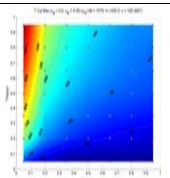	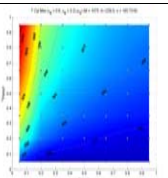	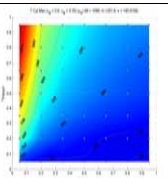	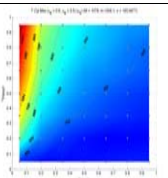	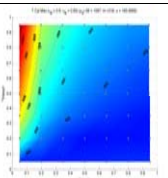	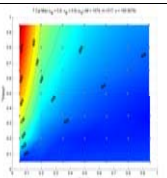	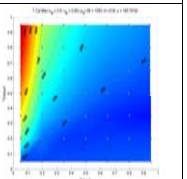
ε = 0.95	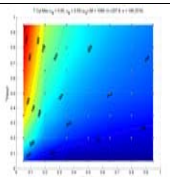	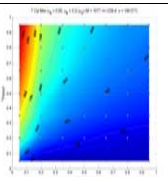	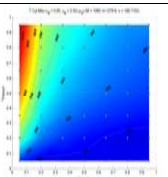	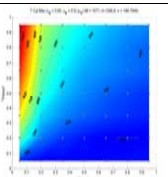	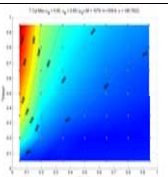	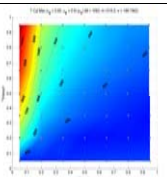	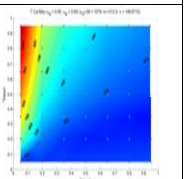

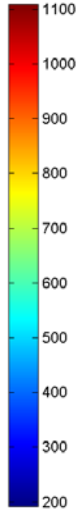

Filter max temperature [°C] – Main parameter: front optical properties - Diffusive reflection

Front	α = 0.05	α = 0.20	α = 0.35	α = 0.50	α = 0.65	α = 0.80	α = 0.95
ε = 0.05	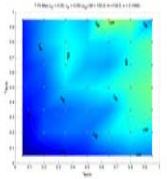	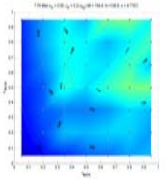	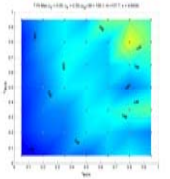	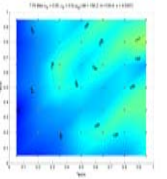	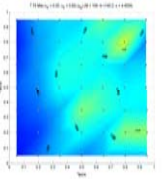	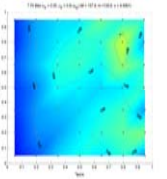	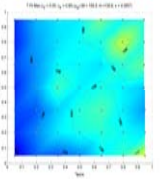
ε = 0.20	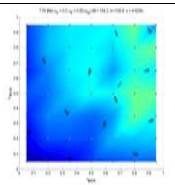	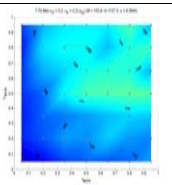	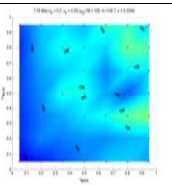	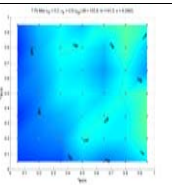	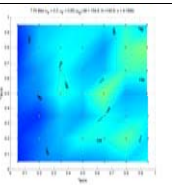	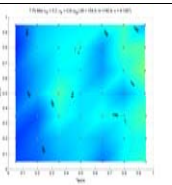	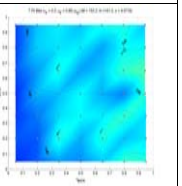
ε = 0.35	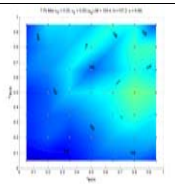	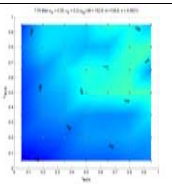	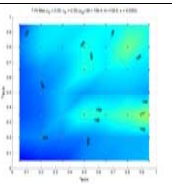	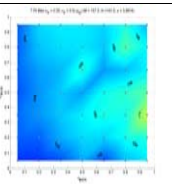	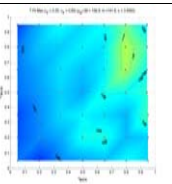	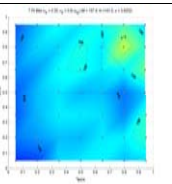	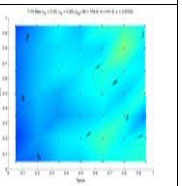
ε = 0.50	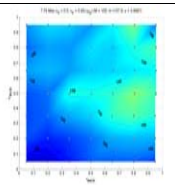	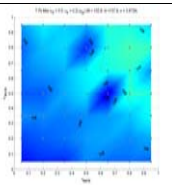	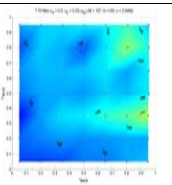	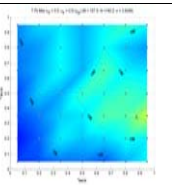	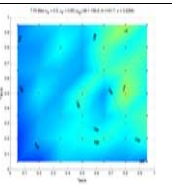	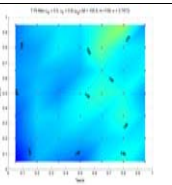	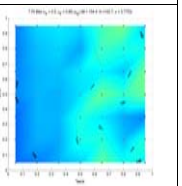
ε = 0.65	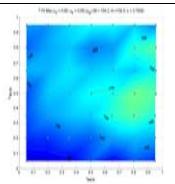	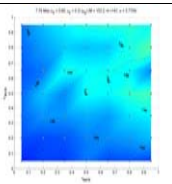	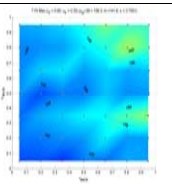	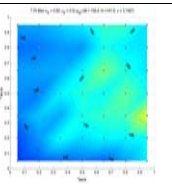	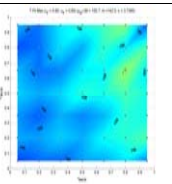	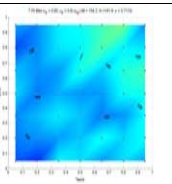	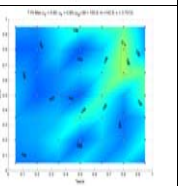
ε = 0.80	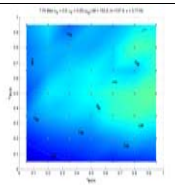	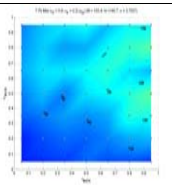	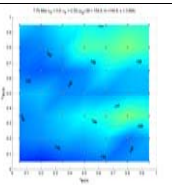	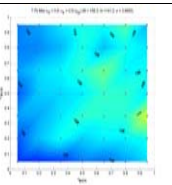	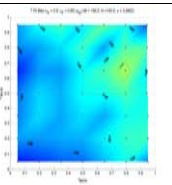	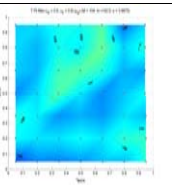	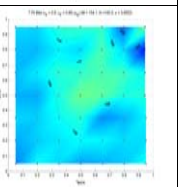
ε = 0.95	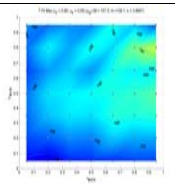	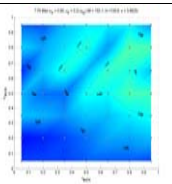	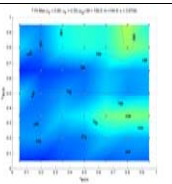	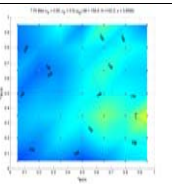	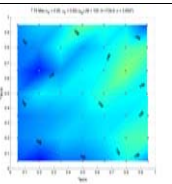	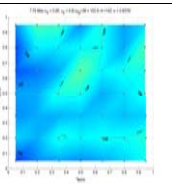	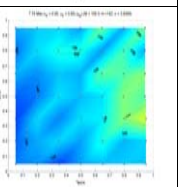

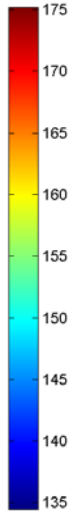

Filter max temperature [°C] – Main parameter: front optical properties - Specular reflection

Front	α = 0.05	α = 0.20	α = 0.35	α = 0.50	α = 0.65	α = 0.80	α = 0.95
ε = 0.05	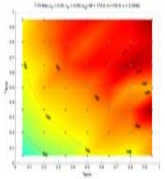	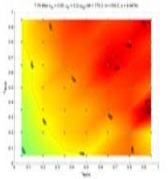	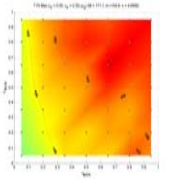	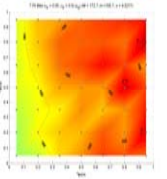	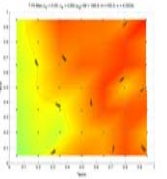	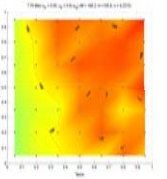	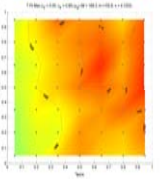
ε = 0.20	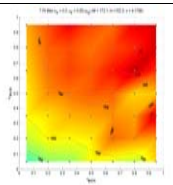	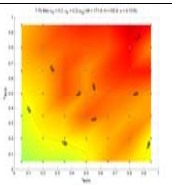	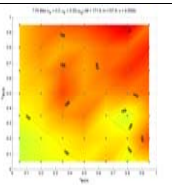	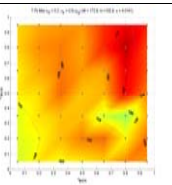	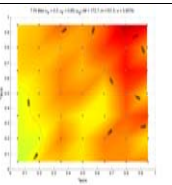	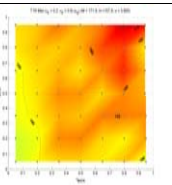	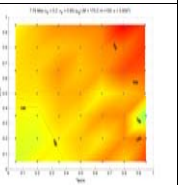
ε = 0.35	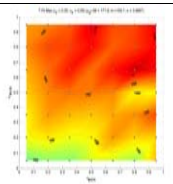	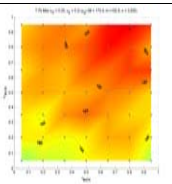	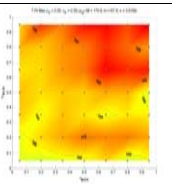	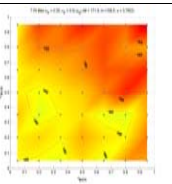	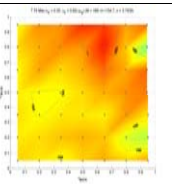	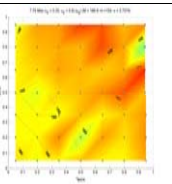	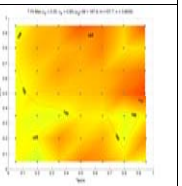
ε = 0.50	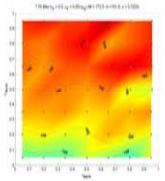	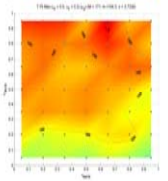	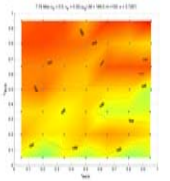	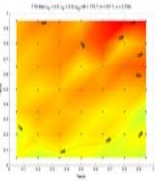	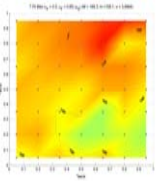	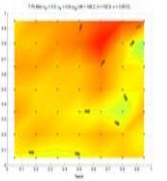	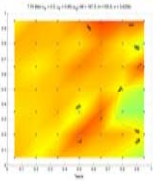
ε = 0.65	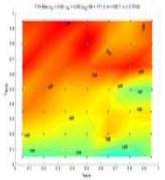	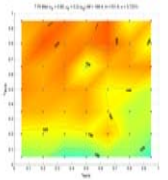	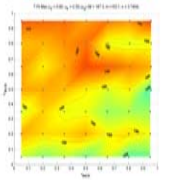	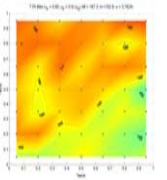	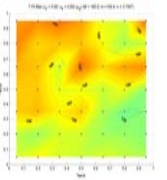	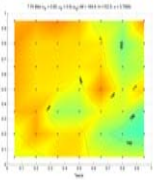	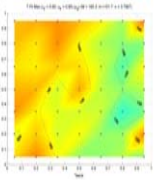
ε = 0.80	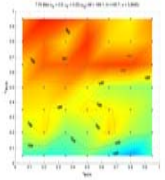	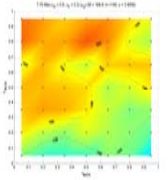	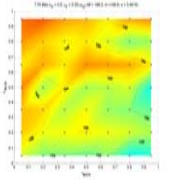	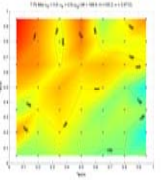	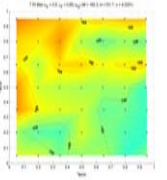	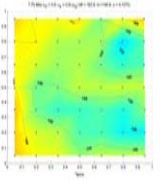	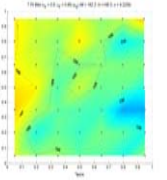
ε = 0.95	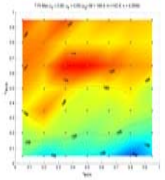	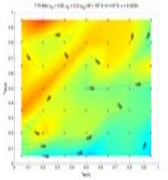	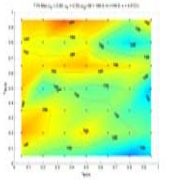	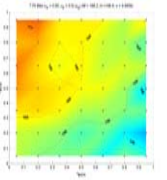	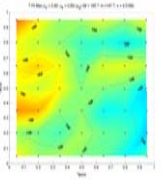	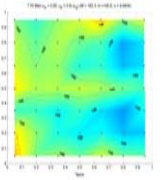	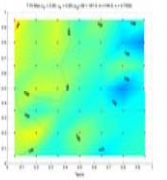

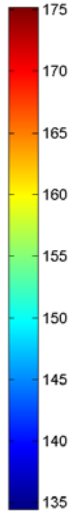

Filter max temperature [°C] – Main parameter: back optical properties - Diffusive reflection

Back	α = 0.05	α = 0.20	α = 0.35	α = 0.50	α = 0.65	α = 0.80	α = 0.95
ε = 0.05	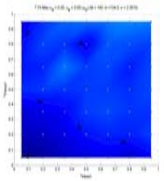	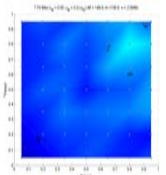	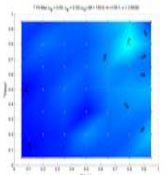	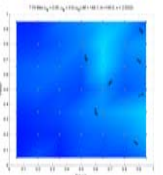	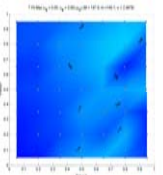	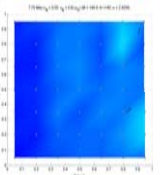	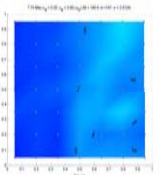
ε = 0.20	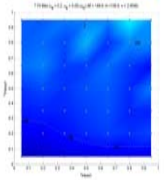	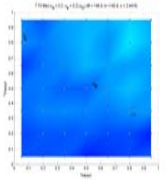	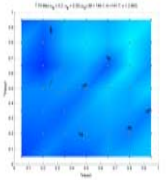	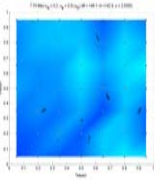	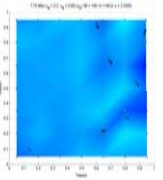	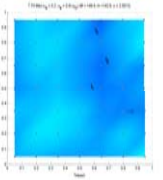	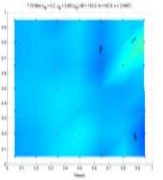
ε = 0.35	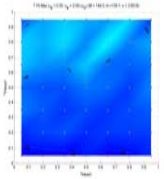	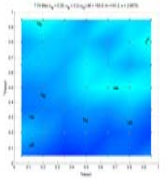	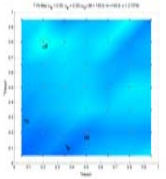	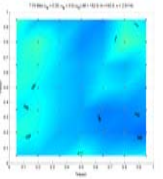	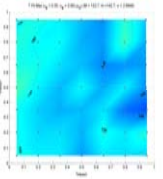	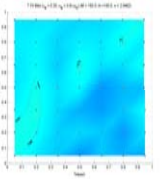	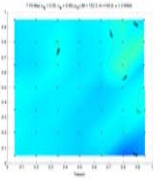
ε = 0.50	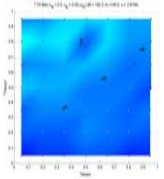	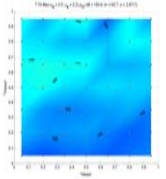	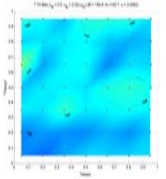	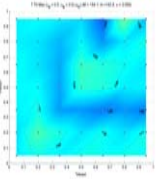	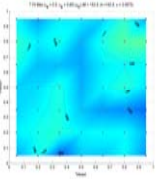	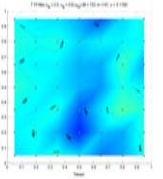	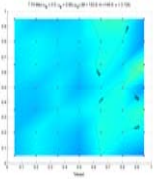
ε = 0.65	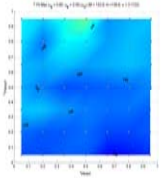	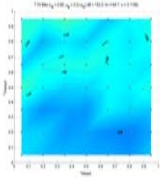	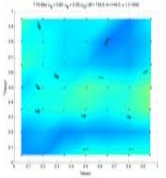	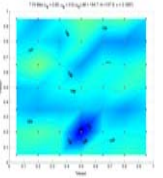	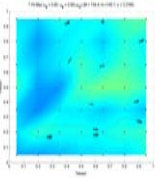	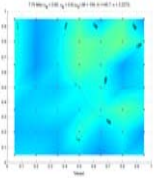	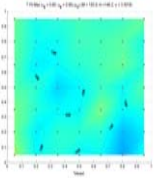
ε = 0.80	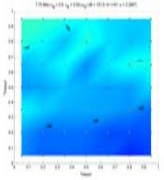	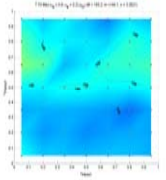	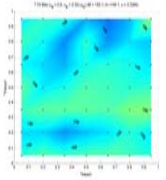	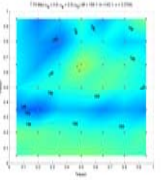	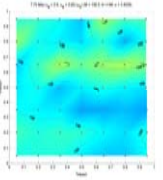	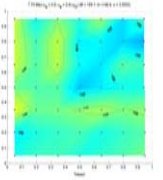	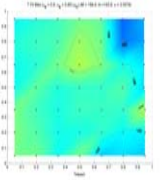
ε = 0.95	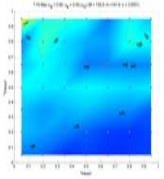	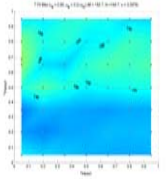	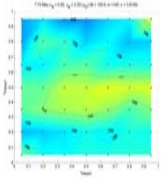	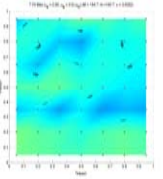	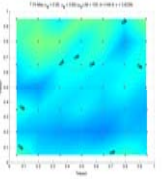	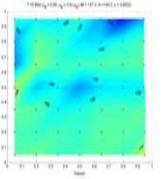	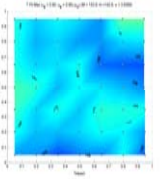

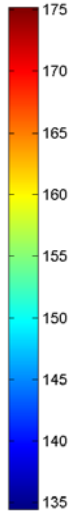

Filter max temperature [°C] – Main parameter: back optical properties - Specular reflection

Back	α = 0.05	α = 0.20	α = 0.35	α = 0.50	α = 0.65	α = 0.80	α = 0.95
ε = 0.05	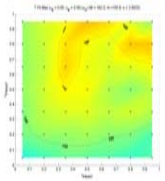	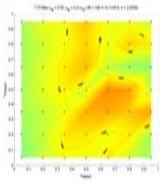	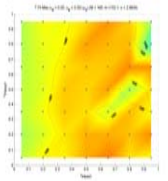	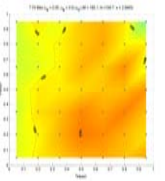	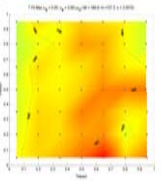	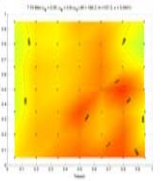	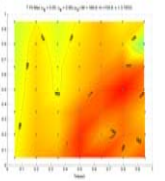
ε = 0.20	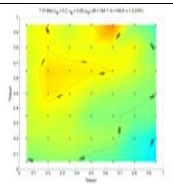	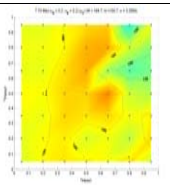	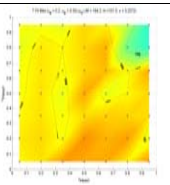	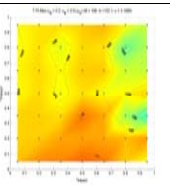	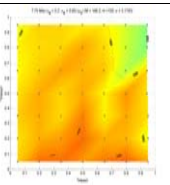	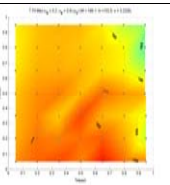	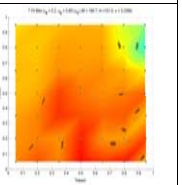
ε = 0.35	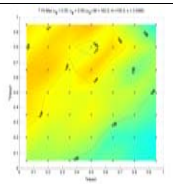	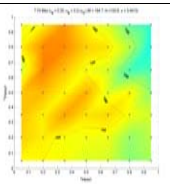	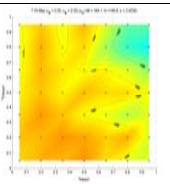	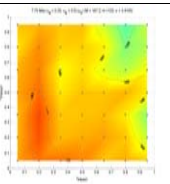	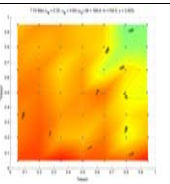	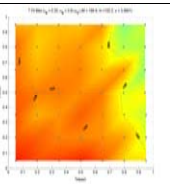	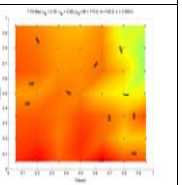
ε = 0.50	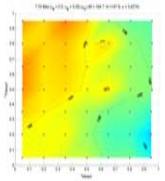	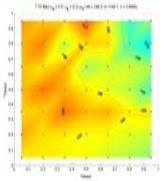	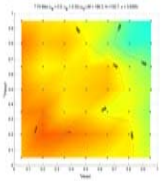	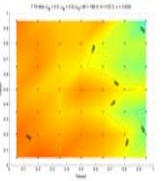	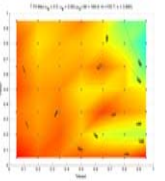	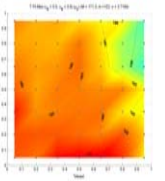	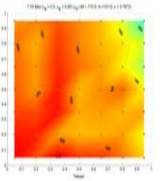
ε = 0.65	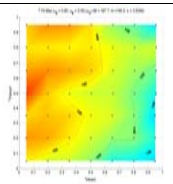	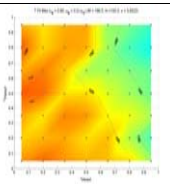	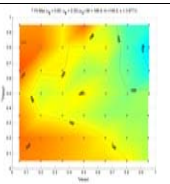	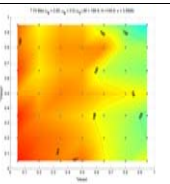	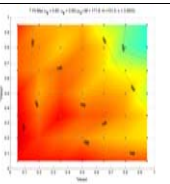	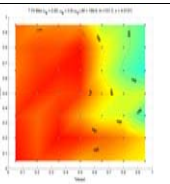	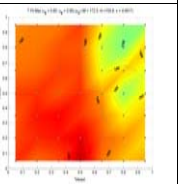
ε = 0.80	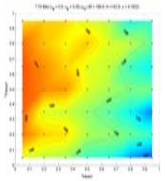	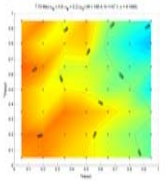	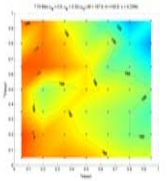	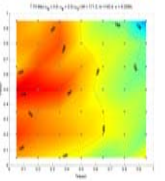	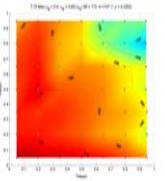	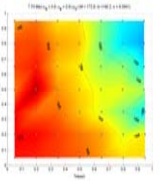	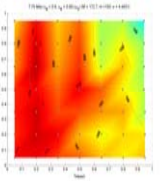
ε = 0.95	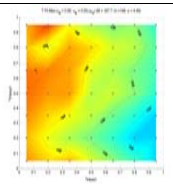	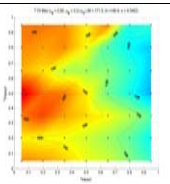	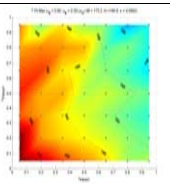	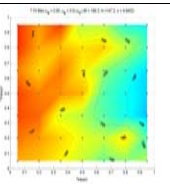	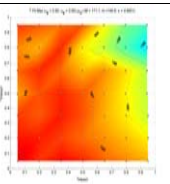	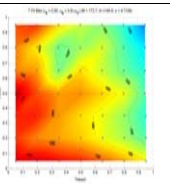	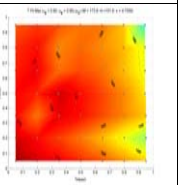

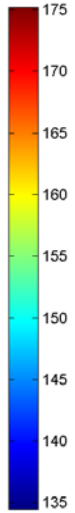

Estratto in lingua italiana

Il presente lavoro consiste nel design termico e nell'ottimizzazione di un sistema di schermatura per l'altimetro laser della missione BepiColombo (BELA), destinato ad operare nell'orbita di Mercurio.
Mercurio, il pianeta piú interno del sistema solare, é tuttora poco conosciuto; la missione ESA BepiColombo sará la prima missione Europea verso questo pianeta, e la prima missione europea nella quale sará sperimentata l'altimetria laser su di un altro pianeta. Come conseguenza delle peculiari condizioni termiche ed ambientali che caratterizzano un'orbita attorno al pianeta Mercurio, fin dalla prima fase della progettazione é stata evidenziata la necessitá di proteggere gli strumenti in modo molto piú estensivo di quanto viene fatto per tipiche missioni spaziali. La missione americana MESSENGER ha scelto di schermare il satellite dalla radiazione ambientale utilizzando un unico grande pannello protettivo, mentre la soluzione adottata dalla missione BepiColombo é stata quella di demandare ad ogni singolo strumento il compito di proteggersi dalla radiazione solare e planetaria. La maggior parte degli strumenti ha quindi sviluppato una specifica unitá per tale scopo.
La progettazione, lo svilluppo e la costruzione della parte transmittente di BELA é di competenza dell'agenzia spaziale tedesca (Deutschen Zentrum für Luft- und Raumfahrt, DLR). Lo strumento, sia nella parte transmittente che ricevente, deve necessariamente puntare verso la superficie di Mercurio: non é quindi possibile oscurare il pianeta per evitare l'irraggiamento, e l'unica soluzione consiste nell'implementazione di un filtro ottico per proteggere BELA dai flussi planetari. I flussi solari, invece, non possono essere efficacemente bloccati adottando un filtro, e si é deciso di adottare un pannello schermante (*baffle* in lingua inglese) per proteggere lo strumento dalla radiazione solare. Due differenti design sono stati proposti prima dell'avvio questo lavoro: il *baffle* cilindrico ed il design Stavroudis. L'analisi, dal punto di vista termico, delle due differenti geometrie e la determinazione della possibile realizzazione é stato il principale compito di questa tesi.
Il *baffle* cilindrico é decisamente semplice e basa il suo funzionamento sul mettere in ombra le componenti sensibili. Tuttavia, una larga parte della radiazione ambientale puó essere riflessa verso l'interno dello strumento, quindi per questa soluzione l'efficienza attesa dello strumento é relativamente bassa. I vantaggi di questo design consistono in leggerezza, poco ingombro, semplicitá ed affidabilitá. L'altra soluzione, chiamato *baffle* Stavroudis, é una complessa unione di ellissoidi ed iperbolidi, ottimizzata per riflettere la radiazione solare. Quest'ultimo design ha provato di essere il piú efficiente in assoluto, ma pone come svantaggi una grande complessitá realizzativa, pesi e volumi maggiori ed una minore affidabilitá.
Le condizioni ambientali dell'orbita di Mercurio sono state analizzate per tutte le anomalie del pianeta nel suo moto di rotazione attorno al Sole, e per tutte le posizioni del satellite attorno a Mercurio. Sono cosí state individuate le orbite critiche nelle quali i flussi ambientali sono massimo o minimi, e nei quali si concentrerá l'analisi termica. Durante queste analisi, l'evoluzione dell'orbita del satellite é stata tenuta in considerazione, ed é stato in tal modo possibile definire le condizioni critiche all'inizio della missione (BOL), al termine della missione nominale (EOL), ed al termine della missione estesa (EEM). Solo le prime due condizioni sono state considerate come dimensionati. Il massimo flusso solare (valore medio per un orbita) é stato calcolato pari a circa 800 $W \bullet m^{-2}$ quando Mercurio é al perielio, ed in tale posizione si ha anche il picco di albedo pari a circa 280 $W \bullet m^{-2}$; la massima radiazione planetaria (sempre in valore medio) si verifica invece quando l'anomalia del pianeta é 138.75°, ed é pari a 2100 $W \bullet m^{-2}$. Per tutti i casi critici caldi, il totale della radiazione ambientale media é pari approssimativamente a 3100 $W \bullet m^{-2}$. Sono state anche analizzate le possibili cause di deterioramente dei materiali e dei rivestimenti superficiali (*coating*) adottati: alte temperature, radiazione UV e V-UV, presenza di particelle cariche.
Sono stati quindi analizzate i possibili *coating* adottati per la versione cilindrica del *baffle* e per quella Stavroudis, valutando le proprietá termo-ottiche dei possibili rivestimenti e dei possibili trattamenti termici,

meccanici e di conversione chimica (anodizzazione). Tutti i *coating* in esame sono stati analizzati dal punto di vista della loro resistenza alle problematiche condizioni ambientali, determinando che la maggior parte di essi non é adatto ad operare nel critico ambiente costituito dall'orbita di Mercurio, e mentre altri non sono ancora stati testati per tale impiego. In conclusione, per la soluzione cilidrica del *baffle* in titanio é stata accertata la possibilitá di utilizzare levigatura meccanica e trattamenti termici (ossidazione), piú probabilmente l'anodizzazione. Il *baffle* Stavroudis, invece, prodotto mediante elettroformazione in nichel, non é adatto ad essere sottoposto a nessun trattamento o all'applicazione di *coating*. Il degradamento delle proprietá termo-ottiche di altri elementi, come per esempio l'MLI dello s/c, é stato determinato o stimato ed implementato nei modelli numerici. Una campagna di test, volta alla misurazione delle proprietá termo-ottiche, é stata svolta per determinare gli effetti di alcuni trattamenti termici e meccanici su alcuni campioni di titanio.

Il presente lavoro presenta una breve panoramica sulla modellazione termica, introducendo il problema differenziale e spiegando come esso venga trasformato in un modello a parametri concentrati ed implementato nei software commerciali, come ESARAD ed ESATAN, i programmi utilizzati nelle simulazioni. Viene anche fornita una breve panoramica su alcune procedure apportate per superare le limitazioni del software, consentendo la modellazione di complesse geometrie tridimensionali e recuperando la dipendenza dalla lunghezza d'onda delle proprietá termo-ottiche. I parametri di prestazione vengono definiti come l'efficienza di reiezione dei flussi ambientali, il valore dei flussi termici trasmessi al satellite e alla parte interna del laser, le temperature massime raggiunte dal *baffle* e dal filtro.

Viene quindi presentata la modellazione del *baffle* cilindrico, in particolare il modello geometrico radiativo ed il modello termico. Questo modello, semplificato, é stato oggetto di una estesa campagna che ha analizzato tutte le possibili combinazioni di proprietá termo ottiche, per individuare la condizione migliore e per studiare il principio di funzionamento del dispositivo al variare delle caratteristiche radiative della superficie. Tra i pochi trattamenti risultati realmente applicabili, i migliori risultati sono stati forniti dall'anodizzazione nella parte esterna del *baffle* e dall'uso di titanio non trattato per quella interna. Questo design ha tuttavia mostrato prestazioni relativamente basse, non soddisfacendo i requisiti termici imposti. Tra i parametri piú rilevanti, si possono citare la minima efficienza (76 %), la temperature massime del *baffle* e del filtro (378 °C e 142 °C rispettivamente), e l'elevato valore di flussi termici scaricati nel laser (2.4 W al picco).

Il design Stavroudis é stato successivamente presentato, mostrando la complessitá dei modelli radiativo e termico. La buona approssimazione geometrica del *baffle* é stata confermata dalla comparazione dei risultati di ESARAD con quelli di un software ottico dedicato, ZEMAX. I risultati di questo design sono molto migliori del precedente modello cilindrico, pur non essendo in grado di soddisfare tutti i requisiti termici. In particolare, l'efficienza é molto piú elevata (valore minimo: 94 %), i flussi assorbiti dallo strumento sono ridotti (< 0.6 W) e le temperature massime di *baffle* e filtro sono inferiori (235 °C e 89 °C rispettivamente).

I due differenti design del *baffle* sono stati comparati sulla base delle prestazioni termiche, strutturali e realizzative, e l'ingegnere di sistema ha optato per la versione che fa uso della geometria Stavroudis. Questa soluzione non é in grado di soddisfare tutti i requisiti, e comporta svantaggi dal punto di vista della massa, della complessitá e dei rischi, del costo economico, e del volume occupato. Un dato significativo riguarda la massa del *baffle* Stavroudis, che corrisponde a 970 g, contro un requisito iniziale di 160 g. Tuttavia é l'unica, tra le due soluzioni esaminate, con prestazioni adeguate allo strumento.

Possibili sviluppi di questo lavoro consistono in un affinamento dei modelli, nella determinazione dei parametri affetti da incertezze e nell'assemblaggio dei diversi modelli termici che compongono lo strumento. Un analisi del problema strutturale-termico-ottico accoppiato sarebbe molto interessante, ma non si conoscono software in grado di eseguire tale analisi in modo soddisfacente.

Acronyms and abbreviations

AO	Atomic Oxygen
AOI	Angle Of Incidence
ASD	EADS Astrium Friedrichshafen
BELA	BepiColombo Laser Altimeter
BOL	Begin Of Life
BSP	Baffle Support Panel
CAMI	Coated Abrasive Manufacturers Institute
CFRP	Carbon Fiber Reinforced Plastic
CTE	Coefficients of Thermal Expansion
DLR	Deutschen Zentrum für Luft- und Raumfahrt
EADS	European Aeronautic Defence and Space Company N.V.
EEM	End of the Extended Mission
EOL	End Of Life
ESA	European Space Agency
ESH	Equivalent Sun Hours
ESTEC	European Space Research and Technology Centre
HT-MLI	High Temperature Multy Layes Insulator
IR	InfraRed
JAXA	Japan Aerospace Exploration Agency
LEO	Low Earth Orbit
LHB	Laser Head Box
MESSENGER	MEercury Surface, Space ENvironment, GEochemistry and Ranging
MGS	Mars Global Surveyor
MLA	Mercury Laser Altimeter
MLI	Multy Layes Insulator
MMO	Mercury Magnetospheric Orbiter
MPO	Mercury Planetary Orbiter
PEL	Planetary Emissivity Laboratory
RBU	Receiver Baffle Unit
RTV	Room-Temperature Vulcanization
s/c	spacecraft
SC	Solar Constant
SPU	Straylight and contamination Protection Unit
Std-MLI	Standard Multy Layes Insulator
TBU	Transmitter Baffle Unit
UV	UltraViolet
VDA	Vapor Deposited Aluminium
VDG	Vapor Deposited Gold
VDS	Vapor Deposited Silver
V-UV	Vacuum UltraViolet
wrt.	with respect to

Bibliography

[1] Edited by D. L. Dominigue and C. T. Russel , “The MESSENGER Mission to Mercury”, Springer, 2007

[2] J. Benkhoff, J. Casteren, H. Hayakawa, M. Fujimoto, H. Laakso, M. Novara, P. Ferri, H. R. Middleton and R. Ziethe , “BepiColombo - Comprehensive exploration of Mercury: Mission overview and science goals”, Planetary and Space Science 58, pp. 2-20, 2010

[3] M. Novara, “The BepiColombo ESA cornerstone mission to Mercury”, Acta Astronautica Vol. 51, No. 1-9, pp. 387-395, 2002

[4] http://nssdc.gsfc.nasa.gov/nmc/spacecraftDisplay.do?id=BEPICLMBO

[5] http://nssdc.gsfc.nasa.gov/nmc/masterCatalog.do?sc=1973-085A

[6] https://www.courses.psu.edu/aersp/aersp055_r81/space_astronomy/mariner10.gif

[7] A. A. Siddiqi, “Deep Space Chronicle – A Chronology of Deep Space and Planetary Probes – 1958-2000”, Monographs in Aerospace History, Number 24, NASA SP-2002-4524, June 2002

[8] http://nssdc.gsfc.nasa.gov/nmc/spacecraftDisplay.do?id=2004-030A

[9] http://www.windows.ucar.edu/tour/link=/space_missions/robotic/messenger/messenger.html

[10] http://www.skyrocket.de/space/doc_sdat/bepicolombo-mpo.htm

[11] H. Yamakawa, H. Ogawa, Y. Kasaba , H. Hayakawa, T. Mukai, and M. Adachi, “Current status of the BepiColombo/MMO spacecraft design”, Advances in Space Research 33, pp. 2133–2141, 2004

[12] http://www.skyrocket.de/space/doc_sdat/bepicolombo-mmo.htm

[13] J. B. Abshire, X. Sun, H. Riris, J. M. Sirota, J. F. McGarry, S. Palm, D. Yi, and P. Liiva, “Geoscience Laser Altimeter System (GLAS) on the ICESat mission: on-orbit measurement performance”, Geophysical Review Letters 32, L21S02, 2005

[14] A. S. McEwen and M. S. Robinson, “Mapping of the Moon by Clementine”, Advances in Space Research, Vol. 19, Issue 10, pp. 1523-1533, 1997

[15] S. M. Som, H. M. Greenberg and D. R. Montgomery, “The Mars Orbiter Laser Altimeter dataset: Limitations and improvements”, MARS Journal, 11th June 2008

[16] G. A. Neumann, F. G. Lemoine and M. H. Torrence, “Laser altimetry and the cartography of Mars, Moon, and 433 Eros”, AGU Fall Meeting Abstracts, 2002

[17] N. Thomas, T. Spohn, J. P. Barriot, W. Benz, G. Beutler, U. Christenses, V. Dehant, C. Fallnich, D. Giardini, O. Groussin, K. Gunderson, E. Hauber, M. Hilchenbach, L. Iess, P. Lamy, L. M. Lara, P. Lognonné, J. J. Lopez-Moreno, H. Michaelis, J. Oberst, D. Resendes, J. L. Reynaud, R. Rodrigo, S. Sasaki, K. Seiferlin, M. Wieczorek and J. Whitby, “The BepiColombo Laser Altimeter (BELA): Concept and baseline design”, Planetar and Space Science 55, pp. 2398-1413, 2007

[18] G. Messina, “Internal Thermal Interface Specification”, Issue 2, Rev. 1, BC-BEL-IF-32001-2-1, 28th December 2008

[19] A. F. Cheng, T. D. Cole, M. T. Zuber, D. E. Smith, Y. Guo and F. Davidson, “In-flight calibration of near Earth asteroid rendezvous laser rangefinder”, Icarus 148, pp. 572-586, 2000

[20] N. Thomas, “BELA Instrument Requirements Document”, BC-BEL-RS-10001-1-3, 8th December 2007

[21] K. Seiferlin, S. Chakraborty, K. Gunderson, J. Fischer, B. Lÿuthi, D. Piazza, M. Rieder, M. Sigrist, N. Thomas and T. Weigel, “Design and manufacture of a lightweight reflective baffle for the BepiColombo Laser Altimeter”, Optical Engineering 46(4), 043003, April 2007

[22] http://www.redoptronics.com/sapphire-optical-material.html

[23] K. Lingenauber, D. Ludena and G. Messina, “TBU design report”, BC-BEL-TN-41008-0-2, Issue 0, Rev. 2, 26th October 2007

[24] D. Radovich, “Elliptic Cylindrical Baffle Assembly”, US Patent 4,217,026 12th August 1980

[25] Contraves Space, "Reflective Baffle for Bepi Colombo Study – Final Report", BELA-CSAG-RP-BAF-00008, Issue 1, August 2005
[26] G. L. Peterson, S. Johnson and J. Thomas, "Specular Baffles – Stray Radiation in Optical Systems II", Proc. SPIE Vol 1573, pp. 65-76, 1992
[27] O. N. Stavroudis, "System of reflective telescope baffles usings conic sections of revolution", US Patent 5,225,931, 6th July 1993
[28] O. N. Stavroudis and L. D. Foo, "System of reflective telescope baffles", Optical Engineering, , Vol. 33, No. 3, pp. 675-680, March 1994
[29] R. N. Pfisterer and G. L. Peterson, "Dual Reflective Baffle System for the BeCoat Telescope", Advanced Optical Manufacturing and Testing IV, SPIE Vol. 1994, pp. 112-121, 1994
[30] W. I. Linlor, "Optical System with Reflective Baffles", US Patent 4,542,963, 1985
[31] W. I. Linlor, "Reflective baffle system with multiple bounces", Proceedings of the SPIE Vol. 0675, Stray Radiation V, pp. 217-239, 1987
[32] R. Winston, "Dielectric compound parabolic concentrators", Applied Optics, Vol. 15, No. 2, February 1976
[33] G. A. Vanesse, "Telescope Baffle System", US Patent 5,189,554, 1993
[34] Edited by E. A. Brandes and G. B. Brook, "Smithells Metals Reference Book", 7th edition,1999, Bath, Great Britain
[35] A. K. Sharma, "Anodizing Ti for space applications", Thin Solid Films XX, 4X 54, 1992
[36] L. Kauder, "Spacecraft Thermal Control Coatings Reference", NASA/TP-2005-212792, 2005
[37] J. H. Henninger, "Solar absorptance and thermal emittance of some common spacecraft thermal-control coatings", NASA-RP-1121, April 1984
[38] H. Hiesinger, J. Helbert and the MERTIS Co-I Team, "The Mercury Radiometer and Thermal Infrared Spectrometer (MERTIS) for the BepiColombo mission", Planetary and Space Science 58, pp. 144–165, 2010
[39] M. Glier and S. Kaiser, "TBU-RBU Baffle Optical Analysis", BC-BEL-AN-35500, Issue 1, Rev. 1, 12th February 2009
[40] NiCoForm Inc., "NiCoForm: Resourceful Solutions for Extraordinary Applications. State of the art.", available on-line at http://www.nicoform.com
[41] Y. A. Çengel, "Introduction to Thermodynamics and heat transfer", McGraw-Hill Companies, Inc., 1997
[42] Maestro Sargento, Pbroks13, http://en.wikipedia.org/wiki/File:Eformschematic.svg
[43] J. Barbe', "Mercury Thermal Model", Technical Note EWP-2190, Issue 1, Rev. 5, ESTEC, 20th August 2003
[44] D. Stramaccioni, "Mercury Environmental Specification (Part I)", BC-EST-TN-00112, Issue 4, Rev. 0, 1st November 2006
[45] MAO Working Paper No. 466, "BepiColombo Mercury Cornerstone Consolidated Report on Mission Analysis", BC-ESC-RP-05500, ESOC
[46] D. R. Williams, "Mercury Fact Sheet", http://nssdc.gsfc.nasa.gov/planetary/factsheet/mercuryfact.html
[47] Compiled by R. E. Smith and G. S. West, "Space and Planetary Environment Criteria Guidelines for Use in Space Vehicle Development, 1982 Revision", NASA Technical Memorandum 82478, 1983
[48] P. Poinas, "ISRR Thermal - Mercury Environmental Specification Complementary Information", ESA/TEC-MCT, 9th May 2007
[49] S. Heltzel, C. O. A. Semprimoschnig and M. R. J. van Eesbeek, "Environmental testing of thermal control material at elevated temperature and high intensity UV radiation", Material Physics and Chemistry Section (TEN-QMC), European Space Agency (ESA-ESTEC)
[50] D. L. Edwards, "Evaluation od chemical conversion material (protective coating) exposed to space environment conditions", CDDF Final Report (No. 90-07), NASA TM-108416, July 1993
[51] ISO/DIS 21348:2005 "Space environment (natural and artificial) - Process for determining solar irradiances", 01st July 2005

[52] R. R. Kamenetzky, J. A. Vaughn, M. M. Finckenor and R. C. Linton, "Evaluation of Thermal Control Coatings and Polymeric Materials Exposed to Ground Simulated Atomic Oxygen and Vacuum Ultraviolet Radiation", NASA Technical Paper 3595, December 1995
[53] The BepiColombo project team, "The Mercury Environment RSSA", available on-line in September 2009
[54] The BepiColombo project team, "Experiment Interface Document – Part A", BC-EST-RS-01140, Issue 1, Rev. 0, ESA, 31st January 2008
[55] ISO 6344-1:1998, "Coated abrasives, sizes and tests"
[56] ISO 6344-2:1998, "Macrogrit, P12 to P220"
[57] ISO 6344-3:1998, "Microgrit, P240 to P2500"
[58] K. C. Mills, "Reccomended values of thermophysical properties for selected commerial alloys", 2002
[59] A. Avila-Garcia and U. Morales-Ortiz, "Thermally and air-plasma-oxidized titanium and stainless steel plates as solar selective absorbers", Elsevier, May 2006
[60] Edited by D. G. Gilmore, "Spacecraft Thermal Control Handbook – Volume I: Fundamental Technologies", The Aerospace Press, El Segundo, California, USA & American Institution for Aeronautics and Astronautics, Inc., Reston, Virginia, USA, second edition, 2002
[61] C. Kramer, URL http://www.valhallaarms.com/wyvern/titanium/anodizing.htm
[62] J.-L. Delplancke, M. Degrez, A. Fontana and W. Winand, "Self-colour anodizing of Titanium", Surface Technology, n. 16, pp. 153-162, 1982
[63] M. Born and E. Wolf, "Principles of Optics", Pergamon, Oxford, 1965
[64] J. P. Mathieu, "Optique", "Volume 1 - Optique Electromagnetique", Société d'Edition d'Enseignement Supérieur, Paris, 1965
[65] S. Tolansky, "Multiple-beam Interference Microscopy of Metals", Academic Press, New York, 1970
[66] F. P. Incropera and D. P. De Witt, "Introduction to heat transfer", ed. By John Wiley & sons, Inc., Singapore, Second edition, 1990
[67] TIODIZE® brochure, available on-line at http://www.tiodize.com/pdf/testingchapter.pdf
[68] A. Maturilli, J. Herbert, A. Witzke and L. Moroz, "Emissivity measurements of analogue materials for the interpretation of tdata from PFS on Mars Express and MERTIS on Bepi-Colombo", Planetary and Space Science 54, pp. 1057-1064, 4th 2006
[69] G. Rybicki and A. P. Lightman, "Radiative Processes in Astrophysics", New York: Wiley-Interscience, p. 25, 1979
[70] W. M. Rohsenhow, J. P. Hartnett and Y. I. Cho, "Handbook of Heat Transfer", Third Edition, McGraw-Hill, 1998
[71] http://en.wikipedia.org/wiki/File:Orbit1.svg
[72] Alstom Aerospace, "ESARAD user manual", UM-ESARAD-024, Issue 7, Rev. 0, October 2007
[73] O. V. Hansen, "Surface temperature and emissivity of Mercury", The Astrophysical Journal 190, pp. 715-717, 15th June 1974
[74] 2006 CODATA recommended values, "NIST Reference on Constants, Units, and Uncertainty", URL http://physics.nist.gov/cuu/Constants/index.html
[75] S. C. F. Sheng, O. Berendsohn, M. R. Schreibman and L. M. Cohen, "Correlation of RTV properties to test data and its effect on the AXAF mirror performance", Advanced Optical Manufacturing and Testing, Vol. 1333, pp. 314–324
[76] F. Toigo, A. Marvin, V. Celli and N. R. Hill, "Optical properties of rough surfaces: General theory and the small roughness limit", Physical Reviews B 15, pp. 5618–5626, 1977
[77] J. A. McGeough, M. C. Leu, K. P. Rajurkar, A. K. M. De Silva and Q. Liu, "Electroforming Process and Application to Micro/Macro Manufacturing", CIRP Annals - Manufacturing Technology, Volume 50, Issue 2, pp. 499-514, 2001
[78] T. Beck, "Thermal Analysis of BELA Baffle", BC-BEL-TN-10001, Version 1, Rev. 1, 17th September 2007